UNIVERSITÉ DE STRASBOURG

ÉCOLE DOCTORALE PHYSIQUE ET CHIMIE PHYSIQUE (ED 182)

Institut Charles Sadron (UPR-22 CNRS)

THÈSE présentée par :

Monika KLUZEK

soutenue le : **10 Octobre 2017**

pour obtenir le grade de : **Docteur de l'université de Strasbourg**

Discipline: Physique
Spécialité : Biophysique

Lipid membrane alteration under exposure to α-Cyclodextrins and pH-responsive pseudopeptide polymers

THÈSE dirigée par :

M. THALMANN Fabrice	Assistant Professor, Université de Strasbourg

RAPPORTEURS :

M. LAMBERT Oliver	Directeur de recherche, Université de Bordeaux
M. GUENOUN Patrick	Ingénieur CEA, Saclay

AUTRES MEMBRES DU JURY :

M. SEDDON John	Professor, Imperial College London
Mme. HELLWIG Petra	Professor, Université de Strasbourg
M. SCHMUTZ Marc (co-directeur)	Ingénieur de recherche, Université de Strasbourg

Preface

This thesis has been submitted as a part of the requirements to obtain a PhD degree at the University of Strasbourg. The work has been conducted at the MCube - Membrane and Microforces, Institut Charles Sadron, Strasbourg, France, in a period from July 2014 to October 2017, under the supervision of Assoc. Prof. Fabrice Thallman and Dr Marc Schmutz. Part of the work was conducted at University of Manchester, U.K., in the Laboratory of Prof. Jian Lu, and in the group lead by Prof. John Seddon at Imperial London College, U.K.

The general scientific field of the thesis is membrane biophysics, and the specific topic is the interaction of nanomaterials with model lipid membranes. This thesis contains three experimental studies and literature review. The study on the interaction of pH-sensitive polymer with cubosomes has been published under the title *Influence of pH-sensitive polymer on the structure of monoolein cubosomes*, the experimental studies on lipid extraction by cyclodextrins are in a peer-reviewing process, while the last study on pH-sensitive polymers still ongoing.

This thesis includes a Motivation for the project (Chapter 1), an Introduction (Chapter 2), an introduction to experimental Materials and methods used in the project (Chapter 3), introduction to Cyclodextrins properties and a summary of the results (Chapter 4). Literature review about non-lamellar lipid phases and summary of the results (Chapter 5). Study of pH-sensitive polymer interplay with model lipid membrane are included in Chapter 6. Concluding remarks can be found in Chapter 7. The introduction should give the reader an overview of the scientific topics of the thesis, including biological background, and the methods and technologies used in the scientific work. The specific methods and data analysis are given together with the full-length manuscripts.

Monika Kluzek, October 2017

List of publications

The paper and manuscripts included for evaluations in this PhD thesis are:

- *Kluzek M.*, Tyler A., Wang S., Chen R., Thalmann F., Marques C.M. Seddon J., Schmutz M. ’Influence of a pH sensitive polymer on the structure of monoolein cubosome’ published
- *Kluzek M.*, Marques C.M., Schmutz M., Thalmann F. ’Kinetic evolution of DOPC lipid bilayers exposed to α-cyclodextrins’ in preparation

The following manuscripts based on work carried out during PhD, but not included for evaluation:

- *Kluzek M.*, Morandi M.I., Ciumac D., Marques C.M., Thalmann F., Lu J.’A SANS study of polystyrene effects on lipid bilayer structure upon phase transition’ in preparation
- Morandi M.I., Sommer M, *Kluzek M.*, Thalmann F., Schroder A. and Marques C. M.’DPPC bilayers in solutions of high sucrose content’ peer-review

One poster abstract of work from the thesis has been published:

- *Kluzek M.*, Thalmann F., Schmutz M., Marques C. ’Ring and Tails: Exploring the intimacy of cyclodextrin – membrane interactions’. Biophysical Journal 112, 223a(2017)

Acknowledgements

Numerous people have had a hand in the completion of my PhD thesis. I have been associated with MCube since July 2014, and have warm feelings to this scientific and social environment. It has been a privilege to work at MCube, and I want to thank all present and former members for having contributed to the MCube atmosphere.

I owe great thanks and am very grateful to:

Fabrice Thalmann, for being my supervisor the last three years. Fabrice has a constant drive and tone of new ideas. I would like to thank him for his advice when helping me communicating my results in writing.

Marc Schmutz, for being my supervisor and mentor since I first came to MCube. Marc always has a good answer for many problems. He is an inspiration for any scientist and microscopist. Marc has always given me opportunities for which I am very grateful.

The members of the graduate committee for accepting to evaluate my work and provide their professional expertise.

Carlos Marques, for creating such an amazing scientific environment at MCube, for his deep insights and inspiring discussions that stimulated my interest in membrane biophysics.

André Schroder, for his encouragement and skilled advice. André’s enthusiasm and interest in this work has been an inspiration and is greatly acknowledged.

John Seddon, for hosting me in his group at Imperial College London during autumn 2015. I have enjoyed the collaboration a lot, and the whole group is an amazing stimulating environment. Hanna Barriga and Arwen Tyler are thanked for good scientific discussions and social interactions.

Jian Lu, for having me as a visitor in his group at the University of Manchester in the autumn of 2016 to learn about SANS technique and data analysis. Daniela Ciumac is

thanked for the outstanding enjoyable collaboration, and for the friendship evolving as its extension.

Rongjun Chen and Shiqi Wang for fruitful collaboration on pH-sensitive polymer project.

Yulia Moskalenko, for a great help and suggestions with NMR analysis.

Laurie Biniek, Rigoberto Ibarra, Mattia Morandi, Agnieszka Kopec, Rafal Jeczalik, Johann Lacava, Amer Sakr, Amparo Ruiz-Carretero, Morgane Diebold, Othmene Benazieb, Magdalena Olesinska, Chanfei Su and Anna Sofia Tascini for valuable friendship and great discussions about everything-and-anything whenever needed.

The ITN Maria Curie-Sklodowska consortium, for project funding, which allowed me essentially unlimited traveling during my PhD. Lots of scientific input and connections has been the outcome.

My family and friends for being encouraging and supportive. The support from them means the world of a difference.

Contents

Abbreviations

1-MO = 1- Oleoyl-rac-glycerol

CD = Cyclodextrin

Chol = Cholesterol

Cryo-TEM = Cryo-transmission electron microscopy

DiI = 1,1’-dioctadecyl-3,3,3’,3’-tetramethylindocarbocyanine

DLS = Dynamic light scattering

DOPC = 1,2-dioleoyl-sn-glycero-3-phosphocholine (18:1 (Δ9-CIS))

DPPC = 1,2-dipalmitoyl-sn-glycero-3-phosphocholine (16:0)

d_{31}POPC = 1-palmitoyl-d_{31}-2-oleoyl-sn-glycero-3-phosphocholine (16:0-d_{31}-18:1)

DSC = Differential scanning calorimetry

HPTS = 8-Hydroxypyrene-1,3,6-Trisulfonic Acid, Trisodium Salt

ITC = Isothermal titration calorimetry

Laurdan = 6-Dodecanoyl -2-Dimethylaminonaphthalene

NMR = Nuclear magnetic resonance spectroscopy

LSCM = Laser scanning confocal microscopy

QCM-D = Quartz crystal microbalance

SANS = Small angle neutron scattering

SAXS = Small angle x-ray scattering

CPP = Critical packing parameter

Symbols

$\boldsymbol{\Delta\Sigma/d\Omega}$ = Macroscopic differential scattering cross section

$\boldsymbol{\Delta\sigma/d\Omega}$ = Differential scattering cross section

$\boldsymbol{\Delta\rho}$ = Excess scattering length density or contrast

$\mathbf{b}$ = Scattering length

$\boldsymbol{\rho}$ = Scattering length density

$\boldsymbol{\sigma}$ = Scattering cross section

$\boldsymbol{R}_g$ = Radius of gyration

$\boldsymbol{\beta}$ = Boltzmann unit

$\boldsymbol{K}_a$ = Association constant

$\boldsymbol{n}_{holes}$ = Number of holes

$\boldsymbol{w}_{holes}$ = Number of lipids extracted per hole

$\boldsymbol{\theta}$ = Fraction of covered surface

$\boldsymbol{R}$ = Universal gas constant

$\boldsymbol{N}_{CD}$ = Number of moles of αCD molecules

$\boldsymbol{N}_{PL}$ = Number of moles of phopsholipids molecules

$\boldsymbol{t}extita$ = Stochiometric ratio of αCD/lipid molecules complexation

1 | Motivation for the project

For the last decade, researchers have diligently worked towards enhancing safety along with maximising efficiency of drug treatment. One of the major obstacles for drug agents to reach the target cell compartments is their limited penetration through biological membranes, a difficulty arising chiefly from physicochemical properties such as poor water solubility, permeability or short circulating half-life time [1]. A large variety of (in)organic nanomaterials [2] is currently employed as drug-delivery carriers, in order to protect their cargo, the drug, from degradation in the cell environment and simultaneously facilitating their transport through biological membranes. This nanoparticle-delivery strategy becomes a powerful platform providing a number of advantages, such as improved solubility of hydrophobic drugs, suppressed immunogenicity and reduced side effects, together with releasing drugs in a stimuli-triggered manner. To date, *i)* liposomes [3] *ii)* quantum dots [4] *iii)* polymeric micelles *iv)* dendrimers [5, 6] *v)* polymer-drug conjugates [7] and *vi)* pH sensitive materials [8–10] have emerged as classes of nanoscale delivery systems. Importantly, many of them already have reached clinical applications.

Despite the numerous positive features of this platform, knowledge about interactions between nanomaterials and cell membranes is still missing [7, 11]. The permeation and transport of a nanomaterial across biological membranes are of crucial importance for the ability of nano-carriers to reach their cellular target. It is then necessary to determine the ways in which nano-carriers interact with a cell membrane. Specifically, the questions of how nanomaterials influence the local structure and composition of the bilayer and how the changes in membrane physical properties modulate the functioning of drug delivery system are of prime importance. In this context, biophysical studies of lipid model systems have been instrumental for understanding forces and interactions between cell membrane and nanoparticles [12].

The motivation for the present study is to gain novel, fundamental insights into the structure-activity relationship of several nano-materials with biological membranes and its impact on the membrane physicochemical properties. We focus on characterizing interactions of three types of drug delivery system with a model lipid membrane:

- Reorganization of lipid membranes mediated by the presence of α-cyclodextrin. We address the cyclodextrin - mediated extraction of lipid from the membrane, a phenomen first reported by Debouzy's [13] using human red blood cell. This is discussed in Chapter 4.
- Characterization of cubosomes and their potential in controlled drug delivery. Our aim here was to take advantage of a pH-stimuli polymer to engineer a new host-guest cubosomal system, with a pH-triggered release switch, as presented in Chapter 5.
- Translocation of a pH sensitive polymer through lysozyme-mimicking membrane. In this review, we focused on how the external pH affects the diffusion through lipid membrane of a stimuli responsive polymer, and how the membrane composition dictates the mechanism of this process. (The results of this study are included in Chapter 6).

We use state-of-the-art visualisation techniques (Cryo-TEM, LSCM), complemented by a body of calorimetry (ITC, DSC), surface characterization (QCM-D) and scattering (SANS, SAXS) data. To the best of our knowledge, there is only a limited literature on this subject [14], therefore we hope to contribute both to the basic and applied research revolved around the nanoparticle/lipid membrane interplay and the drug delivery systems in general.

2 | Introduction

2.1 The plasma membrane

The cell membrane is an essential component of all living cells. It determines the boundaries between the cell interior and the cell external environment, and plays an essential role in the cellular protection. Furthermore, the cell membrane is a selectively permeable barrier for ions, nutrients, wastes and metabolic products, orchestrating their transport between the intra- and extra- cellular environments, leading to an efficient mechanism of communication between the cell and its surroundings. Many important cellular processes, including control and transport of nutrients, molecular recognition and immunological response either take place in the membrane or are mediated by the membrane [15]. Therefore, the membrane integrity and proper functioning is of utmost importance for a healthy cell.

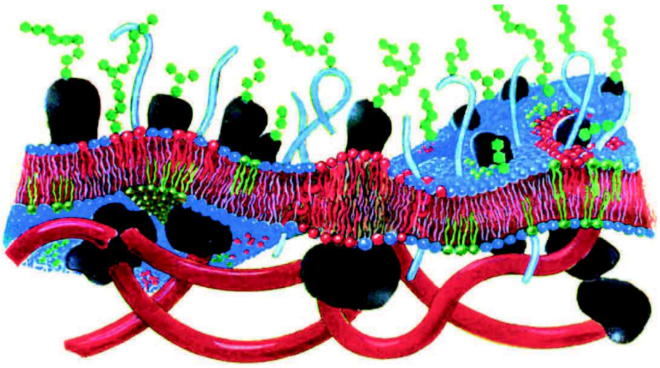

Figure 2.1: Model of the plasma membrane of a eukaryotic cell. The cell membrane displays lateral heterogeneity, lipid domains, and thickness variations. Adapted from [12].

Biological membranes are supramolecular assemblies, composed of a lipid bilayer and protein molecules embedded in the lipid matrix (Figure 2.1). As typical cell membranes consist of hundreds of phospholipid types, cholesterol, and many different types of membrane proteins, membranes are complex environments, difficult to study experimentally. In 2017 the research team of Katsaras [16] has completed the very first scan of a living cell membrane, which gave room for a longstanding debate about membrane functioning. However, membrane-related processes such as nanoparticle translocation in living cell membranes is still beyond the scope of current experimental techniques.

Many critical physicochemical properties of biological membranes can be captured and understood from studies on model lipid bilayers, formed by only one or few types of lipids. The lipid bilayer exhibits numerous properties arising from the cooperative interactions between lipid molecules. It is a two dimensional, two lipid molecules (5 nm) [17, 18] thick sheet-like structure, with two interfaces with water, created by two hydrophilic lipid headgroups, and a non-polar core, formed by hydrophobic lipid tails. Such a structure provides an efficient barrier for the cell, as aqueous solutions are excluded from the bilayer core. Moreover, since the lipid molecules are held together via combinations of weak interactions, such as Van der Waals interactions, hydrophobic effect and electrostatic forces, the lipid bilayer belongs to the class of soft matter materials. Soft materials display a high degree of deformability, therefore their physical properties are largely controlled by entropic contributions. This poses additional challenges in predicting the effects of other molecules and complexes on the membrane structure.

2.2 Plasma membrane lipids

The exact composition of biomembranes varies among different types of organisms, however all cell membranes share a generic lipid bilayer structure. Currently, many individual lipid species have been identified along with their synthetic pathways and physiological relevance [19]. The dual nature of lipids is achieved by their amphiphilic structure: hydrophilic headgroups and hydrophobic acyl chains. When mixed with water, lipids spontaneously self-assemble into regular aggregates, such as spherical micelles, lipid membranes, or more complex systems, as shown in Figure 2.2. The formation of these supramolecular structures is driven by the hydrophobic effect, which minimizes the contact area between water molecules and acyl chains by the rearrangement of lipid head groups. Thus, the geometry of the resulting structures strongly depends on the effective shape of lipid molecules [12]. Lipids display a great range of chemical diversity, which vary in general structure such as chain lengths (number of carbons), degrees of saturation, head group sizes, and charge [12] (Figure 2.2). The structure of membranes and the associated cohesive forces are further discussed in Chapter 5 where we describe nonlamellar lipid aggregates.

Lipids that can be found in mammalian plasma membranes fall into three main classes of lipids: *i)* glycerophospholipids (also named phospholipids, PL), *ii)* sphingolipids (SLs) and *iii)* sterols, such as cholesterol, together with isoprenoids (Figure 2.3).

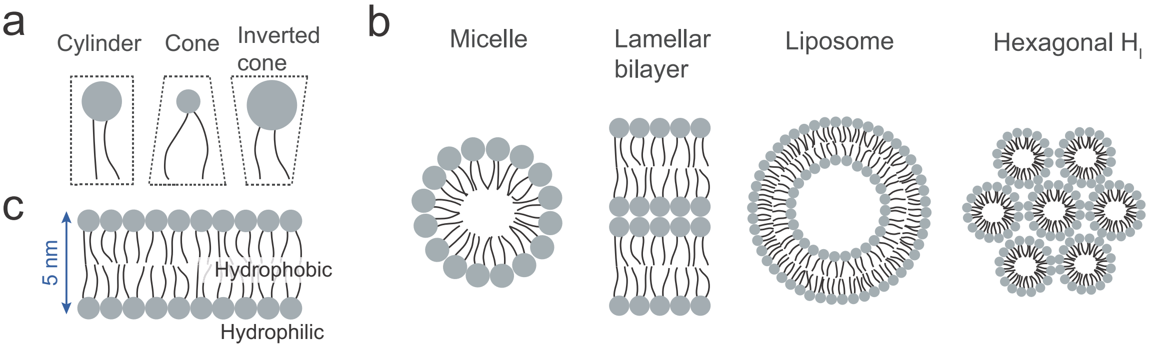

Figure 2.2: Diversity of lipid structures. a) Lipids are amphiphilic molecules comprising hydrophobic tails and hydrophilic heads. Depending on their nature, lipid molecules have different effective shapes b) In aqueous solution lipids self-assemble into different structures c) In lipid membranes, lipids are arranged in a tail-to-tail manner leading to a thickness of ~5nm.

The chemical structure of PLs is based on a glycerol backbone to which two fatty acid hydrocarbon chains are bound in adjacent positions [sn-2 (β), sn-1 (γ)]. The sn-3 position of the glycerol is occupied by a phosphate group linked to an alcohol (e.g. choline, ethanolamine or serine), which constitutes the hydrophilic head. The diversity among fatty acids is large (chain length, degree of unsaturation) and it largely contributes to the elasticity of the membrane.

SLs, another important group of structural lipids, are derivatives of sphingosine, which is a long-chain amino alcohol with an attached hydrocarbon chain. The most common sphingolipids are sphingomyelins: sphingophospholipids with either phosphocholine or phosphoethanolamine headgroups. The structural features of sphingolipids allows them to pack tightly together through the van der Waals interactions explaining the physicochemical properties of these lipids in biological membranes.

Cholesterol is a dominant sterol and is universally present in the plasma membranes of eukaryotic cells, in contrast to prokaryotic cells from where it is universally absent [21]. The structure of cholesterol is peculiar, see Figure 2.3. It has a rigid four-ring hydrocarbon structure with a short hydrocarbon chain attached to it. Further, cholesterol has a small headgroup constituted by just a hydroxyl group. It determines the orientation of cholesterol in the bilayer, and its interactions with polar headgroups of neighbouring lipids. The presence of cholesterol has an important impact on thickness, fluidity, bending rigidity and permeability of a lipid membrane. The cholesterol content of various cell membranes varies from 0% up to 25% [22, 23]. The interaction of cholesterol with sphingolipids is also important for the formation of functional platforms in the membrane, called rafts, as suggested by Simons and Ikonen in 1997 [24]. These domains may limit the diffusion of biomolecules and impart membrane functionality. After years of debate [25], in 2017 for the first time, Katsaras *et al.* [15] reported direct visual evidence of nonuniform mixing within the plasma membrane.

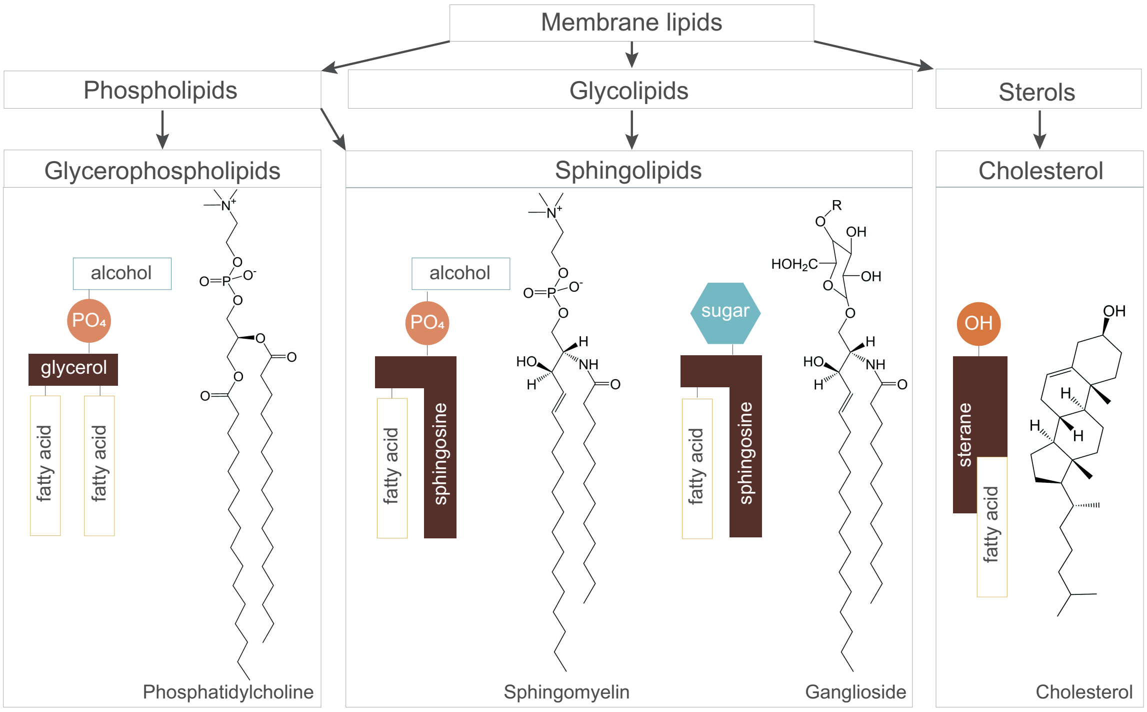

Figure 2.3: Plasma membrane lipid species. Glycerophospholipids are major components of membrane lipids. GPLs are glycerol-backboned molecules with variable fatty acid hydrocarbon chains attached in one side, and various types of headgroups in the other. Sphingolipids are derivatives of sphingosine, which encompass an amino alcohol with a long hydrocarbon chain. Various fatty acid chains are attached to the sphingosine, which is also coupled to either phosphate-alcohol, or to sugar moieties such as glycosphingolipid (GSL). Glycosphingolipids coupled to sialic acids are called gangliosides Cholesterol is a sterol, with four-ring hydrocarbon body and an attached short hydrocarbon chain. The polar headgroup of cholesterol is a single hydroxyl group. Adapted from [20].

Most cell membranes were shown to exhibit an asymmetric lipid distribution between the two leaflets, which are maintained by cellular processes. However, underlying reasons and implications of this asymmetric composition is still poorly understood. The negatively charged lipids are predominantly found in the inner leaflet as a well as the major fraction of zwitterionic ethanolamine (PE) phospholipids [26]. On the other hand, the outer leaflet of membrane contains mainly zwitterionic choline (PC) phospholipids and sphingomyelin (SM). In contrast, cholesterol is equally distributed in both leaflets of the eukaryotic membrane.

The motions of lipid within the lipid bilayer can be divided into three modes, occurring on different timescales. The fastest mode is the rotational motion – the spinning of a lipid around it long axis (parallel to the membrane normal). The second is the lateral mode – essentially a Brownian motion of a lipid within one leaflet, which effectively leads to exchanges of lipid molecules with their neighbours. Finally, the slowest mode is the transverse motion, often called flip-flop. This mode allows lipids to exchange between the leaflets, involving a 180° flip with respect to the membrane centre.

Altogether, the plasma membranes surface, the first site for nanoparticle interactions, has a very distinct lipid organization varying between cells in a number of properties such as charge, lipid type, packing and organization, which affects the effective interaction and translocation of pharmaceutical agents and nanoparticles.

2.2.1 Thermodynamics of lipid membranes

Aqueous dispersion of lipid assembly shows a series of lyotropic and thermotropic phase behaviours. This transition can be evoked by temperature, concentration, ionic strength or effective shape of a lipid molecule [27]. The main transition is predominantly lamellar-lamellar and is associated with melting of the lipid molecule (Figure 2.4). These thermodynamic properties have been studied in detail for the last four decades [23, 28]. Description of fluid–fluid transitions that involve a change of symmetry and/or topology can be found in Chapter 5.

2.2.2 Phase transitions

At low temperatures, the lipid headgroups are packed close together, whilst lipid chains are 'all-in-trans' configuration with minimal entropy. This so-called solid-ordered- (S_o) phase, (alternatively the *gel phase*) shows lower lateral and rotational lipid diffusion as well as smaller area per lipid, which results in more rigid membranes. At higher temperatures, the lipids are able to diffuse laterally, and acyl chains can adopt varying conformations (high entropy). This phase is called the liquid-disordered- (L_d) phase, or simply the *fluid phase*.

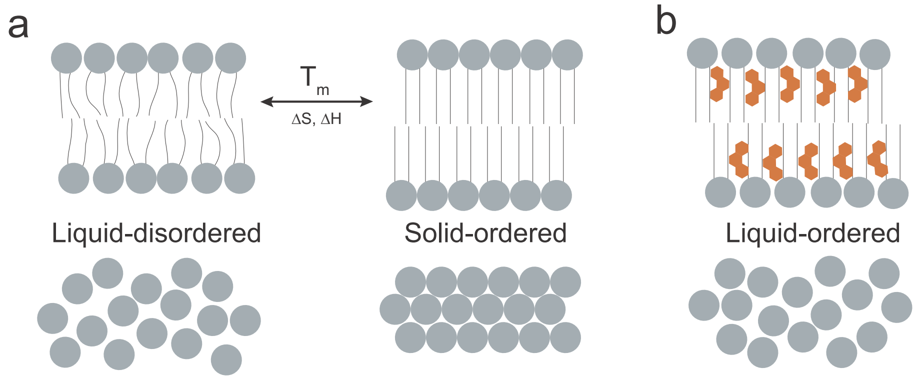

Figure 2.4: Lipid phases. a) In L_d-phase lipids are mobile, expressing various tail conformations. Below transition temperature, T_m , lipids are tightly packed creating ordered-S_o-phase b) L_o-phase with cholesterol. Presence of cholesterol imposes order within tail region.

The transitions between phases is a cooperative phenomenon, and occur at well-defined temperatures. The transition temperature, T_m [29], among other parameters is strongly influenced by the length and degree of unsaturation of acyl chains, head group size and charge [30]. Assuming that lipid chains can adopt just one configuration per phase, the melting point, T_m, can be defined as the temperature at which both the ground state and excited state are equally likely:

$$\frac{P_{disordered}(T_m)}{P_{all-in-trans}(T_m)} = e^{-\Delta G/RT_m} = 1 \tag{2.1}$$

Or by Gibbs free energy difference:

$$\begin{aligned} \Delta G = \Delta H - T_m \Delta S &= 0 \\ T_m &= \frac{\Delta H}{\Delta S} \end{aligned} \tag{2.2}$$

where ΔH is an enthalpy and ΔS is entropy of melting.

It should be noted that ΔH and ΔS values strongly depends on the length and saturation of lipid tails, and thus the value of transition temperature. However, as was reported, other factors, such as cations (divalent ions) [31], addition of neurotransmitters and general anaesthetics (e.g. alcohols, chloroform, etc.) [32, 33] membrane hydration [34, 35], membrane curvature [36], hydrostatic pressure and pH [37] can affect the transition temperature.

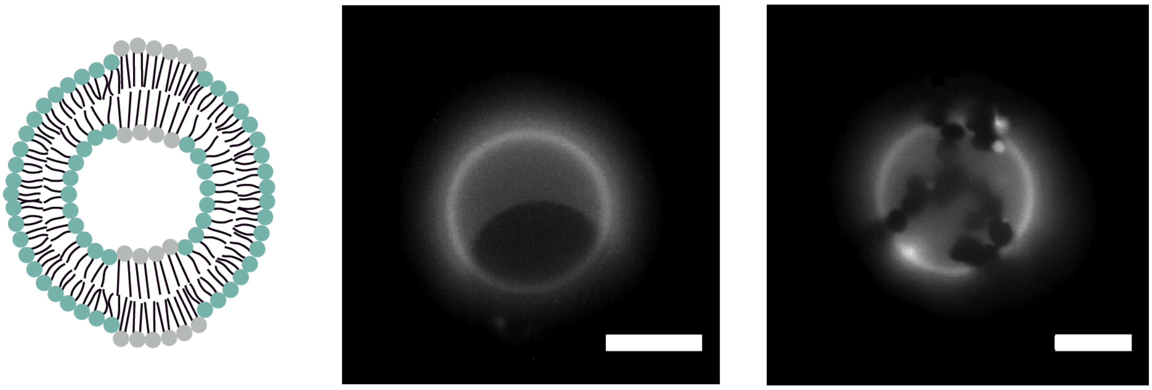

Figure 2.5: Lipid phase separation. Pictures of GUVs composed of DOPC:DPPC 6:4, taken with Bright Field Fluorescence Microscopy. Lipid bilayer was stained with DiI dye, which partitions preferentially in the liquid disordered domain; bright fluorescence indicates liquid phase, lack of fluorescence solid ordered. DOPC has a T_m of – 20°C and DPPC of 42°C, therefore at room temperature (25°C) the membrane consists of liquid domain (DOPC rich) and solid ordered domains (DPPC rich). Depending on individual conditions of membrane tension, different morphologies of domains may appear, ranging from circular to flower and hexagonal shape. Scale bar, 10 μm.

In the late 80s, Ipsen *et al.*[38] published phase diagram of binary mixture of phosphatidylcholines and cholesterol, demonstrating two-phase coexistence: cholesterol-poor liquid-disorder phase and cholesterol- rich *liquid order*-(L_o) phase (Figure 2.4). In the L_o phase, lipid chains are ordered around cholesterol, however still free to diffuse laterally [21, 39]. In 2005 Veatch and Keller [40], followed later by Marsh [41], published refined phase diagram with a gradual evolution from liquid disorder to order phase without a miscibility gap. However, the deep understanding of how the macroscopic phase diagram emerges from the microscopic, molecular scale interactions is still missing.

2.2.3 Membrane heterogeneity and domains

The phase separation near T_m has been demonstrated in model lipid systems by various experiments and also found by computer simulation [39–52]. The temperature range where these domains are observed depends on the cooperativity phenomenon of the phase transition. With the higher cooperativity, domains are more compact, as the system will minimise the length of the energetically unfavourable domain boundaries. With the high line tension, system will form domains of the gel phase, which will coexist with the fluid phase.

The lipid-raft-model in plasma membranes [53, 54] suggests that plasma membrane laterally segregates its constituents and the process is driven by specific intramolecular interactions [55]. The composition [56, 57] and thickness [57–60] of this meta-stable domains ($\sim 10^{-4}$ s) vary depending on membrane matrix. The presence of such membrane domains have strong impact on the biological functions, as it can change communication pathways and membrane dynamics [47]. Moreover, since free energy of lipids in gel and fluid phase show to be similar at the domain interfaces, the fluctuation at this region show to be greater, and therefore, locally change membrane's properties. As a consequence, presence of domains implies changes in macroscopic bilayer properties such as permeability, bending rigidity, binding affinity, and the way how membrane mediate the interactions with nanoparticles.

2.2.4 Model systems of a plasma membrane

To be able to resolve the biological role of lipid membranes as platforms for membrane-related processes and understand processes leading to nanoparticle translocation, one has to understand the physiclochemical properties of lipid molecules. An advantage of working with model membranes is the ability to control the composition, and thereby the complexity of the membrane. Among other approaches, liposomes (lipid vesicles) have greatly improved our understanding of the structure and function of cell membrane. These free-floating bilayer models, introduced by Bangham in the 60s [61], are structurally similar to biological membranes. Lipid vesicles can be produced both efficiently and reproducibly, and in a staggering range of sizes (from 20 nm to over 100 microns), making them suitable for a broad range of experimental techniques such as calorimetry [62–65], spectroscopy [66–69] or Cryo-transmission electron microscopy [70].

A significant breakthrough came with the development of giant unilamelar vesicles [71, 72] (GUVs; 10–100 micron). GUVs are of particular advantage for studying properties of lipid membranes in terms of viscosity [73], hydration as well as information about microscopic structure of domains [74]. Moreover, GUVs with asymmetric lipid distribution between the two leaflets have been recently developed [75]. The large sizes of GUVs give the room for novel studies of many properties of a lipid membrane. For example, they can be punctured by a micropipette without being destroyed. As a result, substances can be accurately microinjected where concentrations of the substances can be precisely controlled [76]. Micropipette techniques have also been used to investigate changes in membrane integrity upon controlled lipid oxidation [77]. Measuring the permeability [78] is another important aspect of the GUVs usage. It has been demonstrated that GUV's membranes formed by electroformation allows for direct visualisation of nanoparticle penetration in real time [79, 80]. All these merits make GUVs appealing platforms for mimicking membrane-related processes of biological cells.

Supported lipid bilayers (SLBs) that sit on glass, quartz (mica), or gold supports allow direct observation of their surface using atomic force microscopy (AFM), fluorescence, and other spectroscopic techniques. They can be prepared by fusion of lipid vesicles on the surface of the support in an aqueous environment or by sequential deposition of monolayers, which allows for formation of asymmetric bilayers. Recent studies highlighted the usefulness of SLB to study lipid microdomains, cellular interfaces [81], lipid-protein and lipid-nanoparticle interactions. However, the forces between the substrate and membrane should be taken into account while designing experiments. The influence of these forces can be minimimized using the right substrate and an aqueous buffer, which can shield the membrane from the substrate. Researchers have also investigated the use of soft cushions between the solid substrate and the model membrane. In 1999 Charitat *et al.* [82] proposed floating planar membranes, where a bilayer is suspended 2-3 nm above a second membrane adsorbed on a solid support. This model has been used for surface scattering studies of a highly hydrated, accessible, and fluctuating bilayer, where the composition of each leaflet can be controlled.

2.3 Membrane interactions with nano-objects

Interactions of nanomaterials with cells and their lipid membranes are of crucial importance in many medical and pharmaceutical applications such as phototherapy, bioimaging and drug delivery. In order to fine-tune nanoparticle characteristics needed for a specific application, a deep understanding and control of nanoparticle interactions with a cell membrane are required. In recent years, a large effort has been invested to clarify the mechanisms of such interactions at the molecular level. However, due to the wide array of processes occurring at the interface between the nano-object and the lipid membrane and to their inherent complexity, the mechanisms are still far from being understood.

The fate of nano-objects in the biological environment is determined by the physicochemical properties of the nanomaterial, the surrounding medium and the properties of the membrane surface. Interactions at the nano-bio interface (Fig. 2.6), comprise a competition between chemical (redox equilibrium, chemical bonding) and physical interactions (Van der Waals, electrostatic or hydrogen bonds). Moreover, the interaction with nanomaterials triggers changes in the cell membrane itself, making the process even more complex. Thus, a nanomaterial interacting with a biological system adds a new level of complexity, making it difficult to attain a comprehensive picture of such phenomena.

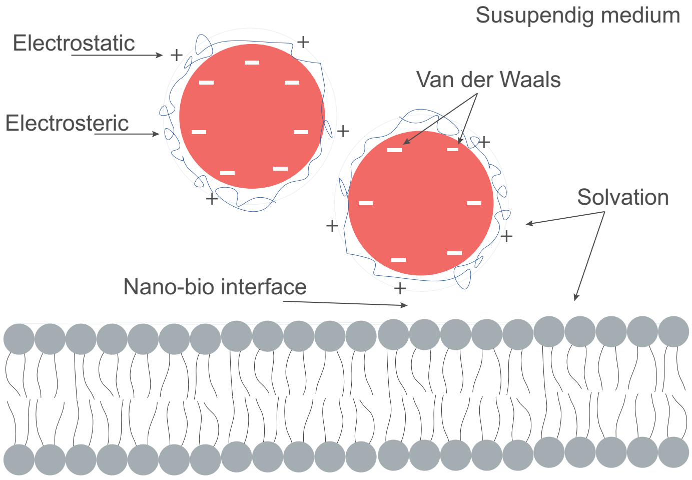

Figure 2.6: Interaction between nanoparticles and lipid bilayer. Schematic representation of the forces for colloidal fabrication (electrostatic, VdW) together with interactions (solvation, molecular depletion) that occur in biological media when particles are in contact with lipid membrane. Adapted from [83].

Characterizing the nanomaterial interface is a key factor to understand its interaction with a cell membrane. Several theoretical and experimental studies indicate that the effective activity is governed by the properties of a nanomaterial, such as chemical composition, surface functionalization, shape, size, surface heterogeneity, and hydrophobicity. Further properties, like effective surface charge, stability, aggregation propensity, and the surface solvation are, to large extent, affected by the surrounding solvent and its physicochemical state, e.g. pH, ionic strength, temperature, a possible presence of a co-solute and so forth. It is important to stress here, that all the changes in nanomaterial properties will have a direct impact on the forces acting between nano-objects suspended in biological media. Such forces include Van der Waals and Coulomb interactions, each with a characteristic decay length, as well as steric forces [84].

Another important phenomenon is solvation of interfaces. When considering the role of hydrophobicity in membrane uptake, the picture is complicated by possible hydration of the particle surface and /or cell membrane. Water molecules adhere to the nanomaterial surface with sufficient energy to form steric bumper layers on their surfaces, making it difficult for pairs of particles to touch or adhere. Thus, solvation forces increase particle stability through *hydration pressure* or *hydrophilic repulsion*. Experimental and computer simulations were performed by Chen and colleagues [85] to understand the hydrophobicity of nanomaterial on its cell entry. Their film-tension model predicts that hydrophobic materials are more easily engulfed by the membrane surface as compared to less hydrophobic ones. It was further explored by Zhu and Jing [86] who showed that disruption of supported lipid membrane (SLM) occurs above critical level of nanoparticle hydrophobicity and concentration. Similar effect was observed in cell culture models, where increasing surface hydrophobicity increases intracellular uptake of polymeric nanoparticles [87]. Moreover, these experiments have been explained by computer simulations based on self-consistent field/ density functional theory and molecular dynamics (MD), respectively.

The effect of the nanoparticle geometry on modulating uptake efficiency and internalization mechanism has also been studied, although the interplay between nano-object's curvature and nano-bio interface has been only scarcely addressed. Using cryo-electron tomography, Le Bihan *et al.* [88] studied intermediate steps of engulfing process of silica nanoparticles of various sizes by DOPC liposomes. Interestingly, Silica nanoparticles with diameters of approximately 15-20 nm remained absorbed on liposome surface, whereas nanoparticles with diameter >30 nm were fully internalized into vesicles. As authors explained, although the small-size nanoparticles interacted with the lipid membrane surface, the adhesive strength was not sufficient to induce a curvature of the lipid membrane and to subsequently trigger the engulfing process. In addition, Chitchrani *et al.* [89] conducted a systematic uptake in vivo study of gold nanoparticles with various shapes and sizes. Authors found that nanoparticle uptake level was higher for particle with a diameter 30 and 50 nm, than 17 or 100 nm ones. Moreover, authors reported that cellular uptake was reduced for rod-shape-like nanoparticles as compared to spherical ones. The authors rationalize their findings by difference in thermodynamic forces required for nanoparticle engulfment. However, this theory was recently challenged by Gratton *et al.* [90], who found that the internalization of rod-like cationic PEG particles occurs more rapidly and efficiently than those of other particle shapes at the same volume and size. It can also be appreciated that a complementary theoretical study of nanoparticle size effect on their interaction with membrane go in line with experimental findings. Yang and Ma [91] simulated the interaction between nanoparticles with different geometries and lipid membranes using dissipative particle dynamics (DPD). The geometrical properties and initial orientation of particles play a complicated role in their physical translocation, but their volume has only an indirect influence. These findings were further investigated by other groups [92, 93].

Experimental studies showed that in terms of surface charge, cationic nano-objects are in general more efficiently internalized, due to stronger interaction with negatively charged cellular surface. However, efficient translocation of negatively charged nanoparticles has been reported as well [94]. Once a nano-object adheres to a membrane surface driven by intramolecular and surface forces, it can lead to membrane reconstruction domain formation and local deformations [95, 96]. These processes lead to high cytotoxicity of cell membranes [97], suggesting that pore formation accompanies nanoparticle adsorption. In planar lipid bilayer models, cationic nanoparticles synthesized from a wide variety of materials are capable of inducing pore formation in the membrane [98]. Moreover, Li and Malmstadt [98] showed that deformation and formation of pores in gian unilamellar vesicles (GUVs) are elicited by cationic polystyrene nanoparticles. Simulation studies show that gold nanoparticles can directly penetrate lipid bilayers given a sufficiently high cationic surface charge density. Granick and coworkers [95] have shown that nanoparticles with both negative and positive surface charges can bind to lipid membranes, inducing changes in the membrane phase structure and leading to morphological deformations. In cell culture-based investigations of nanoparticle toxicity, membrane permeabilization is indicated by leakage of lactate dehydrogenase (LDH) from the cells. Similar cytotoxic effect was observed for a wide variety of nanoparticles [99, 100].

An enhanced understanding of the forces responsible for interactions between nanomaterial and biological system (in particular cell membranes) are, therefore, crucial for better design of nano-objects with applications ranging from nanotoxicity and control of cellular processes.

3 | Materials and methods

In the following chapter, a description of the principal techniques applied in this thesis will be introduced. The microscopy techniques include cryo-transmission electron microscopy (Cryo-TEM) and laser scanning confocal microscopy (LSCM) together with thermodynamic techniques such as isothermal titration calorimetry (ITC) and differential scanning calorimetry (DSC). Moreover, short introduction into quartz crystal microbalance (QCM-D) and scattering techniques (SANS, SAXS) will be presented. In the end of each chapter a description of the different procedures, equipment and materials will be listed.

3.1 Cryo-transmission electron microscopy (Cryo-TEM)

Transmission electron microscopy is a popular technique, developed over 8 decades ago with the first microscope of Ernst Ruska. The technique is applicable for visualizing internal arrangement of almost any structures in the resolution range of millimeter down to 0.1 nm, given optimal conditions. The technique is very sensitive to sample hydration, hence only dry samples under vacuum can be imaged (exemption is a variety of TEM called environmental TEM, which allows some hydration and higher pressures, at the cost of resolution), which sets some demands for sample preparation.

The technique uses an electron gun with a LaB_6 tip to create an electron beam accelerated under 200 keV. Set of parallel electromagnetic lenses focus the electron beam into a narrow spot size down to tens of nanometers with sufficient current and penetration into sample to make an image.

As the electrons pass through sample, the beam interact with the specimen and scattering occurs. A magnified image of the specimen is reconstructed onto a fluorescent screen at the bottom of the column or recorded by CCD camera. A schematic illustration of a classical TEM set-up is shown in Figure 3.1. One significant influence on high resolution and sharp images in TEM is a good calibration of the lens and electron gun set-up and to continuously focus and align the electron spot.

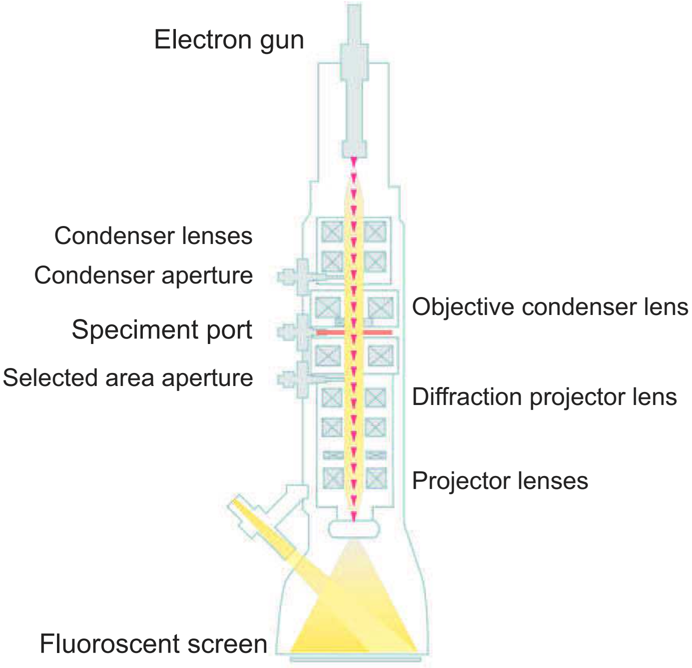

Figure 3.1: A Schematic illustration of Transmission electron microscopy (TEM) setup. (Partially adopted from FEI Tecnai manual). The electron from a source (a tungsten filament heated in vacuum), is made into a parallel beam by set of magnetic lenses. In the latter, beam passes through sample and its projected on fluorescent screen which emits light when struck by electrons. The whole trajectory from source to screen is under vacuum.

The second influence is sample preparation. For the correct visualization of internal structure, it is important that sample is stable (not influenced by the bombardment of electrons) and thin enough to permit the passage of electrons. To date, there is a vast range of research using specific methods of preparing sample for electron microscopy i.e. chemical dehydration and staining or coating of specimen. However, these drying and staining procedures can affect the structure and morphology of sample.

Cryo-TEM is a form of transmission electron microscopy where the sample is studied in a nearby native at cryogenic temperatures by vitrifying the solvent around the sample. This technique involves rapid cooling of sample by plunging it into liquid ethane (or propane) near liquid nitrogen temperature (approximately -140°C). It allows to analyse sample in their ‘native state’.

During sample preparation, a few microliters drop of specimen is deposited onto EM grid and excess solution is removed by blotting with filter paper. Resulting thin film (with a typical thickness 100 nm) has a large surface-to-volume radio, which enables fast heat exchange and ensures efficient verification. However, to prevent evaporation of the solvent from the sample film, grid is kept at humidity close to the 100%. Once sample film is vitrified, it is transferred to a special grid-holder and further to the microscope, while simultaneously keeping it at a temperature below -140°C, to prevent sample perturbation and the formation of ice crystals [101, 102]. The thin film method is, however, limited to thin specimens (typically below 500 nm), because the electrons cannot cross thick samples without multiple scattering events. To observe thicker specimens, samples can be prepared by cryo-electron microscopy of vitreous sections (CEMOVIS) [103] or by freeze-fracture transmission electron microscopy (FF-TEM) [104].

3.2 Laser scanning confocal microscopy (LSCM)

Since pioneering work of Minski [105] and Egger [106], confocal microscopy has become a powerful tool for routine investigation in life and material science. Confocal microscopy gives several advantages over conventional wide-field optical microscopy, namely an improvement in both axial and lateral optical resolution, depth of field, reduction/elimination of background fluorescence and ability to collect multiple optical sections from thicker specimen. Confocal technique allows for investigation of both in-vivo and ex-vivo samples under a variety of conditions with enhanced clarity.

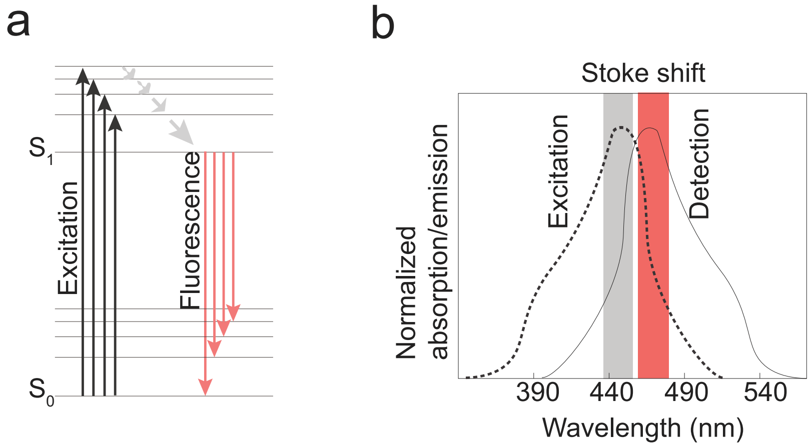

Figure 3.2: Fluorescence in LSCM. a) Jablonski diagram, showing the excitation, followed by spontaneous fluorescence emission after a loss of energy through a dark transition b) Absorption and emission spectra for Laurdan including excitation-, detection- wavelengths. The energy of the emitted light is lower (increased λ) than the excited light. The difference is called the Stokes shift.

LSCM uses the property of a molecule/material to absorb energy from light, and as result emits the energy in form of light. This can be illustrated in Jablonski diagram (Figure 3.2a): a fluorophore absorbes light at λ_{exc} wavelength rising from the ground state to the first electronic state S_1. Once there, the fluorophore is excited and subsequently it returns to the ground state emitting a photon at a higher wavelength λ_{em}. This phenomenon is called fluorescence. In LSCM techniques, the amount of generated fluorescence scales linearly with excitation power, which discern them from multi-photon microscopes. The loss of energy in the dark transition, corresponding to a shift in wavelength between the excited and emitted light, is called the Stokes shift (Figure 3.2b). This

Stokes shift is a fundamental base for fluorescent microscopy experiments. It allows recording of a specific emitted wavelength from a sample separately from effects caused by the incident light.

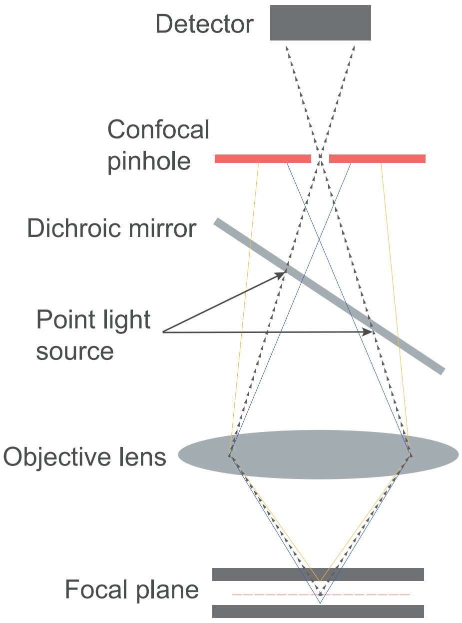

Figure 3.3: Simple schematic diagram of the optical pathways and basic components of confocal microscope. Point light source is employed and generally obtained from the output of a laser coupled to an optical fiber or a laser passing through a pinhole aperture that is located in a conjugate plane with the focal point in the specimen. Yellow and blue line represents emitted light form out of focal plane, which are then removed by confocal pinhole.

The use of fluorescence molecules (e.g dyes) is a powerful tool in microscopy. It allows for precise mapping of the individual fluorophores in the sample. The essential parts of a confocal microscope are shown in Figure 3.3. The sample is illuminated by the coherent light source (laser) focused on the sample by the microscope objective. Light emitted from the sample is then redirected and collected by a detector (photo-multiplier tube). To separate the excitation light from the emitted one, microscope is equipped with filter cube, which contains an excitation filter, dichroic mirror and the emission filter. As the light source is generally broad in the wavelength spectrum, the excitation filter (low pass) excludes the light with a wavelength above a certain value, the dichroic mirror works as a mirror for the excitation light, while Stokes shifted emission light is allowed to pass through. The emission filter is a high pass filter that only allows light above a certain wavelength to pass it.

To remove out-of-focus light emitted from sample, a pinhole is positioned in front of the detector. The fluorescence emitted from the on-plane points passes back through the dichroic mirror and is focused to a point at the detector pinhole aperture. The fluorescence emitted from out-of-focus plane are not confocal with the pinhole and, therefore, are not detected and do not contribute to the final image [107, 108]. To obtain a 3D representation of sample, it is necessary to acquire images at consecutive positions along optical axis (z-scan).

3.3 Small-angle scattering (SAS)

In recent years, scattering techniques, and particularly small-angle scattering (SAS) techniques have become a powerful tool for in-depth structural characterization of soft matter systems, including proteins, colloids, polymers and micelles. Small angle X-ray (SAXS) and small angle neutron scattering (SANS) provide a non-destructive approach to study objects at the nanoscale, thus are frequently used to investigate changes of membrane structures and lipid phase transitions upon interaction with drugs and/or biologically relevant molecules.[1]

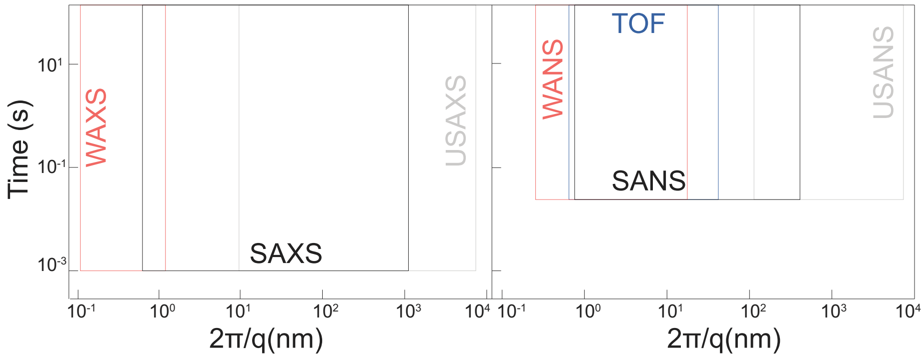

Figure 3.4: Time and length scale for Small angle X-ray and Neutron scattering experiments.

The fundamental difference between SANS and SAXS techniques is mechanism by which the incidental radiation interacts with matter. X-rays are scattered by the electrons surrounding atomic nuclei, whereas neutrons are scattered by atomic nuclei themselves (protons and neutrons). This implies that isotopes of the same element may scatter neutrons in different way, while X-ray is only sensitive to the number of electrons in the atom. In other words, X-ray probes the elements distribution in the sample, whereas the neutrons probe the isotopic distribution in the sample.

While the basic principles underlying scattering remains the same, the choice of radiation fields or a combination of them is dependent on the strength of the respective fields (Figure 3.4).

---

[1] Several books and reviews on small angle scattering techniques served as general references for this thesis. These are: *Structure Analysis by Small-Angle X-Ray and Neutron Scattering* by Svergun and Feigin [109], *Neutrons, X-rays and Light: Scattering Methods Applied to Soft Condensed Matter* by Lindner and Zemb [110] and *Small angle scattering studies of biological macromolecules in solutionr* by Svergun and Koch [111].

3.3.1 Experimental setup and data collection

Figure 3.5 shows the conventional SAXS and SANS experimental setup. The transmitted primary beam from the source is first collimated, and resulting parallel beam passes through the sample where it is scattered. The two-dimensional scattering pattern is radially integrated to provide the one-dimensional scattering function I(q), where q is the length of the scattering vector

$$q = \frac{4\pi}{\lambda} sin\frac{\Theta}{2} \tag{3.1}$$

To obtain the good angular resolution on detector, it is placed from sample at defined distance, which depends on particle size of studied system. The flight path before and after the sample is commonly obtained in vacuum to avoid absorption and background scattering. A beam-stop is placed in front of the detector, in order to protect the detector from the direct beam.

The SAXS and SANS experimental setups are similar. However the neutron flux is lower than the X-ray one at a SAXS instrument. As a consequence, the beam cross-section is larger, which requires a larger sample. In order to gain additional flux, the wavelength distribution of the neutron beam is often extended. Therefore, SANS measurements are typically done at few sample distances, by moving the detector towards sample, to obtain a good q resolution in the whole q-range studied.

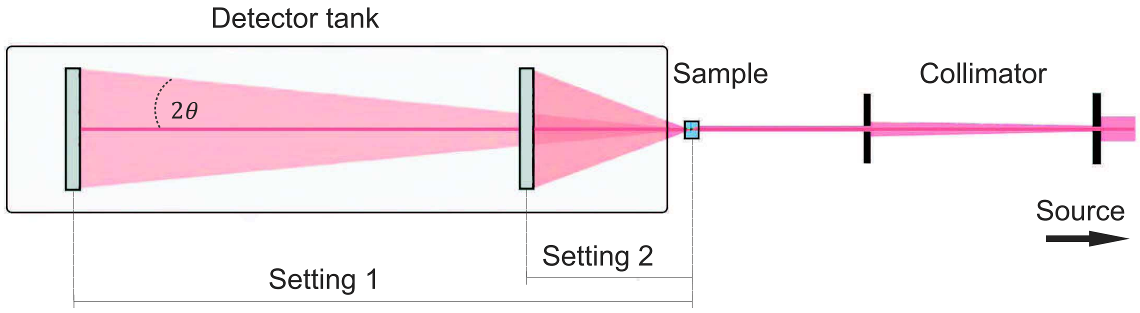

Figure 3.5: Sketch of typical SAS setup. For SANS experiments to cover the desired q-length scale several sample detector distances are used, by moving the detector inside the detector tank (shown as Setting 1 and Setting 2). The SANS data collected at different detector distances, are combined to yield the full scattering curve.

3.3.2 SAS data treatment

The intensity of scattered neutrons / X-rays on the detector can be presented as:

$$I(q)_{sample} = I_0 t A \epsilon(q) T_{cuvette} T_{sample} d_{sample} \frac{d\epsilon}{d\Omega} \Delta\Omega + I_{dolvent} + I_{cuvette} + I_{instrument} \tag{3.2}$$

where I_0-incident flux of neutrons/photons on the sample, t - time, A is a section of the beam, ϵ(q) - efficiency of the detector pixel in the direction q, T_{cuvette} T_{sample} – transmissions of the sample and cuvette, d sample-thickness of the sample, ΔΩ- the solid angle spanned by the detector. $\frac{d\epsilon}{d\Omega}(q_{\mathrm{sample}})$ is differential scattering cross section, which characterize the ability of particle to scatter in the direction q per solid angle and unit sample volume. For X-rays, it is determined by the distribution of electrons within the sample whereas for neutrons it is determined by the samples' isotopic distribution.

It has to be mention that the raw data of scattering intensity include scattering patterns from both particles and solvent, therefore subtracting a background is an essential step prior data analysis.

3.3.3 General scattering theory

The amplitude of a scattered photon or neutron is proportional to the so called scattering length, b, which characterize the scattering potency of an atom

$$E_{scat}(\Theta) = \frac{E_{inc}b}{R}\sqrt{\frac{1-cos^2(2\theta)}{2}} \qquad 3.3$$

where E_{scat}- amplitude of the scattered photons at a distance R, and E_{inc} is the amplitude of the incident photons or neutrons. Examples of scattering length values, b, of biological elements for X-ray and neutrons are listed in Table 3.1.

Table 3.1: Scattering lengths, b, for typical biological elements. The scattering length for X-rays is proportional to the number of electrons whereas the neutron scattering length is isotope specific. Neutron scattering lengths are adapted from [111]

	b (X ray) [cm]	b (neutrons) [cm]
^{1}H	$2.82{\cdot}10^{-13}$	$-3.739{\cdot}10^{-13}$
^{2}H	$2.82{\cdot}10^{-13}$	$6.671{\cdot}10^{-13}$
C	$16.92{\cdot}10^{-13}$	$6.646{\cdot}10^{-13}$
N	$19.74{\cdot}10^{-13}$	$9.36{\cdot}10^{-13}$
O	$22.56{\cdot}10^{-13}$	$5.803{\cdot}10^{-13}$
P	$42.30{\cdot}10^{-13}$	$5.13{\cdot}10^{-13}$
S	$45.12{\cdot}10^{-13}$	$2.847{\cdot}10^{-13}$

The intensity recorded by the detector is equal to absolute square of the scattered field times the area of the detector $I_{scat}=|E_{scat}|^2 \cdot A_{det}$. The incoming flux can be describe as $I_0=|E_{in}|^2$ Therefore, the ratio of scattered to incoming flux of neutrons / photons is defined

$$\frac{I_{scat}}{I_0} = \frac{|E_{scat}|^2 A_{det}}{|E_{in}|^2} = \frac{|b|^2 A_{det}}{R^2} = |b|^2 \Delta\Omega \tag{3.4}$$

$\Delta\Omega$ is a solid angle spanned by the detector at distance R.

Equation 3.4 gives the amount of scattered X-rays and neutrons by the sample in the direction of the detector. To obtain the total scattering into all directions, all solid angles have to be measured where σ- scattering cross section, is the differential scattering section.

$$\begin{gathered} \int_{\Omega} |b|^2 d\Omega = 4\pi |b|^2 = \sigma \\ \frac{d\sigma}{d\Omega} = |b|^2 \end{gathered} \tag{3.5}$$

where σ- scattering cross section, and $\frac{d\sigma}{d\Omega}$ is the differential scattering section.

3.3.4 Contrast

In order to simplify Small angle scattering experiments, scattering length, b, of individual atoms can be easily related with molecular volume, V_m, and associated with *Scattering Length Density* (ρ)

$$\rho = \frac{\sum_{i=1}^{n} b}{V_m} \tag{3.6}$$

Using scattering length density,ρ, the total scattered amplitude from the sample become

$$A(q) = \int_v \Delta\rho e^{-iq\cdot r} dr \tag{3.7}$$

where ($\Delta\rho$) is the excess scattering length density of the particles compared to the solvent

$$\Delta\rho = \rho_{particle} - \rho_{solvent} \tag{3.8}$$

If the solvent and sample express same scattering length density, $\Delta\rho$ vanishes with no scattering from the particle.

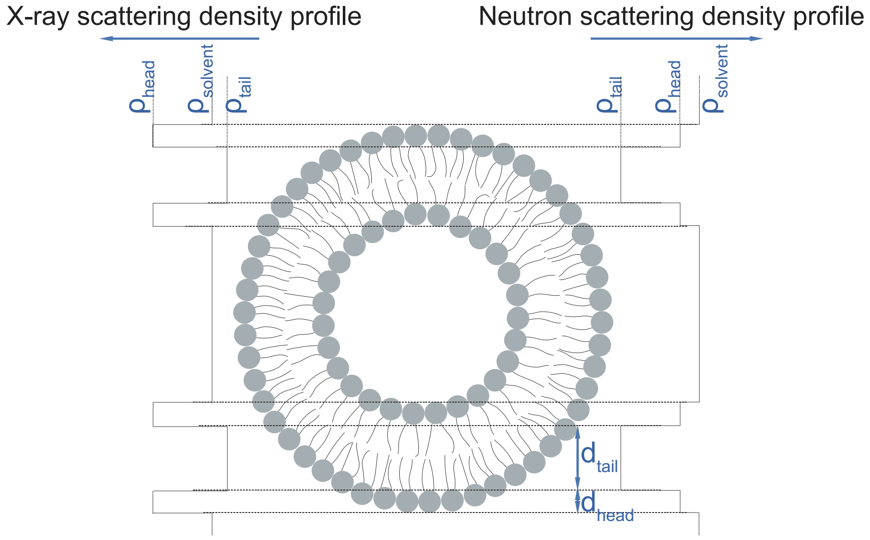

Figure 3.6: X-ray and neutron profiles of the *scattering length density* for single liposome. Adapted from [112].

Scattering length density profiles of a liposome for X-ray and neutron together with exemplary values are presented in Figure 3.6 and Table 3.2. The electron-rich head-groups express a positive contrast for X-rays, whereas the hydrocarbon tail groups are relatively electron-poor, compared to water, and therefore have a negative contrast. For neutrons, phospholipids have a homogenous contrast. Consequently, different parts of the molecular structure of membranes can be highlighted by x-rays and neutron measurements. X-ray scattering gives information on the arrangement of tails and head groups, whereas neutron scattering will give information on the whole molecule.

Table 3.2: Scatterings lengths densities of POPC lipid for X-rays and neutrons. For neutrons the head (PC) and tail (PO) of the phospholipid have similar contrast, whereas there is a significant difference for X-rays

	$\Delta\rho$ (X ray) in H_2O [cm/Å^3]	$\Delta\rho$ (neutrons) in D_2O [cm/Å^3]
POPC	$1.06 \cdot 10^{-15}$	$-6.03 \cdot 10^{-14}$
PC (head group)	$5.10 \cdot 10^{-14}$	$-4.17 \cdot 10^{-14}$
PO (tails)	$-1.61 \cdot 10^{-14}$	$-6.67 \cdot 10^{-14}$

3.3.5 Contrast variation technique

The difference between deuterium and hydrogen in neutron scattering, allows to change the contrast of the sample by simple variation the amount of H_2O in a solvent. Samples with few scattering patterns i.e. samples which shows change in relative contrasts between the regions, gives possibility to increase the amount of information available for SANS analysis. In a 42% D_2O/58% H_2O based solvent polystyrene within membrane shows close to zero contrast. This gives an opportunity to study the changes in lipid membrane vesicles without seeing the incorporated polystyrene. Another possibility for SANS measurements is to use deuterated lipids to study e.g. lipid phase diagram or polymer adsorption on membrane surface, as the signal form the part of lipids is greatly decreased. This kind of approached was already implemented in [113, 114]. Contrast variation technique can improve the information extracted from sample, however special care should be taken. The incoherent scattering increases by adding extra H_2O and for weakly scattering samples, the resulting lower signal to noise ratio may mask structural signal.

3.4 Differential scanning calorimetry (DSC)

When a sample undergoes a physical transformation e.g. when a lipid membrane melts, energy must be supplied in order to break the lattice structure of the ordered phase. Differential scanning calorimetry is a technique that monitors this energy as a function of temperature, and thereby provides information about changes in heat capacity and enthalpy with temperature.

The principle of this technique is shown in Figure 3.7. The DSC consists of two cylindrical cells, measuring and reference cell, closed in an adiabatic box. The temperature of the cells increases linearly as a function of time, while keeping the temperature difference between the two cells at zero (ΔT=0). The calorimeter measures the difference in the electric power between two cells as a function of temperature. When the sample undergoes an endothermic/exothermic process, the resulting deviation in heat flows between the cells will be registered as a peak in DSC profile.

The excess of heat, ΔQ, can be calculated from integration of power, ΔP, with respect to time:

$$\Delta Q = \int_{t}^{t+\Delta t} \Delta P(t')dt' \cong \Delta P \cdot \Delta t \qquad 3.9$$

Since the pressure is constant during the whole process, the molar heat capacity at constant pressure can be easily derived:

$$\Delta C_p = (\frac{\Delta Q}{\Delta T})_p = \frac{\Delta P}{\Delta T/\Delta t} \qquad 3.10$$

where ΔT /Δt is a scan rate.
From heat capacity profile of the sample, enthalpy and entropy, can be easily obtained:

$$\Delta H_0 = \int_{T_g}^{T_f} \Delta C_p dT$$

$$3.11$$

$$\Delta S_0 = \int_{T_g}^{T_f} \frac{\Delta C_p}{T} dT = \frac{\Delta H_0}{T_m}$$

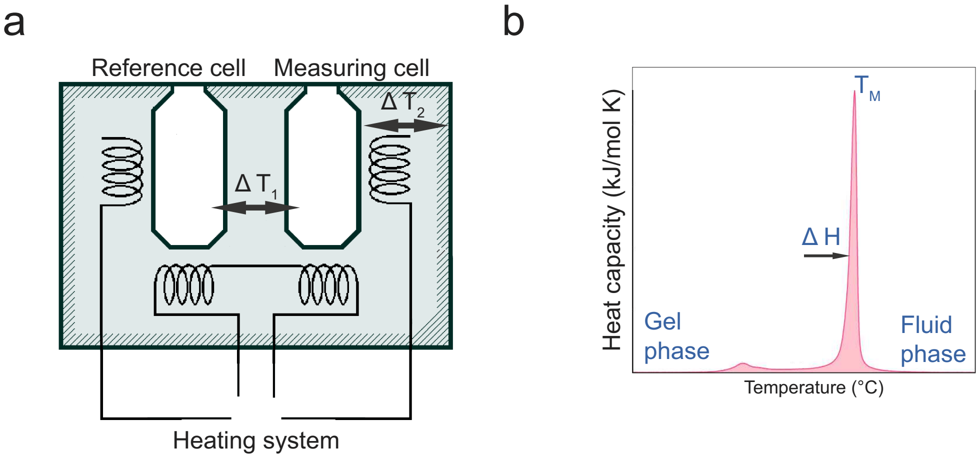

Figure 3.7: a) Schematic diagram of Differential Scattering Calorimeter b) Example of heat capacity profile of multilamellar vesicles.

3.5 Isothermal titration calorimetry (ITC)

The forces driving interactions between lipids and nanoparticles cannot be understood without knowledge of (free) energy differences and barriers involved in the interplay. Isothermal titration calorimetry (ITC) is a well-established technique, which provides a complete thermodynamic and kinetic profile of an interaction process in a single experiment. With a small amount of sample and with no need of chemical modification or labeling, ITC gives a direct measurement of the binding constant, K, the stoichiometry, n, the heat of reaction, and indirect access to other thermodynamic parameter such as entropic binding contribution, ΔS, or Gibbs free energy, ΔG.

ITC experiment follows the evolution of a heat released and /or absorbed during titration of sample solution with small aliquots of reactant in a series of consecutive injections. Similar to DSC, ITC uses measuring and reference cells (see Figure 3.8a). During an ITC-experiment, calorimeter monitors and registers the heat of a reaction as a power consumption needed to maintain zero temperature difference between both cells.

The amount of the heat released or absorbed during titration is proportional to the amount of molecule added to guest solution. Single injection of sample causes ΔN^{trans} moles of compound and is accompanied by a change in molar enthalpy, ΔH^{trans}, therefore the measured by ITC heat of reaction, q, can be shown as:

$$q \cdot q_{dil} = \sum_i \Delta N_i^{trans} \Delta H_i^{trans} \qquad 3.12$$

where q_{dil} is heat of dilution that occur due to changes in particle interactions of the injectant and of guest solution in measuring cell.

As the titration proceeds, the cell becomes more saturated with a reactant, therefore the heat signal diminishes progressively (Figure 3.8b). After integrating the heat as a function of the molar ratio between both reactants, the resulting ITC binding isotherm can be fitted to various models (independent binding sites, sequential binding sites, etc.) and therefore, can provide a full thermodynamic profile of the interaction.

It needs to be noted that titration calorimeters measure the sum of the heat associated with all processes occurring upon addition of aliquots of the titrant. This necessarily includes the heat of dilution of the titrant, but also the heat associated with any undesired reactions, such as precipitation, hydrolysis and redox (in the case of metal ions), as well as any processes that are intrinsically coupled to the desired binding equilibrium. Furthermore, the combination of ITC-experiments performed under different conditions (e.g. changes in temperature) become popular analysis that allows characterization of the energetics of binding in multicomponent systems [115, 116].

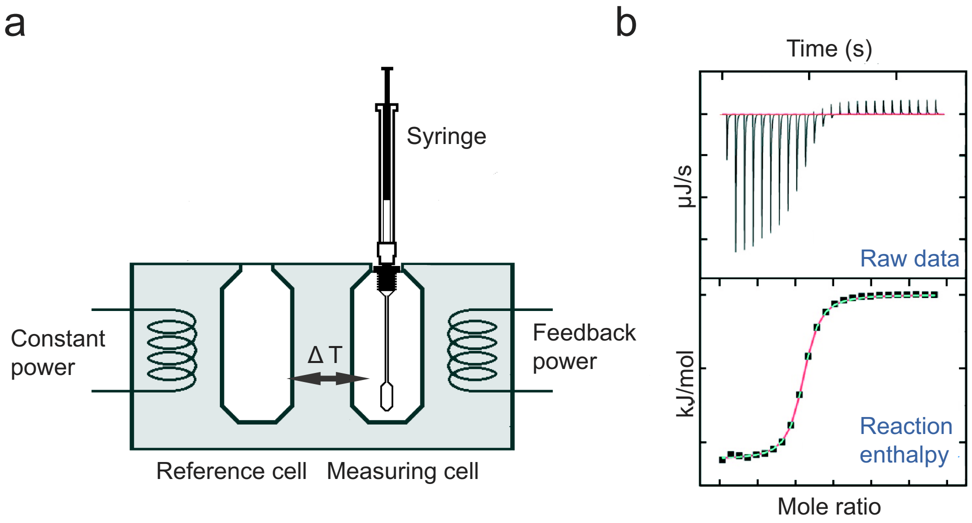

Figure 3.8: a) Schematic drawing of Isothermal titration calorimeter (ITC) b) Sketch of typical ITC heat profile.

3.6 Quartz crystal microbalance with dissipation (QCM-D)

Quartz crystal microbalance with dissipation is a real-time surface sensitive technique that allows to monitor and characterize thin films on a surface in terms of adsorption/desorption, particle interactions, and structural properties. With the QCM-D experiment, two parameters - changes in frequency of the quartz crystal (related to mass and thickness) and dissipation parameter (related to rigidity) - are monitored simultaneously giving full picture on the properties of adsorbed layer.

The QCM-D technique relies on applied voltage to a quartz crystal sensor causing it to oscillate at a specific frequency. Changes in the deposited mass on the quartz surface (Δm) are related to changes in frequency of the oscillating sensor (Δf) through the Sauerbrey relation [117]

$$\Delta m = -C \cdot \Delta f \tag{3.13}$$

where C is the mass sensitivity constant (C = 17.7 $\mathrm{ng \cdot cm^{-2} s^{-1}}$ at 5 MHz).

The Sauerbrey equation can be used for rigid and/or sufficiently thin absorbed layers. For soft matter systems with high viscoelasticity, the Sauerbrey relationship underestimates the deposited mass, since the film is not fully coupled to the motion of the sensor surface. The Voigt-based model described by Voinova *et al.* [118] and Hook [119] corrects for this deviation by including a set of frequency and dissipation overtones and thus allowing for a proper fit of the experimental data for soft films. This model has been already successfully used in many publications studying a variety of experimental systems

The dissipation (D) measurement enables to get insights regarding structural (viscoelastic) properties of adsorbed layers. Dissipation occurs when the voltage applied to the crystal is turned off and the energy from the oscillating sensor dissipates from a system

$$D = \frac{\text{energy lost per oscillation}}{2\pi \text{ total energy stored in system}} \tag{3.14}$$

Measuring the dissipation parameter allows for accurate analysis of soft films that do not obey the linear Sauerbrey relation between change in frequency and change in mass.

4 | Cyclodextrins

4.1 Introduction

Discovered at the end of 19th century by Villiers [120], studied later by Schardinger [121] and Pringsheim, cyclodextrins (CDs) have been recognized as research and pharmaceutical assets. The main reason for this growing interest is the complex macromolecular architecture of cyclodextrins, which enables inclusion of large range of guest molecules, such as drugs [122–124], surfactants [125–127], polymer [128], inorganic salts [129, 130] in CD's apolar cavity, while the hydrophilic exterior renders CDs soluble in water. Such an inclusion masks physicochemical properties (i.e. physical state, instability [131], low solubility [132, 133] or bioavailability) of the guest molecule. Moreover, host-guest complexes of CDs offer physical isolation of incompatible compounds, and control of volatility and sublimation [134, 135]. All these properties,[1] complemented with control-nontoxicity [140] makes CDs complexes highly suitable for large range of applications in food technology [141], analytical chemistry [142], chemical synthesis and catalysis [143, 144], as well as pharmaceutics [145]. To date, there are more than 30 drugs available worldwide where the solubility and stabilization of the active pharmaceutical ingredient have been improved by CDs [146].

Cyclodextrins comprise a family of naturally occurring cyclic oligosaccharides. They are manufactured from starch, a glucose-containing polymer produced by photosynthesis. Degradation of starch by glucosyltransferase, produces cyclic oligomers of α- 1,4-D-glucopyranoside, known as CDs. Depending on the number of glucose residues in its structure, the most common naturally occurring CDs are hexamers (αCD), heptamers (βCD) and octomers (γCD). Figure 4.1 shows a schematic representation of native cyclodextrins.

---

[1] Reviews on cyclodextrin properties served as references for this thesis. These are: *Cyclodextrins and Their Complexes: Chemistry, Analytical Methods, Applications* by Dodziuk [136], *Cyclodextrin Technology* [137], *Introduction and General Overview of Cyclodextrin Chemistry* [138] edited by Szejtli, and *Cyclodextrin Chemistry* by Bender and Komiyama [139].

Given the 4C^1 conformation (chair conformation) of glucopyranose units, all hydroxyl moieties are oriented to the cone's exterior, with primary hydroxyl groups occupying a narrow edge and secondary ones located on a wider edge of CD (Figure 4.1a). High number of hydroxyl groups controls and limits the aqueous-solubility of CDs. For αCD, βCD and γCD the solubility is 13%, 2% and 26% (w/w) respectively. The poor solubility of βCD compared to αCD, is attributed to the formation of a relatively strong internal network of hydrogen-bonds between secondary hydroxyl groups, preventing their hydrogen bond formation with surrounding water molecules. Substitution of hydrogen-forming group in βCD with e.g. lipophilic functional groups is one of the ways to improve βCD solubility up to 60% (w/w). Among the CD derivatives, the most often employed are three classes of modified CDs: methylated (neutral), hydroxypropylated (neutral), and sulfobutylated (negatively charged) [147].

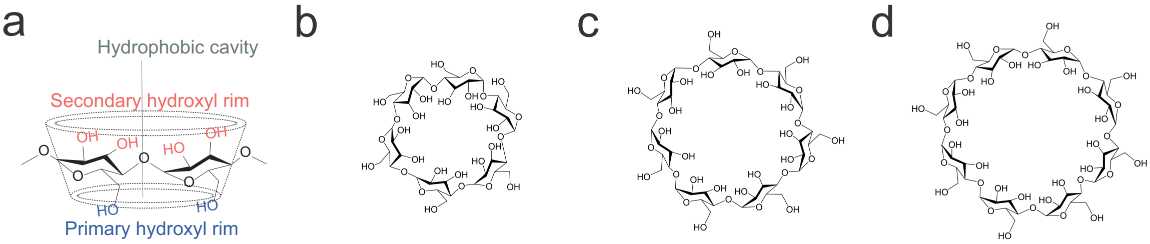

Figure 4.1: Chemical structure of native cyclodextrins a) 2D structure of cyclodextrin showing the arrangement of glucose monomers b) αCD c) βCD d) γCD.

While the external side of CD is hydrophilic, the internal cavity is lined with the skeletal carbons and ethereal oxygen of glucose units, creating a hydrophobic microenvironment. This unique characteristic allows CDs to reversibly entrap a wide range of guest molecules, ranging from apolar compounds, such as aliphatic and aromatic hydrocarbons, to polar compounds like alcohols, acids, amines, and small inorganic anions. The entrapment of apolar compounds is of special interest, as the resulting complex will have an increased solubility in water, with respect to the compound itself.

On the basis of X-ray studies of CDs from 1980s [148, 149], their structure was believed to be a rigid truncated cone (Figure 4.1a). However, the theoretical analysis by Dodziuk *et al.* [150] showed that the structure of CDs as planar rings formed by glyosidic oxygen atoms does not correspond to the energy minimum, and that the energy hypersurface exhibits several energy minima separated by low barriers. Therefore, the nonrigidity of CDs was assigned to the rotational flexibility of each glucose moiety around the glycosidic linkage, and to the changes in the endocyclic torson angle of the pyranose rings. This flexibility is still restrained by intramolecular hydrogen bonds of secondary hydroxyl groups formed between neighboring glucose units. From the experimental point of view, the flexibility of CDs rings was proved by NMR measurements (both in solution and solid state) [151, 152], together with Raman studies of H/D, and D/H exchange rates [153], and neutron diffraction measurements. The toroidal shape and flexibility of cyclodextrin's rings explains well the selective and effective fitting of CDs with guests of various shapes.

The most important characteristic of CDs are summarized in Table 4.1, while other properties such as toxicity and stability treated by various enzymes can be found in *Comprehensive Supramolecular Chemistry* by Szejtli and Schmid [154].

Table 4.1: Selected properties of native CDs

	αCD	βCD	γCD
Number of glucospyranose units	6	7	8
Molecular weight (Da)	972	1134	1296
Approximate inner cavity diameter (pm)	500	620	800
Approximate outer diameter (pm)	1460	1540	1750
Approximate volume of cavity (10^{-6} pm^3)	174	262	427
Solubility in water (room temperature g/100 mL)	14.5	1.85	23.2
Melting temperature range (°C)	225-260	255-260	240-245
Crystal water content (wt.%)	10.2	13-15	8-18
Water molecules in cavity	2	6	8.8
Number of H-donors	18	21	24
Number of H-acceptors	30	35	40

4.1.1 Host-guest interactions

In the review of Szejtli 1996 [151] it was already recognized that *'the driving forces of [cylodextrin] complexation, despite many papers dedicated to this problem, is not fully understood'*. Today, after more than 20 years, this statement still remains valid. The driving forces behind complex formation has been attributed to several factors, such as the release of water molecules from hydrophobic cavity of CD, removal of the hydration shell of the guest molecule, and its entry into the cavity. Inside the cavity, the guest is stabilized mainly by hydrogen bonding and Van der Walls interactions, while water molecules are reorganized around the exposed part of the guest. Thus, during the complexations process, the changes in both entropy and enthalpy contributions are observed, and their values depend on many factors, namely host-/guest-effective fitting, concentrations, charge, and external conditions (nature of solvent, temperature, pH). As the interactions between CD and guest molecule are rather weak and short range, the complex stability depends on a good fit between CD and the guest. In some cases the weak fit can by compensated with the formation of different complex geometries and/or stoichiometries.

To date, there is a vast amount of experimental data on the CDs' complexation process, but, despite these efforts, its full thermodynamic understanding is still missing. All these studies agree however that hydrophobic interactions, together with the release of water from the cavity, are the major forces responsible for CD's inclusion complexes.

Efforts have been made to understand the role of hydrophobicity in stabilizing guest-host complexes [155, 156]. Most of the experimental observations of cyclodextrin-guest associations are accompanied by negative changes in enthalpy and a negative, or close to zero, change in entropy. These observations are inconsistent with the 'classical' entropy driven energetics of hydrophobic-controlled interactions. The detailed experimental analysis of various binding mechanisms in cyclodextrin complexes [157] shows that the process is impaired by several simultaneously occurring interactions. If hydrophobic interactions play key role in CD's complexation process, they must be accompanied by a release and rearrangement of water molecules in the cavity and around the guest. Computational [158], volumetric [156] and calorimetric [159] methods have underlined the expulsion of water from CD cavity by a guest molecule as the crucial factor for the complexation process. In aqueous solution, although the CD cavity is occupied by water molecules, the individual energetic frustration of water molecules is substantial (so called *high-energy* water), as they do not form strong hydrogen bonds with the cavity. It has been shown by interfacial studies that water next to an interface displays different properties from than in the bulk phase [160]. Therefore, the release of water molecules and binding the guest inside the CD cavity is expected to have strong enthalpic contribution to the complexation process. However, the critical role played by the hydration sheath of CDs during complex formation is still not fully understood.

Although much of discussion of CD's complexation focuses on its hydrophobic cavity, the role of the hydrophilic part of cyclodextrins cannot be neglected. There is a growing body of literature reporting coexistence of inclusion and non-inclusion complexes with CD in aqueous solutions [137, 139]. The possibility of formation of inclusion and/or exclusion complexes with a CD makes the interpretation of the experimental data extremely problematic.

4.1.2 Cyclodextrin complexes

Depending on the respective size and conformation of the guest and host molecules the studied stoichiometries of CD complexes varies. The most frequently documented type of CD complex is 1:1, so-called *molecular encapsulation*. The entrapped apolar molecule is oriented in the CD cavity in such a position to achieve maximum cover by cavity and minimize contact with water in solution. Complex formation with larger guest molecules than the CD cavity can also be found in the literature. This type of complexes usually involves higher CD/guest ratio such as 2:1, 2:2 or higher. Interactions of fatty acids with CDs are good examples of complexes with more complicated stoichiometries and structures. The stoichiometry of a complex is strongly related to the size of the CD cavity and the alkyl chain length of the fatty acid. For linoleic acid (C18:2) the molar ratio of 3 was found for αCD, while βCD and γCD shows 2 and 1.5 stoichiometry, respectively. On the other hand, αCD with docosahexaenoic acid (C22:6) forms complex with 6:1 stochiometry, whereas the ratio for βCD and γCD is comparable to one found for linoleic acid. In 1991, Jyothirmayi [161] using NMR studied the structures of αCD and βCD with linoleic acid (C18:2) and arachidonic acid (C20:4). The structures show that the carboxyl chains of both linoleic and archachidonic acids are encapsulated in the cavities, with their double bonds partially covered by CDs. Interestingly, while the double bond at C9 position in linoleic acid was covered by CD molecule, the one at C12 remained uncovered. Similar trend was observed for arachidonic acid, while the double bond at position C5 was covered, the other at position C8 was unmasked. Later, Szejtli have found that stability of complexes of fatty acids with CDs increase with the number of double bonds.

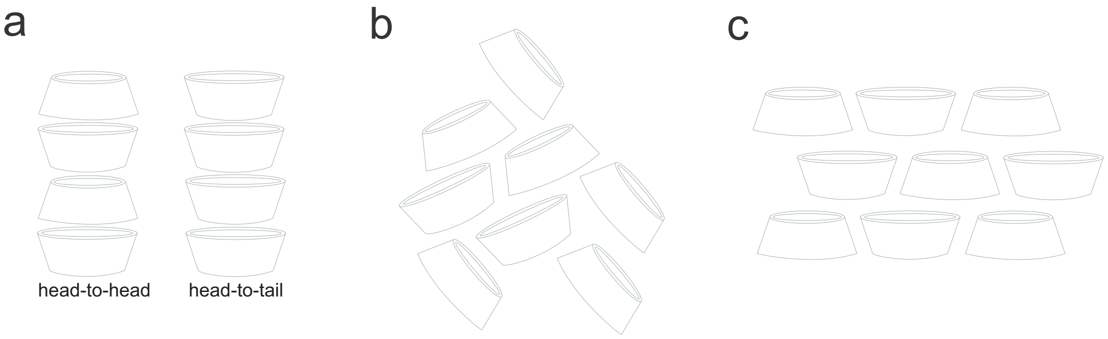

Figure 4.2: Alignment of cyclodextrin rings in complex crystal structures: a) channel b) cage c) layer.

In contrast to inclusion complexes in solution, the ratios of guest to host are usually nonstoichiometric in the crystalline state. This is associated with the three-dimensional structure of crystalline inclusion complexes. In crystals of CDs complexes, the crystal packing is generally governed by the CD's arrangement, since they dominate the intermolecular contacts to form the crystal lattice. However, packing varies depending on the guest molecule. There are three packing types: cage, column (also known as channel) and widely observed layer type (Figure 4.2). The *cage-type* packing is frequently observed for small molecules, which can be entirely enclosed in the host cavity. The *channel* structure has an infinite cylindrical channel that can accommodate a long molecule (e.g. alkyl chain, or linear polymers). The CD's alignment in channel packing can be either *head-to-head* or *head-to-tail* (Figure 4.2a). The first structure is formed by the linear arrangement of *head-to-head* CDs dimers where secondary hydroxyl group of two molecules are facing each other. In the *head-to-tail* type, CDs rings are linearly stacked and the primary hydroxyl side face secondary hydroxyl side of neighbor. The *layer-type* packing was observed when the guest molecule is so large that its part cannot be accommodated within the cavity. CD's molecules arrange each other in plane to make a molecular layer, and two adjusted layers are shifted with respect to each other by a half of molecule, showing brick-like pattern. Both ends of the cavity are open to an intermolecular space of adjusted layers (Figure 4.2c). A part of the guest molecule not in cavity protrudes into the molecular space and is in the contact with host molecule of adjacent layer.

4.1.3 Self-aggregation of cyclodextrins

Another studied factor that may influence CD's complexation is the self-aggregation of CDs in water [162, 163]. However, it is still unclear how large is the fraction of CD aggregates as compared to single CDs in solution. In studies of Coleman [164] followed by Gonzalez-Gaitano *et al.* [165] and Purskus *et al.* it has been shown that α-, β- and γ-CD spontaneously form aggregates stabilized by the network of hydrogen bonds. On the other hand, Valente *et al.* [166] using NMR measurements did not observed any aggregates in CD's solutions. However, as authors pointed, CD's aggregates could be present at concentrations up to 1%. These low fractions aggregates of CD would explain why there is no evidence of aggregates as seen by 1H NMR self-diffusion [167] or intramolecular diffusion, since these methods monitor the entire CD population. Another interesting aspect of CD's aggregates has been stressed by the group of Costas [168], where by applying a variety of techniques such as Dynamic surface tensiometry (DST) and Brewster angle microscopy (BAM), they observed an increase in size of aggregates with time. This ageing of aggregates expressed lower affinity towards water/air interface, as compared to a freshly prepared solution. The experimental observations imply that CD aggregates are in dynamic equilibrium with single CD molecules in the bulk solution. These results are in line with atomistic molecular dynamics (MD) simulations, where it was suggested that the driving forces for formation of CD's aggregates are mostly directed by water mediated H-bonds between CD's molecules, rather than hydrophobic forces. The issue of CD's aggregates in solution has been further discussed in several reviews [163, 169, 170].

The processes behind aggregation of CD and factors contributing to their behavior in aqueous solutions still remain elusive. If CD aggregation occurs, the evaluation of the binding constants in cyclodextrin-containing structures becomes complicated. Finally, the aggregation itself may affect the properties of the guest molecule [171].

4.1.4 Cylodextrins in action

Numerous studies have highlighted the ability of CDs to manipulate a lipid composition of red blood cells. The hemolytic activity of CDs has been attributed to two effects: *i*) an osmotic-hypotonic effect at low concentrations of CD, and *ii*) the complexation of lipid components such as cholesterol or phospholipids at higher concentrations. Ohtani and co-workers [172] showed in 1989 that cyclodextrins promote the release of lipids, in the order $\alpha > \beta > \gamma$, but do not themselves bind to the membrane. The higher effect of βCD has been attributed to sterol extraction, due to a steric factor (size of the cavity). The question how βCDs are able to remove cellular cholesterol is still open. Based on their results, Yancey *et al.* [173] proposed that CD molecules diffuse into immediate proximity of the plasma membrane, where cholesterol molecules can diffuse directly into the hydrophobic pocket without the necessity of completely desorbing through the aqueous phase. Recently, Mascetti *et al.* [174] proposed a model based on polarization modulation infrared absorption spectroscopy (PMIRRAS) and BAM measurments, in which βCD molecules stack parallel to the plane of the membrane and form channel-like structures. Further, the group of Marrink [175] observed that successful extraction of cholesterol is linked directly to the presence of head-to-head dimers of βCD bound to membrane surface via hydrogen bonds. Although βCD monomers are in contact with the membrane surface, authors concluded the preference of 2:1 stoichiometry for βCD with cholesterol. The same stoichiometry ratio was also reported by other authors. The cholesterol extraction strongly depends on the βCD derivative, concentration, incubation time and composition of the lipid bilayer. Computational studies showed that extraction of cholesterol from the liquid-order phase (with lipid/cholesterol ratio 0.3-0.6) was significantly reduced as compared to the extraction from the liquid-disorder membrane fractions. Lopez *et al.* [175] reported that due to the kinetic barrier for cholesterol, the spontaneous extraction by βCD dimers is only observed at high cholesterol levels. However, the selective extraction of cholesterol from membrane domains has not been proved experimentally.

Although the extraction of cholesterol by CD has been studied to some extend, the interactions of CD with membrane phospholipids are not completely resolved. Giocondi *et al.* [176] using atomic force microscopy (AFM) showed that incubation of MβCD leads to formation of holes in the DOPC/SM lipid bilayer, which has opened a new dimension in studies of extraction of lipids by CD. Later, in studies of Leventis *et al.* [177], MβCDs expressed greater redistribution of DPPC molecules between LUVs than transfer of cholesterol. Authors concluded that only outer leaflet of a DPPC bilayer was available, and the presence of MβCDs does not affect flip-flop rate of DPPC. Anderson *et al.* [178] proposed a mechanism of lipid extraction including an initial inclusion complex between the bilayer-phase POPC and a single MβCD molecule, followed by threading three more MβCDs on lipid chains. Accordingly, the first step involves a removal of a POPC molecule from the lipid bilayer into aqueous phase prior to complexation. However, this hypothesis is contrasted by the high energy associated with free-lipid in aqueous solution.

In their studies, Khuntawee *et al.* [179] focused on the interaction of βCD with POPC bilayers. The simulation results showed that βCD interacts with the membrane surface with it secondary rim and readily penetrates the membrane interface within approximately 100 ns. The βCD molecules form hydrogen bonds with it secondary rim between the phosphate groups and glycerol ester-groups of lipids. Moreover, it was shown that head groups of POPC molecules occupy the βCD cavity, while the 7-9 lipid molecules are bound outside the cavity. However, until now, experimental studies support adsorption of CD on the membrane surface, rather its penetration into the lipid interface.

In summary, there is still missing consistent experimental and theoretical data on the interaction of CDs with lipid membranes to describe the full-mechanism of lipid extraction by CDs. Since changes in the lipid organization in the plasma membranes can modify the cellular functions it is of crucial importance to address the phenomenon of lipid/CD complexation

4.2 Project Ia: Kinetic evolution of DOPC giant vesicles and supported lipid bilayers exposed to α-cyclodextrins

Cyclodextrins are cyclic oligosaccharides capable of forming inclusion complexes with a variety of molecules, and as such have been recognized as a pharmaceutical and biotechnological asset [180–182]. Cyclodextrins are known to interact with the components of cell membranes, and this correlates with a significant degree of cytotoxicity. In this work we report on the mechanism of degradation of a model dioleoyl-phosphatidylcholine (DOPC) bilayer exposed to a solution with increasing concentrations of α-cyclodextrins. By combining optical fluorescence microscopy and quartz-crystal microbalance experiments, we study the evolution of supported lipid bilayers (SLBs) and giant unilamellar vesicles (GUVs). The rate of lipid removal displayed a very nonlinear dependence in the cyclodextrin concentration, suggesting the formation of lipid aggregates as intermediates for the membrane degradation.

4.2.1 Results and discussion

4.2.1.1 αCD-induced pore formation on aqueous supported lipid bilayers (SLBs)

To gain insight into the mechanism of αCD-lipid bilayer interactions, we imaged the SLBs in real time. The confocal microscope was focused on the glass surface of the measuring chamber, while DOPC SUVs marked with DiI (1 mol %) were gently injected. The vesicle rupture method, used for the formation of SLBs, results in homogeneous bilayers on glass surfaces as reported elsewhere [183, 184]. In order to remove vesicles in excess, the chamber was washed at least 5 times with glucose solution, and the fluorescence intensity profile, along with the depth profile (z-slices), were collected to control the state of the SLB. Before the injection of αCD solution into the chamber, a blank injection of glucose solution alone on the SLB was imaged for 60 min. This step was done to ensure that the bilayer was stable, with no preexisting alterations and that the injection itself was

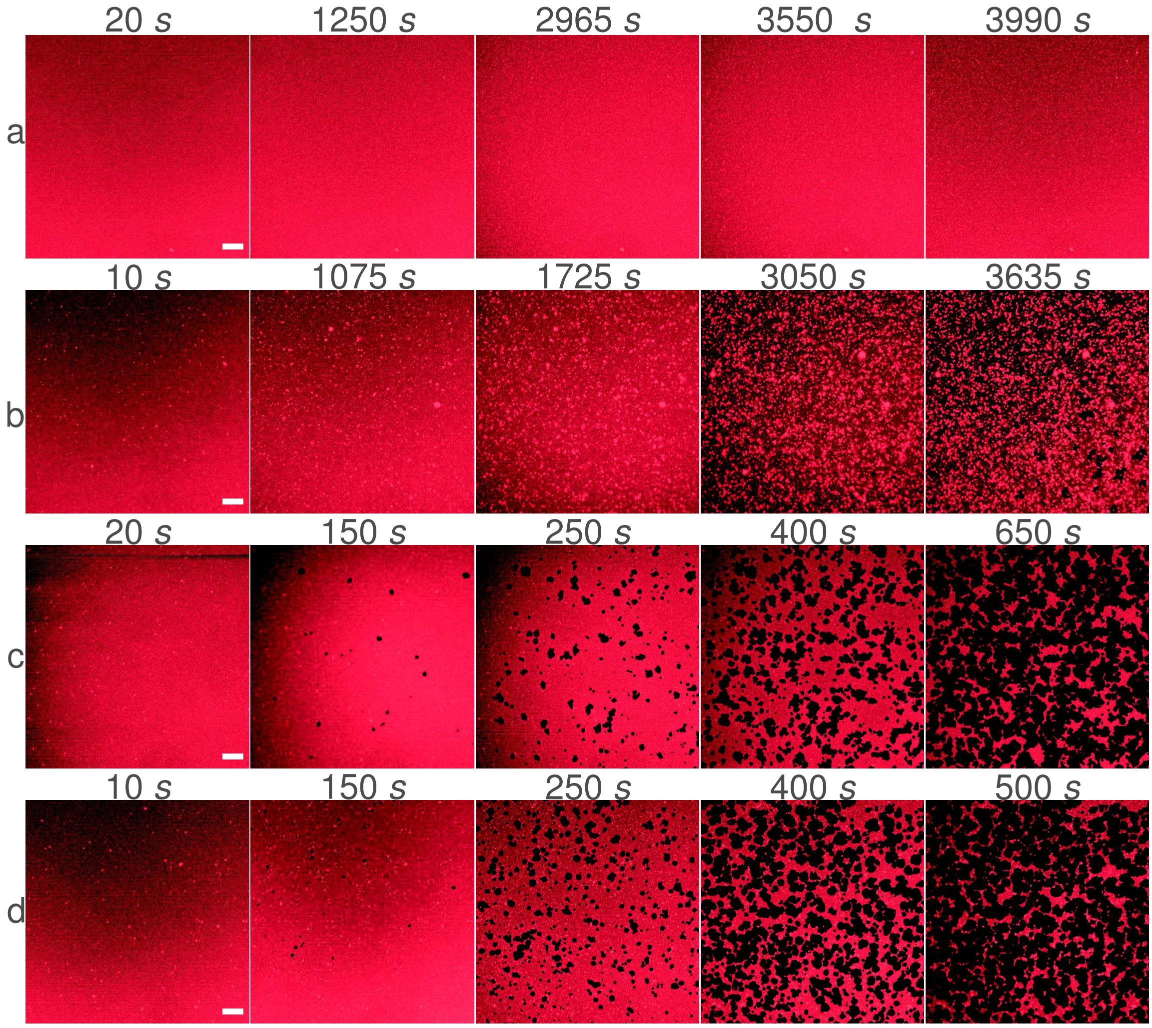

Figure 4.3: Time evolution of DOPC SLB tagged with DiI at various αCD concentrations: a) 5 mM b) 10 mM c) 15 mM d) 20 mM. There is a small lag time of *ca* 3 min between the injection of αCD into the measuring chamber and the beginning of the microscopy acquisition. Scale bar, 10 μm.

not responsible for the formation of the defects. Fig. 4.3 (and Fig. A.1) shows snapshots of SLBs after the addition of αCD at various concentrations. The LSCM imaging in the presence of a 5 mM αCD solution revealed that the lipid membrane was not perturbed. After 60 min of acquisition, a few small fluorescent spots were visible on the membrane surface. After the addition of the 10 mM αCD solution, we observed the formation of many bright spots on the membrane surface. The number and the size of the spots increased continuously with the incubation time (Fig. 4.3b). After 60 min of incubation, the first dark holes were formed. Intensity profiles showed essentially no fluorescence at the center of the holes (Fig. 4.4). At higher concentrations of αCD (15 mM and 20 mM), only 4 min of incubation were needed to observe the appearance of holes in the membrane. The size and shape evolution of the holes with time were similar for each measured concentration.

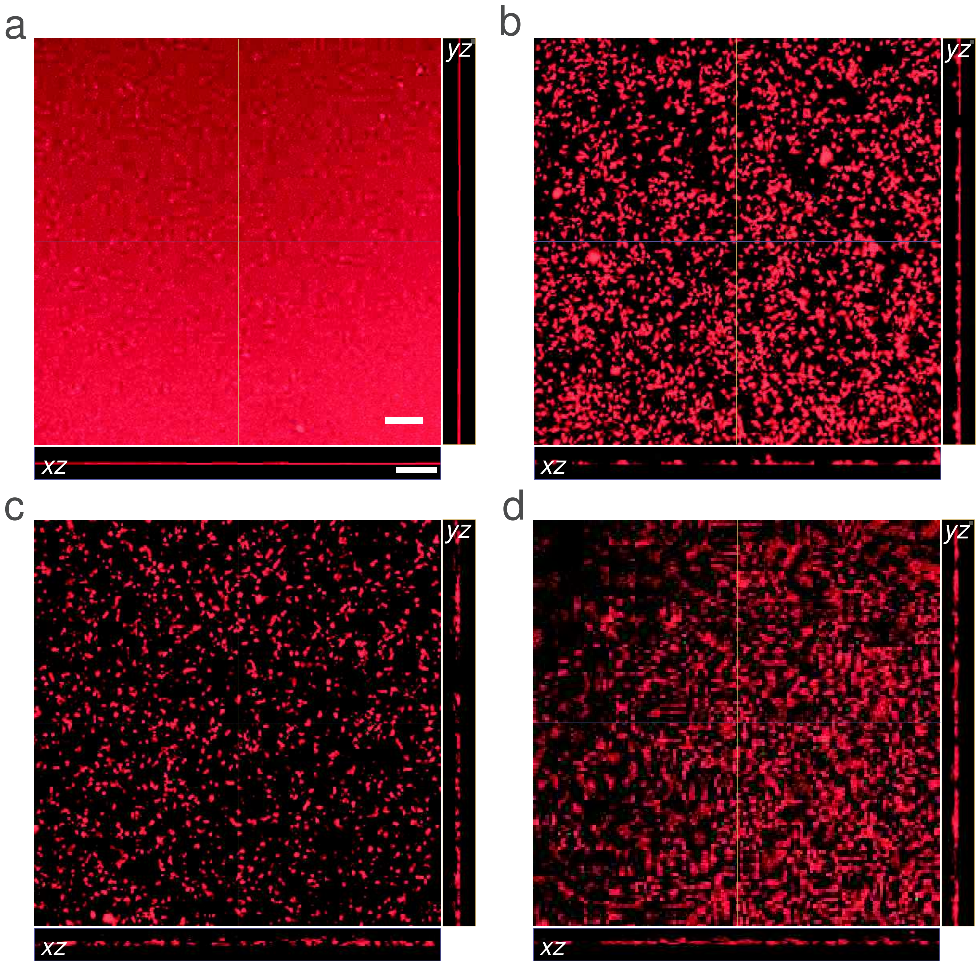

Figure 4.4: Depth-resolved confocal fluorescence microscopy of DOPC SLB, 80 min after injection of αCD concentrations of a) 5 mM b) 10 mM c) 15 mM d) 20 mM. Each panel shows (x, y), (x, z) and (y, z) cuts of the original 3-dimensional image. Scale bar, 10 μm.

The presence of bright spots signifies that a large amount of lipids and fluorophores occupies the focal region of the scanning laser beam. Such brightness is not consistent with the darker red background associated with a single deposited bilayer. We therefore interpret the bright spots as dense lipid-cyclodextrins (and fluorophores) aggregates with a significant rearrangement of the bilayer structure, possibly a thicker multilamellar region. While the presence of cyclodextrin molecules within the aggregates cannot be ascertained, it seems likely that this is indeed the case, cyclodextrins being a necessary ingredient for the formation of these white spots.

We investigated the depth profile (z-slices) of samples before and after injection of αCD (Fig. 4.4). The images revealed remarkable 3-dimensional fluorescent disordered patterns above the surface. Patches of fluorescent materials could be seen floating microns above the silica surface, while still being connected to it. The size and shape of the floating patterns were variable, and no distinctive pattern characteristic of a given concentration could be found. At 10 mM CD concentration, bright spots and floating fragments both covered densely the field of view. For the two largest concentrations, numerous floating fragments were present, with fewer bright spots visible.

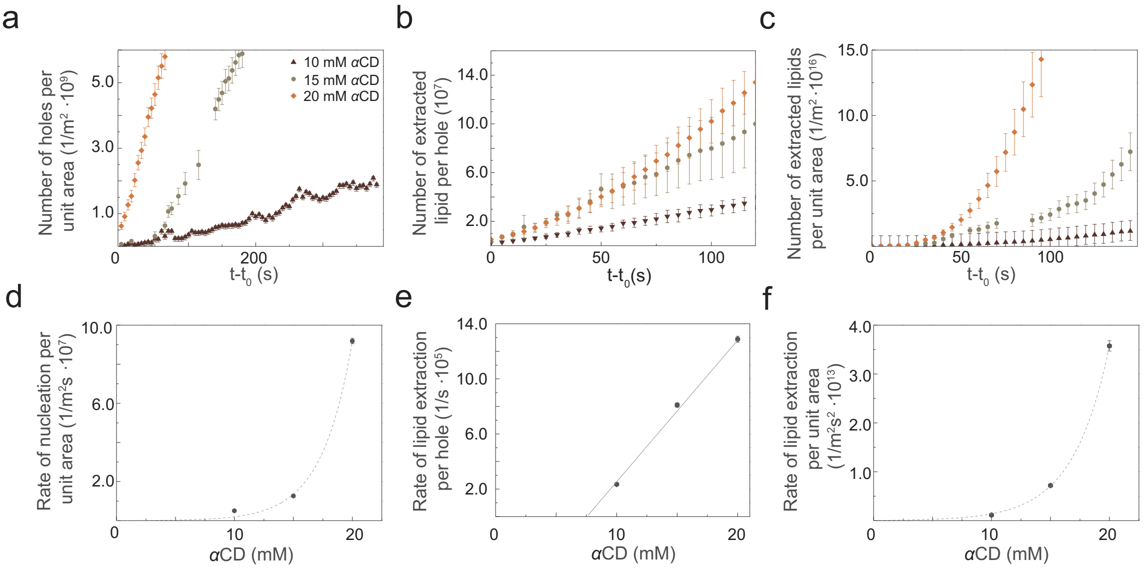

Figure 4.5: a) Number of holes per unit area vs time for DOPC SLBs at 10, 15 and 20 mM αCD concentrations, d) dependence of the rate constant of formation of holes on the concentration (eq. 4.1). b) Temporal evolution of the number of lipids extracted in a single hole (black area) for different αCD concentrations and e) rate β of lipid extraction (eq. 4.2) vs concentration. c) Lipids extracted over time for a whole observation region of size $45 \cdot 10^3$ μm^2, f) represents the concentration dependence of the quadratic coefficient in eq. (4.4) obtained from a quadratic fit of the experimental data.

The kinetic graphs, which summarize the experimental measures performed on the fluorescent supported lipid bilayers, are presented in Fig. 4.5. Using a digital image processing tool (ImageJ plug-in)[185], we estimated the number of holes per unit area (n_{holes}) as a function of time for each concentration. A threshold level of the fluorescent intensity was set to keep only black or white values, representing respectively the holes and the bilayer. The software then counted the number of black components. In order to avoid artifacts, we restricted ourselves to regions of area comprised between 10 and 5000 pixels, thus dismissing single pixels and larger regions formed by the merging of holes. To further avoid artifacts caused by the merging of holes, our calculations were limited to time intervals corresponding to a maximum of 15% of the total SLB area covered by holes, well before their coalescence took place.

The data are consistent with an affine increase in the number of holes with time

$$n_{\text{holes}} = \gamma(t - t_0), \qquad 4.1$$

with t_0 a lag time, and we estimated the kinetic coefficient γ for each concentration. The rate of holes creation γ depends strongly on the αCD concentration (Fig. 4.5a and 4.5d).

We set out to characterize the kinetics of extraction of lipids by αCD by analyzing the area of growing single holes, and calculated the rate of lipid extraction assuming the following affine approximation

$$w_{\text{holes}} = \beta(t - t_{\text{cr}}), \tag{4.2}$$

with β the rate of lipid extraction per hole, t_{cr} the time of appearance of the hole and w_{holes} the area obtained from the number of black pixels pertaining to each hole. The resulting coefficient β, very small for concentrations smaller than a threshold value $[\text{CD}]_s$ = 7.0 mM, shows an affine concentration dependence $\beta = \kappa([CD] - [CD]_s)$ for concentrations above $[\text{CD}]_s$, with a slope $\kappa = 1.18 \times 10^5\ \text{s}^{-1}\cdot mM^{-1}$ (Fig. 4.5 b and 4.5e).

According to equations eqs (4.1) and (4.2), the growth kinetics of the total area $\mathcal{A}_{\text{holes}}$ of the holes seen on a whole SLB image should factorize into product of number of holes creation and growth rate of each hole. We therefore expect that

$$\begin{aligned} \frac{\mathrm{d}\mathcal{A}_{\text{holes}}}{\mathrm{d}t} &= \beta n_{\text{holes}}; \\ \frac{\mathrm{d}n_{\text{holes}}}{\mathrm{d}t} &= \gamma, \end{aligned} \tag{4.3}$$

leading to

$$\mathcal{A}_{\text{holes}} = \frac{\beta\gamma}{2}(t - t_0)^2. \tag{4.4}$$

This quadratic model shows good agreement with experimental data (Fig 4.5 c). We report in Table 4.3 the average rate of lipid extraction as inferred from the growth of the dark regions in the supported lipid bilayers. This average rate $k_{\text{SLB}} = m_{15\%}/t_{15\%}$ is defined here as the inverse of the time $t_{15\%}$ needed to remove 15% of the initial SLB mass, multiplied by the corresponding mass removed ($m_{15\%}$).

4.2.1.2 QCM-D analysis of the resonant frequencies of SLB interacting with αCD

The interaction between αCD and supported DOPC bilayers was further investigated using the QCM-D technique. Monitoring overtones of the QCM-D sensor provides important information about the mechanism of action of αCD on a lipid bilayer adsorbed on a silica (quartz) surface. Generally, changes in resonant frequencies are associated to changes in the mass of the system, either due to adsorption (negative shift in f value) or to desorption (positive shift in f value). In parallel, changes in the dissipation factor are qualitatively related to changes in the mechanical properties of the membrane, whether it becomes stiffer (decrease in D) or more viscous (increase in D).

The formation of the SLB and the consequences of its exposure to αCDs were monitored by recording the frequency and dissipation responses of the QCM-D, as shown in Fig. 4.6. The QCM-D response upon adsorbing DOPC SUVs (in the presence of ions [186]) on silica shows a two-step process. The first step reflects the attachment of a vesicular layer to the QCM-D sensor surface, until a minimum in frequency (Δf_{min}) and a maximum in dissipation ($\Delta \mathrm{D}_{max}$) are reached (Fig. 4.6 a(1)). The second step corresponds to the vesicle rupture-fusion process with the formation of a continuous SLB at the sensor surface. The membrane was then stabilized during the buffer rinse step (Fig. 4.6 a(3)) which removed all intact vesicles and floating lipid fragments. The observed values of the frequency $\Delta f \simeq 24$ Hz and the dissipation $\Delta D \simeq 6 \cdot 10^{-6}$ were consistent with the formation of a stable hydrated SLB (Table 4.2, Table A.1) [187–189]. A buffer solution of αCD was then added (Fig. 4.6 a(4)) to the QCM-D chamber and was allowed to stay in contact with the bilayer for *ca* 100 min, followed by a final buffer rinse step (Fig. 4.6 a(5)). This final rinse allowed for comparison of the system before and after injection of αCD.

The typical frequency response shows an initial decrease in value in all studied systems, suggesting a mass increase on the sensor surface as αCD adsorbs on the exposed bilayer. For the lowest concentration of αCD (5 mM), only a small decrease in Δf (< 2 Hz) was observed for each overtone, and uniform positive values of ΔD ($\simeq 1.5 \cdot 10^{-6}$) were recorded. However, both parameters recovered their initial values after the final buffer rinse (Fig. 4.6 a(4)), which indicates a reversible adsorption of αCDs on the lipid bilayer, with minor changes in mass and viscoelasticity of the membrane. By contrast, upon addition of more concentrated αCD solutions (15 mM and 20 mM, Fig. 4.6 c and d), we first observed a deposition of the αCDs at the SLB surface, followed by sharp positive shifts in frequency and dissipation with splitting of the overtones. The combined values of Δf and ΔD indicate a rapid loss of lipid mass with significant disruption and disorganization within the membrane. The magnitude decreases as the order of the overtones increases, suggesting that the transverse vibrations induced by the sensors were strongly damped on distances comparable to the membrane thickness, and that the vibration period was shorter than the bilayer internal rearrangements. The important dispersion of the dissipation parameters with frequency (overtones) suggests that large portions of the membranes were floating above the surface, dragging the outer solvent solution during their oscillatory motion, while still being connected to the surface. These results are compatible with an absorption of αCD at the surface of a membrane, followed by gradual mass removal, presumably in the form of αCD-lipid aggregates semi-detached from the surface. Results for the 15 mM and 20 mM concentrations follow a qualitatively similar trend, indicating a similar dynamical destabilization mechanism. However, as can be seen from Fig. 4.6 (and Table A.1), it seems that the system with 20 mM αCD reached saturation faster than the 15 mM one. Finally, exposure of DOPC-SLB to 10 mM αCD concentration, showed an intermediate situation as compared to the 5 mM and 15 mM cases. After a short deposition of αCDs at the membrane surface (Δf = -2.96 Hz), Fig. 4.6 b shows positive changes in frequency for all the measured overtones. The relatively uniform increase in Δf for each overtone indicates that the lipids that remained attached to the surface oscillated homogeneously. The changes in dissipation parameter are small for all overtones, suggesting the absence of viscoelastic mechanical response of the membrane. The bilayer seems to be have been removed gradually without desorption of macroscopic pieces of membrane.

The measured values of dissipation and frequency for 10, 15 and 20 mM αCD concentrations after the final buffer rinse, show only small amounts of material remaining at the sensor surface (Table 4.2), which indicates that most of the lipids were removed by the αCD molecules.

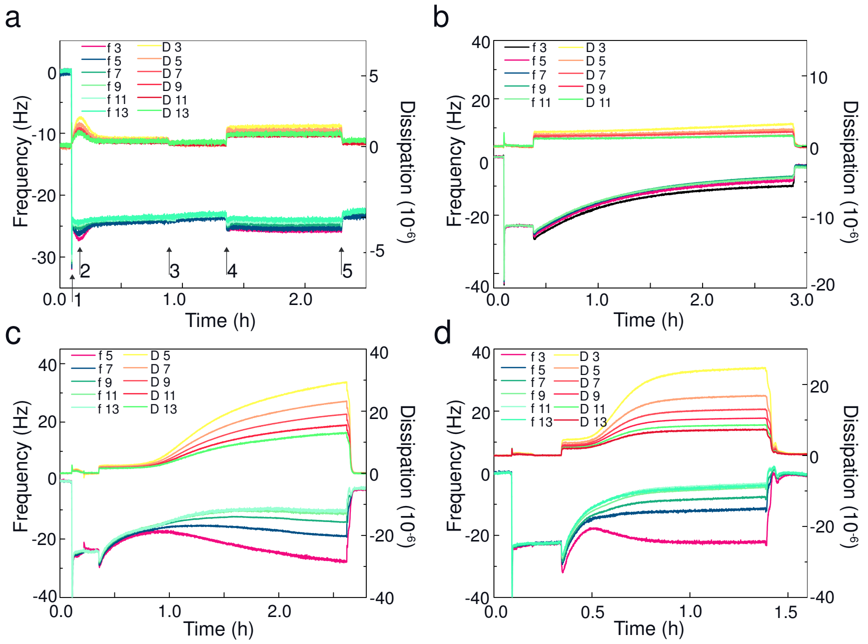

Figure 4.6: Representative plots showing QCM-D frequency (f) and dissipation (D) responses of a DOPC bilayer exposed to αCD at a) 5 mM, b) 10 mM, c) 15 mM, and d) 20 mM concentrations. The set of blue lines represents changes in frequency, and yellow lines in dissipation. Common to all plots: (1) Lipid vesicle deposition, (2 and 4) Buffer rinse, (3) αCD addition. The lines represent different overtone responses for frequency (F) and dissipation (D).

Based on the initial changes in frequency (Table 4.2, Fig. 4.7 a) and using the Sauerbrey equation (4.6), we estimated the initial mass of absorbed αCD at the membrane surface for all concentrations. Our numerical values for the initial mass were obtained from the first maximum of the frequency shift curves (10, 15 and 20 mM) and the plateau value (5 mM) in Fig. 4.7 a.

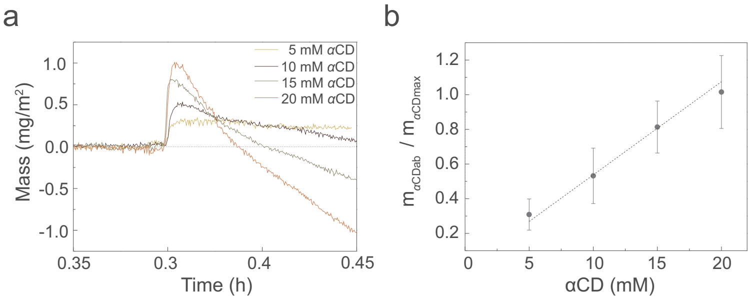

Figure 4.7: a) Changes in mass on the sensor after the injection of αCD at various concentrations (data for the 7^{th} overtone). b) Cover fraction equivalent to one monolayer of αCD on the membrane surface. The dash line represents the best linear adjustment.

We estimated the maximal mass of αCD that could be adsorbed onto the membrane surface, by exposing their wider rim and packing into a single hexagonal compact monolayer (Fig. 4.1). Using the area of the sensor ($A = 1.54 \cdot 10^{-4}$ m^2) as the total area of membrane available, and taking the diameter of the wider rim equal to 13.7 Å[190], we found a theoretical mass value for a dense adsorbed αCD monolayer equal to $m_{\text{max}} = 1.54 \cdot 10^{-4}$ mg.

The ratio of the measured mass deposited at the quartz surface to m_{max} defines a covered fraction (Fig. 4.7 b, Table 4.2). Interestingly, the experimental covered fraction increases linearly with αCD concentration, reaching a maximum value close to 1 at 20 mM. It should be stressed that our model relies on a uniform monolayer of adsorbed αCD, whereas more complex associations of the CDs with the membrane have been reported [191–193].

Table 4.2: Estimated mass changes on the QCM-D sensor, based on changes in frequencies. Mass of deposited bilayer (m_{bilayer}), mass detected at the sensor surface after the last rinse (m_{sensor}), change in frequency after injection of αCD ($\Delta f_{\alpha\text{CDad}}$), corresponding mass of adsorbed αCD (m$_{\alpha\text{CDad}}$), and mass coverage fraction ($m_{\alpha\text{CDad}}/m_{\alpha\text{CDmax}}$). Values are shown as averages over three repeated experiments for each concentration, and the standard deviation is used as an error estimate.

αCD [mM]	m_{bilayer} [mg] 10^{-4}	m_{sensor} [mg] 10^{-4}	$\Delta f_{\alpha\text{CDad}}$ [Hz]	$m_{\alpha\text{CDad}}$ [mg] 10^{-5}	$m_{\alpha\text{CDad}}/m_{\alpha\text{CDmax}}$
5	6.35 ± 0.32	6.29 ± 0.47	-1.74 ± 0.49	4.72 ± 1.34	0.31 ± 0.09
10	6.45 ± 0.13	0.92 ± 1.21	-2.96 ± 0.80	8.14 ± 2.18	0.53 ± 0.16
15	6.80 ± 0.22	0.88 ± 5.82	-4.56 ± 0.93	12.40 ± 2.54	0.81 ± 0.15
20	6.26 ± 0.37	0.29 ± 2.64	-5.72 ± 1.20	15.50 ± 3.25	1.01 ± 0.21

By following changes in mass on the QCM-D sensor, in the regime immediately following the initial adsorption, we calculated the rates $k_{\text{QCM-D}}$ of lipid removal by αCD and compared them with the values obtained from SLBs (Table 4.3).

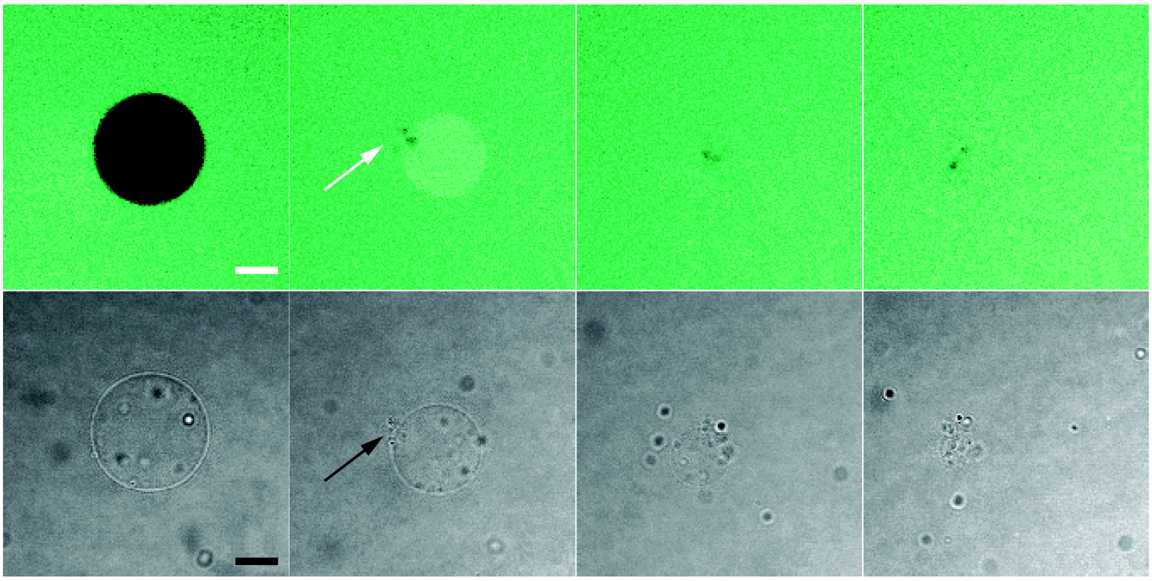

Figure 4.8: Time evolution of DOPC GUVs interacting with 10 mM αCD. a) Laser scanning confocal microscopy of GUVs in a solution containing the water soluble dye HPTS, b) corresponding bright field images. Arrows show an anomalous aggregate at the vesicle surface (bright and dark spots, respectively). There is a small lag time of *ca* 3 min between the GUV/ αCD mixing and the beginning of the microscopy acquisition. Scale bar, 10 μm.

4.2.1.3 Dynamics of GUVs degradation by αCD

To gain more insight into the membrane-disruptive mechanism of αCD, we observed isolated giant unilamellar vesicles. Fig. 4.8 shows the typical temporal evolution of GUVs following exposure to 10 mM αCD. After the αCD aqueous solution was injected into the observation chamber, defects began to develop from the GUVs surface (Fig. 4.8, white and black arrows). The images shows an anomalous aggregate, or protrusion, at the vesicle surface. Beside protrusions being visible at the surface, the GUV shrank gradually, while keeping its spherical shape until the final stages. At the beginning of the shrinking stage and during a short period, the vesicle decreased in size but its interior showed no fluorescence. Then, the vesicle compartment steadily increased its fluorescence intensity, indicating a loss of integrity of the membrane and exchange of larger molecules between the vesicle interior and the external solution (Fig. 4.8). The fact that the HPTS fluorophore used in this measurement has a sizable molecular weight (M_w = 524.37 Da) suggests that membrane permeabilization occurred though pore formation. The entire process took place within 10 min following cyclodextrin injection. This indicates that poration and membrane protrusion occurred in parallel, forming the two sides of a same undergoing membrane degradation mechanism. Concentrations of αCD larger than 5 mM were required to make the degradation of GUVs effective.

The apparent diameter of a few selected vesicles was measured and represented as a function of time (Fig. 4.9). Interestingly, the apparent diameter, and not the area, seems to decrease linearly with time. This shrinking dynamics suggests that losses in membrane surface are compensated by corresponding losses of intravesicular water. Since vesicles remain spherical at all times but the very end, we suggest that lipid extraction from GUVs is a continuous process lasting until the reservoir of available lipids is exhausted.

As for SLB measurements, we noticed a faster than linear evolution of the lipid extraction kinetics with the concentration of αCD in the observation cell. At a low concentration of 5 mM, vesicles remained unaltered during at least 40 min of acquisition. Conversely, under larger αCD concentrations, a morphological response was detected after only few minutes of observation.

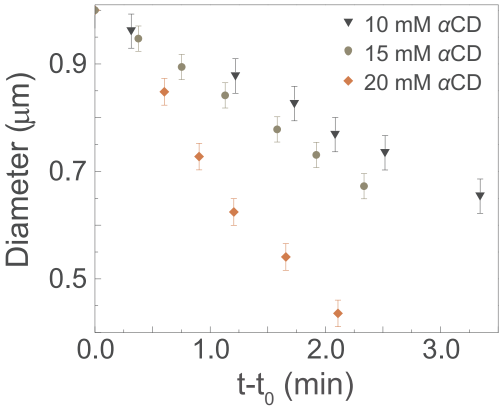

Figure 4.9: Changes in GUV diameter upon interaction with αCD at various concentrations, t_0 observation lag time.

To better quantify the mechanism of the observed αCD-lipid bilayer shrinking phenomenon, we converted the observed decrease in area into a loss of lipid mass, based on a commonly accepted value of the area per lipid (70 Å^2) [194] of a tensionless DOPC bilayer. Considering that αCD interacts only with the outer leaflet, it resulted in a rate of lipid extraction k_{GUVs} (Table 4.3).

Table 4.3: Rate of lipid extraction by αCD calculated from supported lipid bilayers (SLBs) and giant unilamellar vesicles (GUVs) measurements using QCM-D and LSCM techniques. Values are shown as averages of at least 2 measurements for each concentration, and the standard deviation is used as an error estimate

	SLB LSCM	SLB QCM-D	GUVs LSCM
αCD [mM]	k_{SLB} [mg/m^{2}s 10^{-4}]	$k_{\mathrm{QCM-D}}$ [mg/m^{2}s 10^{-4}]	k_{GUVs} [mg/m^{2}s 10^{-4}]
10	2.98 ± 0.08	9.61 ± 0.02	103 ± 56
15	5.64 ± 0.23	18.40 ± 0.05	139 ± 103
20	18.70 ± 0.52	58.60 ± 0.04	399 ± 234

4.3 Discussion

Both supported and vesicle lipid bilayers were found to be strongly damaged by the α-cyclodextrins. The nature and the kinetics of the degradation were consistently dependent on the αCD concentration level in solution. At 5 mM αCD, the bilayer was only marginally altered. The mass adsorption on the SLB was reversible, the SLB appearance stayed uniform for hours and GUVs did not evolve for at least 40 min. At the opposite, a 15 and 20 mM concentration level of αCD brought about fast, strong and irreversible alterations of the bilayers. The entire mass of the SLB was removed while a dissipation level typical of a poorly bound membrane was observed. The fluorescent images of the SLB showed many detached patches of membranes along with fast growing dark regions with no lipid in contact with the surface. GUVs shrinking and permeabilization were fast, although vesicles retained their spherical shapes. Spots at the vesicle surface were visible. The 10 mM case differed qualitatively from the two previous limits. The bilayer evolved in a non-reversible way, but at a significantly slower rate. The degradation then seemed to be both homogeneous and progressive. Bright spots covered the fluorescent SLBs, followed by many slowly growing black holes. The QCM-D signal showed an irreversible loss of mass, but the amount of dissipation remained low with almost superimposed overtones. A slower GUV contraction was observed.

All these observations point to a strongly non linear concentration dependence of the mechanism, both quantitatively and qualitatively. They bear the hallmark of a cooperative multi-molecular process. We hypothesize that the presence of protrusions/aggregates at the GUVs surface (Fig. 4.8) mirrors the similar protrusions/aggregates seen on SLBs images (Fig. 4.3, 4.4). Our assumption is that the lipid removal driving force acting on the bilayers is common to both systems, and is due to the presence of dense CD-lipid aggregates at the surface. Based on our observations, we propose the following mechanism. Aggregates mixing lipids and cyclodextrins grow at the expense of the bilayer and put it under tension. After some time, the membrane is torn apart, causing the porosity of the vesicle and the appearance of dark holes in the supported bilayer. Aggregates need not to be bilayers and could very well display a different molecular organization built on tight cyclodextrin-lipid interactions.

Table 4.3 reveals that the lipid removal kinetic coefficients for SLBs and GUVs differ significantly. As the driving force acting on bilayers is assumed to be common to both systems, the difference in kinetics is likely to originate from a different dissipation mechanism opposing lipid removal. In the case of SLBs, interaction with the surface as well as lipid bilayer friction are strong. This could explain why the rates are relatively lower. In the case of GUVs, the dominant dissipation mechanism could be the viscous resistance of the internal solvent that is expelled during the vesicle shrinking stage. Assuming that the solvent flow across the bilayer is proportional to the vesicle area A, and that the interaction with αCD puts the membrane under constant tension, therefore increasing the internal pressure due to Laplace law, the time derivative of the inner volume V is expected to comply with the following equation

$$\zeta \frac{\mathrm{d}V}{\mathrm{d}t} = -A, \tag{4.5}$$

with constant rate ζ. This behavior leads in turn to a linear decrease in vesicle diameter, as observed.

4.3.1 Conclusion

Using a combination of Confocal Microscopy and Quartz Microbalance experiments, we studied the mechanism of the degradation of a DOPC bilayer exposed to increasing concentrations of αCD in solution. We confirm that αCD is a powerful membrane disruptive agent. For the first time, we could complement the usual QCM-D mass measurements with fluorescent imaging of SLBs under very similar conditions.

We do not favor of single molecular mechanism of lipid extraction, but rather the formation of lipid-cyclodextrin rich aggregates that promotes a local disorganization of the bilayer (lipid protrusion, spots). These aggregates grows at the expense of the bilayer, either shrinking and creating defects in the vesicles or tearing apart the supported bilayers, with the creation of dark holes.

The kinetics of the bilayer degradation is strongly cyclodextrin concentration dependent. With little or slow effects at a concentration of 5 mM, the evolution is both fast and disruptive at concentrations of 15 and 20 mM. The 10 mM case, is an intermediate situation with irreversible loss of mass but little apparent changes in the bilayer structure.

Our study confirms the potency of αCD as a model membrane disruptive agent, which become aggressive to the lipid bilayer at concentrations equal or above 10 mM. We suggest that our observations are related to the cytotoxic character of α-cyclodextrins.

4.3.2 Materials and Methods

Materials

Chloroform solution of DOPC (1,2-dioleoyl-sn-glycero-3-phosphocholine, $C_{44}H_{84}NO_8P$, M_w 786.11) was purchased from Avanti Polar Lipid (Birmingham, AL). DiI Stain (1,1'-Dioctadecyl-3,3,3',3'-Tetramethylindocarbocyanine Perchlorate $C_{59}H_{97}ClN_2O_4$, M_w 933.88) and HPTS dye (8-Hydroxypyrene-1,3,6-Trisulfonic Acid, Trisodium Salt, $C_{16}H_7Na_3O_{10}S_3$, M_w 524.37) were provided by ThermoFisher Scientific (Waltham, MA, USA). α-cyclodextrin ($C_{36}H_{60}O_{30}$ M_w 972.84), Sucrose ($C_{12}H_{22}O_{11}$ M_w 342.3), Glucose ($C_6H_{12}O_6$ M_w 180.16) and Phosphate buffered saline (PBS) were purchased from Sigma-Aldrich (Saint-Quentin, France). All chemicals had high purity and were used without further purification.

Giant unilamellar vesicles (GUVs)

Giant unilamellar vesicles (GUVs) of DOPC were prepared using the polyvinyl alcohol (PVA) gel assisted -formation method as described by Weinberger *et al.* [195]. Briefly, 200 μL of 5% (w/w) PVA solution was spread on a glass slide and dried for 30 min at 80°C. Once prepared the PVA-coated substrate, 5 μL of lipid in chloroform (1 mg/mL) was spread and placed under vacuum for 30 min to evaporate the organic solvent. Using rubber gasket as a temporary chamber, the lipid film was hydrated with a sucrose solution (100 mOsm/kg) and left for incubating 60 mn. After the incubation period, the GUVs were collected and transferred into Eppendorf tubes and diluted with a glucose solution containing the HPTS fluorescent dye (90 mOsm/kg). The osmolarities of the sucrose and glucose solutions were checked with a cryoscopy osmometer Osmomat 030 (Gonotec, Berlin, Germany).

Formation of supported lipid bilayers (SLB) for confocal microscopy

Small Unilamellar Vesicles (SUVs) were prepared from DOPC lipids and DiI fluorescent probes, with a 99:1 ratio. A mixture of lipid and dye (1 mol%) in chloroform was dried in a small vial under N_2 stream, and left overnight under vacuum. Sucrose solution (100 mOsm/kg) was used to re-suspend the lipids to a final concentration of 2 mg/mL. The resulting MLV suspension was sonicated using a tip sonifier (Bioblock VibraCell 72412) at lowest power for 12 min. The resulting SUVs were then filtrated on a 0.22 μm membrane to remove debris from the tip, and diluted with glucose solution (90 mOsm/kg) to reach a 1 mg/mL concentration. After the injection of SUVs on the prepared glass, the vesicles absorbed on the surface undergo rupture and fusion to form an extended planar bilayer. Each supported lipid bilayer was rinsed 5 times with the glucose solution. Note that glucose itself is not necessary to form SUVs or SLBs. It was introduced here to facilitate the comparison between SLBs experiments and GUVs experiments.

Laser scanning confocal microscopy measurements

The visualization of the lipid GUVs, the fluorescent SLBs (DiI) and the detection of fluorophores in solution (HPTS) were performed using a laser scanning confocal microscope (LSCM) Nikon Eclipse TE2000-E equipped with a Nikon d-eclipse C1 confocal unit (Nikon, Amsterdam, Netherlands). The objective was a Nikon 60x water immersion, NA 1.2 (Nikon). Excitation of DiI in supported lipid bilayers was performed at 543 nm (HeNe laser), guided to the sample by a dichromatic mirror (Nikon). The detection of the fluorescence signal was done using a 615 nm bandpass filter and a photomultiplier (PMT). The excitation of HPTS was done with a diod laser at 408 nm (Nikon), and the detection performed using a 454 nm bandpass filter and a photomultiplier.

Glass preparation for fluorescent SLBs

Before each LSCM experiment, the glass coverslip was UV/ozone treated (Novascan Ames, USA) for 15 min and rinsed with ethanol and MilliQ. Then, a second UV/ozone treatment (Novascan Ames, USA) was applied for 15 min, yielding the glass surface highly hydrophilic.

Formation of supported lipid bilayers for QCM-D measurements

The preparation of supported lipid bilayer followed the same step as illustrated for optical microscopy measurements. In case of QCM-D, no addition of DiI fluorophore was needed.

Preparation of αCD solution

The appropriate amount of α-cyclodextrin was dissolved into PBS buffer solution (0.5 mM) and left for 30 min on vortex, prior to use. For all experiments, fresh solutions of α-cyclodextrin were prepared.

QCM-D experiments

The Q-SENSE E4 system (Biolin Scientific, Stockholm, Sweden) was used to monitor the formation of SLBs on quartz surfaces coated with silicon oxide, and to follow changes in membrane properties upon exposure to α-cyclodextrin in real-time. The quartz sensor crystals were placed into the QCM-D chambers and exposed to buffer, lipid and cyclodextrin solutions. The QCM-D technique measure the amplitude of the overtones of the resonant vibration frequency of the quartz crystal, and their dephasing associated with the mechanical dissipation of the sensors.

The adsorption of a mass Δm onto the vibrating quartz results in a negative shift Δf of the resonant frequency. The Sauerbrey equation relates the frequency variation Δf to the mass variation Δm, in the case of rigid film adsorption:

$$\Delta f = \frac{-f_0^2}{A\sqrt{\rho_q \mu_q}} \Delta m \tag{4.6}$$

where f_0 is the resonant frequency of the quartz crystal (5MHz), A is the piezoelectrically active crystal area, ρ_q is the density of quartz (2.648 g/cm^3) and μ_q is a shear modulus of the crystal ($2.947 \cdot 10^{11}$ g/cm·s^2) in the transverse orientation.

In the case of soft films, the Sauerbrey equation must be adjusted to reflect the viscoelastic response of the film coupled to the surrounding bulk solution [119]. The mechanical dissipation consecutive to crystal oscillations is proportional to the out-of-phase amplitude of the displacement. In the case of an homogeneous viscoelastic film, it can be characterized by a ratio D

$$D = \frac{G''}{2\pi G'} \tag{4.7}$$

where G" is the loss modulus and G' the storage modulus of the adsorbed material [196]. Soft, viscous materials tend to show higher D. As the oscillating strain propagation normal to the surface decreases with frequency, different harmonics of the piezoelectric signal probe different thicknesses. In the case of thick adsorbed films, the penetration depth of the strain δ is related to the overtone frequencies nf_0 by the relation

$$\delta = \left(\frac{\eta_f}{n\pi f_0 \rho_f}\right)^{1/2} \tag{4.8}$$

with η_f the low frequency viscosity of the film, n the overtone, ρ_f the film density. The higher the frequency, the lesser the apparent adsorbed mass is [196].

Sensor preparation

Silica-coated sensor crystals were placed into QCM-D flow chambers and cleaned by flowing ultra pure MilliQ water, sodium hydroxide solution (0.1M) and hydrochloric acid (0.1M). The sensors and chambers were dried under N_2 stream. A UV-ozone cleaner (Novascan Ames, USA) was used for 45 min to treat the sensor surfaces before each experiment.

Bilayer formation and exposure to cyclodextrins

Buffer was flowed over crystal sensors at 0.6 mL/min for ~15 min until the frequency and dissipation responses became stable. The SUVs solution was flowed over the crystals at 0.3 mL/min to a form stable supported lipid bilayer. The bilayer was rinsed with buffer in order to remove any unattached lipids. Once the baseline was stable, the 0.6 mL solution of α-cyclodextrin was added at 0.3 mL/min. The QCM-D crystals were exposed to the cyclodextrin solution during 60-90 minutes, after which the bilayer was rinsed again at 0.3 mL/min with a buffer solution, until the frequency stabilized. Each experiment was repeated at least 3 times for each concentration of αCD.

4.4 Project Ib: The formation of host-guest complexes between lipid and α-cyclodextrin

In the present project, we investigate the supramolecular interactions between αCD and DOPC lipid using experimental techniques and theoretical calculations. The high affinity of αCD towards lipid membrane leads to host:guest formation with disruption of the lipid bilayer (see Project Ia). Understanding the mechanism of lipid extraction is important to develop a better strategy for pharmaceutical formulations.

Our Cryo-TEM images reveal that αCD acts on the membrane/water interface, progressively extracting lipid components from the lipid bilayer, resulting in a strong deformation of the membrane structure. Furthermore, by combining small angle X-ray scattering (SAXS) and scanning electron microscopy (SEM), we visualize the surfaces morphology and confirm the existence of αCD/DOPC complex crystals.

We employ isothermal titration calorimetry (ITC) to estimate the αCD affinity for lipid species, as well as both enthalpic and entropic contributions of αCD/lipid interactions. Moreover, we perform theoretical calculations to determine the αCD/DOPC ratio in complexes. Of all proposed supramolecular structures, 3-5:1 αCD/DOPC complexes are proposed to be the most favourable. The stoichiometry is further confirmed by the one-dimensional 1H-NMR analysis of the crystals.

Taken together, our results attempt to provide a comprehensive structural and thermodynamic picture of αCD binding to the model lipid membrane, together with its complex interactions with the lipid components at the membrane/water interface.

4.4.1 Results and discussion

4.4.1.1 Morphological evolution of liposomes exposed to a concentrated solution of αCD

Cryo-TEM makes it possible to image individual liposomes at high resolution, on time scales of the order of a few minutes. A 20 mM αCD solution was mixed with a 1.27 mM DOPC-LUVs dispersion at 25°C and aliquots of sample were taken at different incubation times (see Figure 4.10).

The high resolution Cryo-TEM images of αCD incubated with 100 nm- diameter vesicles reveal ability of αCD to induce structural changes in membrane structure (Figure4.10). To thoroughly investigate the αCD/LUVs interaction, we followed the time evolution of the sample. A 15 min incubation time is sufficient to induce the first adhesion evens between two or more vesicles (Figure 4.10 a, white arrows). White arrow on Figure 4.10 a1 indicates the area of the first contact between two vesicles. In each vesicle we can distinguish both leaflets, however, shows a clear contact between outer-leaflets with a slight indication of matter in between the latter. For comparison, black arrow indicates non-interacting vesicles. Since a control performed with αCD - free LUVs dispersion show no contact points between vesicles, therefore suggests that the process of adhesion is mediated by the presence of αCD (Figure B.3 at page 124).

Further analysis of the sample (Figure 4.10 a2) clearly shows that the presence of αCD triggers the adhesion between vesicles. In Figure 4.10 a2 we observe two vesicles, where bilayers are in close contact. However, the bridging region is rather small as compared to previously reported adhering liposomes [197]. This feature suggests an ongoing process.

Later, in Figure 4.10 a3, a white arrow points to the area where we are no longer able to resolved two bilayers of interacting LUVs. Thus, we observe the beginning of hemifusion process between two liposomes. Moreover, in the studied sample we observed the clustering higher number of vesicles (see Figure 4.10 a4)

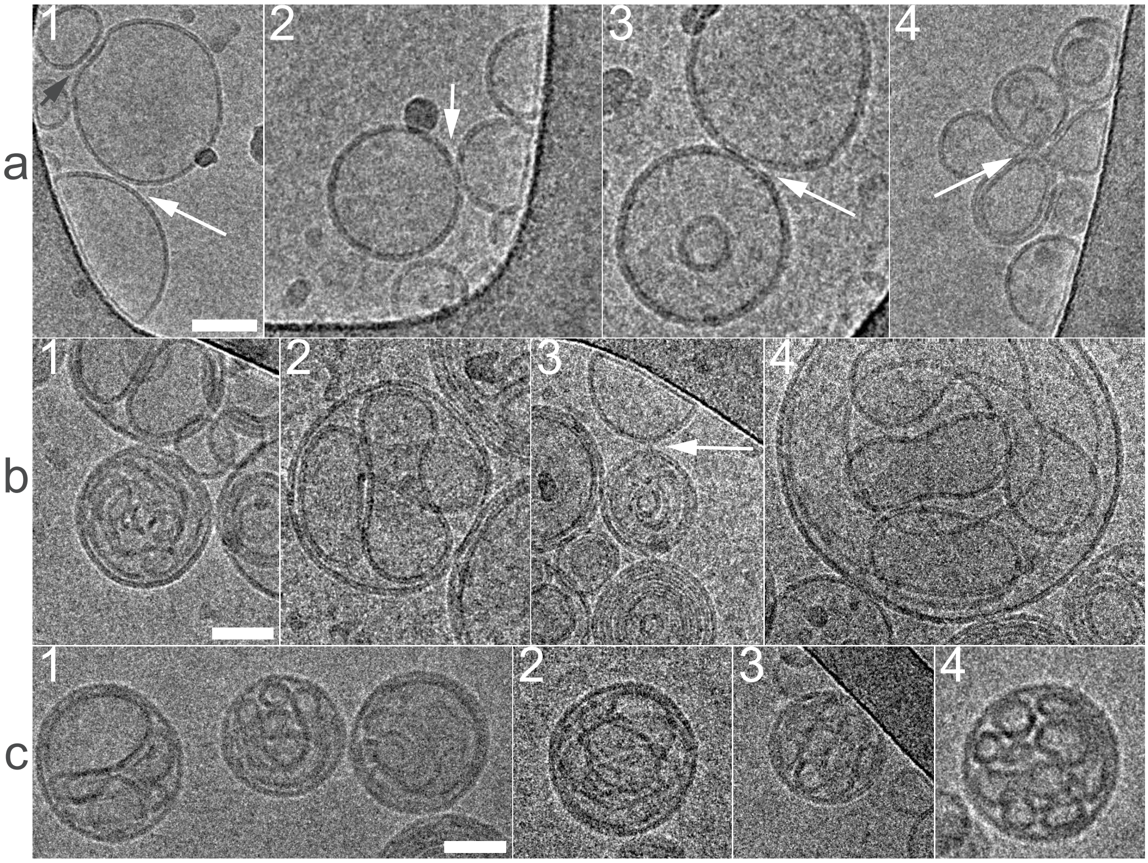

Figure 4.10: αCD induced lipid membrane deformations. The following sequence of incubation times is presented: a) 15 min b) 60 min c) 24 hours. White arrows indicate the interaction between αCD and DOPC-LUVs. Scale bar, 50 nm.

Taken together, the observed interactions between LUVs suggest that αCD has to remove lipid material from outer-leaflets of vesicles. Consequently, the resulting imbalance between outer-and inner- leaflets promotes the fusion and clustering of the vesicles. With increasing incubation time (1h), the number of interacting vesicles increases (Figure 4.10 b). More importantly, we observe the presence of internalized internal structures within vesicles, displaying deformed shapes. Vesicles incubated for ~24h with αCD showed the inclusion of highly curved structures encapsulated into spherical shaped objects. The vesicle interiors are filled with a dense stack of lamellar objects, with no obvious recognizable topology. Contrary to naive expectations, the size of the dense spherical objects do not grow significantly as compared with blank experiments, as a standard mechanism of diffusion limited aggregation for sticking objects would predict.

Describing the evolution of the bilayer membrane based on the above Cryo-TEM pictures is not a trivial task. We first observe that lamellar structures do survive in the presence of concentrated αCD solution, whilst giant vesicles and supported lipid bilayers are subject to significant degradation under similar conditions. There is evidence of lipid bilayer hemifusion in the kissing regions of vesicles in contact after 15 min.

For larger incubation times, we see persistence of the lamellar structures, that we assume to be composed of lipid bilayers decorated with αCD, even though the cyclodextrin molecules do not seem to participate in the contrast of the TEM images. The most natural interpretation of the pictures is that some LUVs survive as vesicles while capturing and internalizing gradually other vesicles. This implies that the αCD provide enough impetus for the outer vesicles to suck in and wrap in other vesicles, or membrane patches, into themselves. A possible explanation would be the presence of a αCD coating that would promote inter-bilayer adhesion strong enough to curve and possibly cut open the liposomes. We could not determine the genus of the wrapped lamellar objects encapsulated into the outer vesicles. Also, it is impossible to tell whether the inner lamellar curvature is intrinsic, caused by inner-outer leaflet composition imbalance [198], or extrinsic and induced by confinement [199]. It would be surprising though that after such a long incubation time and given the strong distortion of the inner bilayers, one could still distinguish among inner and outer leaflets, and we therefore speculate that curvature is more likely due to confinement.

4.4.1.2 Titration of α-cyclodextrins by a DOPC lipid solution

In order to further characterize the interaction mechanism of αCDs with the DOPC bilayer we gradually injected the liposome solution into the αCD solution, depleting progressively the αCD solution while increasing the amount of lipid in solution. The titration process was monitored using an isothermal titration calorimeter (ITC) and also with elastic dynamic light scattering (DLS). The DLS injection steps were chosen to mimic as closely as possible the ITC injection sequences in

Table 4.4: Hydrodynamic diameter and ζ-potential of DOPC vesicles titrated into into 5 mM αCD solution. Values are shown as averages over 2 samples with 10 runs each, and the standard deviation is used as an error estimate

DOPC concentration (mM)	Size (nm)	ζ—potential (mV)
0.10	141.33 ± 1.81	-31.35 ± 1.23
0.21	150.20 ± 1.27	-28.18 ± 0.96
0.31	139.65 ± 1.18	-21.78 ± 1.10
0.40	135.05 ± 1.31	-21.23 ± 0.87
0.59	130.95 ± 1.89	-13.05 ± 0.91
0.78	129.58 ± 1.94	-10.90 ± 0.73
0.95	130.18 ± 0.58	-6.51 ± 0.50
1.12	129.83 ± 1.22	-7.21 ± 0.95
1.28	130.08 ± 1.39	-9.10 ± 0.73
1.44	129.13 ± 0.88	-10.48 ± 0.30
1.59	129.20 ± 0.82	-11.05 ± 0.79
1.74	129.83 ± 0.87	-10.85 ± 0.68
1.88	129.70 ± 0.74	-10.85 ± 0.87
2.08	129.85 ± 1.63	-10.90 ± 1.08
2.08*	125.40 ± 0.88	-12.10 ± 0.35

*sample after 24 h

terms of period, concentration and injected volumes (see Material and Methods). For reasons that will be detailed below, most of the titration experiments were performed at a concentration of ~5 mM, while the concentration of the liposome solution was estimated to be close to 7.8 mM. The target experimental temperature was 25°C but a number of titrations were also performed at 10°C and 40°C in order to outline systematic effects of temperature.

DLS results at 25°C for a 5 mM αCD solution (Table 4.4 and Figure B.2 at page 124) showed that during the final stage of the titration, the liposome size did not evolve significantly. In parallel, the determination of the electrophoretic mobility (ζ-sizer) was consistent with a surface potential of -12 mV, close to the reference value of the control experiment. These results prove that a fraction of the injected lipids survive as liposomes.

Meanwhile, at the end of the titration procedure at 25°C, an insoluble compound was visible in the vials, taking the form of a solid deposit. The amount of solid deposit was found to be a decreasing function of temperature, abundant at 10°C and absent or hardly present at 40°C. It is tempting to identify the deposit with the stable thermodynamical phase of the cyclodextrin-lipid inclusion complexes. In order to gain evidence on the role of the lipid in the deposit, we collected and investigated it by means of scanning electron microscopy (SEM) and X-rays scattering. Finally, NMR spectra of the deposit were acquired after redispersion into DMSO, from which the gross stoichiometry of the solid phase could be estimated. In the paragraphs below, we present first our findings regarding the solid phase, before moving to the analysis of the thermodynamics of the titration process.

4.4.1.3 Nature of the α-cyclodextrin/DOPC complex

The white precipitate formed when mixing lipids and cyclodextrins was separated by centrifuging the solution at 4000 rpm for 5 min. We used first SEM to observe the size and surface morphology of both the pure αCD and the mixed αCD-lipid solid. Figure 4.11 a shows the pure αCD powder. It clearly differs from the αCD-DOPC mixture (Figure 4.11 bcd). Pure αCD material displays prismatic shapes with well-developed facets. In contrast, αCD-DOPC samples feature a thick layer of microdiscs with smooth surfaces. The layout of the microdiscs is anisotropic. They look relatively monodisperse with a typical diameter of 2.0 ± 0.9 μm and thickness on edges of 0.1 ± 0.04 μm. The difference in appearance is a first piece of evidence that the chemical composition of the discs differs from the pure powder, and should contain a significant amount of lipid. As lipid alone do not precipitate, and that αCD is soluble at 5 mM and 25°C it is almost certain that this is the combination of both species, in a physically complexed form, that precipitates as nanodiscs. Regarding the size of nanodiscs and liposomes (100 nm), it appears clear that it is not possible to simply interpret the discs as "liposome ghosts", because the amount of material present in a single disc exceeds the typical amount of lipid contained in a single 100 nm diameter unilamellar vesicle. The relative smoothness of the discs seems consistent with the existence of a well packed, crystalline arrangement of the αCD and DOPC molecules. Unfortunately, SEM alone does not give any indication regarding the stoichiometry of the molecular packing.

Microcrystals formed by αCD complexes upon encapsulation of polymers or formation in oil/water emulsions, have been reported before. However, to date, all reported supramolecular assemblies of αCD show a rod-like morphology [200, 201]. To the best of our knowledge, nanodiscs of αCD crystal are been observed for the first time.

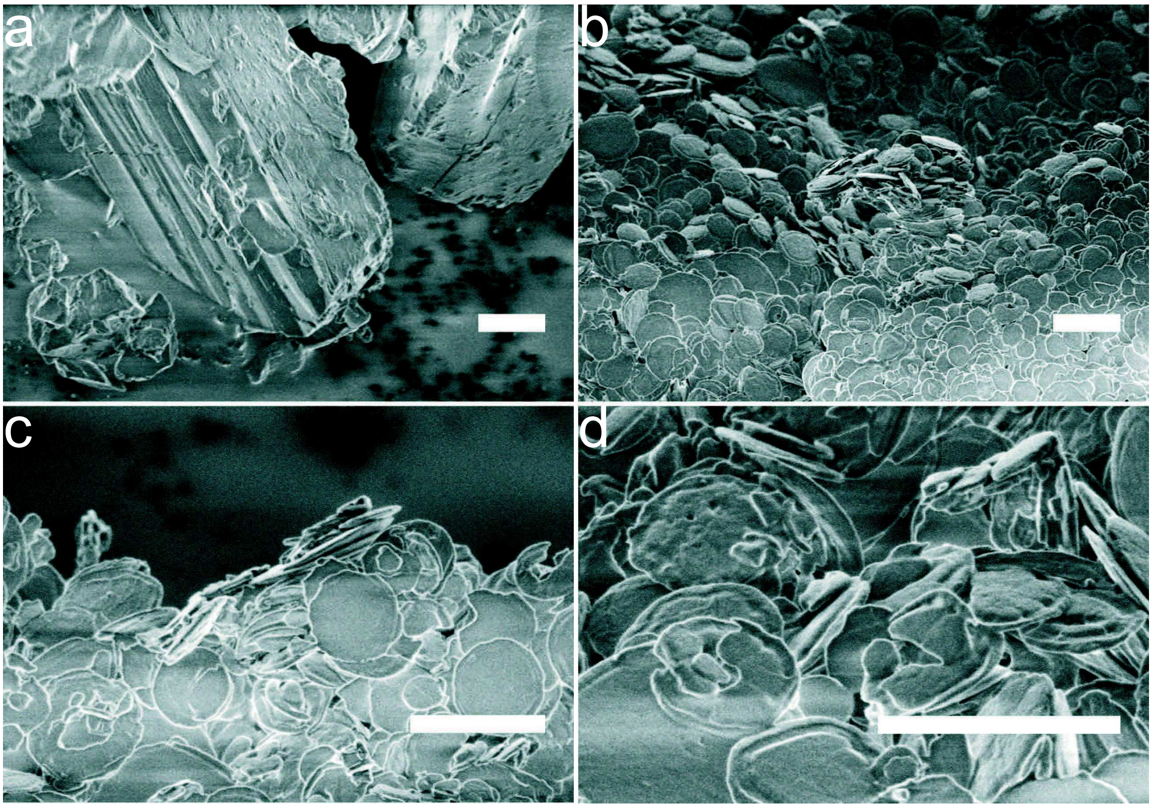

Figure 4.11: SEM images of crystalline samples of αCD powder (a), and mixtures of 5 mM αCD / 7.8 mM DOPC (b, c, d). Scale bar, 3 μm.

To confirm the crystallinity of the mixture, we acquired the X-rays diffraction spectrum of the powder. Figure 4.12 (and Table 4.5) shows the SAXS-WAXS profiles of pure αCD samples (a), and αCD-lipid-water systems (b). The presence of well defined sharp peaks, q, in the powder spectrum points to a well established molecular ordering, probably a crystalline arrangement. The sharp peaks are interpreted as Bragg diffraction peaks, with scattering wavevectors q multiple of $2\pi/d$, d being the repeat distance of a family of diffraction planes.

Two related peaks (Figure 4.12 b), appearing as a rather uniform ring in the 2d powder diffraction picture are consistent with a repeat distance of 11.86 Å. Another two related peaks, appearing as anisotropic arcs in the diffraction picture, indicate a repeat distance of 16.15 Å. the spectrum reveal other possible peaks that are unrelated to the these two families of peaks (at least not simple harmonics of the two previous spacings). We were not able to index all the peaks with reasonable confidence, and the crystalline symmetry of the packing was not determined. As the low q diffusion intensity goes up below 0.3 Å^{-1} there is the possibility that peaks associated to larger crystalline sizes are present but undetectable. The magnitude of the distances obtained by X-rays diffraction seem more directly related to the αCD than to the lipid, and it is likely that these are the αCD geometrical parameters that dictate the molecular arrangement in the powder. As a corollary, one expects the powder to be predominantly composed of αCD.

Table 4.5: Most intense peaks in SAXS profile of αCD and their inclusion complex powder samples. Peak number represents peak marked on Figure 4.12

Peak	Position (Å) αCD	Position (Å) αCD/complex
1	17.15	16.15
2	9.16	11.86
3	7.36	9.50
4	6.58	8.21
5	6.23	6.89
6	5.98	4.46
7	5.59	3.93

The SAXS profile of pure αCD is in line with previously reported data [202, 203]. We hypothesize that the powder consists of a crystalline packing of cyclodextrin complexed with DOPC, in undetermined proportions.

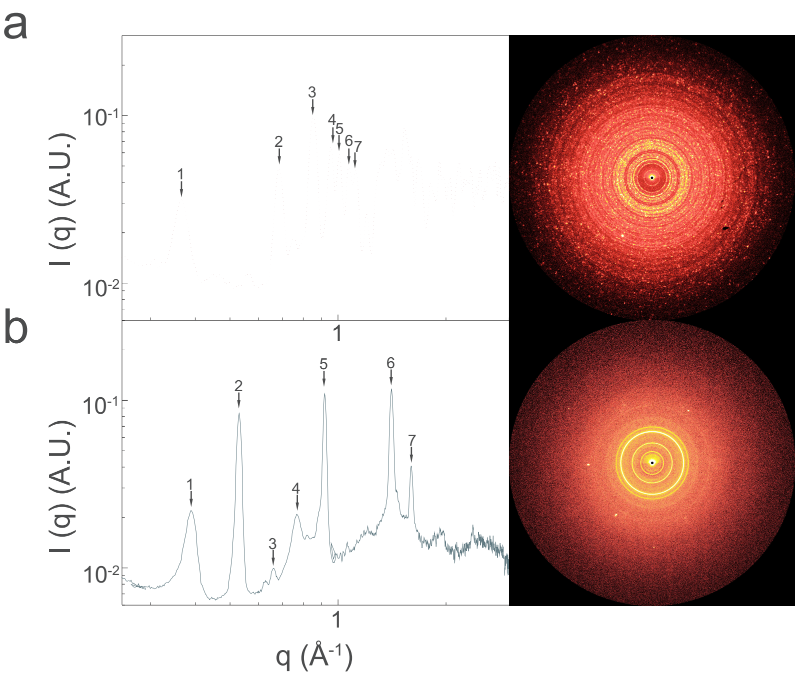

Figure 4.12: Powder X-ray scattering patterns of a) pure αCD and b) αCD/DOPC crystals.

Furthermore, we used 1H-NMR technique (in DMSO) to provide characteristic spectra, enabling structural identification and confirming αCD/lipid complex formation. The characterization has been done individually for αCD, DOPC and αCD/DOPC complex. NMR spectra of pure αCD, DOPC and the complex can be found in Appendix B (Figures B.3, B.4, B.5 at pages 124-125).

The analysis was carried out with the help of Dr Y. Moskalenko. The principle of the analysis is the following: For each species, one characteristic resonance line is selected and the integration of the signal leads to peak intensities associated with a known integer value of equivalent protons. The ratio of two intensities, one coming from the αCD, the other from DOPC molecules, is proportional to the concentration ratio of each species, weighted by the (integer) number of protons participating in the two resonances. Our quantitative NMR analysis of the αCD-cyclodextrin–DOPC complex indicates the presence of a molar ratio of αCD:DOPC of 5.0 ± 0.3.

4.4.1.4 Thermodynamic aspects of the interaction between αCD molecules in solution and DOPC lipid bilayers

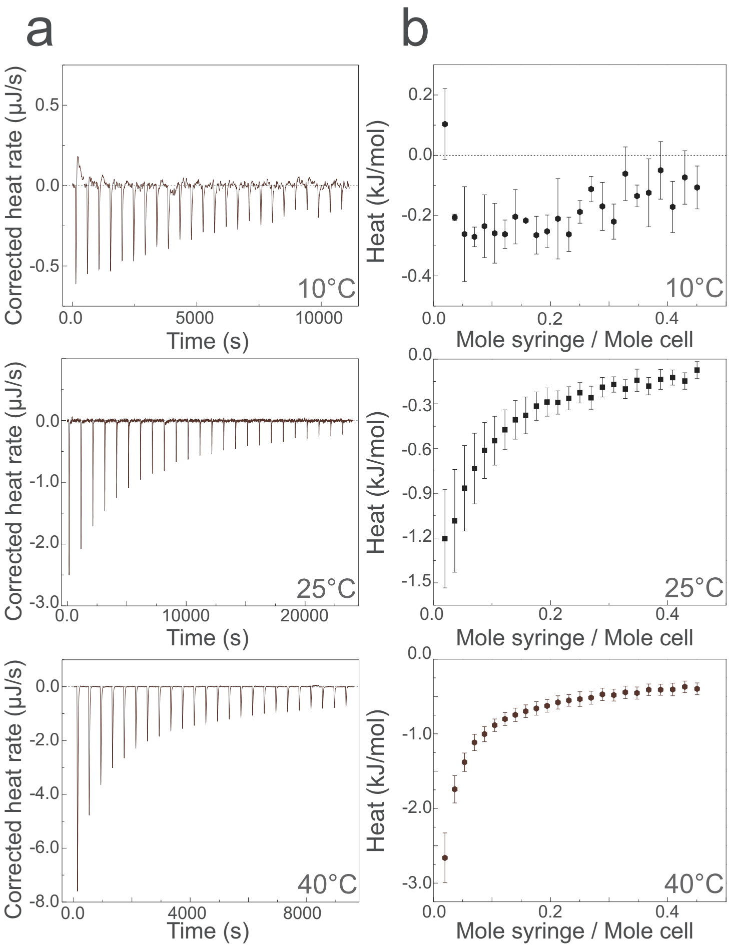

Figure 4.13: Representative ITC profiles for the titration of 5 mM αCD with 7.8 mM DOPC liposomes. The experiment was performed at 10, 25 and 40 °C. a) An example of ITC titration curve after the subtraction of the dilution exothermic signal b) Corrected heat of reaction per mole of DOPC injected as a function of ratio of DOPC/αCD. The data are an average of three separate experiments.

To study the thermodynamics governing the interaction between αCD and DOPC-LUVs, we used isothermal titration calorimetry (ITC). An isothermal calorimeter measures the heat released or absorbed by the sample during the quasi-isothermal and isobaric mixing of a titrant into a solution to titrate. Therefore, it provides a direct access to the changes in enthalpy of mixing (Δh). Depending on situations, the titration profile may reveal the values of the thermodynamic constants that govern the composition of the mixture, such as in the case of a complexation equilibrium. With the enthalpies and the equilibrium constants, the thermodynamics of the complexation reaction is entirely determined. It is worth precising that with the isothermal calorimeter used in the present work, endothermic peaks are associated with negative heat flows (μJ/s). Inversely, exothermic processes induce positive heat flows.

Although the present study mainly focuses on the interaction of cyclodextrins and lipids at room temperature (25°C), we also performed titrations at lower (10°C) and higher (40°C) temperature, as this parameter turned out to influence significantly the magnitude of the enthalpy of complexation. It is only for the 5 mM αCD concentration case that a well defined sequence of titration peaks could be obtained, and this case is discussed first. At larger concentrations (15 and 20 mM), peaks do not separate well, and a significant drift of the baseline was observed, a situation discussed in a second time.

Figure B.6b at page 126 shows the heat flow associated with the stepwise injection of glucose solution into a αCD solution. Each injection produces a weak exothermic peak, and corresponds to an average of 0.55 and 0.6 μJ/injection for 25°C and 10°C respectively. The first three peaks for 40°C are of higher magnitude (0.5 μJ/injection), followed by 22 injections of average 0.2 μJ/injection. The resulting exothermic signals are related to the dilution process. In separated control experiments, the heat of dilution was measured by titration of DOPC-vesicles into a glucose solution.

The titration of a suspension of DOPC vesicles into the 5 mM αCD solution for three temperatures produces endothermic peaks, followed by weak exothermic peaks for 10°C and 25° (Figure B.6a at page 126). The magnitude of the endothermic peak increases with temperature, as shown in Figure B.1a at page 123. The signal was corrected by subtracting the exothermic signal associated to the dilution of DOPC vesicles at the corresponding temperature, and this lead to the disappearance of the exothermic contribution, leaving only an endothermic signal contribution to the corrected titration curves. Figure 4.13 b shows the integrated heats of αCD/DOPC interaction as a function of the molar ratio of αCD to phospholipids. The magnitude of the heat released during the first injection peak displays a quasi-linear dependence on the temperature (Fig 4.14). The resulting linear function has a positive slope, and vanishes close to 10°C. As a consequence, the titration at 10°C produces heat peaks that are close to the instrumental resolution. The variation of enthalpy as a function of temperature is anti-correlated to the amount of precipitate in the sample at the end of the titration. As a matter of fact, the largest amount of sediment was obtained for 10°C, whereas at 40°C almost no precipitate was observed.

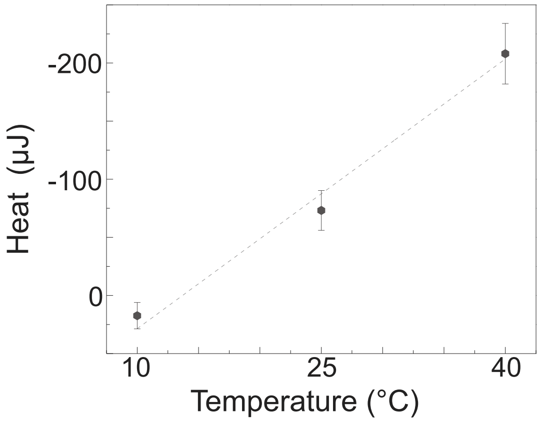

Figure 4.14: An average heat associated with first injection of 7.8 mM DOPC vesicles into 5 mM αCD at different temperatures. Values are shown as averages over 3 measurements, and the standard deviation is used as an error estimate.

Titration profiles at 25 and 40°C and 5 mM αCD concentration reveal endothermic peaks of decreasing magnitude. The smooth variation in the peak intensities is consistent with a reversible thermodynamic process. As a matter of fact, a total reaction limited by the amount of phospholipids would give a sequence of peaks of constant intensity, while a total reaction limited by the cyclodextrins would lead to a sharp cross-over from finite to small or vanishing peaks values.

It is not clear at this stage whether this endothermic reversible process corresponds indeed to the formation of the solid deposit. A reversible surface adsorption phenomenon, preserving the bilayer structure, is also an option to consider. A reverse step transforming microcrystals back to lipid bilayer and molecular αCD is harder to imagine.

We now attempt to provide bounds for the stoichiometry and the equilibrium constant of this endothermic reversible process. Phospholipids (PL) participating in the reaction come as a self-assembled pure bilayer phase, which should be considered as a pure compound with constant thermodynamic activity, *i.e.* the chemical potential of the lipids are expected to depend weakly on their concentration in solution. Upon inspection of the titration profiles, it appears that about 10 injections are sufficient to deplete the titrated compound (αCD) to a point where further injections induce only a much weaker response, or equivalently a marginal change in the advancement of the complexation reaction (Figure 4.13). Within the Langmuir independent adsorption model this suggests that $10 \cdot 10^{-5} \times 0.0078 = 7.8 \cdot 10^{-7}$ mol of PL can neutralize three-quarters of the $4.75 \cdot 10^{-6} \sim 3.6 \cdot 10^{-6}$ mol of αCD initially present in the cell. This assumption leads to a ratio of

4.6 αCD to 1 lipid, or 9.2 αCD to 1 lipid if only the outer leaflets of the vesicles are involved. This ratio is way too large to comply with a single layer of CD coating a PL bilayer. Dividing the total released heat $q_{\text{tot}} \equiv 500\mu$J by the number of moles of participating αCD molecules give an order of magnitude for the enthalpy of complexation per αCD equal to 100 J/mol, a really modest value.

It seems easier to interpret the reversible endothermic process (REP) in the framework of a cooperative, or Hill adsorption model. This model assumes that a number a of αCD molecules simultaneously adsorb as a cluster on the PL bilayer. In addition, we further assume that every a αCD molecules are closely associated to 1 lipid. The advantage of the Hill model is that the advancement of the adsorption (or complexation) reaction decreases significantly as the free αCD concentration is reduced. Heat peaks intensities then decrease significantly without the need of depleting too much the αCD content in the cell. As a result, less αCD per lipid are required in the titration process.

Within the Hill picture, the fraction θ of covered surface depends on the concentration of free cyclodextrin in solution $c_{\text{CD,free}}$ as follows

$$\theta = \frac{K_a C_{CD}^a}{1 + K_a C_{CD}^a} = \frac{C_{CD}^a}{c_\star^a + C_{CD}^a} \qquad 4.9$$

with K_a the equilibrium association constant in M^{-a}, and $c_\star = K_a^{-1/a}$ the half-coverage concentration, *i.e.* the concentration $C_{CD} = c_\star$ for which the surface coverage reaches half of its maximal value. The equilibrium constant $K_a = \exp(a\Delta g/RT)C_0^{-a}$ is directly related to the Gibbs free-energy Δg of complexation per αCD molecule, $C_0 = 1$M being the standard concentration. Within the Hill model, the smooth variation of the heat peaks with the number of injections can only be accounted for if $c_\star \geq 5$ mM. Smaller values of $c_\star$ would bring θ close to the saturation value, and lead to constant heat peaks during the first stage of the titration. With $c_\star = 5$ mM, we obtain $\Delta g \equiv -13$ kJ/mol, a quite robust order of magnitude. In the mean time, the estimated enthalpy Δh increases to $200-500$ J/mol compared with the Langmuir model, as a smaller amount of αCD is used for the same heat release q_{tot}. Whatever the model we use, we find that the reversible endothermic process is strongly entropy driven, with $\Delta h \ll |\Delta g|$.

Our attempts to determine the stoichiometry of this association process were only partially successful. First, the measured heat peaks were subject to significant fluctuations from one titration experiment to another. In addition, direct fitting of the data to Hill or Langmuir models did not give very good agreement (see Appendix B).

Under the assumption of reversible Hill equilibrium, it is possible to extract a lower bound for the Hill exponent a, by resorting to the following argument. If one defines X_i the ratio of the number of phospholipids to the number of αCD initially present in the cell after i injections, and q_i the heat released during the i_{th} injection, then the following inequality is expected to hold for all i (see

Appendix B):

$$\frac{\sum_{j=1}^{i} q_j}{i q_1} \geq (1 - aX_i)^a \qquad 4.10$$

Plotting both sides indicates that a value $a < 2$ is unlikely, while the data seems to be consistent with a comprised between 2 and 3, or possibly larger than 3 (Figure B.8 at page 129)

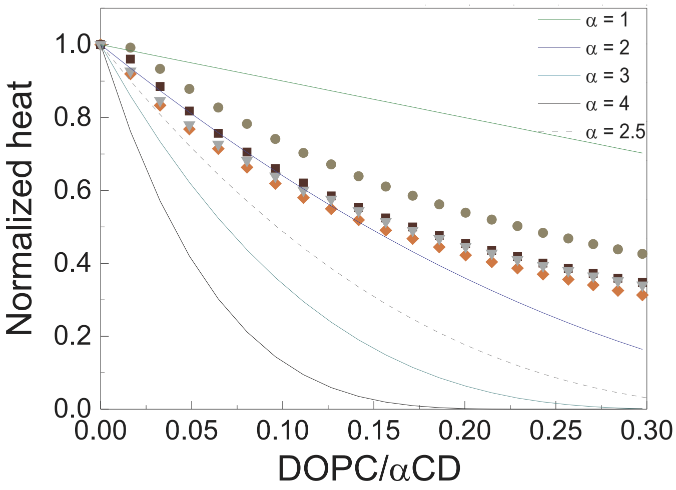

Figure 4.15: Normalized heats plotted versus the DOPC/αCD ratio for experimental data at 25°C (scatter) with theoretical lower bounds calculated for different stoichiometry ratio a.

The ITC data obtained from titrating more concentrated solutions of cyclodextrins differed notably from the situation described above. Figure 4.16 shows an example of the raw data from the calorimetry measurements of DOPC-LUVs titration into αCD solution at higher concentration (10 and 15 mM). Each injection immediately generates sharp exothermic peaks, opposite to the ~5 mM situation. However, immediately following the first injection a strong drift in the baseline is observed (see Figure 4.16). At ~15 mM, the effect is even more pronounced, with a long time tails visible in the heat power curve following each injection. Due to the strong baseline shift, no attempt was done to fit these data to a model.

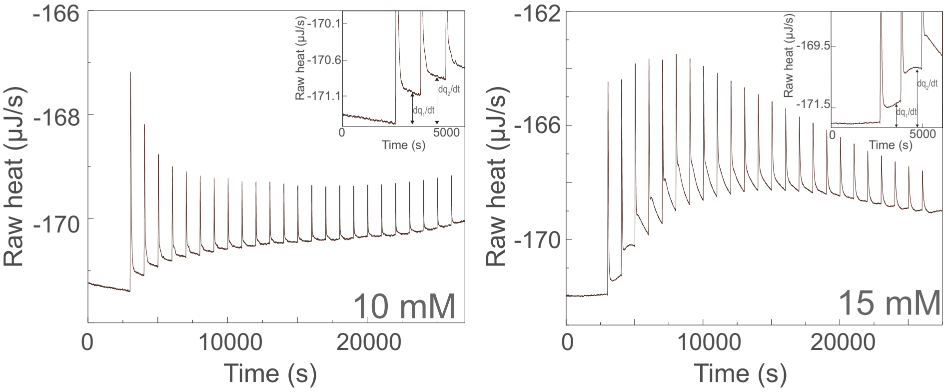

Figure 4.16: ITC-assay of 10 mM and 15 mM αCD titrated with 7.8 mM of DOPC. The inset shows the first two injections of DOPC into the sample cell and the arrows represent the decrease in the heat required at each equilibrium condition.

The shift in baseline and the trailing peak decrease both suggest that a slow exothermic process is taking place. This process does not give rise to well defined stationary peaks for which the amplitudes would be under the control of an equilibrium constant. For these reasons, we will refer to this exothermic process as the irreversible exothermic process (IEP) at large αCD concentrations.

4.4.1.5 Interpretation of the ITC results

All the host-guest complexation reactions involving αCD reported in the literature show exothermic contributions [204–206]. In the case of αCD-surfactant association, which is a relevant case as far as CD-lipid interaction is concerned, Valente and Soderman [207] reported exothermic contribution for a variety of molecules, regardless of temperature, chain length and charge. Therefore, it is tempting to associate the exothermic components in our ITC data to CD-lipid complexation, either taking the form of a solid precipitate (10 and 25°C) or possibly the form of water soluble complexes (40°C).

The endothermic contribution at low αCD concentration reported in the present work is novel and original. The main difficulty in interpreting our ITC data is to find a molecular mechanism that give rise simultaneously to a REP at low αCD concentration and to an IEP at larger αCD concentrations. We learnt from the DLS experiments that in all situations, some lipid material subsist in solution as bilayer (liposomes with well defined hydrodynamic radius). The Cryo-TEM images confirm that sticky lipid bilayers are visible after incubating 24h at 20 mM αCD concentration. It is therefore reasonable to assume that the lipid bilayer, initially injected in the solution is involved in the REP. We could not determine the precise nature of the product of the REP. Based on generic arguments and comparison to Langmuir and Hill adsorption models, we found that the REP involves a minimum of 2 αCD per lipid, and possibly 3 or more αCD per lipid. This stoichiometry ratio is consistent with the end products of the REP being either the final inclusion complex, or an intermediate compound in the reaction pathway leading to the final inclusion complex, or perhaps a coexistence of both.

On the other hand, ITC studies on lipid membranes suggest that endothermic contribution may arise from membrane rearrangements consecutive *e.g.* to the incorporation of pore forming molecules [208–210]. A local enrichment in αCD at the vicinity of the lipid bilayer (whether it comes from adsorption or a more subtle interaction) could also, in principle, give rise to some endothermic signal in our case as well. Such a surface coating would be perfectly consistent with the sticking behavior and the membrane stacking revealed by Cryo-TEM.

Therefore, we hypothesize that both endothermic and exothermic contributions are present in our case. The exothermic contribution would come from the formation of the final inclusion complex, either soluble at large temperatures, or solid in cooler conditions. As the final inclusion complex involves about 5 αCD per lipid (according to the NMR lines analysis), its thermodynamic stability and formation kinetics is expected to depend strongly on the αCD concentration (*e.g.* a large exponent in the law of mass action) and therefore dominates above 10 mM. The endothermic contribution is likely to involve a quasi-equilibrium complexation mechanism with a lipid bilayer, and becomes apparent at lower αCD concentration. Its stoichiometry probably involves a lower αCD to lipid ratio, providing it with a competitive advantage compared to the exothermic process at 5 mM.

At 10°C at 5 mM, the precipitate is abundant, the exothermic term is the largest and compensates for the endothermic contribution. At 40°C at 5 mM, the precipitate is almost absent, the exothermic term is smallest and the endothermic contribution dominates. The 25°C case is an intermediate situation. As a consequence, the REP would arise from the superimposition of two processes, one exothermic and one endothermic, instead of being a single well defined complexation step. The titration analysis of the REP would then be only indicative, in the absence of better modeling of the multiple reaction steps. In addition, the stoichiometry of the REP could be resulting from the superimposition of a 4:1 or 5:1 complex formation and a better balanced reversible surface association of the αCD. Finally, the ITC data reported in the literature involving methylated cyclodextrins at high concentrations may not be relevant in our case as these cyclic molecules do not aggregate under similar conditions.

4.4.2 Conclusion

The αCD-DOPC lipid bilayer interactions were investigated at the nanometer scale, combining a set of electron microscopies, light and X-ray scattering, nuclear magnetic resonance and thermodynamical characterization.

Direct imaging of the DOPC liposomes at 20 mM αCD concentration shows that despite the formation of a solid deposit, lipid bilayers survive for long times, and interact together very strongly, ultimately leading to dense lipid packing of the size of a single liposome, with the bilayer structure still present.

The progressive dilution of the liposomes into 5, 10 and 15 mM αCD solutions leads to the formation of a solid deposit, with many liposomes surviving as demonstrated by dynamic light scattering (DLS). The solid deposit, also referred as microcrystal powder, is believed to play an important role both at large (μm) and small (nm) scales. Visualization by SEM suggests that αCD incorporating DOPC (inclusion complexes) packs into a crystalline order, a fact which was then confirmed by SAXS/MAXS/WAXS analysis. The quantitative study of the NMR spectrum of the powder after dispersion into deuterated DMSO led to the determination of the powder composition, which was found to lie in a range of 4.7 to 5.3 αCD per lipid.

The thermodynamic characterization of the formation of the host-guest complexed proved difficult. A novel reversible endothermic process was unveiled, which dominates at low αCD concentration, and whose intensity is strongly temperature dependent. At larger concentrations, a slow exothermic process is observed, that we link to the final αCD-DOPC complex formation, based on similar reported results in literature. Our only explanation for the endothermic to exothermic transition as a function of the αCD concentration is that both processes take place simultaneously. The endothermic signature is therefore interpreted as the outcome of at least two competitive processes, one being exothermic, the other being endothermic, with the latter dominating at high temperature. The most likely candidate for the endothermic process is the reversible association of some αCD molecules with the lipid bilayers present in solution.

4.4.3 Materials and methods

Materials

Chloroform solution of DOPC (1,2-dioleoyl-sn-glycero-3-phosphocholine, C44H84NO8P, MW 786.113) was purchased from Avanti Polar Lipid (Birmingham,AL). α-cyclodextrin powder ($C_{36}H_{60}O_{30}$ M_w 972.84) and Glucose ($C_6H_{12}O_6$ M_w 180.16) were provided by Sigma-Aldrich, Co. (Saint-Quentin, France). All chemicals had high purity and were used without further purification.

Large unilamellar vesicles (LUVs)

Liposomal suspension of LUVs used for ITC and Cryo-TEM measurements were prepared as described earlier [211]. A defined amount of DOPC lipids in chloroform was transferred to the vial, and the organic solvent was evaporated under argon stream until completely dried, followed by 8h of vacuum pumping. The lipid film was then hydrated with glucose solution (100 mM) and gently vortexed. The resulting multilamellar vesicles suspension was extruded 21 times through a 100 nm diameter pore polycarbonate filter with an Avanti Mini-Extruder. Vesicles prepared in this way generally showed a narrow size distribution (ø = 125.7 ± 0.36 nm, ζ = -11.8 ± 1.04 mV), as confirmed with dynamic light scattering (DLS). The final concentration of LUVs was determined using an enzyme assay kit for choline (Sigma Aldrich). Glucose does not contribute *per se* to the formation of LUVs, but was added here to facilitate the comparison of the current set of experiments with similar α-cyclodextrin degradation assays performed on DOPC giant vesicles, where glucose is commonly used for optical contrast and osmotic matching.

The α-cyclodextrin (αCD) solution

The α-cyclodextrin (αCD) solution was prepared by 2h of vigorous stirring of the powder in a glucose solution (100 mM) at well defined concentration (5 mM, 20 mM).

Isothermal titration calorimetry (ITC) measurement

The ITC measurements were performed with a Nano ITC from TA Instrument (New Castle, DE). The working cell (volume 0.950 mL) was filled with a 5 mM solution of αCD, and the reference cell with the same amount of MilliQ water. One aliquot of 2 μL followed by 24 aliquots of 10 μL of liposomal suspension were injected stepwise at minimum 500 s intervals into the working cell filled with αCD solution. A set of reference blank experiments were also performed, namely the titration of the vesicle suspension into a αCD-free glucose solution, and the titration of a glucose solution into a cell filled with αCD solution. To avoid the presence of air bubbles, all samples were degassed for at least 10 min shortly before each experiment. The sample was constantly stirred at a rate of 310 rpm, and measurements were performed at 10 $^\circ C$, 25 $^\circ C$ and 40 $^\circ C$.

Cryo-transmission electron microscopy (Cryo-TEM)

A laboratory-build humidity-controlled vitrification system was used to prepare the samples for Cryo-TEM. Humidity was kept close to 80% for all experiments and temperature was set at 22°C. A 5 μL droplet of the sample was placed onto the lacey carbon film covered grid (Ted Pella) rendered hydrophilic via glow discharge (Elmo, Cordouan Technologies). Excess sample was removed by blotting with filter paper and the sample grid was vitrified by rapid plunging into liquid ethane (-180 °C). The grids were kept in liquid nitrogen before being transferred into a Gatan 626 Cryo-holder. Cryo-TEM imaging was performed on FEI Tecnai G2 TEM (200kV) under low dose conditions with an Eagle slow scan CCD camera. Cryo-TEM Images analysis was performed by *ImageJ* software (NIH, USA). The error in the determination of membrane thickness from Cryo-TEM images analysis was estimated at ± 5%.

Scanning electron microscopy (SEM)

The αCD pure powder and the αCD/DOPC residual powder, were deposited on a carbon tape. The sample was mounted on SEM sample stub and viewed using a FEG-SEM Hitachi SU 8010

(1kV) without metallisation. SEM Images analysis was performed using the *ImageJ* software (NIH, USA).

Nuclear magnetic resonance (NMR) spectroscopy

1HNMR(400 MHz) spectra were recorded in DMSO with a Bruker Avance 400 spectrometer equipped with an Ultrashield magnet. αCD/DOPC stoichiometry was calculated from the 1H NMR spectra of αCD complex by comparing the integral of proton signal of residual at 5.44 ppm and number of glucose units per αCD molecule.

X-ray scattering measurements

Small angle X-ray scattering (SAXS) experiments were performed by using a diffractometer developed by Molecular Metrology (Elexience), using a Rigaku Micromax 007HF generator with a copper-rotating anode. The wavelength of the incident beam was $\lambda = 1.54$Å, Cu $K_{\alpha 1}$. The diffractometer operates with a pinhole collimation of the X-ray beam focused by a multilayer optic (Osmic) and a two-dimensional gas-filled multiwire detector. The sample to detector distance was set at 0.7 m, leading to a range of scattering vectors covered by the experiment $0.01 < q < 0.32$Å^{-1}.

WAXS. Wide-angle X-ray scattering experiments were carried out from the same diffractometer, by using Phosphor imaging plates from Molecular dynamics as detectors. These plates were set at 0.06 m from the samples, allowing to explore scattering vectors ranging from $q = 0.05$Å^{-1} to 3.5Å^{-1}. The same cells of 1 mm thickness and Mica windows were used as sample holders. Measurements were performed at room temperature.

MAXS. Additional small angle X-ray scattering experiments were performed using a Nanostar diffractometer (Bruker-Anton Paar) that operates with a pinhole collimator and a wire proportional gas 2d detector. A monochromatic ($\lambda = 1.54$Å, and almost parallel beam (divergence = $0.03°C$) was obtained through a confocal mirror with advanced W/Si multilayer coating (XENOCS, SA). The size of the incident beam on the sample was close to 300 μm. The sample to detector distance was set at 22 cm, allowing to explore scattering vectors ranging from $q = 0.05$Å^{-1} to 0.8Å^{-1}

Cells of 1 mm thickness and calibrated mica windows were used as sample holders.

Data reduction. For SAXS, all data were treated according to standard procedures for isotropic small angle X-ray scattering. After radial averaging, the spectra were corrected from electronic noise of the detector, empty cell, absorption and sample thickness. A ^{55}Fe source was used for the corrections of geometrical factors and detector cells efficiency as well as a silver behenate sample, for the q-calibration. The normalization to the unit incident flux was then obtained using water or Lupolen as standard samples. Nevertheless, such measurements on an absolute scale have not been achieved for the WAXS experiments. The spectra were then locked onto the related SAXS ones.

Dynamic light scattering (DLS)

The size and ζ-potential of the DOPC-liposomes were measured with a ZetaSizer Nano ZS (Malvern Instruments, UK) at 25°C. Two separate measurements with a minimum of 10 runs were performed for each sample.

5 | Nonlamellar lipid structures

5.1 Introduction

Lipid molecules such as phospholipids or monoacylglycerols spontaneously self-assemble into a wide range of lyotropic liquid crystalline phases. The structural order within these phases ranges from few nanometers up to hundred nanometers in size. In addition to their great relevance in understanding the structure of biological membranes, the formation of well-defined aggregates with controllable morphology is of high importance for a wide range of applications such as nanoencapsulation, biocatalysts, drug and gene delivery [212, 213].

Aside from the well-known lamellar phase, other classes of lyotropic mesophases are formed upon ordered arrangements of curved interfaces, separating lipid molecules from the water regions. Within this group, three main subclasses can be distinguished: *i)* 2D packing of cylindrical interfaces (discontinuous phases), *ii)* 3D packing of saddle surfaces (bicontinuous phases), and *iii)* 3D packing of spherical/ellipsoidal interfaces (discontinuous phases) [214]. Depending on the system, aforementioned subclasses can occur in both oil-in-water system, where the mesophase has positive interfacial mean curvature, and in water-in-oil system, where the phase demonstrates negative interfacial mean curvature (Figure 5.1).

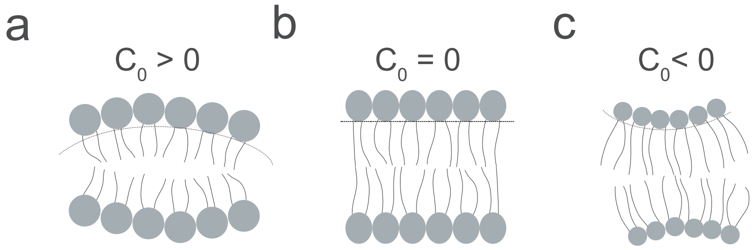

Figure 5.1: Nonlamellar tendencies of lipid monolayer. *Oil-in-water* (Type I) mesosphase is characterized by positive interfacial mean curvature, whereas *water-in-oil* (Type II) phase have negative interfacial curvature.

The hydrophobic effect (introduced by Tanford in 1973) causes spontaneous self-assembly of amphiphilic molecules into well-ordered structures above a certain concentration, called critical micelle concentration, cmc. The cmc value strongly depends on the effective shape of a lipid molecule i.e. the length and number of hydrocarbon chains, type of a headgroup, and solution conditions. Following Israelachvili [215], for zwitterionic, double-chain lipids the value of cmc is low ($\sim 10^{-10}$ M), which is attributed to a larger hydrophobic/hydrophilic ratio of the tail and headgroup parts compared to the single-chain lipids (cmc $\sim 10^{-4}$ M - 10^{-1} M).

The self-assembly of lipids, as a result of competition between hydrophobic effect and geometrical packing (local) constraints, can be quantitatively explained by the *critical packing parameter* (CPP). The CPP is a ratio between the volume of hydrocarbon chain(s), v, and the product of cross-sectional lipid head group area, a (determined as the balance of inter-chain attractive and headgroup repulsive interactions) with lipid chain(s) length, l

$$CPP = \frac{v}{al} \tag{5.1}$$

Following the changes in the CPP value, one can predict order-order transitions associated with changes in lipid/water interface. Lamellar phase is represented by CPP = 1, since it shows no interfacial curvature. The values CPP< 1 correspond to Type I (*oil-in-water*) morphologies of mesophases such as, micelles and Hexagonal H_I phase, whiles CPP > 1 reflect to phase inversion and Type II (*water-in-oil*) structures. Figure 5.2 gives an overview of mesophases with corresponding CPP values [216, 217].

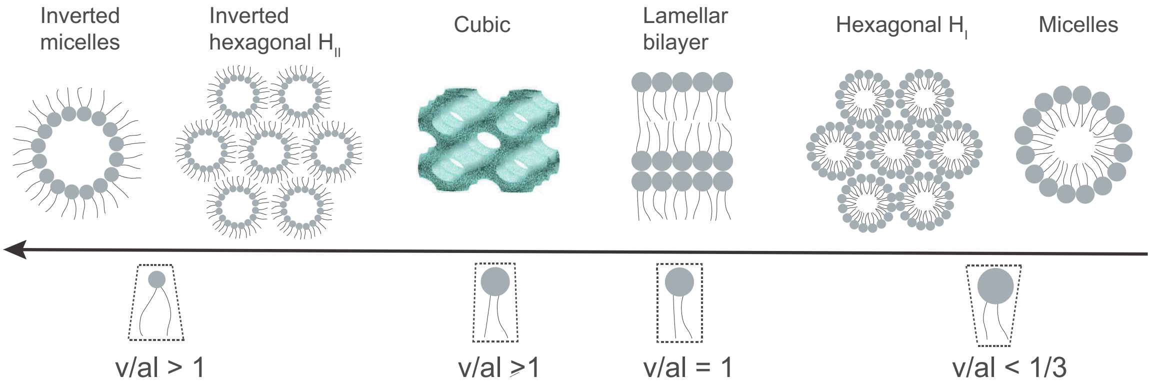

Figure 5.2: Schematic illustration of lamellar and non-lamellar lipid aggregates formed in water. The different structures have different curvature and are arranged in accordance with the value of packing parameter $CPP = \frac{v}{al}$. If the CPP parameter is less than one, the interface between polar and hydrophobic regions curves towards the tail region. In contrary CPP exceeds one, the interface curves towards the polar region of lipid molecule.

Since lipid self-assembly is a consequence of forces of different origins, the CPP value can be easily tuned by changing lipid composition, additives, and environmental conditions (temperature, pH, pressure, ionic strength etc.). These changes impose an imbalance of lateral stress, $\pi(z)$, in the lipid monolayer. As can be seen in Figure 5.3, the lateral pressure profile is built up from three contributions, and therefore, changes e.g. in external environment can affect the lateral stress and consequently the overall curvature of a monolayer. Such an effect can be observed in the lamellar phase, where increase in temperature drives the formation of an inverted hexagonal or cubic phase. An increase in temperature is likely to have repercussions across the lateral pressure profile, such as increasing repulsions in the chain region and/or decreasing the effective headgroup area by changes in its hydration. As a results, the monolayer curves towards the water region (CPP > 1). Interestingly, the pressure-dependent structural transition has opposite trend, where an increase in pressure induce more pronounced curvature towards the hydrophobic region. Furthermore, Engblom [218], and Cherezov [219] have shown that even small amount of charged lipids induce swelling of the lipid/water system. The vast body of literature reports that incorporation of various hydrophobic molecules such as surfactants [220], cholesterol [221], alcohols, hydrocarbons [222, 223], variety of drugs [224], as well as salt concentration [225–227] can promote transitions between mesophases.

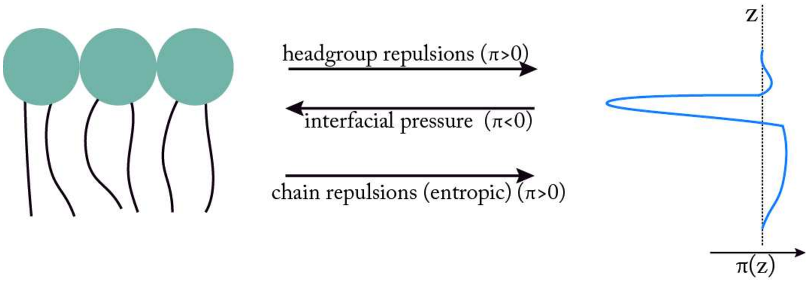

Figure 5.3: Lateral pressure profile across lipid bilayer. Schematic illustration of the forces that act within fluid bilayer. When the bilayer is in equilibrium the sum of forces equals zero (so-called *zeroth moment*). Adapted from [12].

The concept of CPP has been widely used to predict and describe morphology changes within mesophases. Indeed, this is the case for simple closed surfaces, where the interior contains the hydrophobic fraction (CPP < 1). However, the model detailed by Israelachvili fails to predict appearance of the inverse biocontinous phases. The CPP is limited to a qualitative interpretation of the phase diagrams, and cannot bring insight into the interfacial geometry nor on the physical mechanism regulating lipid's self-assembly behavior.

As a matter of fact the critical packing parameter determine only the local interfacial curvature. It can be demonstrated by adapting an equation for differential geometry describing area of parallel surfaces at distance d

$$a(d) = a(0)(1 + 2Hd + Kd^2) \tag{5.2}$$

where H,K are *Mean* ($C_1 + C_2$) and *Gaussian* (C_1C_2) curvatures respectively, for a surface with principal radii of curvature C_1 and C_2. The H is commonly defined to be *positive* for interface curved towards hydrocarbon chains. The negative H describes inverse phases. The sign of the Gaussian Curvature, K characterizes the nature of the surface.

Integrating Eq. 5.1 with respect to distance, d, over lipid length, l, gives the expression for the lipid parameter in terms of curvature of the interface between hydrophilic and hydrophobic regions.

$$\frac{v}{al} = 1 + Hl + \frac{Kl^2}{3} \tag{5.3}$$

Equation 5.3, shows that Mean and Gaussian curvatures can vary cooperatively with no influence on CPP value. Therefore, the critical packing parameter provides information only about local curvature of the interface, while the full morphology of phase, depends on minimum of the free energy of the aggregates.

5.1.1 Chain packing frustration

Because of this, more rigorous approaches have been developed, which consider the total free energy of the system, consisting of assemblies of lipid and water molecules Since the CPP model proposed by Israelachvili fails to describe more complex lipid structures, more rigorous approach has been developed, which consider total free energy of the lipid/water system. First given by Gruner *et al.* [228] and refined later, the expression for the total free energy of a lipid system is given by:

$$g_{total} = g_c + g_p + g_{intern} \tag{5.4}$$

where g_c is a contribution from the membrane curvature, g_p is the cost of packing of the hydrocarbon chains and g_{intern} represents various interactions, together with hydration force and electrostatic contributions. In practice, g_{intern} is negligible, therefore the curvature elasticity and hydrocarbon chain packing are the main terms governing the total free energy of the system.

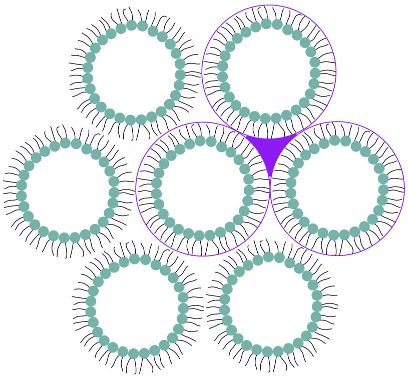

Figure 5.4: Illustration of packing frustrations in the H_{II} phase. The pink area indicates the void that exists in hexagonally packed cylindrical rods. As a consequence, energetically costly differences in chain extension or tilt angles are required in order to fill the void.

Packing of hydrocarbon chains, known also as *packing frustration* arises from the need of lipid chains to fill all available hydrophobic volume. For the lamellar phase, the space on the side of each interface is filled by the hydrocarbon lipid chains with uniform thickness. However, this state cannot be achieved in case of curved inversed systems, for example in inverse hexagonal phase (Figure 5.4). It is related to the fact that the distance from the center of hexagonally packed cylindrical rods to the unit cell boundary is not constant. In figure 5.4 it can be seen that different hydrophobic chain extensions [229] or tilt angles [230] are needed to fill the triangular 'voids' at the center points [231, 232]. This difference makes a significant energetic contribution in one-component system, where the chain length is constant. The void volume of a given amphiphile is inversely proportional to the interfacial curvature, and thus proportional to the diameter of water channels [231]. Therefore, reversed hexagonal phase exhibits small water channels and high interfacial curvatures. Controlling the water content in the system is one way to manipulate water channel radius. Other factors such as lipid chain unsaturation, branching, bigger chain length or temperature can tune the spontaneous curvature of the phase. In their work, Templer *et al.* [232] using a model based on competition of bending energy and packing frustration, calculated packing frustrations for a binary fatty acid/phospholipid mixture at 35°C. For inverse hexagonal phase packing frustration was equal to 54% of the total free energy, while it was 1% for the inversed bicontinuous cubic phase. This result signifies that the packing fraction plays a key role for the stability of the reversed hexagonal phase, whereas bending energy dominates in inverse bicontinuous cubic phases. Another approach to study the curvature elasticity pursued by Rand *et al.* [233], was the addition of alkane to lipid/water system in order to relieve packing stress. Further, a detailed study done by Khoo *et al.* [234, 235] demonstrated that addition of a long-chain alkyl to 1-monoolein (MO), forces the system to go through series of phase transitions (Q_{II} - H_{II} - $Fd3m$ - L_{II}). Addition of alkyl have relieved the packing frustration, and therefore favored phases with increasing inverse in interfacial curvature.

5.1.2 Bending interfaces

The common understanding of the energetics of membrane shaping is largely based on the seminal Helfrich theory [236] (from 1973), which reduces lipid bilayer to infinitely thin elastic surface that allows to treat it mathematically. The general expression for elastic bending energy per unit area, g_c, for a membrane is:

$$g_c = 2\kappa(H - H_0^2) + \kappa_g K \tag{5.5}$$

where H_0 is a spontaneous mean curvature of a stress-free surface determined by the distribution of the lateral stress, κ - the mean curvature (bending) modulus and κ_G represents a Gaussian modulus of the surface which expresses the bending energy and hence the shape of the interface.

A tendency in morphological changes can be predicted as a function of κ, κ_G and spontaneous curvature H_0. Deviations of the mean curvature from H_0 cost elastic energy, determined by the membrane bending κ. The measured values of κ for phospholipid membrane range between 5- 40

k_BT, and is assumed to be proportional to the square of the hydrocarbon thickness, and inversely proportional to area per headgroup to some power *p* (*p* comprise between 3 and 5) [237]. Single-chain lipids display values of κ fivefold smaller. Sherman *et al.* [238] have listed bending modulus, κ and κ_G/κ for some common membrane lipids and 1-monoolein (MO). Interestingly, results on 1-MO show that its bending modulus is comparable to thermal energy at room temperature, $k_B T \sim 4$ 10^{-21} J, which may imply that 1-MO is prone to thermal bending fluctuations, even when consider as a bilayer.

The Gaussian modulus, κ_G, plays a key role in controlling the topological complexity of the membrane. This follows from the Gauss–Bonnet theorem [239]. For lamellar phase the gaussian contribution to the bending energy vanishes, while for closed shaped membranes, like vesicles, its contribution is $\kappa_g = 4\pi(1\text{-g})$, where the genus g describes the topology of any closed interface. However, κ_G has no effect as long as the curvature fluctuations take place at constant topology. The value of Gaussian modulus is practically inaccessible to direct measurements. However, indirect measurements of κ_G has been exploited by Siegel and Kozlov [240].

5.1.3 Inverse bicontinous cubic phase

The majority of cubic phases observed for water/lipid systems are inverse biocontinous cubic phases. These structures were first reported by Luzzati [241] and Husson in 1962, however more detailed studies started in the mid-1980s. Scriven [242] defined biocontinuous cubic phases as single, continuous bilayer, where bilayer midplane is coincident with an infinite periodic minimal surface and subdivides the space into two interpenetrating, but not connected water channels. Following the mathematical argument of periodic minimal surfaces, three inverse biocontinous cubic phases are currently known: the double-diamond ($Q_{II}{}^D$, space group Pn3m), the primitive ($Q_{II}{}^P$, space group Im3m) and the gyroid ($Q_{II}{}^G$, space group Ia3d) (Figure 5.5). Alternative inverse discontinuous cubic phase structures are observed in more complex systems, including lattices with space groups Fd3m and Pm3m.

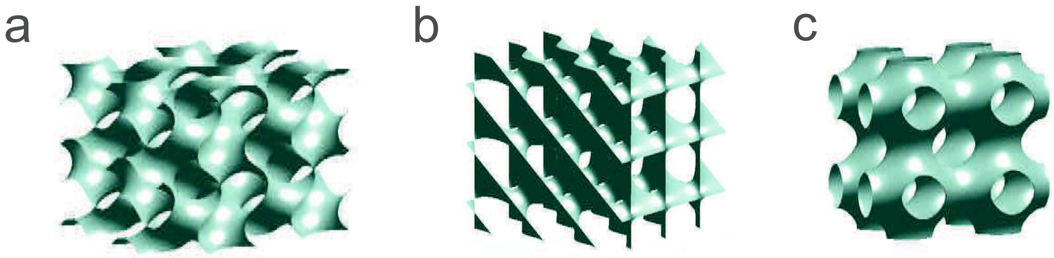

Figure 5.5: Mathematical representation of biocontinous cubic morphologies based on periodic minimal surfaces [243] a) Gyroid (Pn3m) b) Diamond (Ia3d) c) Primitive (Im3m).

Changes between two non-lamellar phases are fluid-fluid transitions, which involve changes in symmetry and/or topology. Such transitions between phases are mostly driven by the water content [244], pressure and temperature. One of the most well characterized lipid/water systems are monoacylglycerols, in particular 1-monoolein (MO) [245]. Its phase diagram was initially proposed by Lutton [246]. After further developments of Hyde *et al.* [245] the final and detailed version of the diagram was published in 2000 by Qiu and Caffrey [247], see Figure 5.6. An increase in the water content results in a transition from the lamellar phase to the gyroid (G) cubic phase then to the double-diamond (D) cubic phase. An increase in temperature results in transition from biocontinous cubic phase into an inverse hexagonal phase, (H_{II}) and finally micellar phase (L_2). The interesting feature of GMO-water system is excess-water phase separation region. Above certain water content, phase separation occurs into a structured phase coexisting with water excess indicating the maximum solubilization capacity for water of each phase. This excess-water phase separation can be further use to form so-called isasomes [213, 222] and other structured emulsions [248].

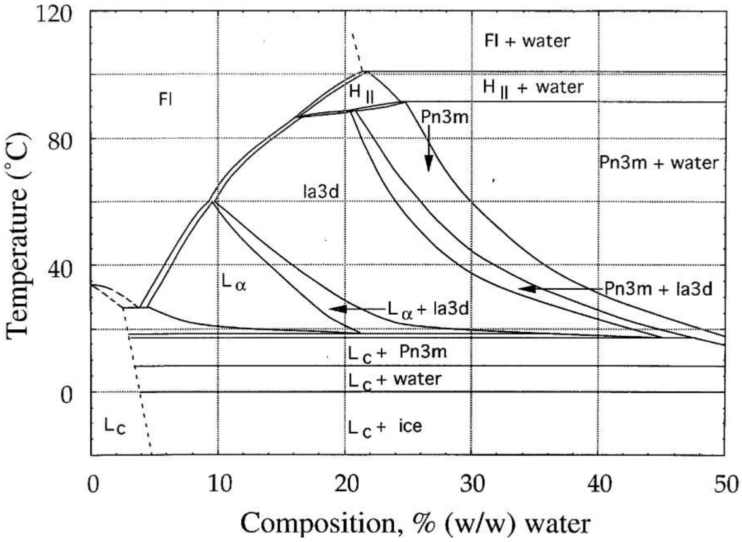

Figure 5.6: Experimental temperature–composition phase diagram for the MO/water system. Reprinted from [247].

Owing to their stability against dilution in excess of water, bicontinuous cubic and hexagonal phases can be dispersed into nanosized nanoparticles, known as a cubosomes and hexosomes [213]. the size of these nanoparticles are typically 200 – 300 nm in diameter and they retain most of the properties of the bulk material, which make them interestingl for drug delivery, where low viscosity nanoparticles are required for the intravenous administration of amphiphile-based drug formulations. Developed by Landh in 1994 [249], preparation of cubosomes and hexosomes involves use of nonionic block copolymers to colloidally stabilize dispersion of cubic phase. Pluronic F127 (also known as a Poloxamer 407) [250] is the most used dispersing agent. It is composed of polyethylene oxide (PEO) and polypropylene oxide (PPO) blocks: $PEO_{98}PPO_{67}PEO_{98}$. While the hydrophobic PPO part is adsorbed onto or incorporated into the surface of the particle, the hydrophilic part, PEO, extends to cover the surface and stabilize the dispersion [251]. A minimum of 4 wt% Pluronic 127 is required to obtain a stable dispersion of cubic nanoparticle. Handa and coworkers [252] reported a decrease in particle size at high (10 wt%) polymer/lipid ratio. Moreover, SAXS measurements done by Stroem *et al.* [253] revealed that the higher content of polymer evokes the coexistence of two phases: double diamond (D) and primitive (P), whilst only D type cubic phase is observed at lower concentrations. The observed transition is attributed to the high hydrophobicity of polymer, which induces positive curvature of cubic phase.

To date, the nature and properties of various cubsomes and hexosomes have been characterized with a vast variety of techniques, such as by small-angle X-ray scattering (SAXS) [254, 255], cryo-transmission electron microscopy (Cryo-TEM) [256] and cryo-FESEM [257, 258], cryo-scanning electron microscopy (SEM) [253] and differential scanning calorimetry (DSC) [248].

5.2 Project II: Influence of a pH-sensitive polymer on the structure of monoolein cubosomes

Cubosomes are stable nanoparticle dispersions formulated from bulk cubic phases (Fig. 5.7). They have been gathering increasing attention due to their potential applications in nanomedicine. However, pure MO systems alone do not respond to biological or external stimuli such as temperature, light, pH or ionic strength. Hence, significant efforts are being made towards more accurately controlled release of target biomolecules [259, 260] and on modulating the release properties of the host-guest lipid cubic phases in response to specific external conditions [261–265]. This approach recently led to the development of stimuli responsive cubosome-based drug-delivery systems with the capacity of releasing their content in response to external triggers.

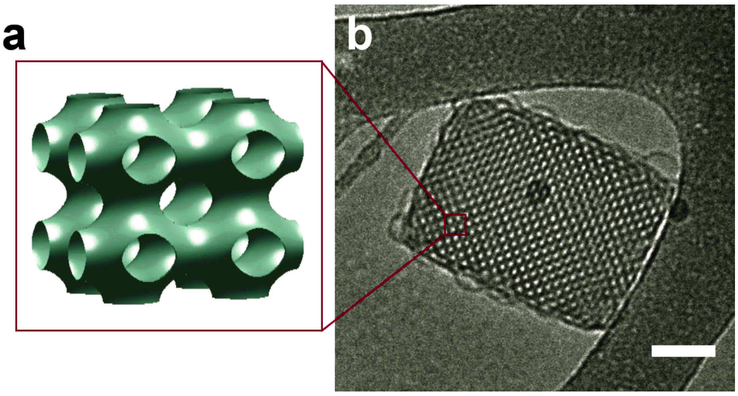

Figure 5.7: a) Graphical picture of an inverse cubic phase with primitive type structure *Im3m* b) Cryo-TEM image of a monoolein cubosome stabilized with 5 wt % Pluronic F127. Scale bar, 100 nm.

Negrini and Mezzenga [266] studied the effect of pH changes on the transport properties of monolinolein/linoleic acid (97:3 wt % ratio) bicontinuous cubic phases. The system that they designed was shown to reversibly change from an *Im3m* cubic phase to an inverted hexagonal H_{II} phase in response to acidic (pH 2) conditions. This strategy was further exploited by Negrini *et al.* [265] who presented a pH-responsive cubic phase, where controlled release of cargo is achieved by adapted host-guest electrostatic interactions.

In this work, we describe a new MO-based pH-sensitive cubosome system we have developed, loaded with a pH-sensitive polymer (see Fig. 5.8). This polymer, a poly (L-lysine-*iso*-phthalamide) grafted with L-phenylalanine at the degree of grafting of 50% hereafter referred as PP50 (see Chapter 6), is a promising pseudopeptidic polymer whose hydrophilic/hydrophobic balance depends on external pH [267–269]. It is by design capable of mimicking the activity of membrane-penetrating peptides. The presence of carboxylic acid side groups causes reversible conformational changes in an aqueous environment from extended charged polyelectrolyte chains at neutral pH, to a globular state at acidic pH, resulting in a higher binding affinity for the lipid membrane, causing its subsequent disruption. Thus, PP50 is an appealing example of a stimulus-responsive material, potentially able to minimise drug losses at neutral pH while conversely triggering rapid intracellular drug release from the cubic phase in an acidic environment.

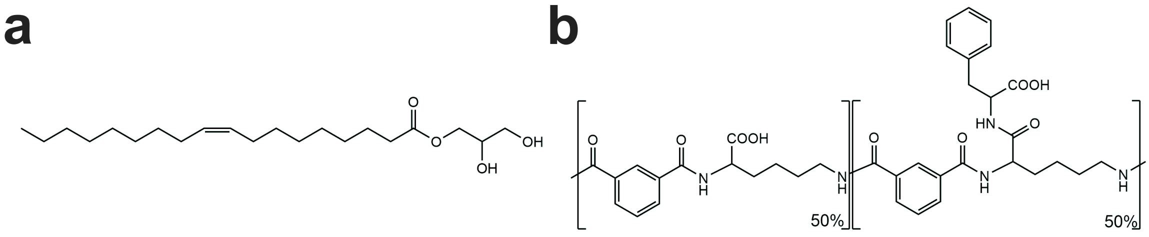

Figure 5.8: The chemical structures of a) Monoolein (MO) and b) Poly(L-lysine-*iso*-phthalamide) chain grafted with phenylalanine (PP50).

In this project, we describe how the pseudopeptide PP50 can be associated with standard MO cubosomes prepared by sonication and stabilization with the nonionic Pluronic F127 surfactant [250]. We have studied the structure of MO cubosomes incorporating a small amount (10 wt %) of PP50 at two distinct pH values: pH 7.5 and pH 5.5. The crystallographic structure and the cubic cell size were determined by by SAXS, whilst the morphology and topology of the MO-cubosomes were characterised by Cryo-TEM.

It was found that under neutral pH conditions, the presence of polymer preserves the original *Im3m* cubosome structure, while a significant amount of structural disruption, with a partial disappearance of the cubic phase, is observed under acidic conditions. This suggests that our novel system has a strong potential for developing pH-responsive encapsulation vectors based on cubosomes.

5.2.1 Results and discussion

5.2.1.1 Effect of the addition of polymer on the nanoparticle size

Prior to structural analysis, cubosomes with and without polymer and the polymer solution (3 mg mL^{-1}) were characterised in terms of particle size and ζ-potential (Table 5.1). As previously reported, the polymer-free cubosome particles formed stable, milky dispersions with particle sizes ranging from 170 to 220 nm under both pH conditions studied. Incorporation of 10 wt % PP50 into the cubic phase at physiological pH moderately increased the size of the nanoparticles, whilst at pH 5.5 the change was more significant (283 nm). The polydispersity index (PDI) was estimated to be in the approximate range of 0.2-0.3, for all systems studied, indicating moderately heterogeneous systems. Moreover, particle dispersions stored at room temperature over a week showed no significant changes in the size and PDI, indicating physically stable systems.

The ζ-potentials of unloaded cubosomes were -1.2 and 1.1 mV for pH 7.5 and 5.5 respectively, and only a slight decrease of these values was observed upon polymer incorporation. This points to a marginal surface coverage of the particles by the negatively charged polymers.

5.2.1.2 SAXS measurements

The liquid-crystalline structure of MO cubosomes incorporated with the polymer was investigated using SAXS. Reference samples without polymer, at pH 7.5 and 5.5 (Fig. 5.9a,b), showed a sequence of three well-defined diffraction peaks with relative positions at ratios of $\sqrt{2}$, $\sqrt{4}$ and $\sqrt{6}$ respectively, which corresponds to a primitive *Im3m* cubic structure. For the sample without polymer at pH 7.5, the next peaks of this space group symmetry ($\sqrt{10}$ and $\sqrt{12}$) were also visible. The

Table 5.1: Hydrodynamic diameter and ζ-potential of cubosomes w/wo polymer and the pure PP50 solution under different pH conditions. Values are shown as averages over 3 samples with 10 runs each, and the standard deviation is used as an error estimate. As anticipated, the polymer was well dispersed at pH 7.5 and aggregated at pH 5.5 (DLS sizing data column)

Sample	Size (nm)		ζ—potential (mV)	
	pH 7.5	pH 5.5	pH 7.5	pH 5.5
Cubosomes	178.1 ± 5.2	220.9 ± 4.2	-1.2 ± 0.8	1.1 ± 0.4
Cubosomes with PP50	212.7 ± 4.7	283.3 ± 3.6	-2.1 ± 1.0	0.11 ± 0.7
PP50	N/A*	50.7 ± 4.2	-13.1 ± 2.1	-28.4 ± 1.0

[*] *Not enough scattering from the linear dispersed polymer chains*

[**] *Measured by SAXS*

[***] *Obtained from Cryo-TEM images analysis of 7 cubosome nanoparticles*

Table 5.2: Lattice parameters (a), calculated water volume fraction (ϕ_w) and water channel radius (r_w) of MO cubosomes w/wo polymer as a function of pH

Sample	a** (Å)		a*** (Å)		ϕ_w (%)		r_w (Å)	
	pH 7.5	pH 5.5	pH 7.5	pH 5.5	pH 7.5	pH 5.5	pH 7.5	pH 5.5
Cubosomes	143.0 ± 0.1	137.3 ± 0.4	140.2 ± 0.2	139.0 ± 0.4	44.5 ± 0.1	42.5 ± 0.1	25.8 ± 0.1	24.0 ± 0.1
Cubosomes with PP50	163.2 ± 0.1	167.2 ± 0.1	163.0 ± 0.5	156.0 ± 0.9	50.4 ± 0.1	50.4 ± 0.1	31.8 ± 0.1	33.0 ± 0.1

corresponding lattice parameters, a = 143.0 ± 0.1 Å and a = 137.3 ± 0.4 Å for cubosomes at pH 7.5 and pH 5.5 respectively, were in agreement with previously published data.[270] The SAXS profile of the cubosomes prepared with 10 wt % of polymer at pH 7.5 (Fig. 5.9 c) displayed the same sequence of peaks, showing that the *Im3m* structure was preserved. The positions of the peaks indicated a lattice parameter of a = 163.2 ± 0.1 Å larger than the reference case, while the peak intensities relative to the diffuse background appeared slightly reduced (Fig. 5.9 and Table 5.2).

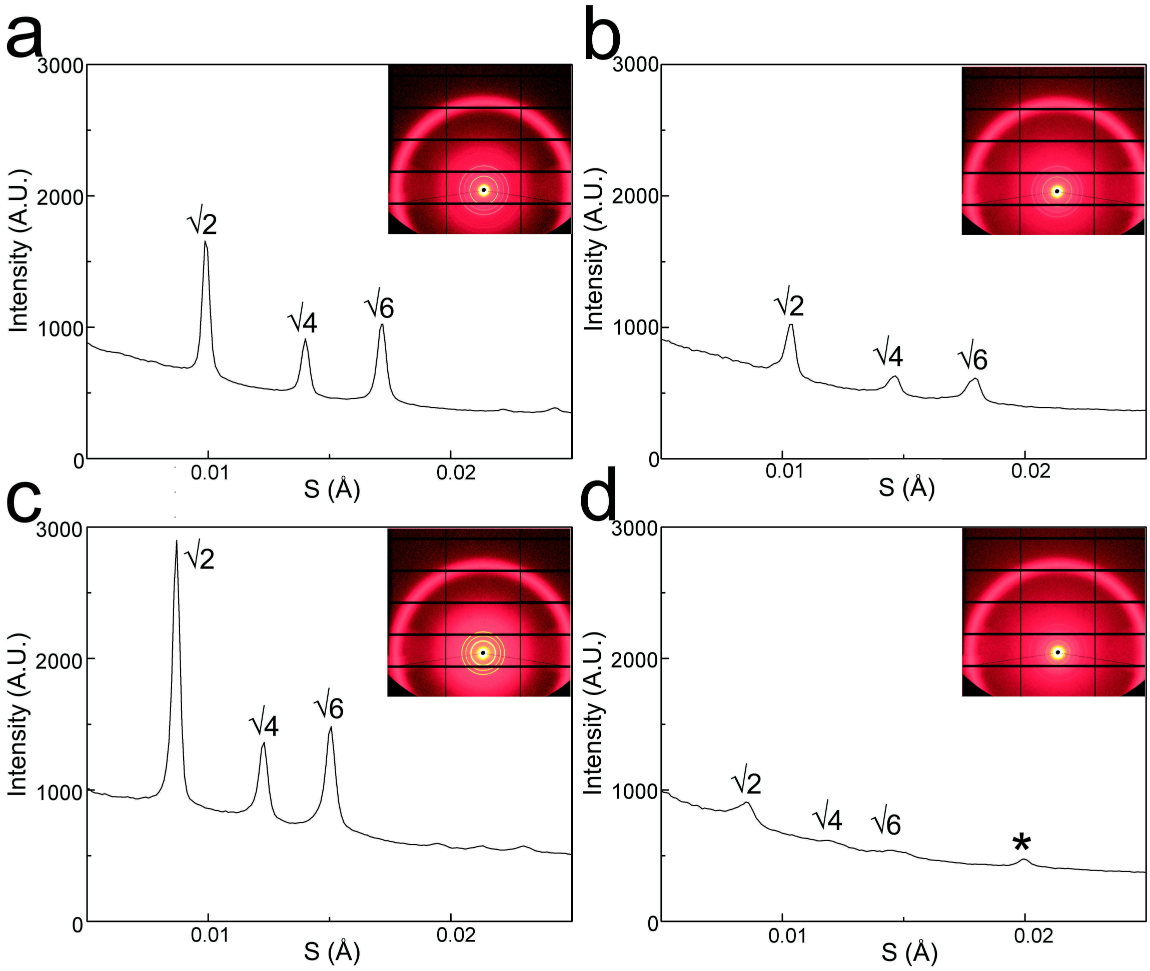

Figure 5.9: 1-D diffraction plots of intensity vs. scattering parameter $S = q/2\pi$ for MO-cubosomes doped with 10 wt % PP50 polymer. a) Cubosomes at pH 7.5 (lattice parameter a = 143.0 ± 0.1 Å, Peak positions: 100.8 Å, 71.4 Å, 58.2 Å); b) cubosomes at pH 5.5 (lattice parameter a = 137.3 ± 0.4 Å, Peak positions: 96.6 Å, 68.5 Å, 55.8 Å); c) cubosomes with polymer at pH 7.5 (lattice parameter a = 163.2 ± 0.1 Å, Peak positions: 114.9 Å, 81.6 Å, 66.8 Å); d) cubosomes with polymer at pH 5.5 (lattice parameter a = 167.2 ± 0.1 Å, Peak positions: 116.7 Å, 84.2 Å, 68.5 Å, 50 Å). The peak indicated by * corresponds to a spacing of 50 Å.

At lower pH (Fig. 5.9 d), the SAXS data of the cubosome solution incubated with PP50 polymers looked significantly more diffuse. A sequence of well visible but smaller peaks with relative positions at $\sqrt{2}$, $\sqrt{4}$ and $\sqrt{6}$ respectively was observed, still consistent with a P-type *Im3m* structure with a = 167.2 ± 0.1 Å. In addition, a new peak at 50 Å (indicated by *) appeared, which was not related to the previous family of diffraction peaks.

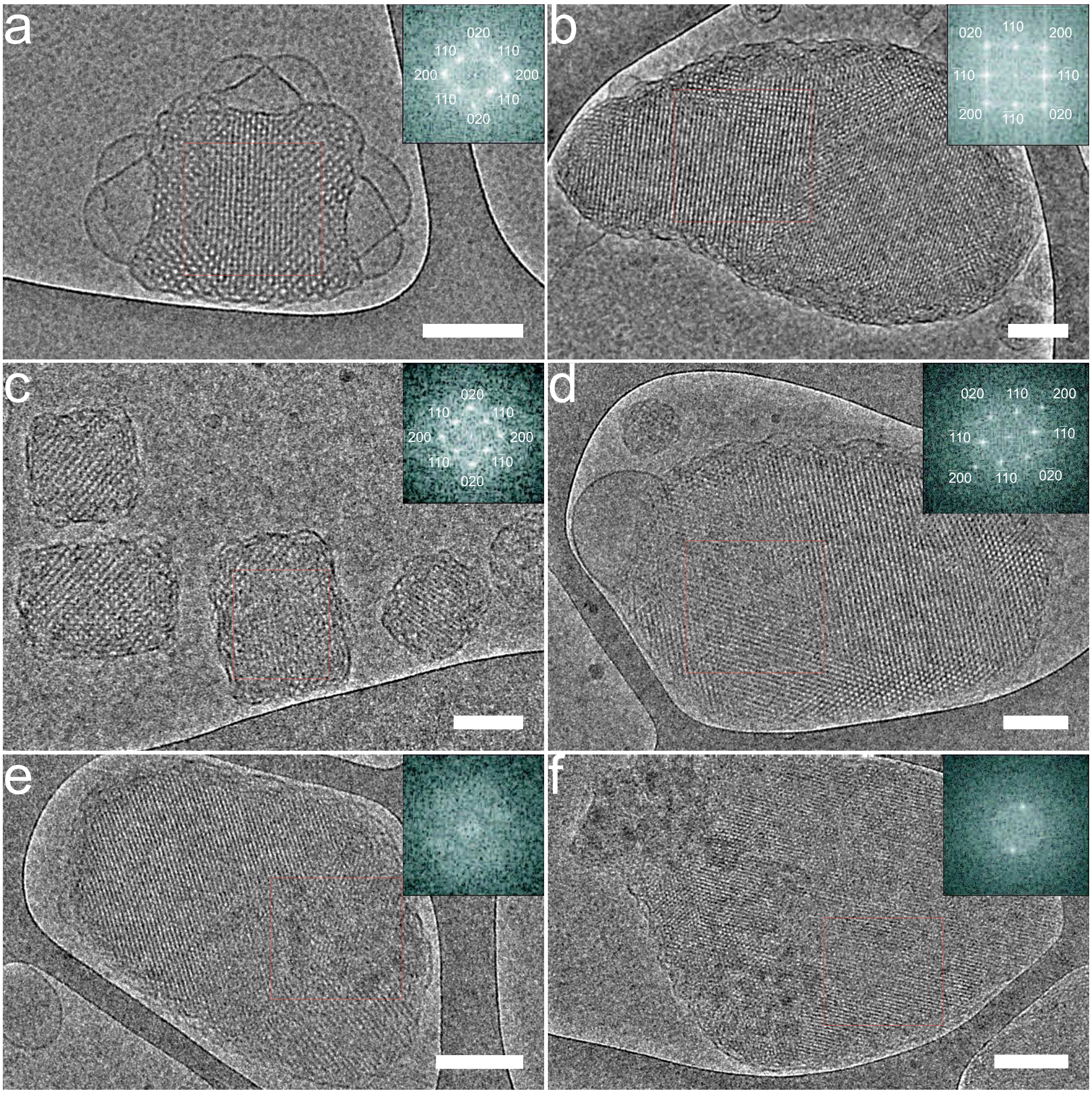

Figure 5.10: Representative Cryo-TEM images of cubosome dispersions used in this study, with the corresponding Fast Fourier Transform (FFT) of red box areas (insets). Unloaded cubosome: a) pH 7.5; b) pH 5.5; c), d) cubosome/PP50 at pH 7.5. e), f) cubosomes/PP50 at pH 5.5. FFT was used for determination of the structure of the liquid crystalline particles, independently from SAXS. Scale bar, 100 nm.

5.2.1.3 Cryo-TEM observations

We used Cryo-TEM to visualize the nanostructure of the cubosome particles in both physiological pH 7.5 and acid pH 5.5 environments. Cryo-TEM images (Fig. 5.10 a,b), combined with Fast Fourier Transform (FFT) analysis, revealed that at both pHs, the reference samples formed stable bicontinuous cubic phases with an *Im3m* symmetry and a measured lattice parameter of the order of 140 Å as commonly observed in previous preparations [271, 272]. This indicates that pH alone does not influence the stability of MO cubosome particles. Moreover, the bilayer thickness, as determined by image analysis, was about ~36 Å (Table 5.2) which was in excellent agreement with values reported elsewhere [271].

The structural symmetry of the primitive *Im3m* cubic phase was clearly preserved upon incorporation of the polymer at physiological pH (Fig. 5.10 c,d). More importantly, a corresponding analysis of the structural parameters showed that the presence of the polymer expanded the unit cell size a. This increase in lattice parameter was similar to what was observed in SAXS (Fig. 5.9 c and Table 5.2). From the FFT analysis of a number of selected particles, a mean lattice parameter of 160 Å was obtained.

Remarkably, in the low pH regime (5.5), where PP50 is expected to interact strongly with the lipids, some clear disruption of the underlying cubic phase structure was observed (Fig. 5.10e and Fig. 5.11). A number of changes varied from particle to particle, and within a given particle. There was in some regions a significant collapse of the structure, with disappearance of the lattice structure. FFT analysis confirmed the absence of periodicity. In other regions, the cubic regions were preserved as in the reference sample.

Finally, one could find regions in particles displaying some apparent lamellar ordering, with an anisotropic orientation confirmed by FFT analysis. Whether the cubic structure disappeared totally or only partially, our Cryo-TEM images demonstrated the pH dependent disruptive action of the polymer on the MO-bilayer within the cubic phase.

Measurements of cubic lipid phases, pure or with additives, are commonly carried out in buffer solutions of various chemical compositions, ionic strengths etc. It has been reported that such parameters, like the presence of salts of different chemical natures, the exact pH, temperature and pressure values, might all influence the phase behaviour of these lyotropic liquid crystals. In the present study, the addition of 10 wt % polymer (with respect to the lipid mass) was accompanied by a 12% increase in the value of the unit cell size (from 143 to 163 Å) in HEPES buffer (pH 7.5).

Although the polymer cannot be unambiguously located within the sample, the Cryo-TEM images and the sharp appearance of the SAXS peaks indicate that the particles were spatially homogeneous and that, if present inside, the polymer was evenly distributed. From the geometry of the primitive cubic structure, one could estimate the amount of water present in the particles compared to the bulk aqueous solution. Ignoring the Pluronic F127 and PP50, it is possible to relate the volume fraction of lipid Φ_l to the cell size a, and lipid length l in the parallel surface approximation:

$$\Phi_l = 2A_0(\frac{l}{a}) + \frac{4\pi\chi}{3}(\frac{l}{a})^3 \qquad 5.6$$

where A_0 and χ are respectively the ratio of the area of the minimal surface in the unit cell to the quantity (unit cell volume)$^{2/3}$, and the Euler-Poincare characteristic, which depends on the symmetry of the cubic phase [273, 274]. In the case of the *Im3m* structure, the values are A_0=2.3451,and χ=-4. Using the standard monoolein value l = 18 Å in the absence of PP50 at pH 7.5 (consistent with the bilayer thickness of 36 Å seen in Cryo-TEM), one gets Φ_l= 0.555. According to this value, 50 mg of monoolein were hydrated by about 40 mg of water. The free water (1 g or more) was present in much larger amount, showing that the cubosome structures were in equilibrium with excess water. If PP50 did not penetrate the nanoparticles and was thus present only in the excess free aqueous solution, it could still act on the cubic phase indirectly, in a solvent-mediated way. An obvious mechanism would be depletion, with PP50 lowering the water chemical potential in the excess solvent region. One would expect to see in this situation a dehydration of the lipid phase, and some decrease in the lattice size, which was contrary to our present observations. With the PP50 being deprotonated at pH 7.5, its adsorption onto the cubosome particles' outer surface should confer them with a negative surface charge, with a correspondingly negative zeta potential. Table 5.1 indeed reveals that the zeta potential of cubosomes decreased by 0.9 mV in the presence of PP50. The change has the expected sign but was small in magnitude. We, therefore, doubt that PP50 covered the particle surface extensively. The most likely scenario was that PP50 penetrated into the cubic phase water channels. The PP50 sample used in the present study has a number average mass of M_n = 23.0 kDa, while the segment represented in Figure 5.8 b has a molar mass of 350 Da, with an estimated length of 30 Å for a diameter of 14 Å (using a molecular model). Taking b = 30 Å as the Kuhn segment length of the repeat units, the polymer consisting of 70 segments has a gyration radius $R_g = \sqrt{70}/\sqrt{6}\, b$ = 100 Å. On the other hand, the water channel radius, r_w, can be estimated using the relation between r_w and the lattice parameter a [275]:

$$r_w = 0.305a - l \qquad 5.7$$

with a = 163 Å and l = 18 Å one finds r_w= 32 Å. Penetration of PP50 chains in the cubic nanostructure therefore seems a reasonable assumption. The magnitude of the cell size variation, the uniformity of the structures and the relative size of the polymer and the cubic cell make of the penetration of PP50 into the cubosome particles the most likely possibility.

We discuss now the possible mechanisms for the cell size increase in the presence of the polymer. We observed first that pH reduction only marginally decreased the measured unit cell size of the reference samples by 6 Å. By comparison, the addition of PP50 at pH 7.5 increased this value by 20 Å. The change of electric charge on the polymer backbone when decreasing pH from 7.5 to 5.5 did not seem to be a prominent factor. The measured lattice parameter at pH 5.5 in the absence and presence of PP50 were 137 and 167 Å respectively. This suggests that electrostatic repulsion is not a likely candidate for explaining the observed swelling. Moreover, all experiments were done under buffered conditions, in which electrostatic interactions were strongly screened. At pH 7.5 it is unlikely that the polymer inserts deeply into the bilayer. Modifications are probably therefore induced by the interaction between the water-soluble polymer and the monoolein interface. Whether the polymer is depleted or adsorbed by the membrane, its presence between the bicontinuous channels changes the free-energy at two levels. First, it induces direct interactions between different parts of the bilayer over the range of the polymer size. Secondly, the polymer-membrane interaction changes the curvature elastic constants of the bilayer, the bending rigidity κ and the Gaussian rigidity $\overline{\kappa}$. For depletion and equilibrium adsorption this is expected to decrease κ and increase $\overline{\kappa}$, while for inserted polymers, an increase in κ and a decrease in $\overline{\kappa}$ are expected [276].

The observed swelling of the cubosomes at pH 7.5 suggests that the presence of PP50 promoted a reduction in the magnitude of the spontaneous monolayer curvature. Hence, the spontaneous curvature of the lipid bilayer towards the water region decreased, resulting in a higher water uptake capacity.

Table 5.2 lists the variation of the lattice parameter a, measured by SAXS, the size of water pores r_w and the water volume fractions Φ_w. As can be observed, the water channel size increased while some polymer was incorporated into the cubic phase. At physiological pH, this suggests that the polymer behaved like a hydration-modulating agent i.e. favoured the hydration of the *Im3m* phase without changing the structure (Fig. 5.9 c,d). Similar swelling behaviour of cubic phases upon addition of additives has been reported previously by Angelov [277] and Negrini *et al.* [264].

5.2.1.4 Polymer-induced structural changes under acidic pH conditions

The well-resolved diffraction peaks obtained in SAXS (Fig. 5.9 a,b,c) at pH 7.5 or pH 5.5 without PP50 indicate well-ordered cubic phases. The Cryo-TEM images of a selection of particles show cubic ordering established across the whole particles. FFT image analysis displays characteristic fourfold symmetric patterns depending on the orientation of the particles with respect to the electron beam (Fig. 5.10 a,b,c,d). We conclude that the reference sample and the polymer loaded sample at pH 7.5 are composed of crystalline pieces of *Im3m* bicontinuous cubic phase.

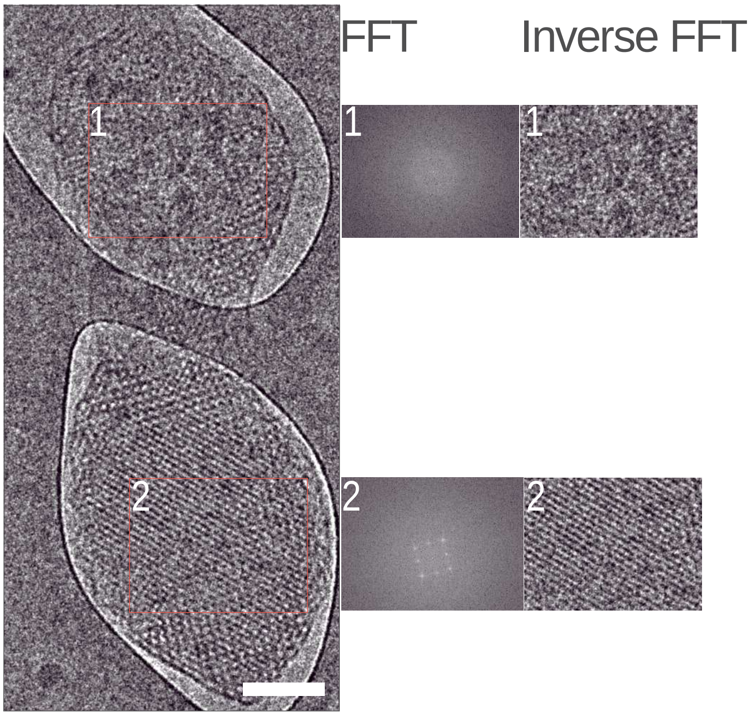

Figure 5.11: Cryo-TEM images of a single cubosome at pH 5.5 with incorporated polymer. The red boxes represent the areas used for FFT calculations. Scale bar, 100 nm. (a = 156.0 Å). 1) upper part of particle 2) lower part of particle.

Figure 5.10 e,f and Figure 5.11 show a selection of nanoparticles with PP50 at pH 5.5. We could see large disordered regions, with no visible periodic ordering, confirmed by the absence of peaks in the FFT image analysis. Disordered and cubic ordered regions coexisted, sometimes within the same particle. Fig. 5.11 shows a single particle in the same field of view: the upper part of the particle was mostly disordered, while the bottom of the particle still presented a cubic ordering. The particle in Fig. 5.10 f displayed some apparent lamellar order, associated with two spots in its FFT pattern. Therefore, cubosomes with polymer in acidic conditions can be seen as a collection of totally or partially disordered particles coexisting with cubic and lamellar ordered particles. The image analysis performed on the lamellar regions leads to a repeat distance comprised between 65 and 75 Å. The TEM observations account well for the observed SAXS patterns. Indeed, with only a small fraction of the particles retaining their cubic order, the *Im3m* diffraction peaks are faint in Fig. 5.9 d. The observed peak at q^* is consistent with a lamellar phase with a repeat distance d = 50 Å rather different from the lamellar periodicity estimated by Cryo-TEM. This discrepancy might be due to a slow time evolution of the cubosome structure interacting with the hydrophobic polymer. The SAXS and the Cryo-TEM measured values could correspond to different ageing stages of the samples.

5.2.2 Conclusions

We prepared pH-sensitive cubosomes from monoolein by adding a pH sensitive polymer to the cubosome dispersions. The dispersions were stable and well-ordered at neutral pH. In acidic buffer, the presence of the polymer resulted in significant structural changes in the particle structure, leading to large disordered regions.

5.2.3 Materials and methods

Materials

Monoolein powder (1-Oleoyl-rac-glycerol, C18:1c9, M$_w$ = 356.54 Da), Pluronic F127 (PEO$_{99}$-PPO$_{67}$-PEO$_{99}$, M$_w$ = 12600 Da) and buffer components (HEPES, Citrate buffer) were supplied by Sigma-Aldrich, Co. (Saint-Quentin, France). All chemicals had purities of >98% and were used without further purification.

Polymer synthesis and characterisation

The polymer PP50 was synthesised as described previously [278]. Briefly, the parent polymer PLP (poly(L-lysine-*iso*-phthalamide)) was synthesized by polycondensation of L-lysine methyl ester dihydrochloride and *iso*-phthaloyl chloride followed by ester hydrolysis. After purification, PLP was conjugated with L-phenylalanine methyl ester hydrochloride by DCC-coupling reaction followed by ester hydrolysis. The final PP50 was obtained after dialysis using a Visking membrane tubing (molecular weight cut-off, 12000-14000 Da). PP50 is a linear copolymer, composed of a sequence of 50% unsubstituted and 50% phenylalanine substituted L-lysine *iso*-phthalamide monomers (see Fig. 5.8 b). The polymers used in the present study had a number averaged molecular weight M$_n$ = 23.0 kDa, and a mass averaged molecular weight M$_w$ = 45.8 kDa, as determined using an aqueous gel permeation chromatography (GPC) system (Viscotek, UK).

Sample preparation

Colloidal dispersions of cubosomes were prepared as described by Landh [249]. Briefly, for each sample, 50 mg of pure lipid was dispersed in chloroform, and the organic solvent removed under a nitrogen stream followed by overnight vacuum pumping.

SAXS samples: The lipid deposit was hydrated with 94 wt % buffer solution (0.707 mL), and then subjected to 10 freeze-thaw cycles. The resulting lipid dispersion was a cubic phase in excess water (*Pn3m*, characterisation not shown). Following the freeze-thaw cycles, a Pluronic F127 aqueous solution was added (2.68 mg surfactant in 0.30 mL buffer) for the polymer free reference samples, while Pluronic F127 (2.68 mg) dispersed with PP50 (4.84 mg) in 0.294 mL of buffer solution, was added for polymer loaded samples, corresponding to a total volume of 1 mL of buffer.

Cryo-TEM samples: The preparation followed similar steps to the preparation of the X-ray samples, but using larger volumes of buffer. The lipid deposit was first hydrated with a buffer solution (1.288

mL), followed by 10 freeze-thaw cycles, and 2.68 mg of Pluronic F127 and 4.84 mg of PP50 polymer dispersed in 1.288 mL of buffer (2.576 mL total volume of a buffer) were added.

Samples were probe-sonicated (Bioblock VibraCell 72412) at 30% amplitude for 5 min total time at 1 on/off cycle period to prevent overheating. The two hydration solutions used in the study were set to pH 7.5 with HEPES buffer (20 mM) and to pH 5.5 with citrate buffer (100 mM) prior to mixing with lipids. Hydration, sonication and stabilisation with the surfactants transformed the bicontinuous cubic phase into cubosome dispersions. Samples were then characterised by SAXS or Cryo-TEM. Cryo-TEM imaging was performed with fresh samples (a couple of hours) while SAXS samples had to be prepared a day before being placed in the Synchrotron beam.

Cryo-transmission electron microscopy (Cryo-TEM)

A laboratory-built humidity-controlled vitrification system was used to prepare the samples for Cryo-TEM. Humidity was kept close to 80% for all experiments and the temperature was set at 22°C. A 5 μL of the sample was placed onto a grid covered by the lacey carbon film (Ted Pella), which was rendered hydrophilic via glow discharge (Elmo, Cordouan Technologies). Excess sample was removed by blotting with filter paper and the sample grid was vitrified by rapid plunging into liquid ethane (-180°C). The grids were kept in liquid nitrogen before being transferred into a Gatan 626 Cryo-holder. Cryo-TEM imaging was performed on an FEI Tecnai G2 TEM (200 kV) under low dose conditions with an Eagle slow scan CCD camera.

Cryo-TEM Image Analysis

Fast Fourier transform and sizing of the nanoparticles were performed using ImageJ software (NIH, USA) software. The error in the determination of the lattice parameter from Cryo-TEM images analysis was estimated at ± 5%.

Small angle X-ray scattering (SAXS)

The cubosome structures were determined by small-angle X-ray scattering using beamline I22 at Diamond Light Source (DLS) with X-ray wavelengths of 0.73 Å. The 2-D powder diffraction pattern was recorded on an image-intensified Pilatus 2M detector. Silver behenate (a = 58.38 Å) was used to calibrate the small angle X-ray diffraction data for all measurements. SAXS data were analysed using the IDL-based AXcess software package, developed at Imperial College London. Details of the use of AXcess for data analysis can be found in ref [279].

Dynamic light scattering (DLS)

The size and ζ-potential of the lipid nanoparticles were measured with a ZetaSizer Nano ZS (Malvern Instruments, UK) at 25°C. Triplicate measurements with a minimum of 10 runs were performed for each sample.

6 | pH-sensitive polymers

6.1 Introduction

The cell membrane is a dynamic structure which regulates and coordinate the entry and exit of small and large molecules. Essential ions and small molecules are transported through the action of specialized membrane-transport proteins channels. Nano size materials, such as drug delivery systems, are internalized through endocytosis upon contact with the cell membrane. This endosomal pathway starts with the formation of early endosomes vesicles and continues via progressive maturation and deliver the cargo to various intracellular compartments, where cargo is recycled to the external milieu or degraded without its release into the cytosol. A crucial element of this process is the gradual acidification (from pH ~6.0 to ~4.5) of the maturing vesicle, generated and maintained by the V-ATPase proton pumps [280]. Depending on the properties of nanomaterials and type of the cell, endocytic pathway can occur (Figure 6.1) via phagocytosis or pinocytosis.

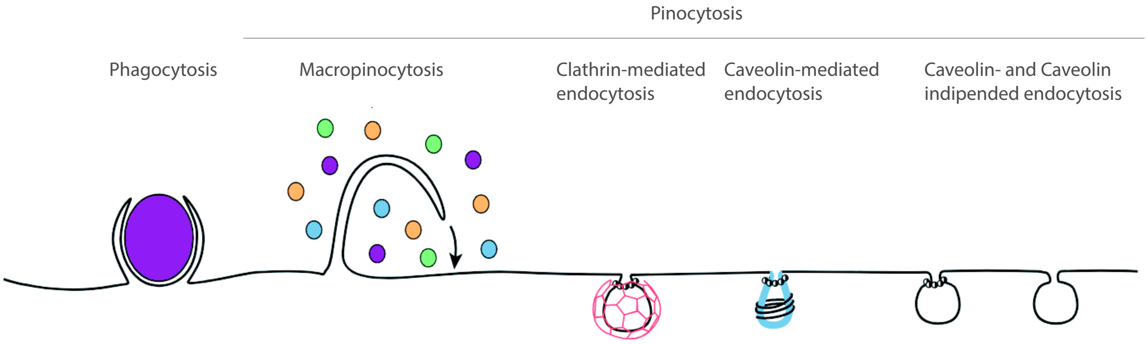

Figure 6.1: Diverse mechanisms of nanomaterial internalization by the cell membrane. Adapted from [281].

In order to avoid this endosomal fate, an effort has been devoted to developing a new generation of nanocarriers that can disrupt the endosomal membrane. One of the promising directions involves tailoring the properties of nanocarriers to work in a triggered manner. To date, cationic and anionic delivery systems, polymeric micelles [282], poly (amino acids) [283] and pseudo-peptidic polymers [284] have been studied as potential pH-sensitive nanocarriers [285].

A nanocarrier with pH-sensitive capability can discern the pH-shift after endosomal capture and, as a response, facilitate the release of the drug into the cytosol by a lipid membrane rupture. It is clear that the presence of the pH-tunable moieties (e.g. carboxyl or tertiary amino groups) within the nanocarrier structure plays a key role in the release of a cargo in response to the trigger. Upon a variation of pH, pH-sensitive domains undergo (de)protonation, subsequently changing the hydrophobicity of the whole polymeric nanocarrier. These co-operative interactions i.e. ionization and H-bonding between moieties evoke reversible conformational changes from extended charged chains to clumped up or globular state [286]. This behavior results in higher binding affinity to the endosomal membrane and its subsequent disruption, consequently leading to release of the cargo into the cytoplasm.

Despite significant progress in this field, knowledge is still missing about the translocation process of pH-sensitive nanocarriers through a lipid membrane under different pH values. It is therefore essential to gain more insight into the structure-activity relationship of pH-sensitive materials with cell- and endosomal- membranes in order to design more efficient drug delivery systems.

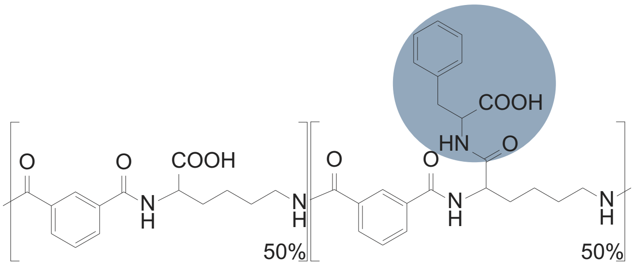

Figure 6.2: The poly(L-lysine isophthalamide) chain with L-phenylalanine grafted at the pendant carboxylic acid residue (grey circle).

Amphiphilic pseudo-peptides have been designed and synthesized to mimic behavior of fusogenic peptides [287, 288]. Recently, Chen *et al.* developed a new acid-responsive polymer, where phenylalanine was grafted onto the poly(L-lysine isophthalamide) backbone with at 50% stochiometric molar substitution (PP50, Figure 6.2). The hydrophobic backbone with carboxyl groups undergoes random-coil to globular conformational transitions. The pH-mediated conformational change is regulated by the balance between the hydrophobic moieties and the charged carboxyl groups. The activity of this polymer is reportedly aligned to the pH-environment of endosomes (pKa=6.5). Following acidification, protonation of the exposed carboxylic acid groups, the polymer displays changes of conformation from extended chain to collapsed hydrophobically stabilized structures. This feature leads to increased binding of the polymer to cell membranes and subsequent membrane distribution

It has been demonstrated *in vitro* that PP50 can serve as a nanocarrier for a vast range of molecules. PP50 has been employed to successfully deliver trehalose into human erythrocytes and human cells [289, 290]. It was reported that at pH 7.0 the polymer adsorbs on the membrane surface, yielding to its thinning and limited intake of the sugar. This phenomenon has been explained in terms of the hydrophilic/hydrophobic balance due to the partial protonation of the polymer. For lower pH, the change in conformation and hydrophobicity of PP50 resulted in an increase of membrane permeability to trehalose. Novel approaches involving delivery of proteins or SiRNA [291] into the cytoplasm of cells have also been recently developed, opening a broad array of possible applications. These studies have also confirmed the biocompatibility of PP50 and its derivatives. Despite a great deal of work on the subject [287, 292], the detailed mechanism of membrane-mediated action of given pH-sensitive polymer remains elusive. A better understanding of this interplay is crucial in developing new strategies and enhance the polymer efficiency. Therefore, in this work we aim at investigating the effects of PP50 on lipid model membranes. We employed Cryo-TEM, SANS and differential scanning calorimetry (DSC) to obtain information on the bilayer structure upon interaction with the polymer.

6.2 Project III: Action of the pH-sensitive polymer PP50 on fluid phospholipid bilayers

6.2.1 Results and discussion

6.2.1.1 Cryo-TEM visualization of interaction between DOPC-LUVs and pH sensitive polymer PP50

Our first approach to assess the membrane-lytic properties of PP50 was to perform Cryo-TEM imaging of large unilamellar vesicles (LUVs) incubated with polymer at two different pH: 7.5 and 5.5. Therefore, buffer solution of polymer (3 mg/ml) was incubated with DOPC-LUVs (1.5 mg/ml) for 60 min. As seen in Figure 6.3, systems at both pH show no appreciable alteration of membrane morphology with respect to pure lipid systems. Since our results on the interaction of the polymer with monoolein cubosomes (see Chapter 5) clearly demonstrate the ability of PP50 to disrupt the lipid structure at low pH conditions, we decided to replicate the preparation of the sample. DOPC-lipid films were directly hydrated with a solution of PP50 at both physiological (pH 7.5) and acidic (pH 5.5) pH and subjected to tip sonication for 15 min.

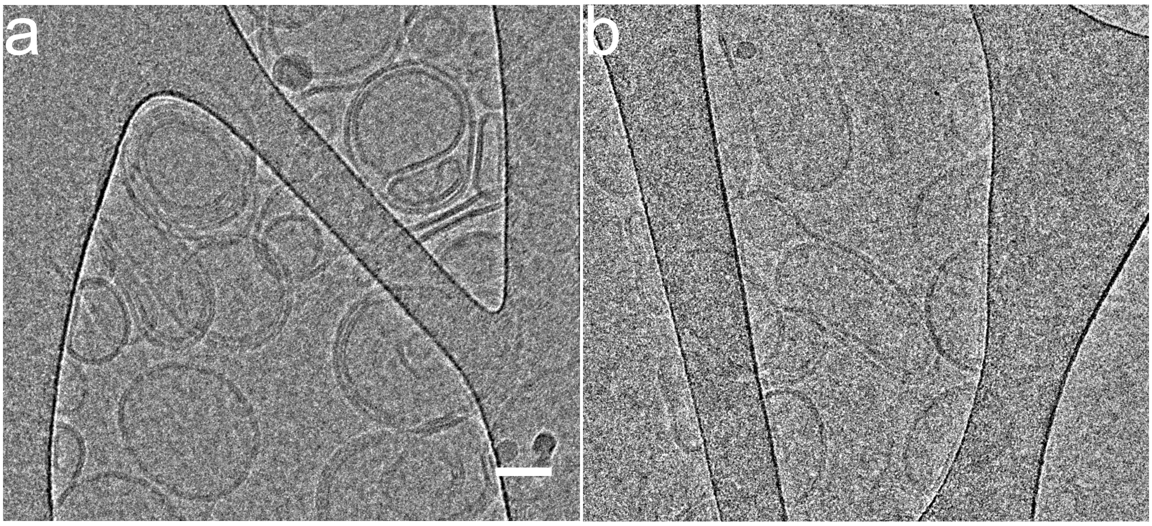

Figure 6.3: Cryo-TEM images of DOPC-liposomes incubated with polymer PP50 at a) pH 5.5 and b) pH 7.5. Scale bar, 50 nm.

Fig 6.4 shows liposomes formed in polymer solution at pH 7.5. The liposomes display standard morphology with no detectable changes in membrane structure, which indicates no disruption of membrane structure at the presented length scale. On the other hand, CryoTEM images of liposomes prepared by hydration with polymer at pH 5.5 show large material aggregates (Figure 6.5) together with portions of intact vesicles (as indicated by black arrows).

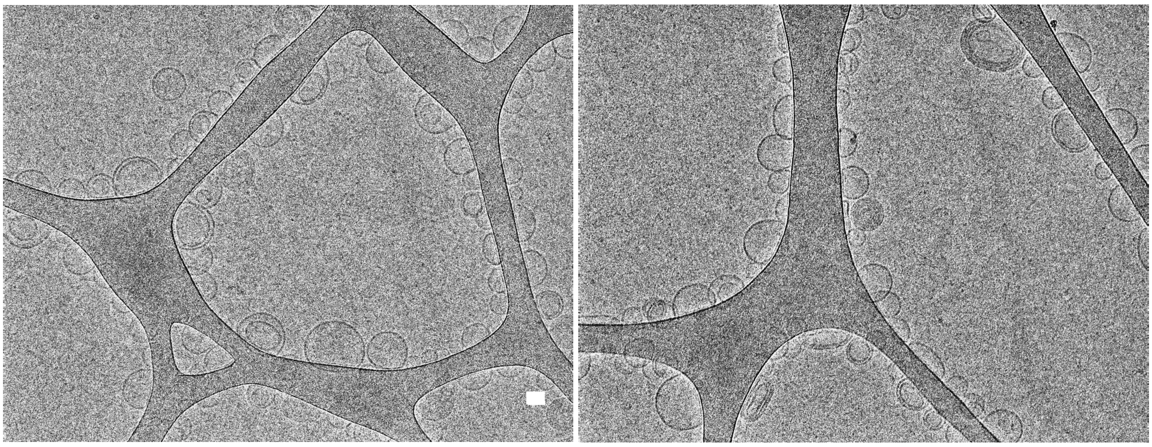

Figure 6.4: Cryo-TEM images of DOPC-LUVS (1.5 mg/ml) prepared by hydration with polymer solution at pH 7.5 (3 mg/ml). Scale bar, 50 nm.

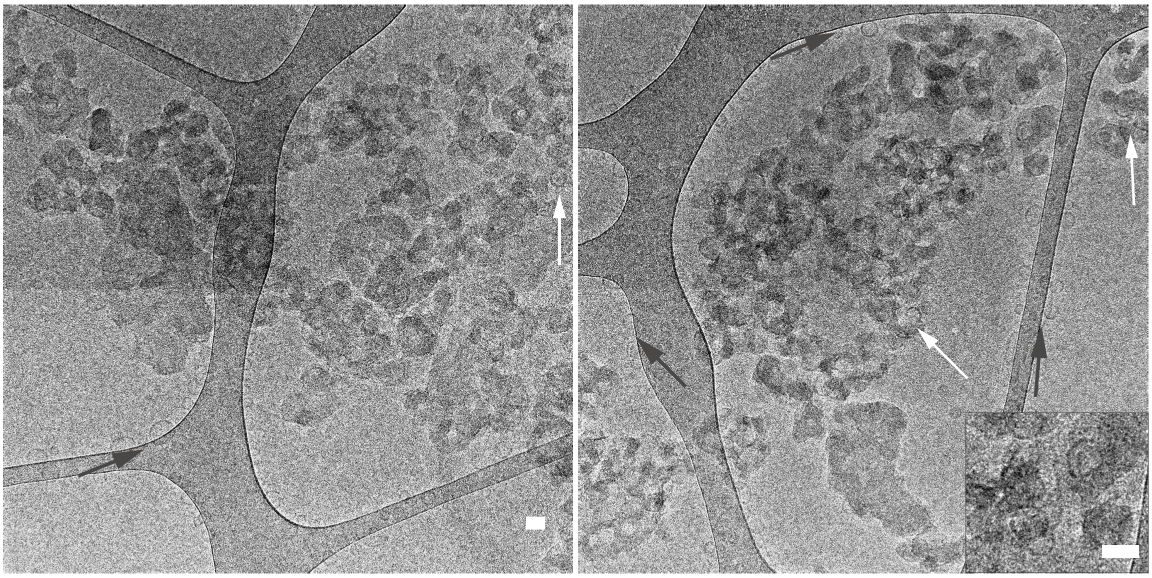

Figure 6.5: Cryo-TEM images of DOPC-LUVS prepared by hydration with polymer solution at pH 5.5 (3 mg/ml). The vesicles interacting with PP50 are indicated by white arrows. Black arrows show intact vesicles. Inset shows zoomed-in images of lipids/PP50 aggravates with portion of bilayer. Scale bar, 50 nm.

To fully check whether the presence of the observed clusters is really due to the presence of polymer/lipid aggregates under acidic pH conditions, rather than to sample preparation, we used the LUVs/PP50 samples formed at pH 7.5 (Figure 6.4) and rapidly decreased the pH of the sample by adding HCl. Figure 6.6 presents a set of Cryo-TEM images which were acquired immediately after the drop of pH in the sample.

The images show similar aggregates to the ones observed in Figure 6.5, however the disruption of liposomes appear to be more pronounced. The Cryo-TEM images reveal a small number of intact vesicles, indicating that a change of pH from physiological to acidic has a higher effect on the membrane-lytic properties of polymer than in the system where polymer/liposome system is directly prepared in pH 5.5. We argue that observed difference can be explained by the localization of the polymer at pH 7.5. In physiological conditions, we expect PP50 to occupy the water/lipid interface, with no influence on the membrane structure. Upon rapid acidification, the polymer becomes hydrophobic, which triggers its membrane-lytic properties. In the case of a system prepared directly in pH 5.5 the polymer is already in a globular state, which might have consequences on its transfer towards the lipid membrane.

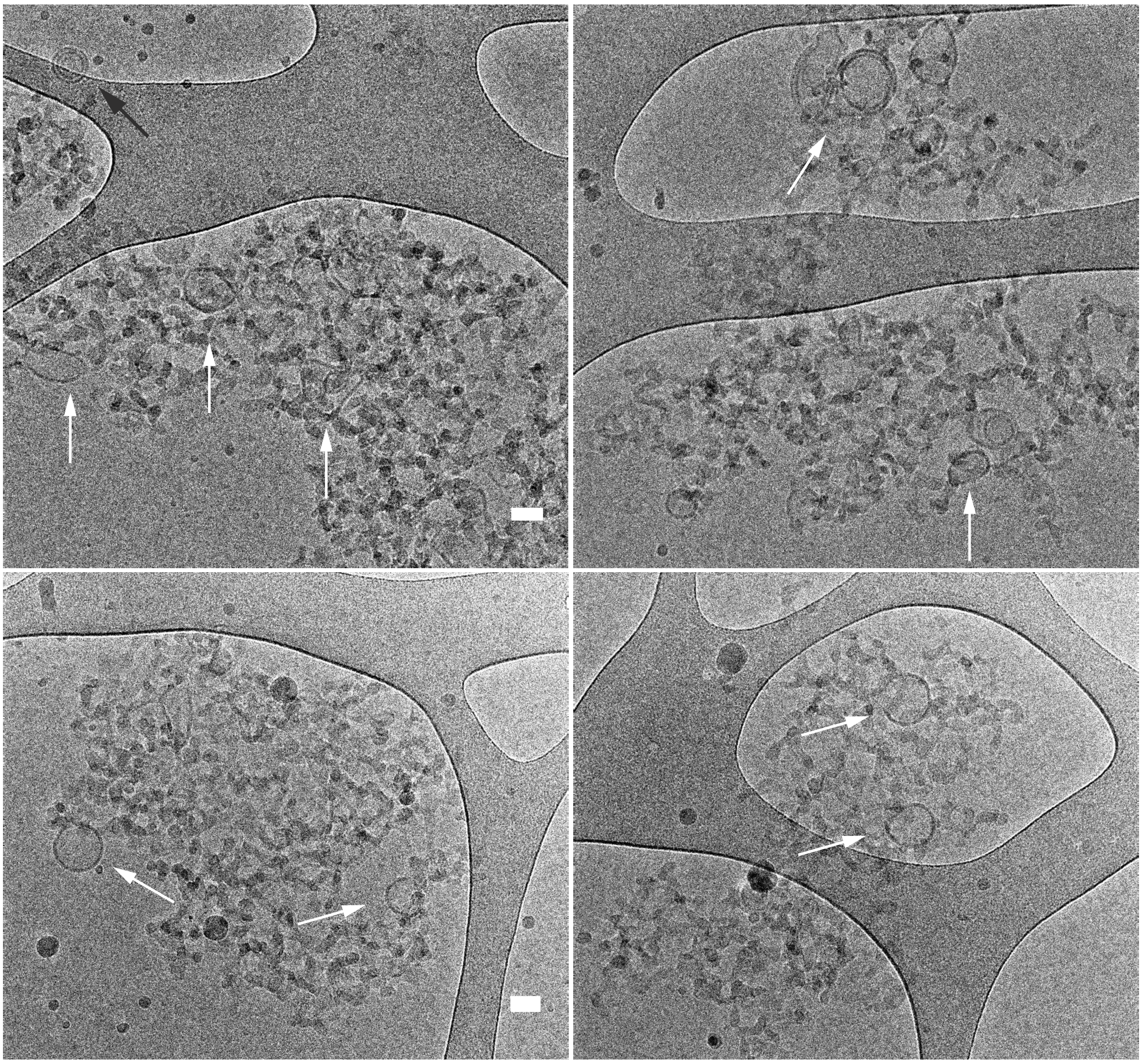

Figure 6.6: DOPC-LUVs/PP50 system after addition of HCl. The vesicles interacting with PP50 are indicated by white arrows. Black arrows show intact vesicles. Scale bar, 50 nm.

6.2.1.2 Effect of the polymer on the lipid phase transition

To further assess the mechanism of membrane disruption upon interaction with PP50, we performed differential scanning calorimetry measurements. The rationale of these experiments is that the intimate association of a polymer inserted in the hydrophobic bilayer core with the phospholipid tails should give rise to changes in the DSC thermograms at the vicinity of the main transition temperature, such as a shift in the melting temperature, a widening of the measured specific heat or a change in the enthalpy of melting. As DOPC bilayers are fluid above -20°C, this approach requires to select a phospholipid with a melting temperature closer to experimentally accessible values. In the following set of experiments, we used DPPC, with all the preparation steps performed in the high temperature fluid phase (cf Material and Methods).

We followed an approach similar to the Cryo-TEM experiments, by first analyzing systems of DPPC liposomes incubated for 60 min with the polymer. Fig 6.7 shows the DSC curves for DPPC vesicles incubated with PP50 for a wide range of pHs. All curves appear sharp with the same value of the transition temperature (T_m) and similar intensities. At pH 7.5 the curve presents a wide high temperature shoulder, centered around 42°C. The secondary contribution gradually disappears with more acidic pH, with almost no trace at pH 5.3 (Fig. 6.8).

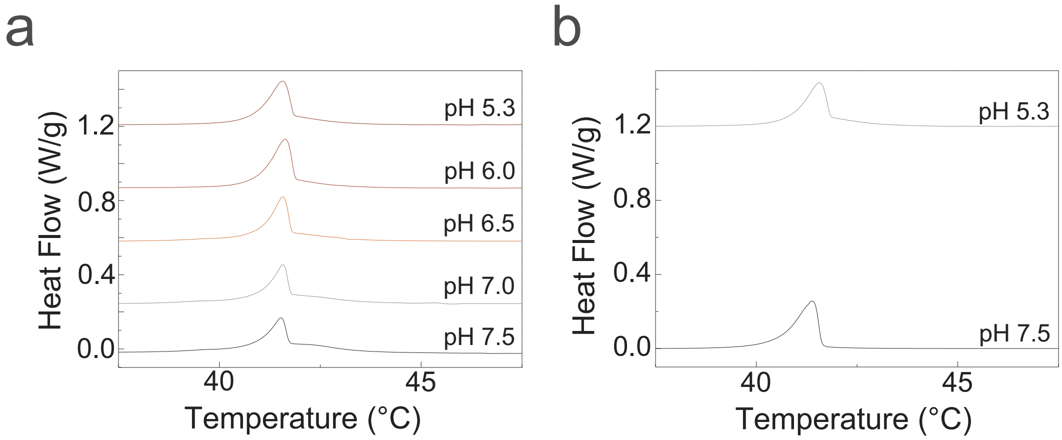

Figure 6.7: Exemplary DSC thermograms of a) DPPC-liposomes (10 mg/ml) incubated with 20 mg/mL of PP50 b) DPPC-LUVs at various pH.

The determination of the enthalpy of melting ΔH and the main transition temperature T_m were carried out for all the curves and are summarized in Fig 6.7. For pure DPPC systems at pH 7.5 and 5.3 the enthalpy change and T_m are consistent, and the values show good agreement with those reported by other authors [293, 294]. Moreover, the values of the enthalpy difference are in line for both measured pH, suggesting no appreciable changes in the transition between the two pH conditions. It is worth noting the high temperature shoulder is not observed in pure systems, whatever pH value is considered.

In all the measured pH conditions, the incubation of liposomes with PP50 do not influence the value of the transition temperature (41.5 ± 0.3°C). Similarly, the enthalpy jumps at all pHs are within error bar similar (33.3 ± 1.8 kJ/mol). This result are consistent with the Cryo-TEM investigations which cannot distinguish among vesicles incubated at pH 7.5 or 5.5.

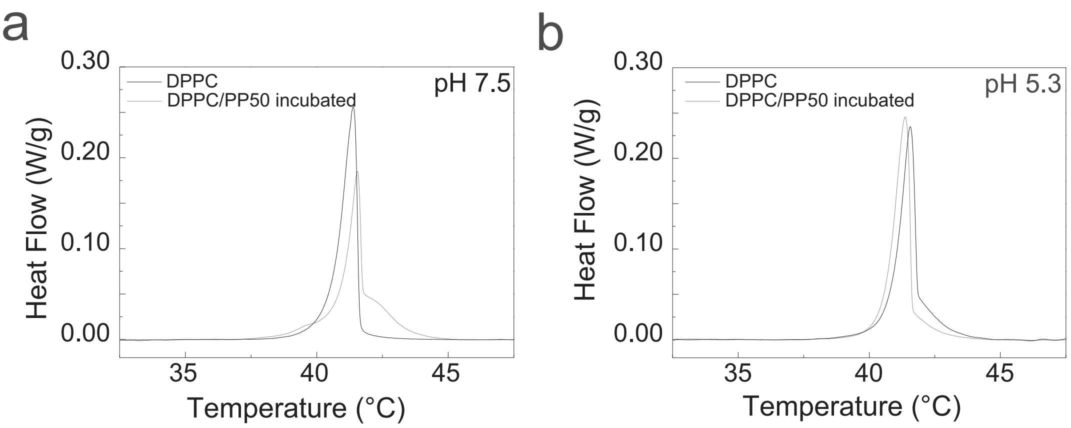

Figure 6.8: Exemplary DSC thermograms of liposomes incubated with 20 mg/mL of PP50 at a) pH 7.5 and b) pH 5.3.

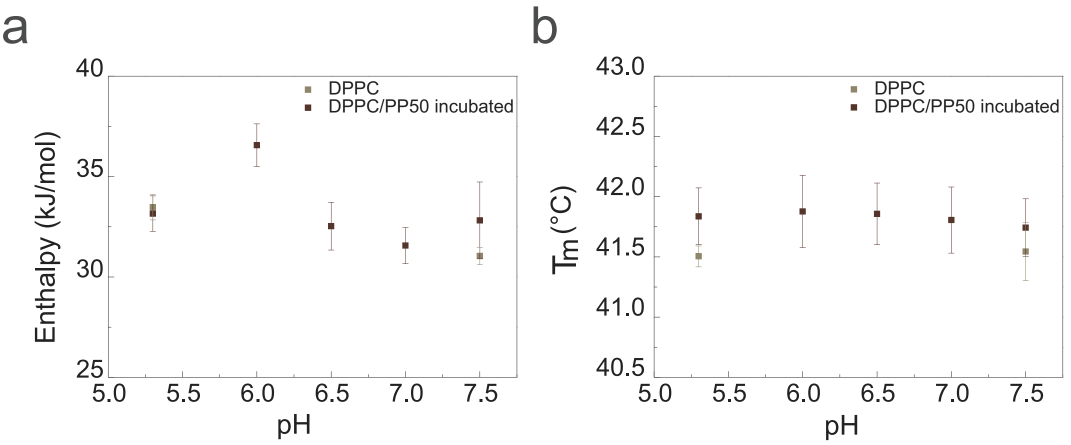

Figure 6.9: Calculated a) enthalpy and b) transition temperature (T_m) of pure DPPC system and DPPC-LUVs incubated with PP50 at various pH. Error bars are estimated on the standard deviation of 6 DSC runs.

Based on our Cryo-TEM observations, where it was shown that the preparation of the DOPC/PP50 sample plays a key role in determining the level of membrane disruption, we analyzed the phase behavior of LUVs prepared by hydration with the polymer solution. Figure 6.10 presents the DSC scans for pure DPPC-LUVs solution and LUVs prepared in polymer solution at pH 7.5 and 5.3.

At pH 7.5 the curve of DPPC/PP50 system is centered at 41.5 ± 0.2°C, with a measured enthalpy variation of 33.3 ± 1.8 kJ/mol, which is agreement with DSC measurements of pure DPPC-LUVs. The signal however is much broader for incubated DPPC compared to pure DPPC sample (Fig 6.10). The signal for the liposomes prepared in PP50 displays a bimodal signature, one sharp component being similar to the pure DPPC curve, and one component superimposed to the incubated DPPC curve, visible as a broad shoulder in the high temperature side of the peak (Fig. 6.12).

Since the calculated values of the enthalpy jump and T_m are close to the ones obtained for pure DPPC-LUVs (Fig. 6.11), we can assume that a total melting of the lipid chains is occurring in all cases, and that the observed broadening of the specific heat curve is caused by the interaction with PP50. As previously reported by Cater *et al.* [295], small amounts of drug molecules can affect the long-range organization in the bilayer structure of both the lipid chains and the polar groups. As a result, the adsorption of hydrophilic molecules at the membrane surface can reduce the cooperativity of the gel-to-liquid transition, which correlates to a widening of the transition over a larger temperature interval.

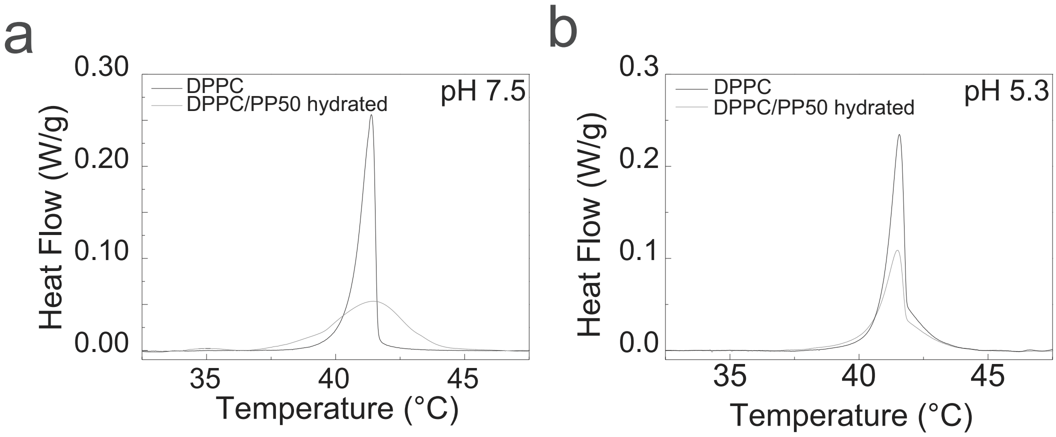

Figure 6.10: Exemplary DSC curves of blank and liposomes formed in PP50 solution at a) pH 7.5 and b) pH 5.3.

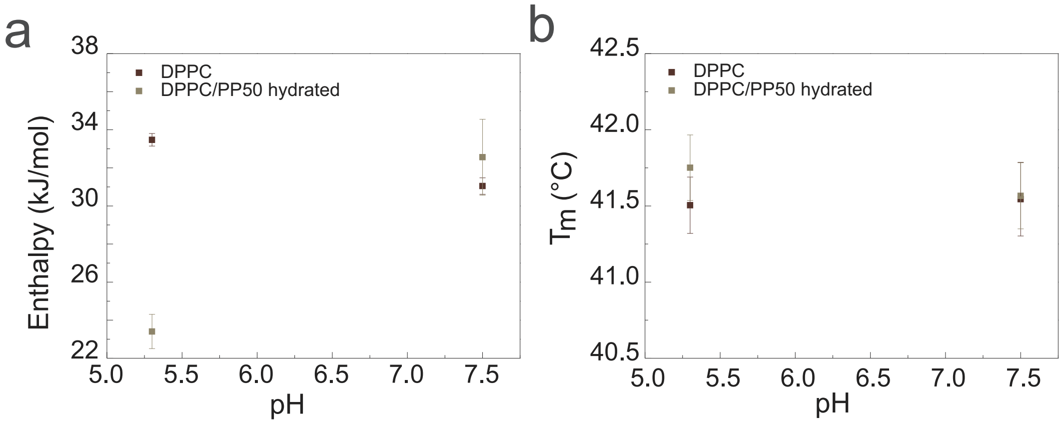

Figure 6.11: Calculated a) enthalpy and b) transition temperature (T_m) for pure DPPC-LUVs and liposomes formed in PP50 solution at various pH. Error bars are estimated on the standard deviation of 6 DSC runs.

On the other hand the formation of liposomes in polymer solution under acidic conditions results in a significant reduction of the measured enthalpy of melting, equal to 23.4 ± 0.1 kJ/mol, whereas the peak position T_m does not change appreciably. The transition peak remains sharp, similar to pure DPPC system at the same pH (Fig 6.10b).

It has been reported that the incorporation of hydrophobic polymer within a lipid bilayer tend to lower the transition temperature of the phase transition by facilitating the lipid expansion [296]. The phase transition temperature can be affected by the presence of 'impurity' molecules in an analogous way to that exhibited by water or liquid when an added solute lowers the freezing point. In our case however T_m remains unchanged. As a rule, it is very difficult to change the enthalpy ΔH and entropy of melting ΔS of a first order thermodynamic transition without changing significantly the coexistence temperature $\Delta H/\Delta S$. In the present case, our observations are better accounted for by postulating that the transition at pH 5.3 is similar to the one at pH 7.5, but acting on a smaller amount of lipid bilayer material. Therefore, we rather assume that the polymer destroys or prevents the formation of vesicles, and reduce the amount of lipid bilayer present in the sample. This is consistent with the Cryo-TEM images where less vesicles are visible. As a corollary, there must be some amount of lipid material found in a different, non bilayer form, due to the strong interaction with PP50. This nonlamellar lipid-PP50 material does not seem to give rise to a thermodynamic melting signal in the expected range of transition temperature.

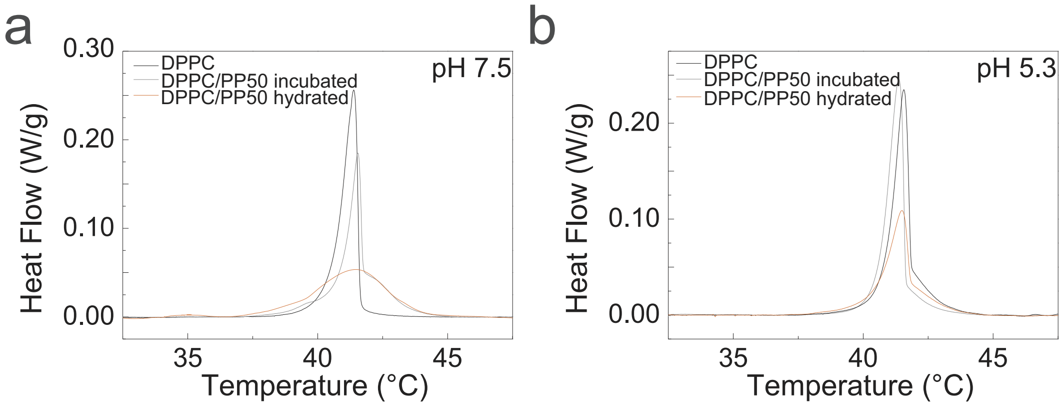

Figure 6.12: Comparison of exemplary DSC curves of pure DPPC-LUVs, liposomes incubated with PP50 (DPPC/50) and liposomes formed in PP50 solution (DPPC in PP50) at a) pH 7.5 b) pH 5.3.

Comparison of the DSC curves of two systems, DPPC incubated with polymer and DPPC-LUVs prepared in PP50 solution, provides information on the interaction between polymer and the lipid bilayer. At physiological pH the DSC profile for DPPC hydrated in PP50 shows a broad peak, whereas for the second system the transition remains sharp with a high temperature shoulder (Fig. 6.12). The differences in the two profiles can be explained in terms of accessible membrane surface to the polymer. When liposomes are directly hydrated with PP50, the polymer is also present in the inner volume of the vesicles, therefore can interact with both leaflets of the membrane and the effect is more prominent. In case of liposomes incubated with PP50, only the outer membrane is available and the alteration of the transition is thus lower.

Under acidic pH condition, the difference between hydrated and incubated systems is mainly the integrated enthalpy jump at the transition (Fig. 6.13), as both peaks show the same sharp profile. We argue that accessibility of the membrane plays a significant role in explaining these differences. In the case of liposomes incubated with PP50, the polymer does not interact significantly with the membrane due to its hydrophobicity and large size, therefore the transition is not affected by the presence of the polymer. For liposomes hydrated with PP50 at pH 5.3, on the other hand, the formation of vesicles is inhibited by the polymer which can aggregate with lipid molecules and reduce the total amount of lipid bilayer participating in the transition. This assumption is further strengthened by the pH drop experiment performed with Cryo-TEM, which shows that if the polymer has access to the membrane surface, the conformational change can greatly disrupt the lipid bilayer.

At pH 5.3 the membrane is unaltered when the polymer is added to already formed liposomes, but the enthalpy change of the transition is greatly affected in systems where liposomes are formed within a PP50 solution. Therefore the hydrophobic conformation of polymer disrupts the formation of lamellar structure.

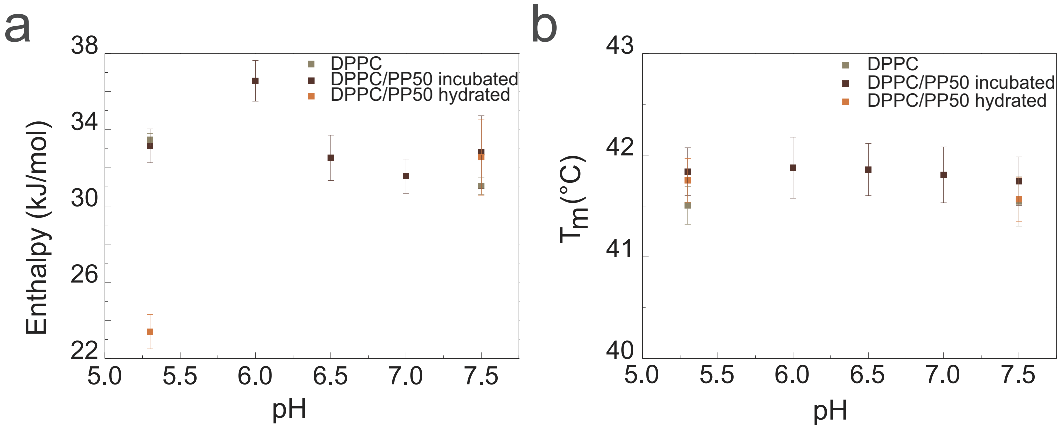

Figure 6.13: Summary of calculated a) enthalpy and b) transition temperature for pure DPPC-liposomes, liposomes incubated with PP50, and liposomes formed in PP50 solution for all measured pH. Error bars are estimated on the standard deviation of 6 DSC runs.

6.2.1.3 Small angle scattering studies of the interaction between liposomes and PP50

In order to understand in detail the effect of the polymer on the lipid membrane structure, we performed small angle neutron scattering measurements on relatively diluted LUVs systems composed of DOPC, DOPC/Chol and d_{31}POPC. To increase the contrast of the hydrogenated lipid molecules with the solvent, DOPC and DOPC/Chol LUVs suspension were prepared in a D_2O solution. This approach was previously employed to study the effect of cholesterol [297, 298] or styrene [299] on the lipid bilayer structure. To gain knowledge on the localization of the polymer in the liposomal suspension, we additionally performed SANS experiments using partially deuterated lipids, d_{31}POPC, which were re-suspended in H_2O. The reason for working with this POPC was that perdeuterated DOPC molecules were not commercially available.

The combination of various contrast should allow to better understand changes in the membrane structure upon interaction, as well as to determine the distribution of the polymer at the lipid/membrane interface. A full analysis of the experimental data is currently pursued. In this paragraph, we show preliminary results.

The absolute scattering intensity $I(q)$ as a function of the scattering vector modulus $q = 4\pi sin(\theta)/\lambda$ of the pure PP50 solution depending on pH is represented in Figure 6.14. The curves reveal variations in the polymer conformation and aggregation state upon changing the pH. The obtained raw data were fitted to a Gaussian model using the SasView Software. As expected, the highest radius of gyration, R_g = 221 Å, is observed for a pH corresponding to the known pKa (i.e. 6.5) of the polymer, while for pH 7.5 R_g shows the lowest value of 56 Å.

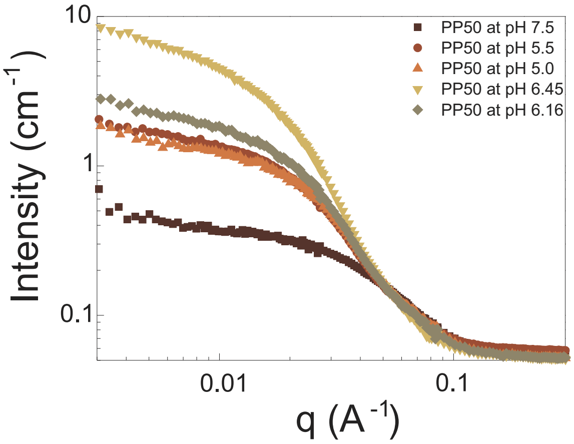

Figure 6.14: SANS raw data of pure polymer PP50 (3 mg/ml) in D_2O measured at various pH.

The scattering curves of LUVs (1.5mg/ml) incubated with 3 mg/mL PP50 solutions at various pH are presented in Figure 6.14. For clarity, we present curves for pH 7.5 and 5.5 only. The full SANS spectra of all studied pH can be found in Figure C.2 at page 135.

Figure 6.15 shows that all measured samples display similar scattering profiles: a flat Guinier regime (low q), a characteristic intermediate regime with q^{-4} dependence, ending with flat scattering decay at large q. The results are consistent with a spherical morphology of the scattering objects and are in line with data reported before [31, 300, 301]. The intensity in the intermediate regime in all measured samples depends on pH (Figure 6.14). This results suggest that the presence of the polymer, even at physiological pH, is visible in the bilayer structure.

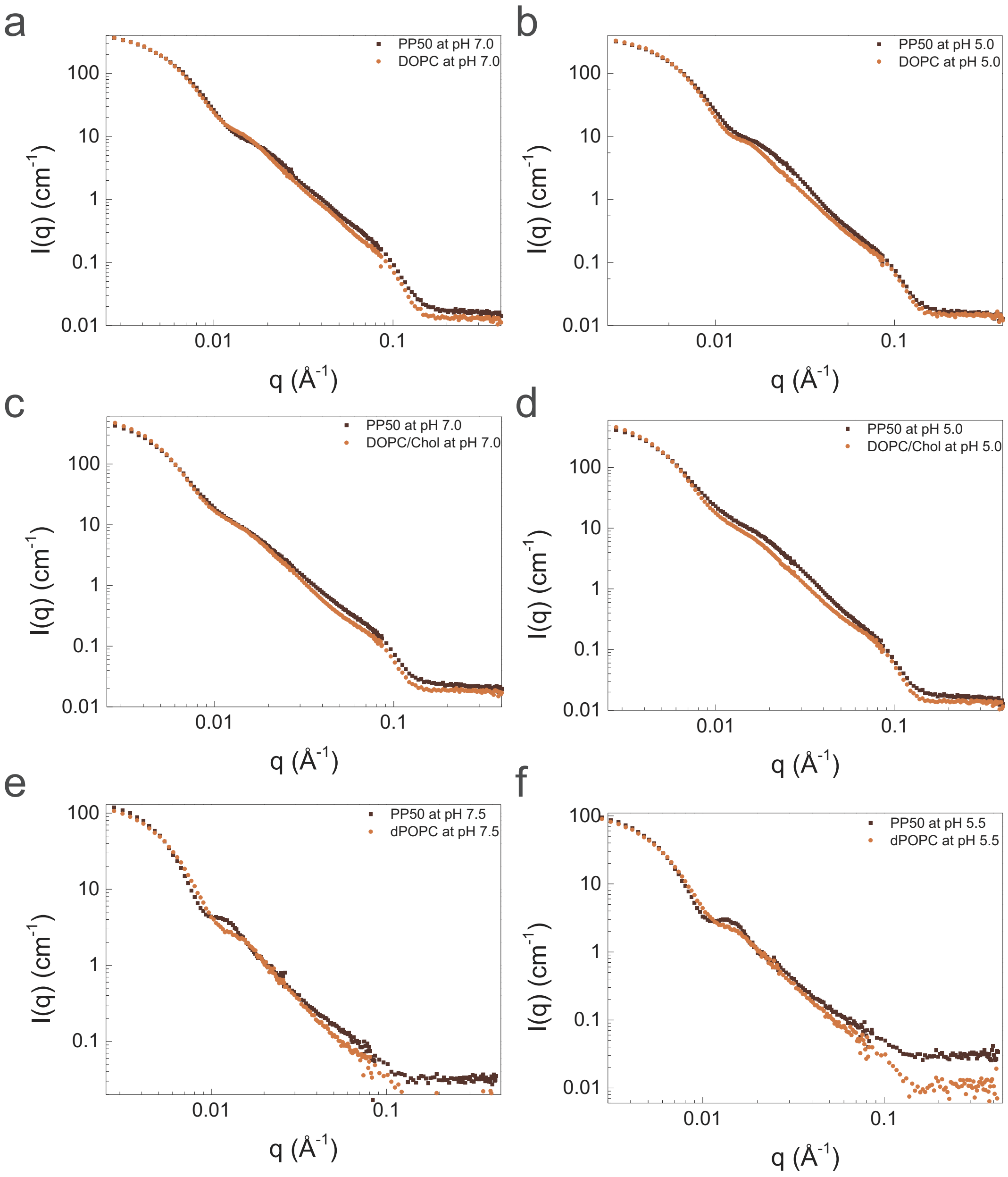

Figure 6.15: Comparison of SANS curves for LUVs and LUVs/PP50 system for a) DOPC at pH 7.5 b) DOPC at pH 5.5 c) DOPC/Chol at pH 7.5 d) DOPC/Chol at pH 5.5 e) d_{31}POPC at pH 7.5 and f) d_{31}POPC at pH 5.5.

6.2.2 Conclusion

We performed a set of experiments involving three types of samples under at least two pH conditions. The three types of samples are *i)* pure phospholipids (control), *ii)* phospholipids incubated with PP50 polymer after the formation of the vesicles, *iii)* phospholipid vesicles prepared in the presence of PP50 (Figure 6.16). Cryo-TEM and DSC experiments were done on the three types of samples, while SANS experiments involved only the pure and the incubated samples.

The combined results of the three techniques are consistent. We found that pH changes were not, only little effective in disrupting the membrane structure in the case of the incubated samples. Alternatively, PP50 prevents the formation of vesicles (LUVs) under acidic condition, with the evidence of lipid-PP50 piece of material not forming a bilayer structure. The lipid bilayer obtained when preparing the vesicles in the presence of the polymer at pH 7.5 is massively disrupted when the pH is lowered by the addition of HCl solution.

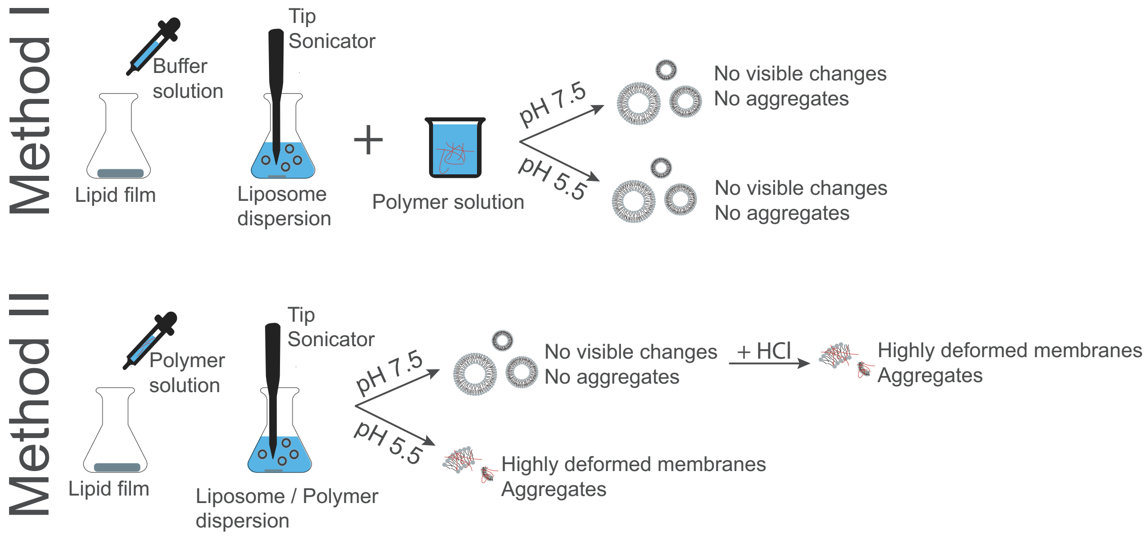

Figure 6.16: Scheme representing the two methods of sample preparation used: Method I - Incubation of polymer with liposome dispersion; Method II - Hydration of lipid film with polymer solution.

We conclude that the capacity of the PP50 polymer to interact with the lipid bilayer depends on the preparation method. Under acidic conditions, the polymers is likely to be found as rather large aggregates with low solubility, and 1h of incubation time does not allow it to find its way to the lipid bilayer, in spite of its strong disruptive power. When the preparation method brings the polymer in contact to the lipid prior to vesicle formation, the disruptive power of PP50 is then very effective.

The nature of the lipid-polymer mixture at low pH is unknown and deserves to be investigated in the future.

6.2.3 Materials and methods

Materials

Chloroform solution of DOPC (1,2-dioleoyl-sn-glycero-3-phosphocholine, $C_{44}H_{84}NO_8P$, M_w 786.11), DPPC (1,2-dipalmitoyl-sn-glycero-3-phosphocholine, $C_{40}H_{80}NO_8P$, M_w 734.039), Cholesterol (cholesterol, ovine wool, $C_{27}H_{46}O$, M_w 386.654) and d_{31}POPC (1-palmitoyl-d31-2-oleoyl-sn-glycero-3-phosphocholine, $C_{42}H_{51}NO_8PD_{31}$, M_w 7791.267) was purchased from Avanti Polar Lipid (Birmingham, AL). HEPES ($C_8H_{18}N_2O_4S$ M_w 238.30), Trisodium citrate dihydrate ($HOC(COONa)(CHC_2COONa)_2$ M_w 294.10) and Citric acid ($HOC(COOH)(CH_2COOH)_2$ M_w 192.12) were purchased from Sigma-Aldrich (Saint-Quentin, France). All chemicals had high purity and were used without further purification.

Large unilamelar vesicles (LUVs)

A defined amount of lipids in chloroform was transferred to the vial, and organic solvent was evaporated using an argon stream until completely dried followed by 8h of vacuum pumping. The lipid film was then hydrated above phase transition, with appropriate buffer or polymer solution (HEPES or Citrate buffer) and gently vortexed.

Liposomes for Cryo-TEM measurements: Resulting MLVs suspension was subjected to radiation using titanium-tip sonicator (Bioblock VibraCell 72412) at 30% amplitude for 15 min total time at 1 s on/off cycle to prevent overheating.

Liposomes for SANS measurements: The MLVs suspension was extruded using an Avanti Mini-Extruder. The sample was first extruded 21 times through 200 nm, subsequently 21 times through 100 nm and finally 21 times through 50 nm diameter pore polycarbonate filters.

Multilamellar vesicles (MLVs)

A dispersion of MLVs of DPPC was used for DSC measurements. A defined amount of lipid in chloroform was transferred to a glass vial, and the organic solvent was evaporated using an argon stream followed by 8h of vacuum pumping. The lipid film was then hydrated with buffer solution (HEPES or Citrate buffer) at 70°C. The resulting MLVs suspension was placed in a bath sonicator for 15 min above the main phase transition (41°C) to disperse larger aggregates.

Polymer (PP50) solution

The appropriate amount of polymer PP50 was dissolved into HEPES buffer solution (20 mM, NaCl 150 mM) or Citrate buffer (100 mM) and left overnight on lab shaker, prior to use. For SANS experiments, the polymer solutions were prepared in D_2O.

Cryo-transmission electron microscopy (Cryo-TEM)

A laboratory-build humidity-controlled vitrification system was used to prepare the samples for Cryo-TEM. Humidity was kept close to 80% for all experiments and the temperature was set at 22°C. A 5 μL of the sample was placed onto lacey carbon film covered grid (Ted Pella) rendered hydrophilic via glow discharge (Elmo, Cordouan Technologies). Excess sample was removed by blotting with filter paper and the sample grid was vitrified by rapid plunging into liquid ethane

(-180°C). The grids were kept in liquid nitrogen before being transferred into a Gatan 626 Cryoholder. Cryo-TEM imaging was performed on FEI Tecnai G2 TEM (200kV) under low dose conditions with an Eagle slow scan CCD camera. Cryo-TEM Images analysis was performed by ImageJ software (NIH, USA). The error in the determination of the membrane thickness from Cryo-TEM images analysis was estimated at ±5%.

Differential scanning calorimetry (DSC)

The impact of the polymer PP50 on the thermal properties of lipid membranes was estimated using differential scanning calorimetry (DSC). The measurements were performed with a high sensitivity differential scanning calorimeter (DSC Setaram) and volume of twin cells was 0.5 mL each. The measuring cell was filled with the analyzed sample (MLVs, with or without polymer PP50), while the reference cell was filled with the same buffer as used for preparation of the samples. The temperature of the cells was changed with a constant rate (heating rate: 0.5 K/min, cooling rate: 0.3 K/min). Differences in the heat uptake between the sample and the reference cell provided direct information about the energy of thermally-induced processes in the sample. The analysis of DSC data was performed using OriginPro 9.0 (Northampton, Ma, USA).

Small angle neutron scattering (SANS)

The samples were mounted in a 2 mm thick quartz cuvettes (Hellma). The small angle neutron scattering data were collected on the beam line D11 at the Institut Laue-Langevin (ILL) in Grenoble., France The DOPC and DOPC/Chol samples were prepared in D_2O while, d_{31}POPC (one deuterated chain) in H_2O to provide maximal contrast in scattering length density across the bilayer profile. The neutron wavelength resolution was $2 \cdot \Delta\lambda/\lambda = 0.1$. All scattering data were corrected for background, and incoherent scattering from 1 mm thick D_2O or H_2O solutions were used to correct for the deviation in uniformity of the detector response. The final data were converted to absolute scale. All experiments were performed at room temperature (25°C).

7 | Concluding remarks

In order to improve the therapeutic effect of a drug, a great deal of research is currently being conducted to develop drug delivery systems that are meant to facilitate the transport of a pharmaceutical compound in the human body. Amongst these systems, agents able to interact and modify the properties of lipid membranes are of particular importance, as membranes are critical structural and functional elements in all living cells. At the same time however, too drastic modifications of a membrane might lead to toxic effects of a given delivery system. A better understanding of interactions between the carrier and the membrane will enable the intelligent design of novel materials, ultimately paving the way for more efficient and safer therapeutic interventions.

In this PhD project, we have successfully studied different aspects of the interaction between nanocarriers and model lipid membranes. The area of our investigation was focused on two different nanocarriers, namely α-cyclodextrin and pH-sensitive polymer (PP50). In all instances, our studies provided deep insights, at nanoscale resolution, into the mechanism of action of the nanocarriers in model membrane system. The major part of this thesis contributes to the understanding of the behaviour of α-cyclodextrin in a model membrane, together with its detailed thermodynamic description. The novelty of this work is based on a combination of multidisciplinary techniques, which together provide a thorough exploration of the α-cyclodextrin / membrane interactions.

The studies on α-cyclodextrin were divided into two subprojects. As first we evaluated the effect of α-cyclodextrin on planar membrane objects i.e giant unilamellar vesicles and supported lipid bilayers. By coupling information obtained from confocal microscopy and quartz crystal microbalance, we investigated and visualized pore formation in supported lipid membranes caused by the presence of α-cyclodextrins The results provided a quantitative kinetic description of the lipid extraction process. Furthermore, we explored the effect of α-cyclodextrin on a individual giant unilamellar vesicles (GUVs). We observed a shrinking of the vesicle upon its interaction with α-cyclodextrin. Moreover, the analysis of the translocation of a fluorescent dye upon lipid extraction confirmed the pore formation observed in supported lipid bilayers. We also recognized a novel structural perturbation at the membrane surface upon addition of α-cyclodextrin. For the first time, we reported the 3D structures formed on both Supported lipid bilayer and GUV surfaces. Thus we propose that the formation of these membrane/CD complexes is a major driving force for the pore formation and the final membrane disruption. Secondly, we explored the ability of α-cyclodextrin to extract lipids in highly curved small unilamellar vesicle systems. Using the Cryo-TEM technique we studied time-evolution of changes in membrane structure upon interaction. We demonstrated that α-cyclodextrin causes vesicle fusion and structural deformation of the membrane.

Moreover, we attempted to unravel the α-cyclodextrin mechanism of action at the nanoscopic scale. Using isothermal titration calorimetry, we measured the free energy of the interactions, together with its enthalpic and entropic contributions. We also demonstrated the temperature-dependence of the process. Lastly, we attempted to decipher the complex formation between single α-cyclodextrin molecule and lipids. Using scanning electron microscopy together with small angle x-ray scattering technique, we demonstrated the α-cyclodextrin/lipids form crystals with compact crystalline structure, and well-defined morphology. To conclude, the α-cyclodextrin has been known for more than sixty years, and there are still open questions regarding, for instance, the mechanism of lipid extraction and complexation. Our work presented in this thesis provided several novels exciting insights and suggested new research directions that will be undoubtedly pursued in the years to come.

The second focus of this PhD project was on the investigation of the behaviour of the pH-responsive polymer (PP50) in model lipid systems. PP50 and its derivatives have been intensively studied within our cross-institutional ITN-SNAL network. Previously, our collaborators has shown that PP50 indeed increased the permeability of lipid membrane to its payload. Interaction of PP50 with red blood cells (RBC) enhanced the loading of the impermeable sugar trehalose in the cytosol of cells, with a consequent increase of the viability of RBCs during cryopreservation. In order to fully understand the molecular mechanisms of these phenomena, we have started our own biophysical investigations of PP50's interactions with model lipid membranes. By combining Cryo-TEM technique with Small angle X-ray Scattering technique, we have explored how the physicochemical properties of PP50 vary in solutions with different pH values, and, therefore, how pH affects the polymer ability to locally perturb the internal structure of cubosomes. The demonstrated effectiveness of PP50 to interact with lipid membrane motivated us to study the pH-sensitive feature of PP50 in a model liposomal system. Our first attempt, involving simple incubation of polymer with lipid vesicles, showed that PP50 at both neutral and acidic pHs had minor effects on the lipid membrane. Concretely, Cryo-Tem visualizations demonstrated no changes in the membrane structure, nor in the number of lipid vesicles. We, therefore, cross-validated the results of Cryo-TEM and differential scanning calorimetry (DSC) using more invasive sample preparation (sonication in the presence of polymer). We were surprised, as the studies confirmed that sample preparation plays a significant role in enhancing interactions of the polymer with the lipid membrane.

We conclude that further studies involving the analysis of the mechanism by which PP50 disrupts the lipid bilayer, are needed to fully understand membrane-lytic properties of the polymer. By applying Small angle neutron scattering technique, together with GUVs analysis, we hope to obtain an exhaustive picture of PP50 / membrane interactions.

8 | Résumé de thèse en français

Au cours des dernières décennies, les chercheurs ont accompli de nombreux efforts pour améliorer la sécurité ainsi que maximiser l'efficacité des traitements médicamenteux. L'un des principaux obstacles que les vecteurs de médicaments rencontrent pour atteindre les compartiments cellulaires cibles est leur pénétration limitée à travers les membranes biologiques, en raison de leurs propriétés physico-chimiques telles qu'une mauvaise solubilité dans l'eau, ou un temps de demi-vie de circulation trop court. Une grande variété de nanomatériaux (in)organiques est actuellement testée comme vecteurs de délivrance de médicaments, afin de protéger leur charge, c'est-à-dire le principe actif, d'une dégradation dans l'environnement physiologique et en facilitant simultanément leur transport au travers des membranes cellulaires.

Cette livraison au moyen de nanoparticules constitue une stratégie procurant un certain nombre d'avantages, tels qu'une solubilité améliorée des médicaments hydrophobes, une suppression de l'immunogénicité et des effets secondaires réduits, et permettant la libération de médicaments d'une manière controlée et déclenchable. À ce jour, *i)* liposomes *ii)* points quantiques *iii)* micelles polymériques *iv)* dendrimères *iv)* polymère-médicament conjugués et *vi)* les matériaux sensibles au pH ont émergé comme classes de systèmes de livraison à l'échelle nanométrique. Fait important, beaucoup d'entre eux ont déjà atteint l'étape des applications cliniques.

Malgré les nombreuses succès de ces systèmes, la connaissances sur les interactions entre les nanomatériaux et les membranes cellulaires sont encore insuffisantes. La perméation et le transport d'un nanomatériau à travers les membranes biologiques sont d'une importance cruciale pour déterminer la capacité des nanoparticules à atteindre leur cible cellulaire. Il est donc nécessaire de comprendre comment les nanoparticules interagissent avec une membrane cellulaire. Plus précisément, les questions de l'influence des nanomatériaux sur la structure locale et la composition de la bicouche lipide et les changements de propriétés physiques induits sont essentielles.

Dans ce contexte, les études biophysiques de systèmes modèles lipidiques sont incontournables pour comprendre les forces et les interactions entre membranes cellulaires et nanoparticules. La motivation de la présente étude est de gagner en compréhension sur le mécanisme d'action de plusieurs nanomatériaux avec des membranes biologiques et leur impact sur les propriétés physicochimiques de ces membranes. Nous nous concentrons sur la caractérisation des interactions de trois types de vecteurs potentiels de médicaments.

- Réorganisation des membranes lipidiques médiée par la présence de cyclodextrine-α. Nous étudions l'extraction des lipides de la membrane causée par ces cyclodextrines, un phénomène révélé pour la première fois par Debouzy en utilisant des globules rouges humains. Ceci est discuté au Chapitre 4.
- Caractérisation des cubosomes et de leur potentiel concernant l'administration contrôlée de médicaments. Notre objectif est ici de tirer profit d'un polymère sensible au pH pour concevoir un nouveau système cubosomal hôte-invité, avec un interrupteur de déclenchement activé par le pH, comme présenté au Chapitre 5.
- Translocation d'un polymère sensible au pH à travers une membrane imitant le lysozyme. Dans cette étude, nous nous sommes concentrés sur la façon dont le pH externe affecte la diffusion à travers la membrane lipidique d'un polymère stimuli-sensible, et comment la composition de la membrane dicte le mécanisme de ce processus. Les résultats de cette étude font l'objet du Chapitre 6.

Nous utilisons des techniques de visualisation (Cryo-TEM, SCLM), complétées par des méthodes de calorimétrie (ITC, DSC), de caractérisation de surface (QCM-D) et de diffusion de rayonnement (SANS, SAXS). À notre connaissance, la combinaison de ces techniques n'a fait l'objet que de peu de travaux publiés. Nous espérons donc apporter une contribution originale tant du point de vue fondamental qu'appliqué autour des interactions nanoparticule/membrane lipide et des systèmes de transport de médicaments en général.

Membrane cellulaire et bicouche lipide

La membrane cellulaire est un composant essentiel de toutes les cellules vivantes. Elle détermine les frontières entre l'intérieur de la cellule et l'environnement externe, et joue un rôle essentiel dans la protection cellulaire. De nombreux processus cellulaires importants, y compris le contrôle et le transport des nutriments, la reconnaissance moléculaire et la réponse immunologique ont lieu dans la membrane ou sont médiés par elle. Par conséquent, l'intégrité de la membrane et son bon fonctionnement sont d'une importance capitale pour une cellule saine.

De nombreuses propriétés physicochimiques critiques des membranes biologiques peuvent être capturées et comprises à partir d'études sur des bicouches lipides modèles, formées d'un nombre d'espèces lipides réduit. La bicouche lipide présente de nombreuses propriétés découlant des interactions coopératives entre les molécules qui la composent. Il s'agit d'une structure bidimensionnelle formée de deux feuillets accolés de molécules tête-bêche d'épaisseur nanométrique (5 nm), avec deux régions interfaciales et un coeur apolaire formé par des queues hydrocarbonées hydrophobes.

L'avantage de travailler avec des membranes modèles vient du contrôle de la composition, et donc de la complexité de la membrane, afin de mieux comprendre les processus conduisant à des interactions avec les nanomatériaux. De nombreuses applications médicales et pharmaceutiques de nanoobjets tels que la photothérapie, la bioimagerie et la délivrance de médicaments nécessitent un réglage fin des propriétés des nanoparticules pour une fonction donnée, et donc une compréhension détaillée et un contrôle des interactions nanoparticules avec une membrane cellulaire sont nécessaires.

Déformation de la membrane lors de l'interaction avec les cyclodextrines α

Les cyclodextrines (CD) sont des oligosaccharides cycliques formés par dégradation bactérienne de l'amidon, et contiennent typiquement six (α-CD), sept (β-CD) ou huit (γ-CD) unités de glucose (Fig. 8.1). Alors que le côté externe des CD est hydrophile, la cavité interne crée un microenvironnement hydrophobe. Cette caractéristique unique permet aux CD de piéger de manière réversible un large éventail de molécules invitées, et de rendre les molécules CD potentiellement candidates à la délivrance de médicaments et à la séquestration du cholestérol, parmi d'autres applications.

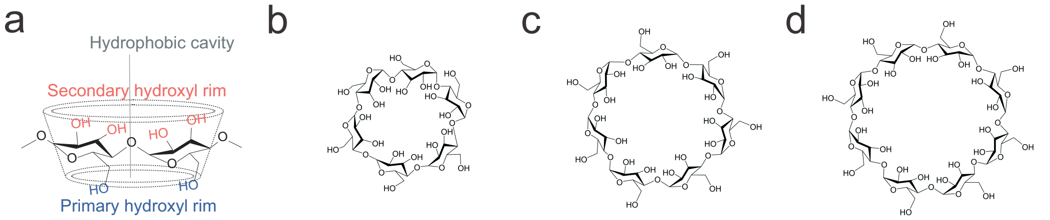

Figure 8.1: Structure chimique des cyclodextrines natives a) Structure 2D de la cyclodextrine montrant l'arrangement des monomères de glucose b) αCD c) βCD d) γCD.

Malgré de nombreux efforts, il manque toujours des données expérimentales et théoriques cohérentes sur le mécanisme d'interaction de la CD avec la membrane cellulaire et sa capacité à complexer les composants lipidiques. Puisque les changements dans l'organisation des lipides dans les membranes plasmiques peuvent modifier les fonctions cellulaires, il est d'une importance cruciale de traiter le phénomène de complexation lipide-CD. Notre objectif dans ce projet est de rendre compte du mécanisme de dégradation d'une bicouche modèle exposée à des concentrations croissantes de cyclodextrine α.

Pour commencer, nous avons évalué l'effet de la cyclodextrine sur les objets membranaires planaires ou peu courbés, comme les bicouches lipidiques supportées et les vésicules unilamellaires géantes composées de phospholipides zwitterioniques (DOPC). Les changements dans la structure des GUV exposés à des solutions de CD de concentrations variables ont été suivis en utilisant la microscopie de fluorescence et de transmission. À faible concentration de CD (5 mM), les vésicules semblent stables sur une échelle de temps de plusieurs heures. À des concentrations plus élevées, les vésicules rétrécissent tout en conservant leur forme sphérique et une intégrité apparente de la membrane (Fig. 8.2). En observant les vésicules individuelles, il semble que le rayon apparent (et non la surface) diminue linéairement avec le temps.

Le taux de réduction du rayon (en μm/s), lorsqu'il est mesurable, est extrêmement dépendant de la concentration. Un examen précis des images révèle la présence de taches lumineuses (fluorescence) ou sombres (transmission) avec une suspicion d'accumulation de matière à une échelle inférieure à la résolution optique. Le sort des lipides qui sont retirés de la surface des vésicules ne peut pas être déterminé sur une base de microscopie optique. Cependant, les indices obtenus par d'autres techniques (voir ci-dessous) suggèrent que les taches observées sur les surfaces des vésicules sont des agrégats croissants mixtes de lipides et de CD, et que leur croissance est la force motrice de la contraction des vésicules. Une combinaison de nucléation et de croissance d'agrégats pourrait expliquer la diminution linéaire en temps du rayon observée.

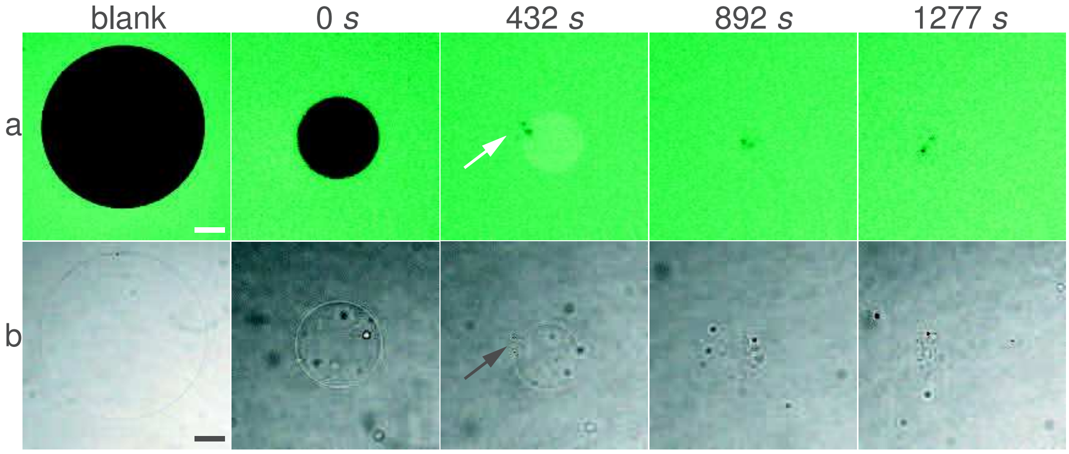

Figure 8.2: Évolution temporelle des vésicules unilamellaires géantes de DOPC interagissant avec une solution de concentration 10 mM de α-CD. a) Microscopie confocale à balayage laser de GUV dans une solution contenant le colorant hydrosoluble HPTS, b) Images de champ clair correspondantes. Les flèches montrent un agrégat anormal à la surface de la vésicule (taches brillantes et foncées, respectivement). Il y a un petit décalage de *ca* 3 min entre le debut du mélange GUV/α-CD et le début de l'acquisition de la microscopie. Barre d'échelle, 10 μm.

Pour confirmer ces observations, nous avons effectué deux études distinctes sur des bicouches lipides supportées formées de DOPC (SLB), par dépôt et fusion de petites vésicules. Tout d'abord, les SLB marquées par fluorescence, déposée sur des surfaces de verre, qui ont été suivies par microscopie de fluorescence.

Ces échantillons ont confirmé dans leur intégralité les deux observations sur les GUV concernant le rôle de la concentration de CD et la présence d'agrégats (taches) qui se nucléent de manière homogène et déclenchent la contraction du tapis de lipide et son retrait de la surface du verre (Fig. 8.3).

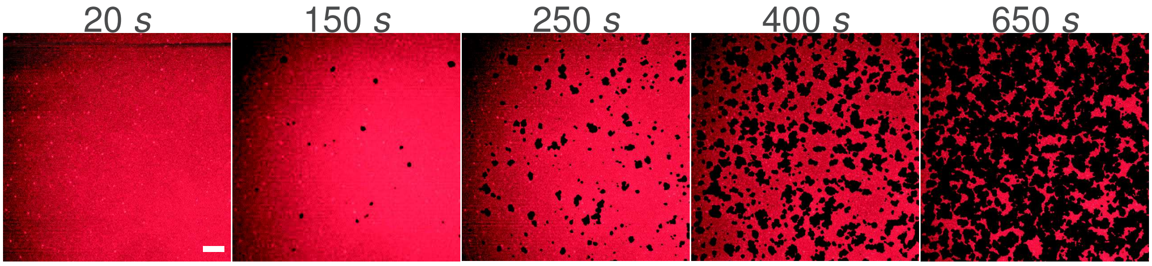

Figure 8.3: Evolution temporelle de la DOPC SLB marquée par fluorescence à une concentration de 15 mM αCD. Il y a un léger décalage de *ca* 3 min entre l'injection de αCD dans la chambre de mesure et le début de l'acquisition de la microscopie. Barre d'échelle, 10 μm.

Des mesures quantitatives ont pu être faites, tant pour le taux de nucléation que pour le nombre de lipides éliminés par seconde.

Deuxièmement, des bicouche supportées non marquées ont été déposées sur des surfaces de quartz résonantes pour des mesures de microbalance à quartz (QCM-D). Cette technique détermine précisément le poids du matériau adsorbé/désorbé. De plus, le signal déphasé fournit des informations sur la dissipation visqueuse dans la couche limite cisaillée. On observe un dépôt réversible de CD à faible concentration (5mM). En revanche, toutes les concentrations plus élevées conduisent à une élimination partielle (10 mM) ou totale des lipides (15 mM, 20 mM) de la surface. En couplant les informations obtenues à partir de la microscopie confocale et de la microbalance à cristaux de quartz, nous sommes en mesure de fournir une description cinétique quantitative du processus d'extraction des lipides. Pendant ce temps, la dissipation déphasée trahit la présence probable de membranes non confinées au-dessus de la surface, ce qui pourrait être une contrepartie des décorations floues observées par fluorescence sur les GUV.

Pour mieux comprendre le mécanisme disruptif membranaire des molécules de cyclodextrines, nous avons étudié l'action de ces molécules sur les lipides dans de petits systèmes de vésicules unilamellaires très courbés (SUV). Nos images Cryo-TEM révèlent que l'αCD est active à l'interface membrane/eau, en extrayant progressivement les composants lipides de la bicouche. Par conséquent, le déséquilibre qui en résulte entre les feuillets externe et interne favorise la fusion et le regroupement des vésicules. Avec l'augmentation du temps d'incubation, nous observons la présence de structures internalisées dans les vésicules, affichant des formes déformées. Pour des temps d'incubation plus longs, les intérieurs des vésicules sont remplis d'un empilement dense d'objets lamellaires, sans topologie reconnaissable évidente. Ceci implique que les CD fournissent suffisamment d'énergie pour que les vésicules externes s'infiltrent et s'emballent au sein d'autres vésicules ou autour d'elles-mêmes.

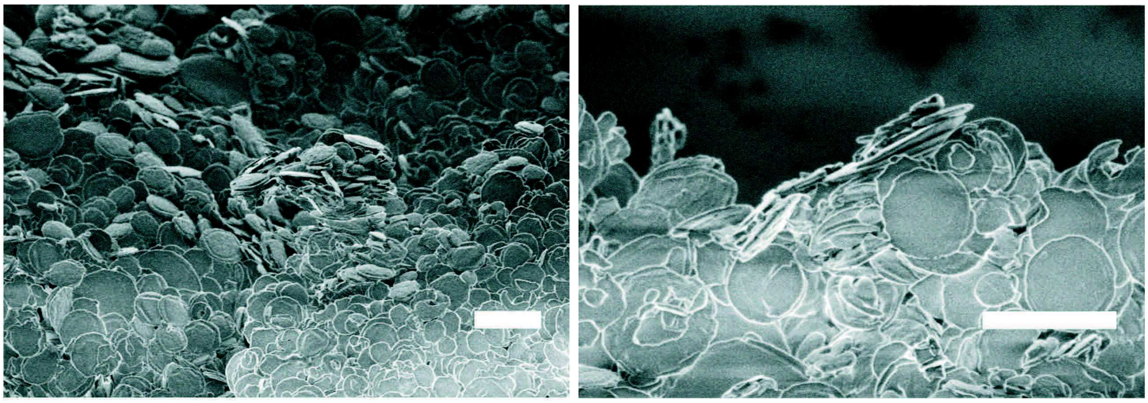

Figure 8.4: Images SEM d'échantillons cristallins de mélanges de 5 mM α-CD / 7.8 mM DOPC. Barre d'échelle, 3 μm.

De plus, nous avons tenté de démêler le mécanisme d'action de la cyclodextrine à l'échelle nanoscopique. En utilisant la calorimétrie de titration isotherme, nous avons mesuré l'énergie libre des interactions, ainsi que ses contributions enthalpiques et entropiques. Nos calculs théoriques, ainsi qu'une analyse RMN, ont estimé le rapport α-CD/DOPC dans les complexes. De toutes les structures supramoléculaires proposées, les complexes CD/DOPC 3-5:1 apparaissent comme étant les plus favorables. Enfin, nous avons tenté de déchiffrer la formation de complexes entre la molécule de α-cyclodextrine unique et les lipides. La microscopie électronique à balayage a révélé l'existence de structures (poudre) d'apparence cristalline que nous associons à des empilements denses α-cyclodextrine/lipides de morphologie bien définie (Fig. 8.4). Notre suspicion d'agencement moléculaire cristallin a été confirmée par l'analyse SAXS/WAXS, qui a révélé la présence de pics de corrélation de Bragg compatibles avec des tailles de cellules cristallines de l'ordre de 1 nm. La structure diffère de celle de la CD cristallisée pure et ne peut être obtenue qu'en présence de lipide DOPC. Même si la détermination cristalline précise de la structure est toujours manquante, toutes les preuves suggèrent que ces agrégats cristallins ont un lien avec les agrégats observées en fluorescence sur les GUV ou sur les SLB.

En conclusion de ces multiples investigations, notre proposition est que la dégradation des bicouches induite par la cyclodextrine n'est pas due à l'extraction moléculaire individuelle des lipides en solution, mais à la nucléation suivie de la croissance d'empilements ordonnés, denses et insolubles de cyclodextrines stabilisées par les lipides. Ces agrégats fournissent une force motrice assez forte pour rétrécir et finalement éliminer complètement la bicouche lipidique.

Effet disruptif d'un pseudo-peptide dépendant du pH (PP50)

Des pseudo-peptides amphiphiles ont été conçus et synthétisés pour imiter le comportement des peptides fusogènes. Récemment, nos collaborateurs du réseau ITN-SNAL ont développé un nouveau polymère sensible à l'acidité de l'environnement, où des groupements phénylalanines ont été greffés sur le squelette poly(L-lysine isophthalamide) avec 50% de substitution molaire stoechiométrique (Fig. 8.5), qui pourrait servir de véhicules nanométriques. Le squelette hydrophobe avec des groupes carboxyles subit des transitions de conformation de filament aléatoire à globulaire. Le changement de conformation médiée par le pH est régulé par l'équilibre entre les fragments hydrophobes et les groupes carboxyle chargés. L'activité de ce polymère est optimisé pour réagir au pH ambiant des endosomes (pKa = 6.5). Après l'acidification, la protonation des groupes d'acide carboxylique exposés, le polymère présente des changements de conformation de la chaîne étendue à des structures stabilisées hydrophobes effondrées. Cette caractéristique conduit à une liaison accrue du polymère aux membranes cellulaires et à la distribution subséquente de la membrane. Il a été rapporté par nos collaborateurs qu'à pH faible, le changement de conformation et d'hydrophobicité de la PP50 entraînait une augmentation de la perméabilité membranaire.

Malgré de nombreux travaux sur le sujet, le mécanisme détaillé de l'action membranaire du polymère sensible au pH reste insaisissable. Une meilleure compréhension de cette interaction est essentielle pour développer de nouvelles stratégies et améliorer l'efficacité du polymère. Par conséquent, dans ce travail, nous avons étudié les effets du PP50 sur les membranes modèles lipidiques. Nous avons utilisé la Cryo-TEM et la calorimétrie différentielle (DSC) pour obtenir des informations sur la structure de la bicouche lors de l'interaction avec le polymère.

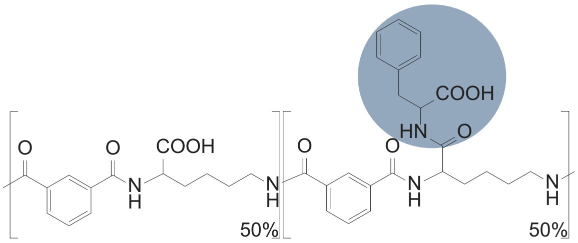

Figure 8.5: La chaîne poly(L-lysine isophtalamide) avec de la L-phénylalanine greffée sur le résidu d'acide carboxylique (cercle gris).

Notre première tentative, impliquant une simple incubation du polymère avec des vésicules lipidiques, a montré que la PP50 à des pH neutre et acide avait des effets mineurs sur la membrane lipidique. Concrètement, les visualisations de Cryo-TEM n'ont démontré aucun changement dans la structure de la membrane, ni dans le nombre de vésicules lipidiques. Nous avons donc validé les résultats de Cryo-TEM et de DSC en utilisant une préparation d'échantillons plus invasive (sonication en présence de polymère). Nous avons été surpris, car les études ont confirmé que la préparation des échantillons joue un rôle important dans l'amélioration des interactions du polymère avec la membrane lipidique (Fig. 8.6).

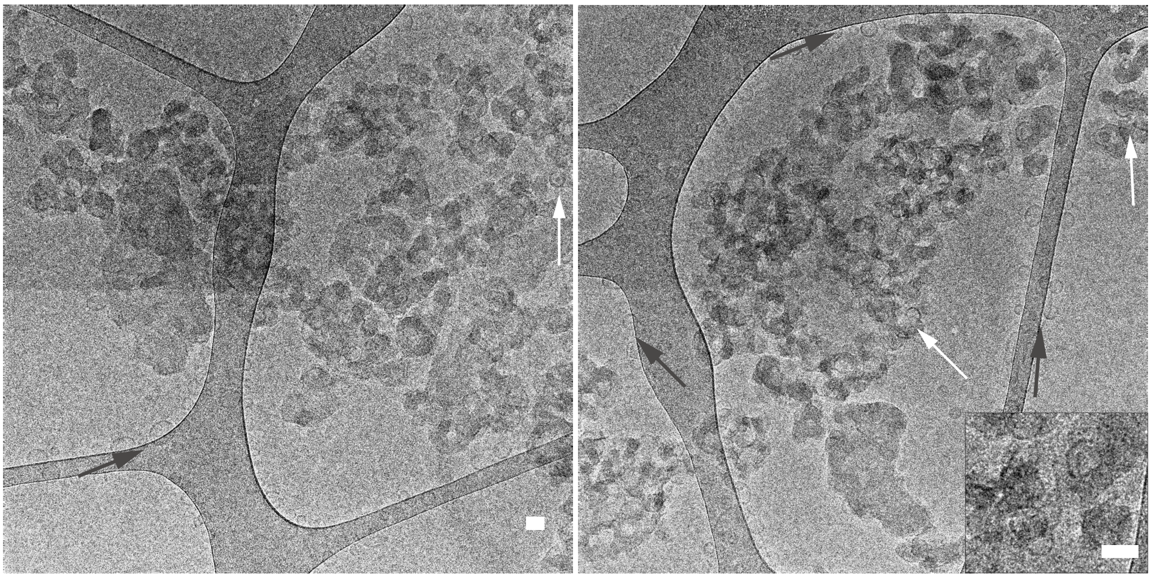

Figure 8.6: Images Cryo-TEM de LUVS de DOPC préparées par hydratation avec une solution de polymère à pH 5.5 (3 mg/mL). Les vésicules interagissant avec PP50 sont indiquées par des flèches blanches. Les flèches noires montrent des vésicules intactes. L'encart montre une image agrandies des lipides/PP50 où la bicouche n'est plus visible. Barre d'échelle, 50 nm.

Enfin, nous avons étudié l'effet du PP50 sur un système lipidique non-lamellaire: les phases cubiques stabilisées par des tensioactifs non ioniques (Pluronic) de la mono-oléine de glycérol (MO), également connues sous le nom de cubosomes. Les cubosomes attirent de plus en plus l'attention en raison de leurs applications potentielles en nanomédecine. Cependant, les systèmes MO purs ne répondent pas seuls à des stimuli biologiques ou externes tels que la température, la lumière, le pH ou la force ionique. Par conséquent, notre idée était d'incorporer le polymère sensible au pH, PP50, dans la structure des cubosomes pour améliorer leur réponse environnementale.

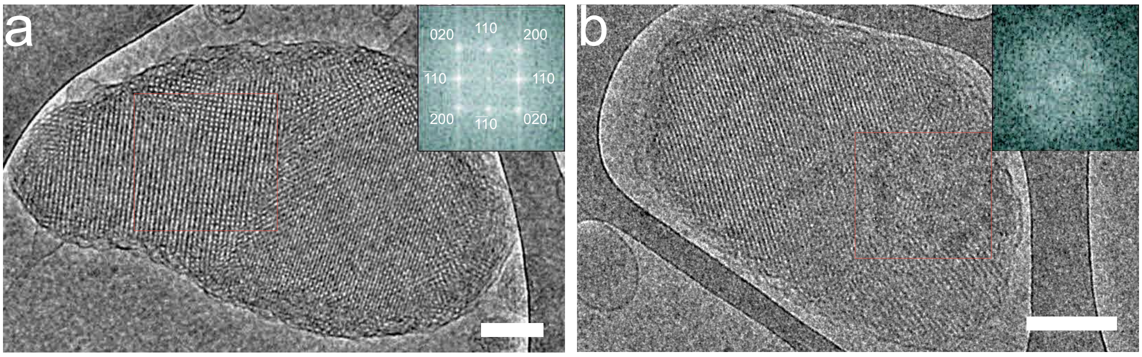

Figure 8.7: Images Cryo-TEM représentatives des dispersions de cubosomes utilisées dans cette étude, avec la transformée de Fourier rapide (FFT) correspondante des zones de boîtes rouges (encarts). Cubosome non chargé: a) pH 5.5 b) cubesomes / PP50 à pH 5.5. La FFT a été utilisée pour la détermination de la structure des particules cristallines liquides. Barre d'échelle, 100 nm.

En combinant les données de SAXS du synchrotron avec la Cryo-TEM, nous avons d'abord établi que la taille des cellules cubiques a été élargie en présence de PP50, ce qui indique une interaction étroite entre les lipides et les polymères (Table 8.1). La nature du gonflement observé à pH 7.5 est encore indéterminé (ceci pourrait être dû à des interactions électrostatiques, à une pression osmotique en solution ou à une adsorption de polymère sur la bicouche de MO). A pH 5.5, l'intensité de diffusion de la phase cubique diminue sans disparaître. Ceci suggère qu'une fraction importante de la phase cubique originale est détruite (Fig. 8.7). De nouvelles structures émergent, comme une phase lamellaire possible associée à un nouveau pic de diffusion dans les spectres, ou une phase désordonnée, à la suite de l'action perturbatrice de la molécule PP50.

Table 8.1: Paramètres de maille (a) et le rayon du canal d'eau (r_w) des cubosomes de MO avec/sans le polymère en fonction du pH.

Échantillon	a^{**} (Å)		a^{***} (Å)		r_w (Å)	
	pH 7.5	pH 5.5	pH 7.5	pH 5.5	pH 7.5	pH 5.5
Cubosomes	143.0 ± 0.1	137.3 ± 0.4	140.2 ± 0.2	139.0 ± 0.4	25.8 ± 0.1	24.0 ± 0.1
Cubosomes avec PP50	163.2 ± 0.1	167.2 ± 0.1	163.0 ± 0.5	156.0 ± 0.9	31.8 ± 0.1	33.0 ± 0.1

** *Mesuré par SAXS*

*** *Obtenu à partir de l'analyse d'images Cryo-TEM de 7 nanoparticules cubiques.*

Nous avons donc observé que la capacité du polymère PP50 à interagir avec la bicouche lipidique dépend non seulement des changements de pH, mais aussi de la méthode de préparation. Lorsque la méthode de préparation met le polymère en contact avec le lipide avant la formation des vésicules, le pouvoir perturbateur de la PP50 est alors très élevé. La structure du mélange lipide-polymère à faible pH est inconnue et mérite d'être étudiée à l'avenir.

Conclusions

Dans cette thèse de doctorat, nous avons étudié avec succès différents aspects de l'interaction entre nanoporteurs et membranes lipides modèles. Le domaine de notre étude était centré sur deux nanotransporteurs différents, à savoir la cyclodextrine α et le polymère sensible au pH (PP50). Dans tous les cas, nos études ont fourni des informations approfondies, à la résolution nanométrique, sur le mécanisme d'action des nanoporteurs dans un système de membrane modèle. La majeure partie de cette thèse est consacrée à la compréhension du comportement de la cyclodextrine α avec une membrane modèle, ainsi qu'à sa description thermodynamique détaillée.

La nouveauté de ce travail est basée sur une combinaison de techniques multidisciplinaires, qui ensemble fournissent une image approfondie des interactions entre cyclodextrines α et membranes. Notre travail sur l'interaction entre les polymères sensibles au pH et les membranes lipides a fourni plusieurs nouvelles idées intéressantes et suggéré de nouvelles directions de recherche qui seront sans aucun doute poursuivies dans les années à venir.

A | Appendix A

A.1 Supporting Information

Project Ia: Kinetic evolution of DOPC giant vesicles and supported lipid bilayers exposed to α-cyclodextrins

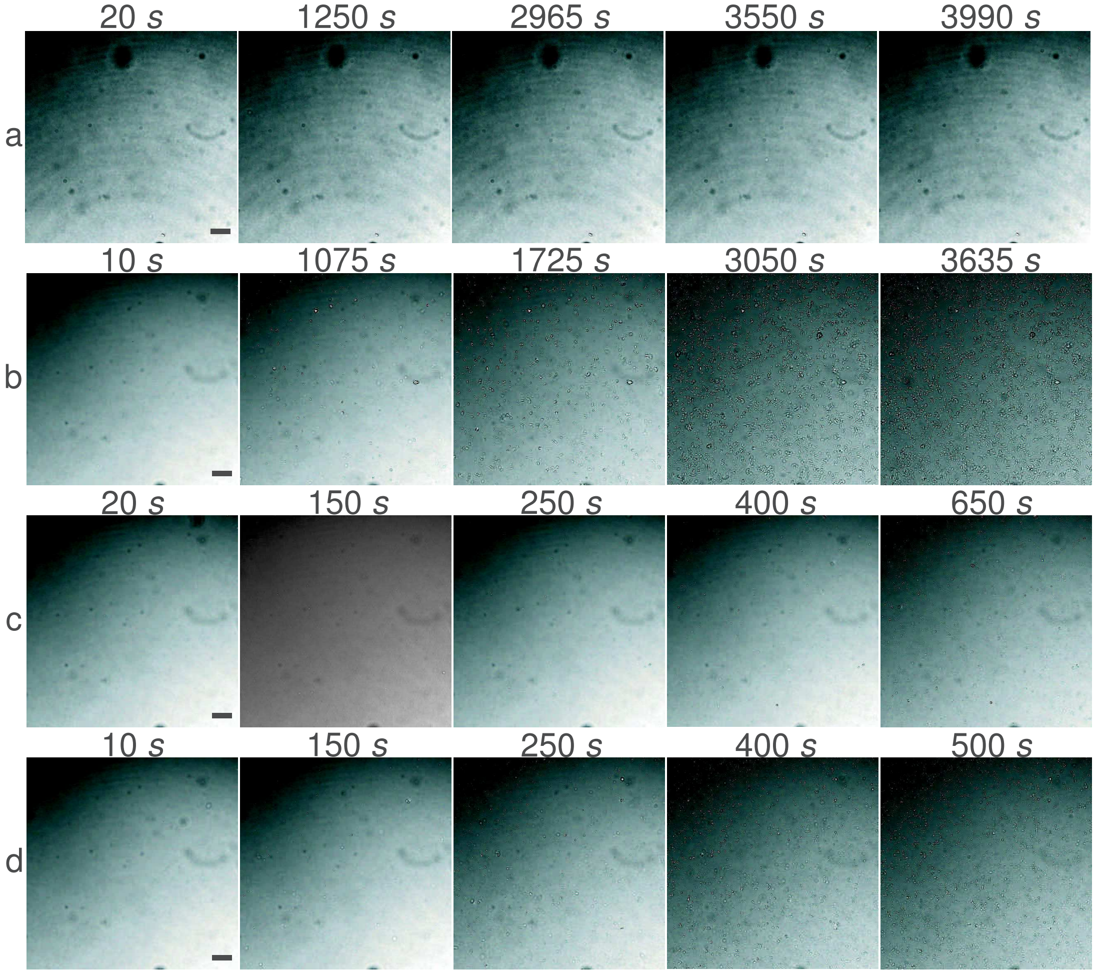

Figure A.1: Bright field images of DOPC SLB marked with DiI at various αCD concentrations: a) 5 mM b) 10 mM c) 15 mM d) 20 mM. There is a 120 s lag time between the injection of αCD into the measuring chamber and the beginning of the microscopy acquisition.

Table A.1: Frequency (Δf) and dissipation (ΔD) shifts resulting from the action of αCD on a DOPC membrane, at various concentrations. The change reveals homogeneous (at 5 mM and 10 mM concentration of αCD) and heterogeneous (15 mM and 20 mM concentrations) interactions, after exposure of the lipid bilayer to αCD for more than 1 h. Values are averages over 3 different samples, and the standard deviation is used as an error estimate

αCD concentration	5 mM	10 mM	15 mM	20 mM
Overtone	Δf (Hz)			
3	-1.05 ± 0.35	12.65 ± 0.92	-11.05 ± 14.14	3.77 ± 5.66
5	-0.10 ± 1.98	14.05 ± 1.49	3.60 ± 10.89	10.93 ± 2.49
7	-0.75 ± 0.35	14.80 ± 1.56	10.25 ± 6.01	14.67 ± 1.53
9	-0.50 ± 0.28	15.65 ± 1.34	14.45 ± 5.59	16.43 ± 1.29
11	-0.45 ± 0.64	15.80 ± 0.85	17.10 ± 4.95	20.10 ± 3.76
13	-0.05 ± 0.35	17.20 ± 2.26	10.61 ± 3.25	17.83 ± 3.76
Overtone	ΔD ($\cdot 10^{-6}$)			
3	1.12 ± 0.25	3.17 ± 0.11	31.80 ± 9.62	19.90 ± 5.17
5	0.93 ± 0.25	2.31 ± 0.01	23.60 ± 8.49	13.25 ± 4.59
7	0.65 ± 0.07	1.95 ± 0.06	18.51 ± 6.72	10.60 ± 2.51
9	0.58 ± 0.18	1.64 ± 0.06	15.18 ± 5.41	8.40 ± 2.01
11	0.59 ± 0.13	1.43 ± 0.01	12.45 ± 4.17	7.13 ± 1.55
13	0.49 ± 0.13	1.90 ± 0.92	10.61 ± 3.25	6.08 ± 1.24

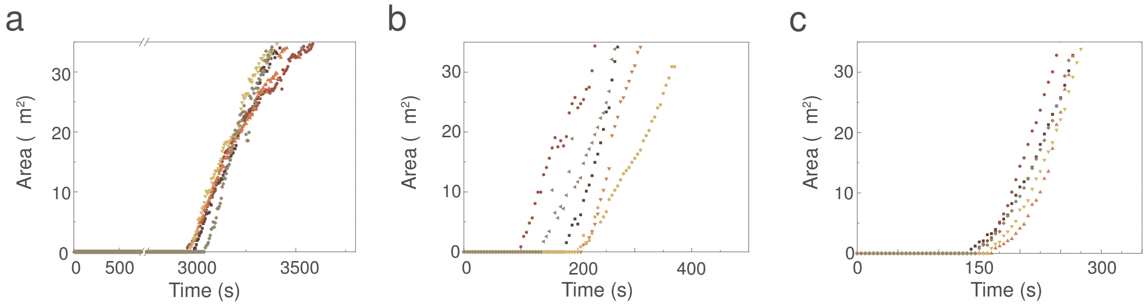

Figure A.2: Time evolution of the single hole areas on SLBs upon interaction with a) 10 mM b) 15 mM c) 20 mM αCD.

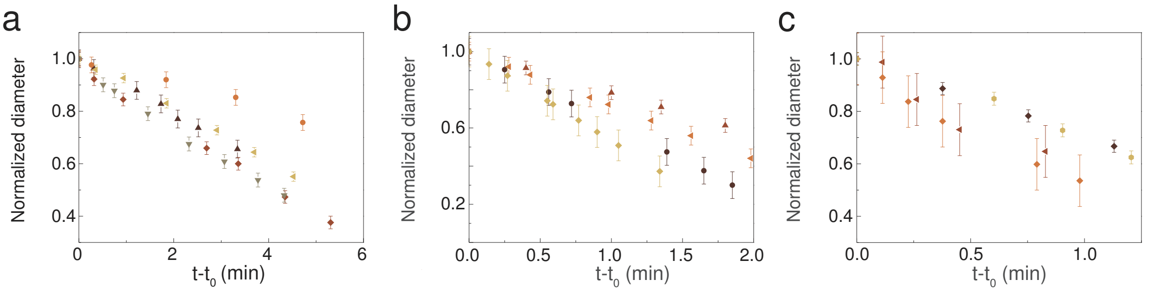

Figure A.3: Changes in diameter of 3 individual GUVs upon interaction with αCD at various concentrations: a) 10 mM b) 15 mM c) 20 mM.

B | Appendix B

B.1 Supporting Information Project Ib: The formation of host-guest complexes between lipid and α-cyclodextrin

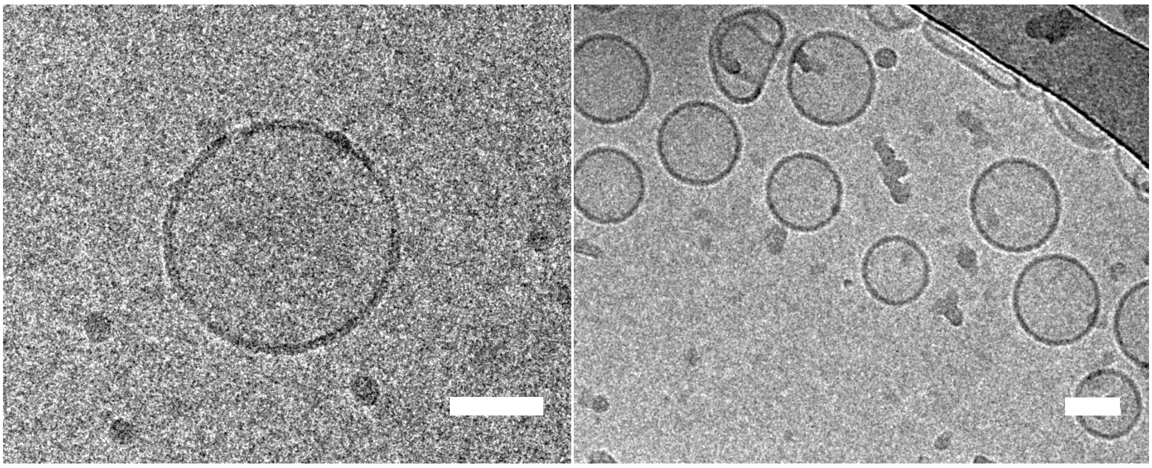

Figure B.1: Cryo-TEM images of pure DOPC-LUVs prepared by extrusion technique. Scale bar, 50 nm.

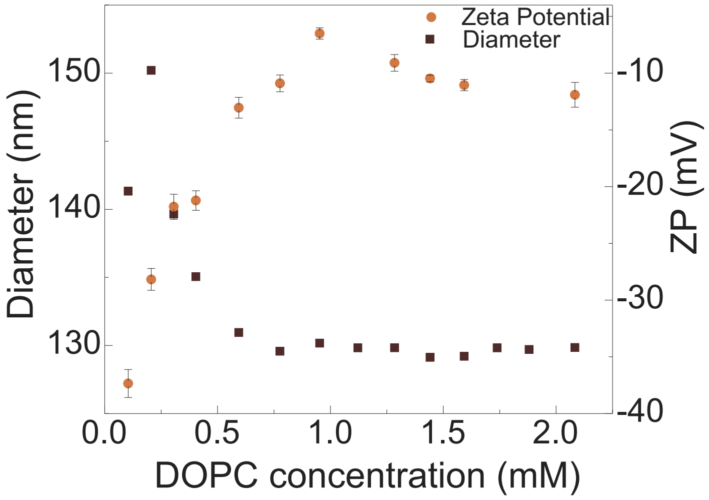

Figure B.2: Changes in hydrodynamic diameter and ζ-potential of DOPC-LUVs upon titration into 5 mM αCD solution.

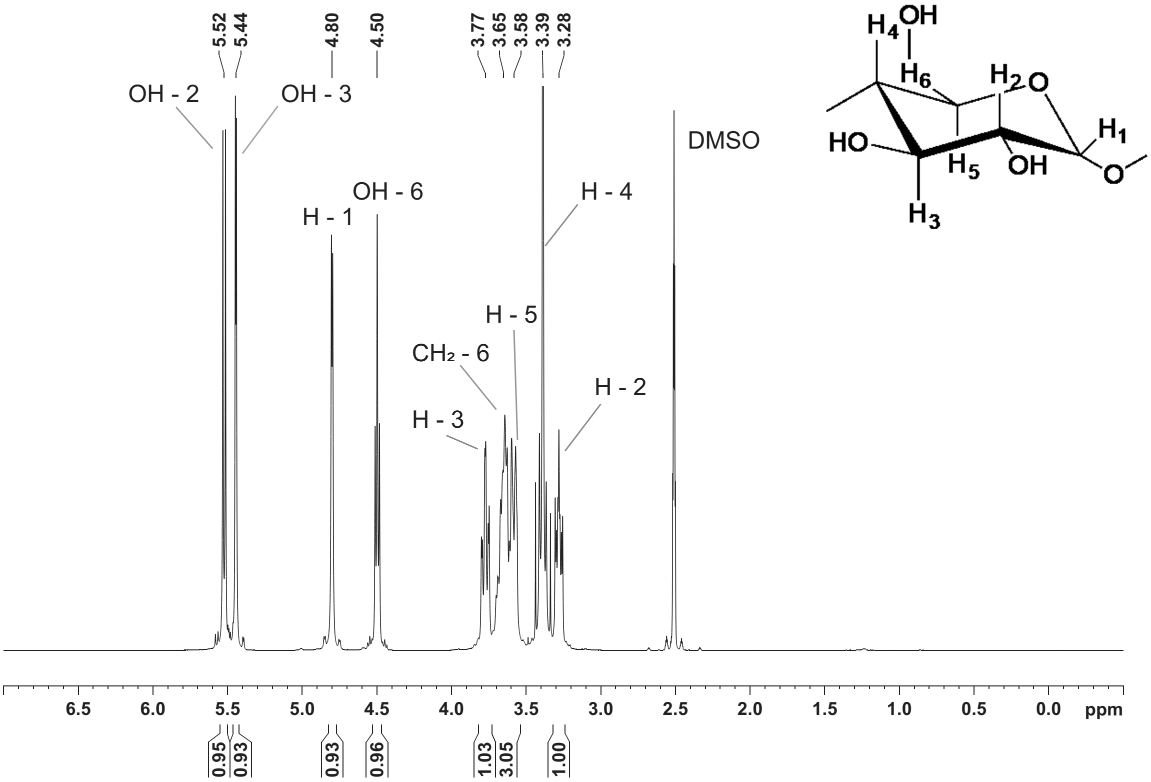

Figure B.3: R^{1}H NMR spectra of αCD powder dispersed in DMSO.

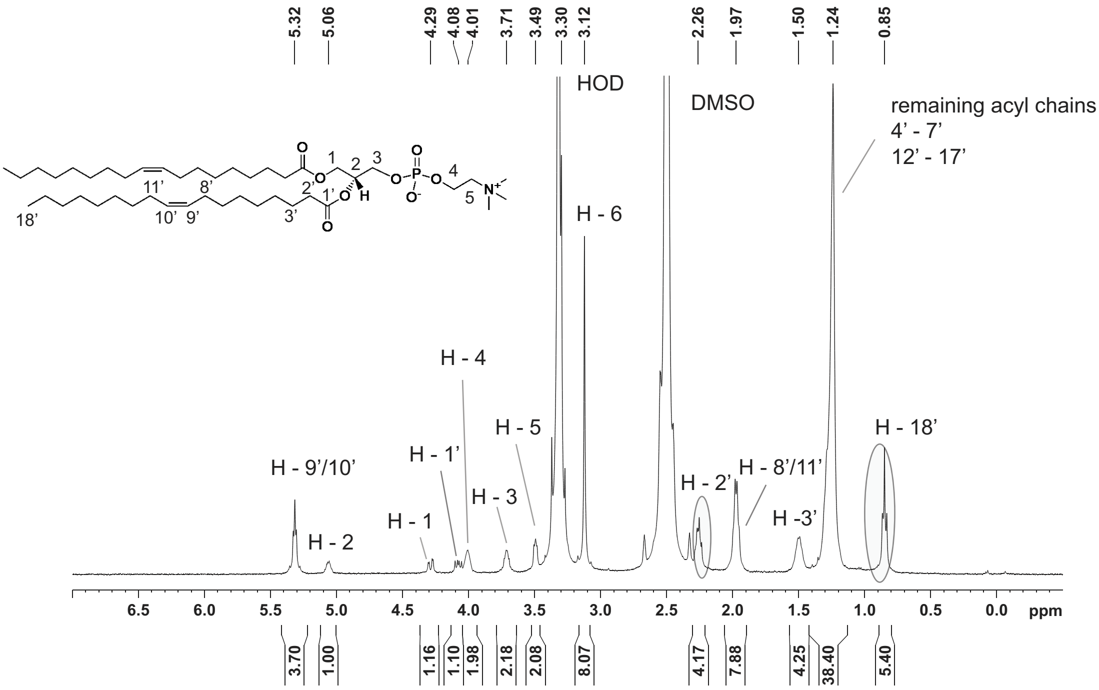

Figure B.4: ^{1}H NMR spectra of DOPC in DMSO.

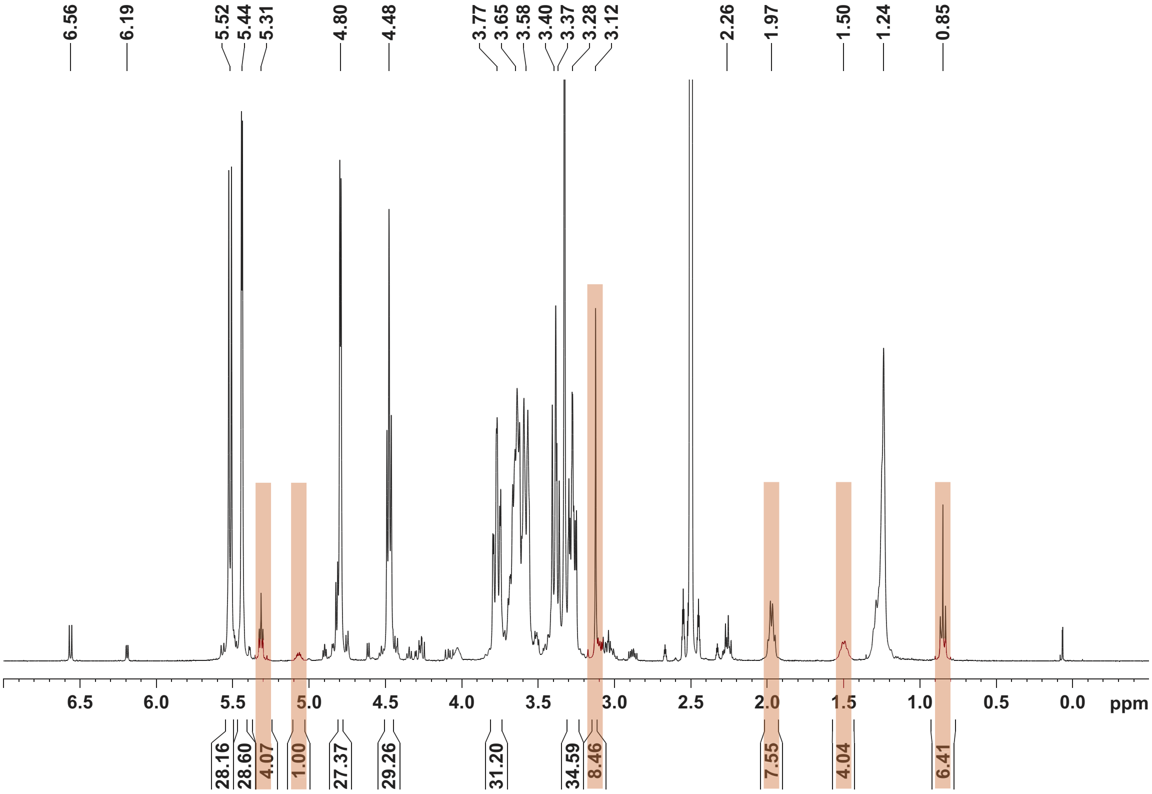

Figure B.5: ^{1}H NMR spectra of DOPC/αCD complex re-dispersed in DMSO. Highlights represent signals from DOPC lipid.

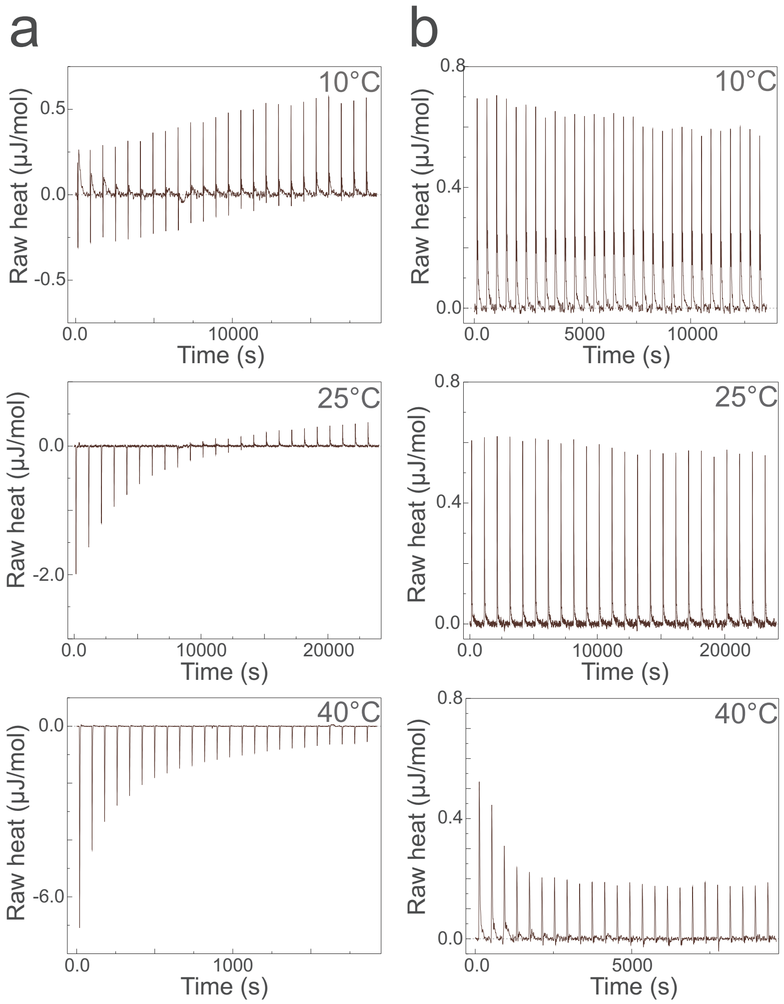

Figure B.6: Isothermal titration calorimetry profiles of a)titration of 7.8 mM DOPC into 5 mM αCD at various temperatures. Panel b) control measurement in which DOPC-LUVs are injected into the αCD-free glucose solution.

B.2 A lower bound for the cooperativity exponent a

We assume a Hill equilibrium and neglect overfills consecutive to injections in the measure cell. Let c_i be the concentration of free CD in solution after i injections, and c_0 the initial concentration. Let $X_i = c_{PL}/c_0$ the ratio of the concentration c_{PL} of PL to c_0 after i injections.

If the reaction was total with a CD for 1 lipid, the number of free CD in solution would be equal to $c_0(1-aX_i)$. Therefore, we have

$$c_0 \geq c_i \geq c_0(1-aX_i) \tag{B.1}$$

and following,

$$K_a c_0^a \geq K_a c_i^a \geq K_a c_0^a (1 - aX_i)^a \tag{B.2}$$

As the covered surface reads $\theta = K_a c_i^a / (1 + K_a c_i^a)$ and as $x/(1+x)$ is a growing function of its argument x, one deduces that

$$\theta_i = \frac{K_a c_i^a}{1 + K_a c_i^a} \geq \frac{K_a c_0^a (1 - aX_i)^a}{1 + K_a c_0^a (1 - aX_i)^a} \geq \frac{K_a c_0^a (1 - aX_i)^a}{1 + K_a c_0^a} \tag{B.3}$$

The total integrated released heat is proportional to θ_i and to the number of phospholipids present n_{PL}. One can write

$$q_1 + q_2 + \ldots + q_i = f_q n_{PL} \theta_i \geq f_q n_{PL} \frac{K_a c_0^a (1 - aX_i)^a}{1 + K_a c_0^a} = f_q n_{PL} \theta_1 (1 - aX_i)^a \tag{B.4}$$

with f_q the enthalpy released per complexed lipid. All injections being identical and small, one has $f_q n_{PL} \theta_1 = i q_1$, leading to the desired result

$$\sum_{j=1}^{i} q_j \geq i q_1 (1 - aX_i)^a \tag{B.5}$$

B.2.1 ITC data analysis

The intensity of the ITC signal for 10°C is low and comparable to background noise (Fig 4.13 at page 58), with no distinguishable thermodynamic characteristic of the αCD-DOPC interaction.For 40°C the signal displays two consecutive regimes: a progressive decrease of the peaks, followed by a quasi-constant value and never reaches plateau, as if the titration is interrupted. Because of this feature the full analysis with thermodynamical model is hindered. Therefore only ITC data for 25°C will be further analyzed.

The relatively large error bars for the intensity observed in the curve of Fig 4.13 b (25°C) can be explained by the sample preparation. Due to extrusion process we are not able to fully control the final concentration of the liposomes. Moreover, it was reported that αCD can aggregate in aqueous solution,either by ageing or high concentration, which might have an influence on the lack of reproducibility of the experimental curves. Despite these fluctuations the signal trend is alike for all experimental curves.

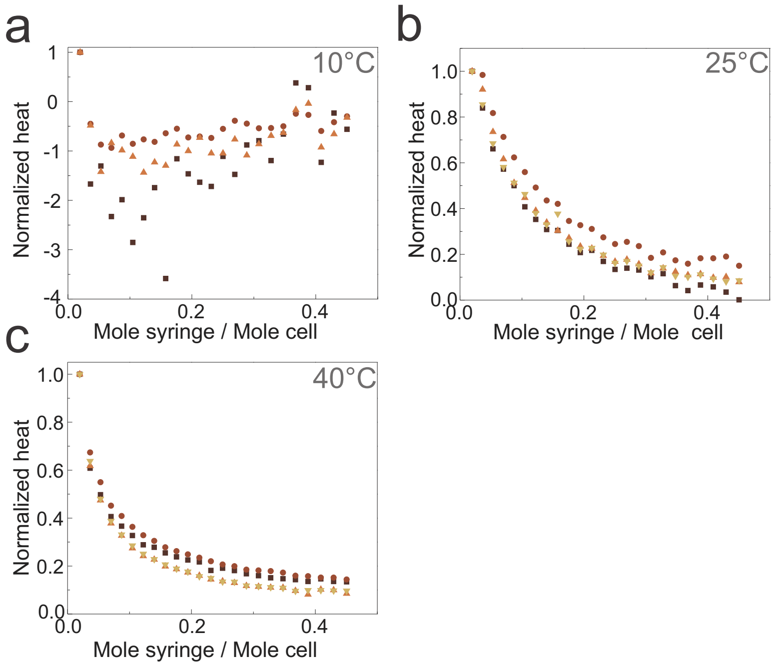

Figure B.7: Normalized heat peaks of separate ITC experiments measured at a) 10°C b) 25°C c) 40°C.

To compare the ITC data, the curves were normalized by the heat of the first injection (Fig 4.16). In all cases the curve reaches a final value close to zero, indicating completion of the reaction. Moreover, the decrease in value halts rapidly after ten (Fig 4.13 at page 58) injections, where the plateau is reached. Assuming homogeneous mixing, it is possible to derive the concentrations in the measuring cell using:

$$
\begin{aligned}
N_{CD}[0] &= 4.75 \cdot 10^{-6} \quad mol \\
N_{PL}[0] &= 0 \quad mol \\
N_{CD}[i] &= N_{CD}[i-1]\frac{V_{cell}-V_{inj}}{V_{cell}} \quad mol \\
N_{PL}[i] &= N_{PL}[i-1]\frac{V_{cell}-V_{inj}}{V_{cell}} + 7.8 \cdot 10^{-8} \quad mol
\end{aligned}
\tag{B.6}
$$

where $N_{PL}[i]$, $N_{CD}[i]$ are the total number of moles of phospholipid and cyclodextrins respectively, that are found in the cell after i injections. After complete titration, a rough stoichiometry can be calculated

$$
\frac{5 \quad mM \cdot V_{cell}}{7.8 \quad mM \cdot 10 \cdot V_{inj}} \simeq 6 \tag{B.7}
$$

which corresponds to 6 αCD molecules neutralized by a single lipid molecule.

Existing ITC models are inadequate in characterizing the observed αCD/DOPC interactions, therefore we attempted to fit the experimental data with a theoretical adsorption model. The frequently used Langmuir adsorption model proved to be unsuccessful in describing the experimental data.

In this work a cooperative Hill adsorption model is proposed. The main assumption of the model is that a certain number of αCD molecules must bind simultaneously to the surface. The mechanism can be described, independently of the αCD and/or αCD/DOPC aggregates structure, in terms of the surface fraction, θ, covered by the aggregates, as:

$$\theta = \frac{K_a c^a_{CD,free}}{1 + K_a c^a_{CD,free}} \qquad \text{B.8}$$

where K$_a$ is the association constant between the lipid and αCD molecule, c$_{CD,free}$ is the concentration of free αCD molecules in solution and a is the number of molecule of a single cluster. It is also possible to define the association constant K$_a$ for such a model by simply considering the variation of free energy due to the transfer of one molecule from a reference solution (in this case c$_0$ = 1M) to an aggregate of a molecules.

$$K_a = c_0^{-a} \exp(\beta a \Delta g_{cl}) \quad M^{-a} \qquad \text{B.9}$$

where Δg_{cl} is the free energy of adsorption for one αCD molecule and β is the Boltzmann unit defined as $\beta = 1/(k_b \cdot T)$.

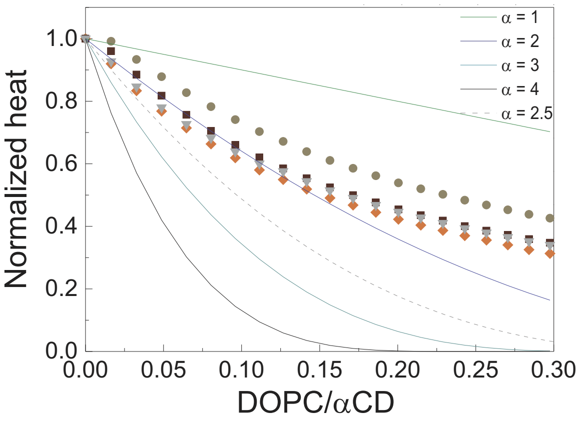

Figure B.8: Normalized heats plotted versus the DOPC/αCD ratio for experimental data at 25°C (scatter) with theoretical lower bounds calculated for different stoichiometry ratio a.

Plotting the normalized heat peaks in a X[i] vs $\sum q[i]/q[1]$ representation, the curve (1-αX[i])^a is a lower bound for the stoichiometry. The graph of experimental data with theoretical lower bounds for a= 1,2,3,4 shows that the totality of the peaks are below or intersecting a=2. The obtained stoichiometry however takes into account an irreversible complexation between αCD and lipids. In case of a reversible process, the lower bound is raised and values for a might be comprised between 3 and 5.

B.2.2 Hill's thermodynamical model

The full treatment of Hill' s adsorption model can be also used to obtain thermodynamic picture of the reaction, including enthalpy and association constant. From Eq. B.8 it is possible to express Hill's equation as

$$K_a c^a_{CD,free} = \frac{\theta}{1-\theta} \tag{B.10}$$

and by analyzing the coefficients that linearize the ln(n_{CD}) vs ln($\theta/1-\theta$) plot it is possible to extract the thermodynamical parameters of the reaction.

Any change in surface coverage θ leads to a heat contribution $q[i]$ which can be expressed as

$$f_q q[i] = \left[\theta[i]N_{PL}[i] - \theta[i-1]N_{PL}[i-1]\frac{V_{cell}-V_{inj}}{V_{cell}}\right] \tag{B.11}$$

and a change of free αCD molecules in the solution.

$$N_{CD} = n_{CD,free} + f_m\theta N_{PL} \tag{B.12}$$

where f$_q$ and f$_m$ are two adjustable parameters that must be determined. Equations B.11 and B.12 can be further reduced to

$$\theta[i] = \frac{f_q q[i] + \theta[i-1]N_{PL}[i-1]\frac{V_{cell}-V_{inj}}{V_{cell}}}{N_{PL}[i]} \tag{B.13}$$

$$n_{CD,free}[i] = N_{CD}[i] - f_m\theta[i]N_{PL}[i] \tag{B.14}$$

Optimization of the parameters involves the minimization of χ^2

$$\chi^2 = \frac{1}{N_{inj}}\sum_{i=1}^{N_{inj}}(y_i - ax_i - b)^2 \tag{B.15}$$

where x_i is $ln(n_{CD,free})$, y_i is $ln(\theta/1-\theta)$, and a, b are the slope and intercept of the linear fitting of the plot for a set of f_q and f_m. The values of f_q and f_m fluctuate strongly, however the product $f_q \cdot f_m$ is consistent throughout the analysis. By combining eq. B.11 and eq. B.12 it is possible to obtain an expression for the enthalpy of the reaction, which was found to be

$$\Delta H = -\frac{1}{f_m f_q} \simeq 0.767 \quad kJmol^{-1} \tag{B.16}$$

The linear slope of the plot (see B.9) is equal to the stoichiometric ratio, which was consistently found to be $a \simeq 4.0$

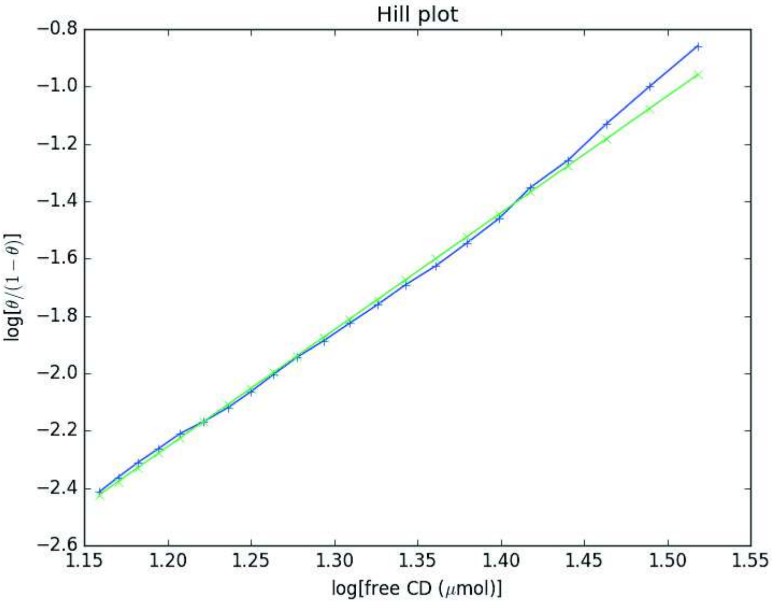

Figure B.9: An example of fitting experimental data (25°C) with Hill's adsorption model. The last two points are not included in fitting.

C | Appendix C

C.1 Supporting Information. Project III: Action of the pH-sensitive polymer PP50 on fluid phospholipid bilayers

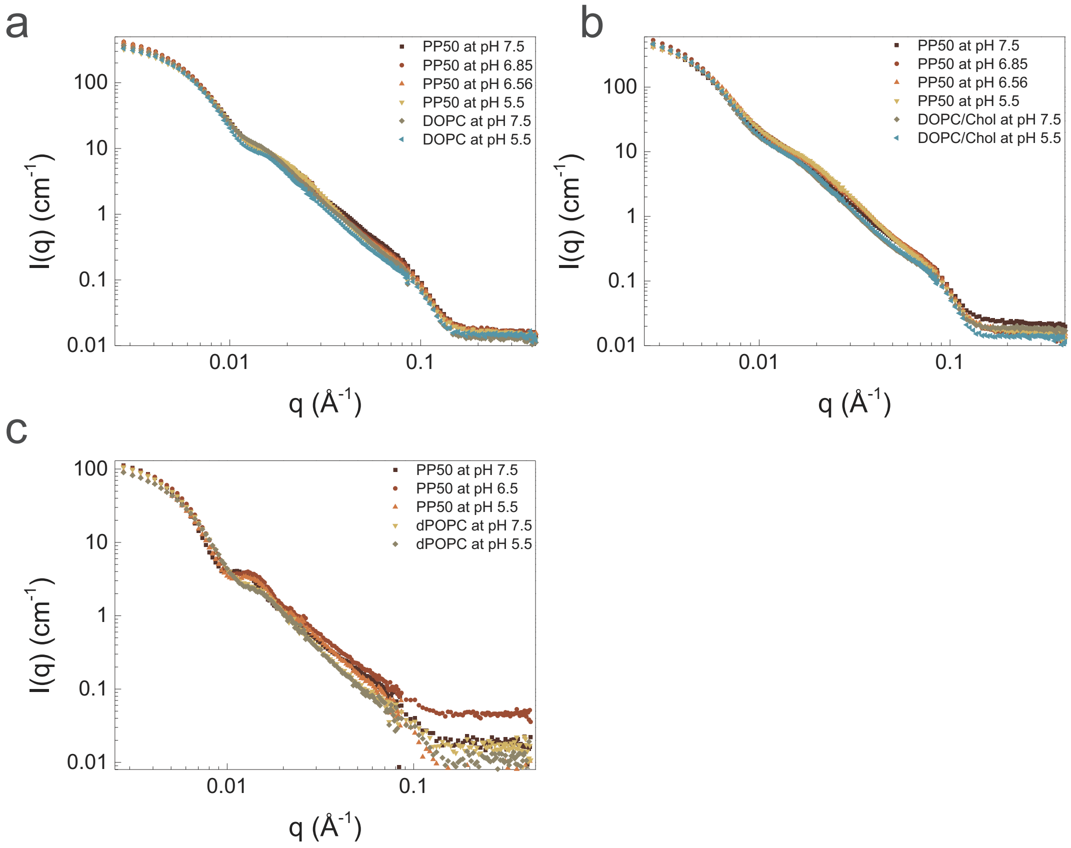

Figure C.1: SANS raw data of interaction between PP50 with LUVs composed of: a) DOPC in D_2O, b) DOPC/Chol (8:2) in D_2O c) d_{31}POPC in H_2O.

The SANS curves were first analyzed using the model-free approach proposed by Gordeliy [302]. The model is tailored for diluted systems, where only independent particle scattering occurs, and offers an initial analysis and quality check of the SANS data.

Guinier Approximation. The very first analysis of SANS data is the Guinier approximation, which provides a quick way of evaluating changes in the radius of gyration (R_g) of LUVs upon interaction with the polymer. This Guinier regime reads:

$$I(0)(1-\frac{q^2R_g^2}{3}) \approx I(0)e^{-q^2R_G^2/3} \qquad \text{C.1}$$

The value of R_g can be extracted from the Guinier plot $\ln(I(q))$ *vs* q^2. Figure (C.2) presents Guinier plots of the systems at low q-range ($7.7\cdot10^{-6} < q^2 < 1.4\cdot10^{-5}$ Å^{-2}). Comparing the calculated R_g results of DOPC-LUVs incubated with polymer and pure DOPC-vesicles (Figure 6.16 a), we observe a small variation of R_g at pH corresponding to the *pKa* of the polymer (pH 6.56). Interestingly, the radius of gyration for systems at acidic pH (5.5) shows no change in value compare to pure DOPC systems. For liposomes with incorporated Cholesterol (8:2) the incubation with polymer at pH 5.5 results in a minor decrease in R_g from 410 Å down to 385 and 390 Å. On the other hand the system of deuterated POPC with PP50 shows no change in R_g regardless of pH.

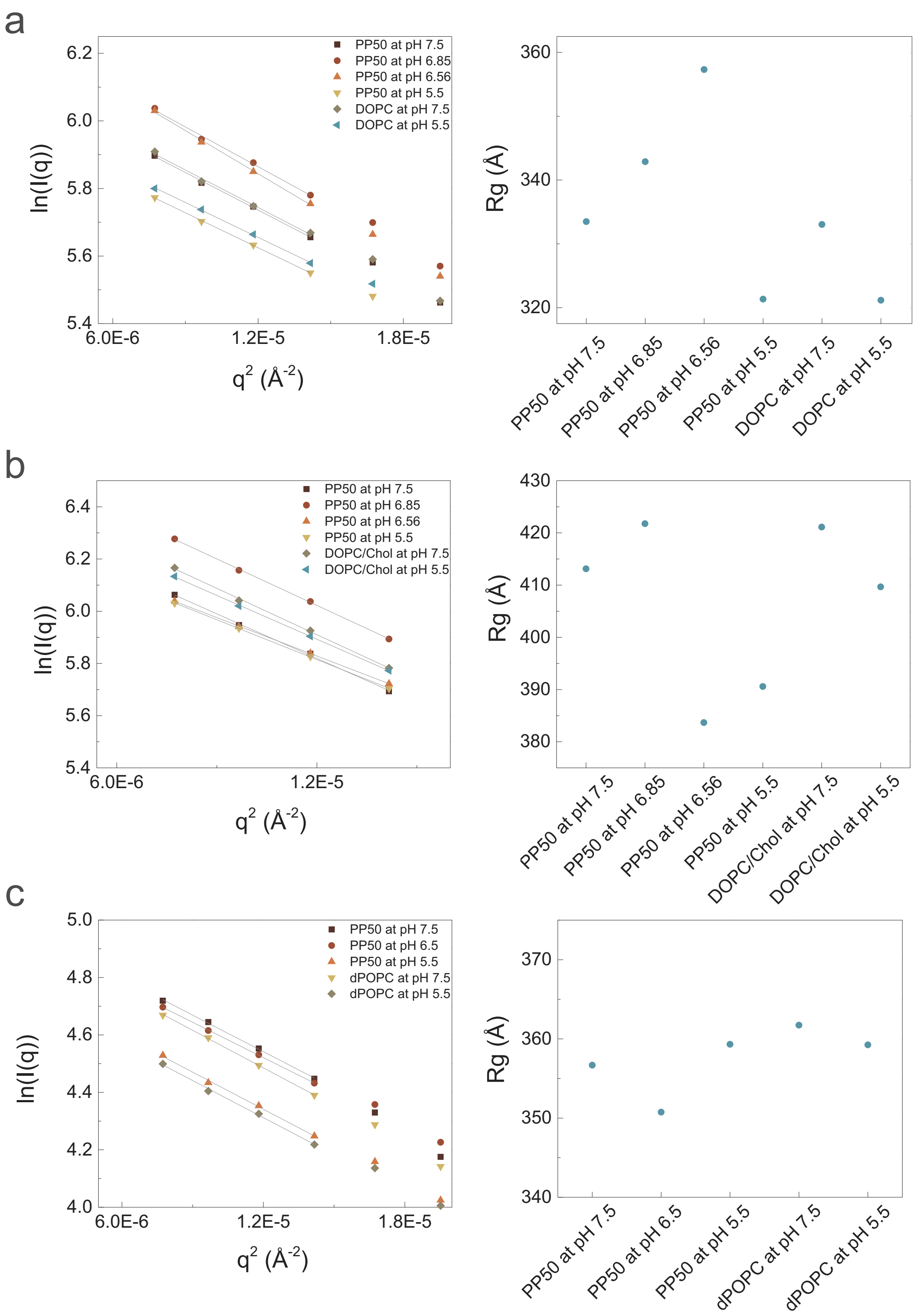

Figure C.2: Guinier plots for pure liposomes and mixture of PP50 with LUVs composed of a)DOPC b)DOPC/Chol(8:2) c)d$_{31}$POPC at various pH. Right site of the figure represents the corresponding R_g values for all systems.

Determination of the membrane thickness using the Kratky-Porod plot. It was shown by several authors [301, 303–307] that the thickness of a two-dimensional planar sheet can be easily extracted from a *Kratky-Porod plot*. The Kratky-Porod analysis is based on the assumption that in a small range of scattering vectors, the scattering intensity of LUVs in D_2O can be estimated using an equation similar to eq (C.1). By plotting the data as $\ln(I(q)q^2)$ vs q^2, the membrane thickness can be evaluated using the relation:

$$d^2 = 12R_k^2 \tag{C.2}$$

A typical Kratky-Porod (KP) plots of experimental SANS data, together with results from our fits are presented in Figure (C.3). At lower q-values ($q^2 < 8 \cdot 10^{-3}$ Å^{-2}) data show a non-linear behavior, whiles in the higher q-regime ($q^2 > 2 \cdot 10^{-2}$ Å^{-2}) a larger dispersion of the values is observed. Therefore we have selected the region of ($8 \cdot 10^{-3} < q^2 < 1.6 \cdot 10^{-2}$ Å^{-2}) for the fitting of experimental data. However is should be noted that the values from fits are very sensitive to the choice of the fitting interval.

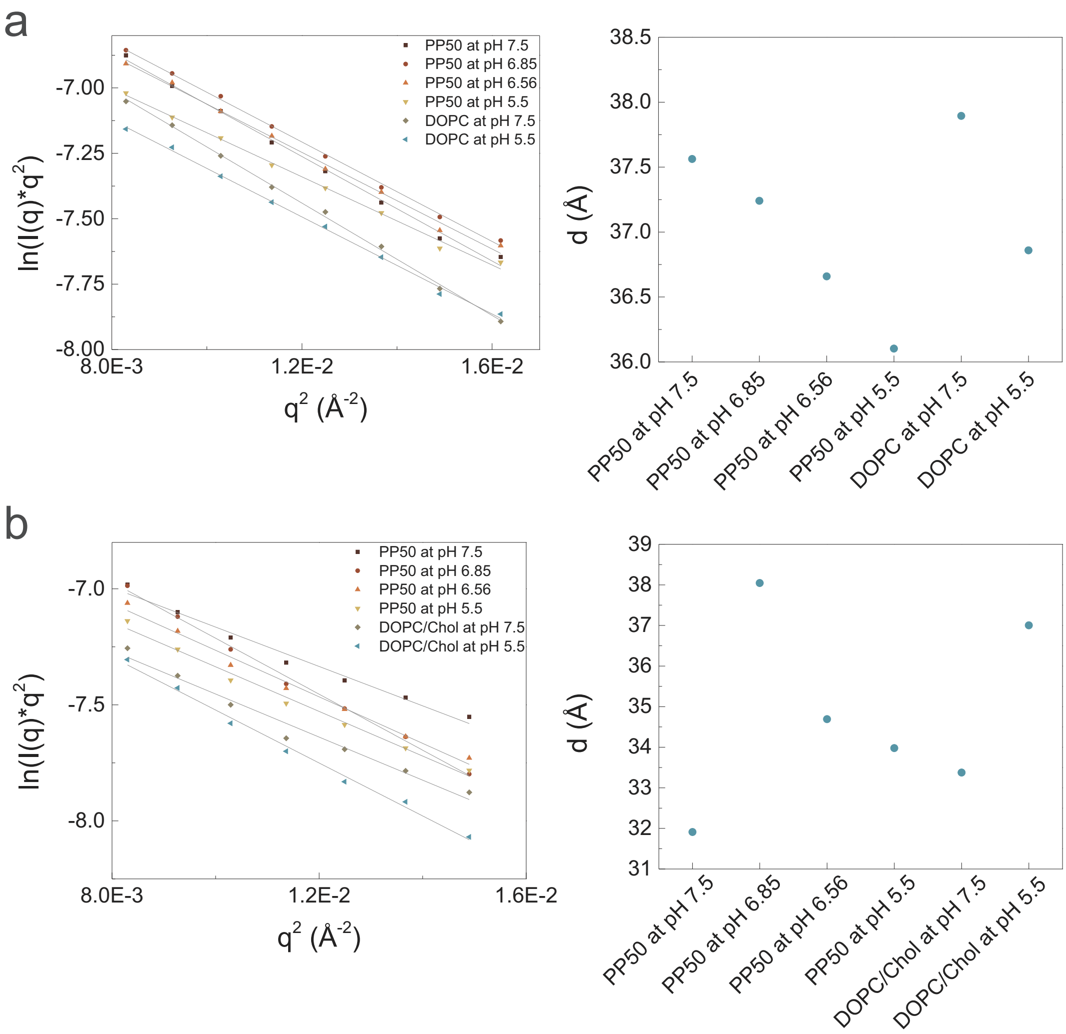

Figure C.3: Kratky-Porod plot and corresponding membrane thickness of a) DOPC-LUVs and b)DOPC/Chol-LUVs incubated with PP50. The solid line represents the fits to experimental data.

The calculated membrane thickness of DOPC and DOPC/Chol LUVs (Figure C.3) shows rather small values ranging from 32 Å up to 40 Å. However, such lower thickness of the membrane in fluid phase has been reported before by Nagel and Nagel [194].

The incubation of the DOPC-liposomes with polymer results in a minor decrease in membrane thickness upon acidification. However, the incorporation of 20% of cholesterol in DOPC liposomes, seems to play significant role (Figure C.3 b) in the LUVs/Polymer interaction. The variation of membrane thickness for DOPC/Cholesterol Liposomes change from 32 Å up to 38 Å with its maximum at pH 6.85.

Model-dependent SANS data analysis. The SANS 3D information on the scattering curve is lost due to 1D projection form of the data (Fig 6.15) Therefore, to retrieve full structural information about system it is essential to apply the model-based data analysis. The model for the scattering particle is constructed based on information from other sources in order to make up for the loss of the structural information. The SANS intensity *I(q)* of a collection of monodisperse scattering particles is proportional to :

$$I(q) = N\,|F(q)|^2\,S(q) \qquad \text{C.3}$$

where *N* is number of scattering objects in the sample, *F(q)* is a form factor of the object, and *S(q)* the structure factor coming from interaction between the objects (for diluted samples *S*=1). The form factor,*F(q)*, is the Fourier transform of the contrast $\Delta\rho$ between the scattering length densities of the object and the solvent. For unilamellar vesicles it can be written as:

$$F(q) = (4\pi/q)\int_{\mathrm{innerradii}}^{\mathrm{outer\,radii}} \Delta\rho(r)\sin(qr)rdr \qquad \text{C.4}$$

Most of the publications dealing with neutron scattering of unilamellar vesicles resorted to fitting the scattering data to a simple one-strip model where the scattering length density is an average of the tail region and the headgroups. However, this approach neglects the internal structure of the lipid membrane and therefore might overlook changes upon interaction with the polymer. Therefore, we are currently trying to implement a three-stripes model, where the bilayer structure is divided into one hydrophobic and two hydrophilic regions. We hope that full analysis of SANS data will complement our existing data and help to fully evaluate the impact of the polymer on the membrane structure.

Bibliography

[1] Theresa M Allen and Pieter R Cullis. Drug delivery systems: Entering the mainstream. *Science*, 303(5665):1818–1822, 2004.

[2] Jinjun Shi, Alexander R Votruba, Omid C Farokhzad, and Robert Langer. Nanotechnology in drug delivery and tissue engineering: from discovery to applications. *Nano Letters*, 10(9): 3223–30, 2010.

[3] Theresa M Allen. Liposomal drug delivery systems: From concept to clinical applications. *Adv Drug Deliver Rev*, 65(1):36–48, 2013.

[4] Guimiao Lin, Feng Yin, and Ken-Tye Yong. Expert opinion on drug discovery. *Science*, 9 (9):991–994, 2014.

[5] Didier Astruc, Elodie Boisselier, and Caatia Ornelas. Dendrimers designed for functions: From physical, photophysical, and supramolecular properties to applications in sensing, catalysis, molecular electronics, photonics, and nanomedicine. *Chemical Reviews*, 110(4): 1857–1959, 2010.

[6] Ruohai Guo, Jian Mao, and Li-Tang Yan. Unique dynamical approach of fully wrapping dendrimer-like soft nanoparticles by lipid bilayer membrane. *ACS Nano*, 7(12):10646–53, 2013.

[7] Leo YT Chou, Kevin Ming, and Warren CW Chan. Strategies for the intracellular delivery of nanoparticles. *Chemical Society Reviews*, 40(1):233–245, 2010.

[8] Carolina de Alarcon, Sivanand Pennadam, and Cameron Alexander. Stimuli responsive polymers for biomedical applications. *Chemical Society reviews*, 34(3):276–85, 2005.

[9] Dirk Schmaljohann. Thermo- and pH-responsive polymers in drug delivery. *Advanced Drug Delivery Reviews*, 58(15):1655–1670, 2006.

[10] Anna Bogomolova, Sandro Keller, Johannes Klingler, Marian Sedlak, Dmytro Rak, Adriana Sturcova, Martin Hruby, Petr Stepanek, and Sergey K Filippov. Self-Assembly thermodynamics of pH-Responsive Amino-Acid-Based polymers with a nonionic surfactant. *Langmuir*, 30(38):11307–11318, 2014.

[11] Sulin Zhang, Huajian Gao, and Gang Bao. Physical principles of nanoparticle cellular endocytosis. *ACS Nano*, 9(9):8655–71, 2015.

[12] Ole G Mouritsen. *Life — As a Matter of Fat*. Springer, Berlin, Heidelberg, 1 edition, 2005.

[13] JC Debouzy, F Fauvelle, S Crouzy, L Girault, Y Chapron, M Göschl, and A Gadelle. Mechanism of α-cyclodextrin induced hemolysis. 2. a study of the factors controlling the association with serine-, ethanolamine-, and choline-phospholipids. *J Pharm Sci*, 87(1):59–66, 1998.

[14] Matthias Schulz, Adekunle Olubummo, and Wolfgang H Binder. Beyond the lipid -bilayer: interaction of polymers and nanoparticles with membranes. *Soft Matter*, 8(18):4849–4864, 2012.

[15] Jonathan D Nickels, Sneha Chatterjee, Christopher B Stanley, Shuo Qian, Xiaolin Cheng, Dean AA Myles, Robert F Standaert, James G Elkins, and John Katsaras. The in vivo structure of biological membranes and evidence for lipid domains. *Plos Biol*, 15(5), 2017.

[16] Valerica Raicu and Aurel Popescu. *Cell Membrane: Structure and Physical Properties*. Springer, 2008.

[17] Drew Marquardt, Frederick A Heberle, Denise V Greathouse, Roger E Koeppe, Robert F Standaert, Brad J Oosten, Thad A Harroun, Jacob J Kinnun, Justin A Williams, Stephen R Wassall, and John Katsaras. Lipid bilayer thickness determines cholesterol's location in model membranes. *Soft Matter*, 12(47):9417–9428, 2016.

[18] Rana Ashkar, Michihiro Nagao, Paul D Butler, Andrea C Woodka, Mani K Sen, and Tadanori Koga. Tuning membrane thickness fluctuations in model lipid bilayers. *Biophys J*, 109(1): 106–112, 2015.

[19] Andrej Shevchenko and Kai Simons. Lipidomics: coming to grips with lipid diversity. *Nat Rev Mol Cell Bio*, 11(8):593–598, 2010.

[20] Jacques Fantini, Nicolas Garmy, Radhia Mahfoud, and Nouara Yahi. Lipid rafts: structure, function and role in hiv, alzheimer's and prion diseases. *Expert Reviews in Molecular Medicine*, 4(27), 2004.

[21] Ole G Mouritsen and Martin J Zuckermann. What's so special about cholesterol? *Lipids*, 39 (11):1101–13, 2004.

[22] M Parmahamsa, Rameswara K Reddy, and N Varadacharyulu. Changes in composition and properties of erythrocyte membrane in chronic alcoholics. *Alcohol Alcoholism*, 39(2):110–112, 2004.

[23] Thomas Heimburg and Andrew D Jackson. The thermodynamics of general anesthesia. *Biophys J*, 92(9):3159–3165, 2007.

[24] Kai Simons and Elina Ikonen. Functional rafts in cell membranes. *Nature*, 387(6633):569–572, 1997.

[25] Gerrit van Meer, Dennis R. Voelker, and Gerald W. Feigenson. Membrane lipids: where they are and how they behave. *Nature Reviews Molecular Cell Biology*, 9(2):112–124, 2008.

[26] Robert F.A. Zwaal and Alan J. Schroit. Pathophysiologic implications of membrane phospholipid asymmetry in blood cells. *Blood*, 89:1121–1132, 1997.

[27] Peter Laggner and Manfred Kriechbaum. Phospholipid phase transitions: kinetics and structural mechanisms. *Chem Phys Lipids*, 57(2-3):121–145, 1991.

[28] HJ Hinz and JM Sturtevant. Calorimetric studies of dilute aqueous suspensions of bilayers formed from synthetic l-a-lecithins. *J Biological Chem*, 247(19):6071–5, 1972.

[29] Ole G. Mouritsen. Theoretical models of phospholipid phase transitions. *Chem Phys Lipids*, 57(2-3):179–194, 1991.

[30] John F Nagle. Theory of the main lipid bilayer phase transition. *Annual Review of Physical Chemistry*, 31:157–195, 1980.

[31] Daniela Uhríková, Norbert Kučerka, José Teixeira, Valentin Gordeliy, and Pavol Balgavý. Structural changes in dipalmitoylphosphatidylcholine bilayer promoted by ca2+ ions: a small-angle neutron scattering study. *Chemistry and Physics of Lipids*, 155(2):80–89, 2008.

[32] William W. van Osdol, Qiang Ye, Michael L. Johnson, and Rodney L. Biltonen. Effects of the anesthetic dibucaine on the kinetics of the gel-liquid crystalline transition of dipalmitoylphosphatidylcholine multilamellar vesicles. *Biophys. J.*, 63(4):1011–1017, 1992.

[33] Heiko M Seeger, Marie L Gudmundsson, and Thomas Heimburg. How anesthetics, neurotransmitters, and antibiotics influence the relaxation processes in lipid membranes. *The journal of physical chemistry. B*, 111(49):13858–66, 2007.

[34] Anne S. Ulrich, Malkit Sami, and Anthony Watts. Hydration of DOPC bilayers by differential scanning calorimetry. *Biochimica et Biophysica Acta*, 1191(1):225–30, 1994.

[35] Natalia Markova, Emma Sparr, Lars Wadsö, and Håkan Wennerström. A calorimetric study of phospholipid hydration. simultaneous monitoring of enthalpy and free energy. *J Phys Chem B*, 104(33):8053–8060, 2000.

[36] Bernd Gruenewald, Alfred Blume, and Fumiyuki Watanabe. Kinetic investigations on the phase transition of phospholipid bilayers. *Biochimica Et Biophysica Acta BBA - Biomembranes*, 597(1):41–52, 1980.

[37] Thomas Heimburg. *Membrane Structure, in Thermal Biophysics of Membranes*. Wiley-VCH Verlag GmbH & Co. KGaA, 2007.

[38] Hjort J Ipsen, G Karlström, O.G. Mourtisen, H Wennerström, and M.J. Zuckermann. Phase equilibria in the phosphatidylcholine-cholesterol system. *Phys Rev E*, 905(1):162–172, 1987.

[39] Morten Nielsen, Ling Miao, John H. Ipsen, and Martin J. Zuckermann. Off-lattice model for the phase behavior of lipid-cholesterol bilayers. *Physical Review E*, 1999.

[40] Sarah L Veatch and Sarah L Keller. Miscibility phase diagrams of giant vesicles containing sphingomyelin. *Phys Rev Lett*, 94(14), 2005.

[41] Derek Marsh. Liquid-ordered phases induced by cholesterol: A compendium of binary phase diagrams. *Biochimica Et Biophysica Acta BBA - Biomembranes*, 1798(3):688–699, 2010.

[42] Luis A Bagatolli and Enrico Gratton. A correlation between lipid domain shape and binary phospholipid mixture composition in free standing bilayers: A Two-Photon fluorescence microscopy study. *Biophysical Journal*, 79(1):434–447, 2000.

[43] Luis A. Bagatolli and Enrico Gratton. Direct observation of lipid domains in free-standing bilayers using two-photon excitation fluorescence microscopy. *Journal of Fluorescence*, 2001.

[44] FM Goñi, A Alonso, LA Bagatolli, and RE Brown. Phase diagrams of lipid mixtures relevant to the study of membrane rafts. *Biochim Biophys Acta*, 1781:665–684, 2008.

[45] Chad Leidy, Willem F Wolkers, Kent Jørgensen, Ole G Mouritsen, and John H Crowe. Lateral organization and domain formation in a Two-Component lipid membrane system. *Biophys J*, 80(4):1819–1828, 2001.

[46] Benjamin L Stottrup, Daniel S Stevens, and Sarah L Keller. Miscibility of ternary mixtures of phospholipids and cholesterol in monolayers, and application to bilayer systems. *Biophys J*, 88(1):269–276, 2005.

[47] Agnieszka E Hac, Heiko M Seeger, Matthias Fidorra, and Thomas Heimburg. Diffusion in Two-Component lipid Membranes—A fluorescence correlation spectroscopy and monte carlo simulation study. *Biophys J*, 88(1):317–333, 2005.

[48] Siewert J Marrink, Jelger Risselada, and Alan E Mark. Simulation of gel phase formation and melting in lipid bilayers using a coarse grained model. *Chem Phys Lipids*, 135(2):223–244, 2005.

[49] Jelger H Risselada and Siewert J Marrink. The molecular face of lipid rafts in model membranes. *Proc National Acad Sci*, 105(45):17367–17372, 2008.

[50] Matthias Fidorra, Aritz Garcia, John H. Ipsen, S Härtel, and Luis A. Bagatolli. Lipid domains in giant unilamellar vesicles and their correspondence with equilibrium thermodynamic phases: A quantitative fluorescence microscopy imaging approach. *Biochimica et Biophysica Acta BBA - Biomembranes*, 1788(10):2142–2149, 2009.

[51] H.M. Seeger, G Marino, A Alessandrini, and P Facci. Effect of physical parameters on the main phase transition of supported lipid bilayers. *Biophys J*, 97(4):1067–1076, 2009.

[52] Heiko M Seeger, Laura Aldrovandi, Andrea Alessandrini, and Paolo Facci. Changes in single k+ channel behavior induced by a lipid phase transition. *Biophys J*, 99(11):3675–3683, 2010.

[53] A Pralle, P Keller, EL Florin, and K Simons. Sphingolipid–cholesterol rafts diffuse as small entities in the plasma membrane of mammalian cells. *The Journal of cell biology*, 2000.

[54] Paulo Almeida, Antje Pokorny, and Anne Hinderliter. Thermodynamics of membrane domains. *Biochimica et Biophysica Acta (BBA) - Biomembranes*, 1720(1-2):1–13, 2005.

[55] Michael Edidin. Shrinking patches and slippery rafts: scales of domains in the plasma membrane. *Trends Cell Biol*, 11(12):492–496, 2001.

[56] Reinhard Lipowsky and Rumiana Dimova. Domains in membranes and vesicles. *Journal of Physics: Condensed Matter*, 15:S31–S45, 2002.

[57] Wolfgang H. Binder and Veronique Barragan. Domains and rafts in lipid membranes. *Angewandte Chemie*, 42:5802–5827, 2003.

[58] Fuyuki Tokumasu, Albert J Jin, Gerald W Feigenson, and James A Dvorak. Nanoscopic lipid domain dynamics revealed by atomic force microscopy. *Biophys J*, 84(4):2609–2618, 2003.

[59] Peter I Kuzmin, Sergey A Akimov, Yuri A Chizmadzhev, Joshua Zimmerberg, and Fredric S Cohen. Line tension and interaction energies of membrane rafts calculated from lipid splay and tilt. *Biochimica et Biophysica Acta (BBA) - Biomembranes*, 88(2):1120–33, 2004.

[60] Sergey A Akimov, Peter I Kuzmin, Joshua Zimmerberg, and Fredric S Cohen. Lateral tension increases the line tension between two domains in a lipid bilayer membrane. *Phys Rev E*, 75 (1), 2007.

[61] A.D. Bangham, M.M. Standish, and J.C. Watkins. Diffusion of univalent ions across the lamellae of swollen phospholipids. *J Mol Biol*, 13(1):238–252, 1965.

[62] B.D Ladbrooke and D Chapman. Thermal analysis of lipids, proteins and biological membranes a review and summary of some recent studies. *Chemistry and physics of lipids*, 3: 304–356, 1969.

[63] RA Demel, J Jansen, and PWM Dijck. The preferential interactions of cholesterol with different classes of phospholipids. *Biochimica et Biophysica Acta (BBA)*, 1977.

[64] Nicholas E Grossoehme, Anne M Spuches, and Dean E Wilcox. Application of isothermal titration calorimetry in bioinorganic chemistry. *J Biological Inorg Chem*, 15(8):1183–1191, 2010.

[65] Nichola C Garbett and Guy N Brock. Differential scanning calorimetry as a complementary diagnostic tool for the evaluation of biological samples. *Biochimica et Biophysica Acta*, 1860 (5):981–9, 2016.

[66] Sandro Keller, Matthias Böthe, Michael Bienert, Margitta Dathe, and Alfred Blume. A simple Fluorescence-Spectroscopic membrane translocation assay. *ChemBioChem*, 2007.

[67] Villalain, José, Aranda, Francisco J, and Gómez-Feández, Juan C. Calorimetric and infrared spectroscopic studies of the interaction of α-tocopherol and α-tocopheryl acetate with phospholipid vesicles. *European Journal of Biochemistry*, 158(1):141–147, 1986.

[68] Ruthven Lewis, Yuan-Peng Zhang, and McElhaney, Ronald N. Calorimetric and spectroscopic studies of the phase behavior and organization of lipid bilayer model membranes composed of binary mixtures of dimyristoylphosphatidylcholine and dimyristoylphosphatidylglycerol. *Biochimica et Biophysica Acta*, 1668(2):203–14, 2005.

[69] Klaus B Stark, James M Gallas, Gerry W Zajac, Melvin Eisner, and Joseph T Golab. Spectroscopic study and simulation from recent structural models for eumelanin: i. monomer, dimers. *The Journal of Physical Chemistry B*, 107(13):3061–3067, 2003.

[70] Shen Helvig, Intan DM Azmi, Seyed M Moghimi, and Anan Yaghmur. Recent advances in Cryo-TEM imaging of soft lipid nanoparticles. *AIMS Biophysics*, 2(2):116–130, 2015.

[71] Miglena I Angelova and Dimiter S Dimitrov. Liposome electroformation. *Faraday discussions of the Chemical Society*, 81(0):303–311, 1986.

[72] Morales-Penningston, Nelson F, Jing Wu, Elaine R Farkas, Shih Goh, Tatyana M Konyakhina, Judy Y Zheng, Watt W Webb, and Gerald W Feigenson. GUV preparation and imaging: Minimizing artifacts. *Biochimica et Biophysica Acta - Biomembranes*, 1798 (7):1324–1332, 2010.

[73] Honerkamp-Smith, Aurelia R, Francis G Woodhouse, Vasily Kantsler, and Raymond E Goldstein. Membrane viscosity determined from Shear-Driven flow in giant vesicles. *Phys Rev Lett*, 111(3):038103, 2013.

[74] Nicoletta Kahya, Dag Scherfeld, Kirsten Bacia, and Petra Schwille. Lipid domain formation and dynamics in giant unilamellar vesicles explored by fluorescence correlation spectroscopy. *J Struct Biol*, 147(1):77–89, 2004.

[75] Salvatore Chiantia, Petra Schwille, Andrey S Klymchenko, and Erwin London. Asymmetric GUVs prepared by MβCD-Mediated lipid exchange: An FCS study. *Biophys J*, 100(1): L1–L3, 2011.

[76] Roger Wick, Miglena I Angelova, Peter Walde, and Pier Luisi. Microinjection into giant vesicles and light microscopy investigation of enzyme-mediated vesicle transformations. *Chem Biology*, 3:105–111, 1996.

[77] Georges Weber, Thierry Charitat, Maurício S Baptista, Adjaci F Uchoa, Christiane Pavani, Helena C Junqueira, Yachong Guo, Vladimir A Baulin, Rosangela Itri, Carlos M Marques, and André P Schroder. Lipid oxidation induces structural changes in biomimetic membranes. *Soft Matter*, 10(24):4241–4247, 2013.

[78] K Olbrich, W Rawicz, D Needham, and E Evans. Effect of chain length and unsaturation on elasticity of lipid bilayers. *Biophys J*, 79(1):321–327, 2000.

[79] Jiaojiao Liu, Naiyan Lu, Jingliang Li, Yuyan Weng, Bing Yuan, Kai Yang, and Yuqiang Ma. Influence of surface chemistry on particle internalization into giant unilamellar vesicles. *Langmuir : the ACS journal of surfaces and colloids*, 29(25):8039–45, 2013.

[80] Omar Mertins and Rumiana Dimova. Insights on the interactions of chitosan with phospholipid vesicles. part II: membrane stiffening and pore formation. *Langmuir*, 29(47):14552–14559, 2013.

[81] TJ Crites, M Maddox, K Padhan, and J Muller. *Supported lipid bilayer technology for the study of cellular interfaces*. John Wiley and Sons, Inc, 2015.

[82] T Charitat, Bellet-Amalric, E, G Fragneto, and F Graner. Adsorbed and free lipid bilayers at the solid-liquid interface. *The European Physical Journal B*, pages 583–593, 1999.

[83] AE Nel, L Mädler, D Velegol, T Xia, and EMV Hoek. Understanding biophysicochemical interactions at the nano–bio interface. *Nature Materials*, 8:543–557, 2009.

[84] Hye Young Kim, Jorge O. Sofo, Darrell Velegol, Milton W. Cole, and Amand A. Lucas. Van der waals dispersion forces between dielectric nanoclusters. *Langmuir*, 23(4):1735–1740, 2007.

[85] Hongming Chen, Robert Langer, and David A. Edwards. A Film Tension Theory of Phagocytosis. *Journal of Colloid and Interface Science*, 190(1):118–133, 1997.

[86] Benxin Jing and Yingxi Zhu. Disruption of supported lipid bilayers by semihydrophobic nanoparticles. *Journal of the American Chemical Society*, 133(28):10983–10989, 2011.

[87] Hongtao Chen, Sungwon Kim, Li Li, Shuyi Wang, Kinam Park, and Ji-Xin Cheng. Release of hydrophobic molecules from polymer micelles into cell membranes revealed by förster resonance energy transfer imaging. *Proceedings of the National Academy of Sciences*, 105 (18):6596–6601, 2008.

[88] Olivier Le Bihan, Pierre Bonnafous, Laszlo Marak, Thomas Bickel, Sylvain Trépout, Stéphane Mornet, Felix De Haas, Hugues Talbot, Jean Christophe Taveau, and Olivier Lambert. Cryo-electron tomography of nanoparticle transmigration into liposome. *Journal of Structural Biology*, 168(3):419–425, 2009.

[89] B. Devika Chithrani, Arezou A. Ghazani, and Warren C. W. Chan. Determining the size and shape dependence of gold nanoparticle uptake into mammalian cells. *Nano Letters*, 6(4): 662–668, 2006.

[90] S. E. A. Gratton, P. A. Ropp, P. D. Pohlhaus, J. C. Luft, V. J. Madden, M. E. Napier, and J. M. DeSimone. The effect of particle design on cellular internalization pathways. *Proceedings of the National Academy of Sciences*, 105(33):11613–11618, 2008.

[91] Kai Yang and Yu-Qiang Ma. Computer simulation of the translocation of nanoparticles with different shapes across a lipid bilayer. *Nature Nanotechnology*, 5(8):579–583, 2010.

[92] Luca Monticelli, Emppu Salonen, Pu Chun Ke, and Ilpo Vattulainen. Effects of carbon nanoparticles on lipid membranes: a molecular simulation perspective. *Soft Matter*, 5:4433–4445, 2009.

[93] Liping Chen, Shiyan Xiao, Hong Zhu, Lei Wang, and Haojun Liang. Shape-dependent internalization kinetics of nanoparticles by membranes. *Soft Matter*, 12:2632–2641, 2016.

[94] Gulen Yesilbag Tonga, Krishnendu Saha, and Vincent M. Rotello. 25th anniversary article: Interfacing nanoparticles and biology: New strategies for biomedicine. *Advanced Materials*, 26(3):359–370, 2014.

[95] B. Wang, L. Zhang, S. C. Bae, and S. Granick. Nanoparticle-induced surface reconstruction of phospholipid membranes. *Proceedings of the National Academy of Sciences*, 105(47): 18171–18175, 2008.

[96] Yanjing Chen and Geoffrey D. Bothun. Cationic gel-phase liposomes with “decorated” anionic spio nanoparticles: Morphology, colloidal, and bilayer properties. *Langmuir*, 27(14): 8645–8652, 2011.

[97] Dagmar Fischer, Youxin Li, Barbara Ahlemeyer, Josef Krieglstein, and Thomas Kissel. In vitro cytotoxicity testing of polycations: influence of polymer structure on cell viability and hemolysis. *Biomaterials*, 24(7):1121 – 1131, 2003.

[98] Su Li and Noah Malmstadt. Deformation and poration of lipid bilayer membranes by cationic nanoparticles. *Soft Matter*, 9(20):4969, 2013.

[99] Julie Muller, François Huaux, Nicolas Moreau, Pierre Misson, Jean François Heilier, Monique Delos, Mohammed Arras, Antonio Fonseca, Janos B. Nagy, and Dominique Lison. Respiratory toxicity of multi-wall carbon nanotubes. *Toxicology and Applied Pharmacology*, 207(3):221–231, 2005.

[100] S.M. Hussain, K.L. Hess, J.M. Gearhart, K.T. Geiss, and J.J. Schlager. In vitro toxicity of nanoparticles in brl 3a rat liver cells. *Toxicology in Vitro*, 19(7):975 – 983, 2005.

[101] Marc Adrian, Jacques Dubochet, Jean Lepault, and Alasdair W. McDowall. Cryo-electron microscopy of viruses. *Nature*, 308(5954):32–36, 1984.

[102] Lijuan Shi, Ying Wei, Nan Sun, and Liqiang Zheng. First observation of rich lamellar structures formed by a single-tailed amphiphilic ionic liquid in aqueous solutions. *Chem Commun*, 49(97):11388–11390, 2013.

[103] Heiner Friedrich, Peter M Frederik, Gijsbertus de With, and Nico Sommerdijk. Imaging of Self-Assembled structures: Interpretation of TEM and Cryo-TEM images. *Angewandte Chemie Int Ed*, 49(43):7850–7858, 2010.

[104] Al-Amoudi, Ashraf, Jiin-Ju Chang, Amélie Leforestier, McDowall, Alasdair, Laurée Salamin, Lars PO Norlén, Karsten Richter, Nathalie Blanc, Daniel Studer, and Jacques Dubochet. Cryo-electron microscopy of vitreous sections. *Embo J*, 23(18):3583–3588, 2004.

[105] US Patent 3,013,467.

[106] Davidovits, Paul and Egger, David M. Photomicrography of corneal endothelial cells in vivo. *Nature*, 244(5415):366–367, 1973.

[107] James B Pawley. *Points, Pixels, and Gray Levels: Digitizing Image Data*. Springer, 2006.

[108] Ustione, A and Piston, D.W. A simple introduction to multiphoton microscopy. *Journal of Microscopy*, 243(3):221–226, 2011.

[109] LA Feigin and DI Svergun. *Structure Analysis by Small-Angle X-Ray and Neutron Scattering*. Springer, 1987.

[110] Th Zemb and P Lindner. *Neutron, X-rays and Light. Scattering Methods Applied to Soft Condensed Matter*. Elsevier, 1 edition, 2002.

[111] Dmitri I Svergun and Michel HJ Koch. Small-angle scattering studies of biological macromolecules in solution. *Reports on Progress in Physics*, 66(10):1735, 2003.

[112] Emanuela Di Cola, Isabelle Grillo, and Sandra Ristori. Small angle x-ray and neutron scattering: Powerful tools for studying the structure of drug-loaded liposomes. *Pharmaceutics*, 8(2), 2016.

[113] Mitsuhiro Hirai, Hiroki Iwase, Tomohiro Hayakawa, Masaharu Koizumi, and Hiroshi Takahashi. Determination of asymmetric structure of Ganglioside-DPPC mixed vesicle using SANS, SAXS, and DLS. *Biophys J*, 85(3):1600–1610, 2003.

[114] Shuo Qian and William T Heller. Peptide-Induced asymmetric distribution of charged lipids in a vesicle bilayer revealed by Small-Angle neutron scattering. *J Phys chem B*, 115(32): 9831–9837, 2011.

[115] Alekos D Tsamaloukas, Sandro Keller, and Heiko Heerklotz. Uptake and release protocol for assessing membrane binding and permeation by way of isothermal titration calorimetry. *Nature Protocols*, 2(3):695–704, 2007.

[116] Tjelvar SG Olsson, John E Ladbury, Will R Pitt, and Mark A Williams. Extent of enthalpy–entropy compensation in protein–ligand interactions. *Protein Sci*, 20(9):1607–1618, 2011.

[117] Gunter Sauerbrey. Verwendung von schwingquarzen zur wagung dunner schichten und zur mikrowagung. *Zeitschrift F R Physik*, 155(2):206–222, 1959.

[118] M.V. Voinova. ‘Missing mass’ effect in biosensor’s QCM applications. *Biosensors and Bioelectronics*, 17(10):835–841, 2002.

[119] Fredrik Höök, Bengt Kasemo, Tommy Nylander, Camilla Fant, Kristin Sott, and Hans Elwing. Variations in coupled water, viscoelastic properties, and film thickness of a mefp-1

protein film during adsorption and Cross-Linking: a quartz crystal microbalance with dissipation monitoring, ellipsometry, and surface plasmon resonance study. *Anal Chem*, 73(24): 5796–5804, 2001.

[120] Grégorio Crini. Review: a history of cyclodextrins. *Chemical Reviews*, 114(21):10940–75, 2014.

[121] Franz Schardinger. Über thermophile bakterien aus verschiedenen speisen und milch. *Z.Unter.Nahr*, 6(19):865–880, 1903.

[122] Deborah Michel, Jackson M Chitanda, Réka Balogh, Peng Yang, Jagbir Singh, Umashankar Das, El-Aneed, Anas, Jonathan Dimmock, Ronald Verrall, and Ildiko Badea. Design and evaluation of cyclodextrin-based delivery systems to incorporate poorly soluble curcumin analogs for the treatment of melanoma. *Eur J Pharm Biopharm*, 81(3):548–556, 2012.

[123] Ana Figueiras, JMG Sarraguça, Rui A Carvalho, AACC Pais, and Francisco JB Veiga. Interaction of omeprazole with a methylated derivative of β-Cyclodextrin: phase solubility, NMR spectroscopy and molecular simulation. *Pharm Res*, 24(2):377–389, 2007.

[124] A Bom, M Bradley, K Cameron, and JK Clark. A novel concept of reversing neuromuscular block: chemical encapsulation of rocuronium bromide by a cyclodextrin-based synthetic host. *Angewandte Chemie*, 2002.

[125] A Cooper, MA Nutley, and P Camilleri. Microcalorimetry of chiral surfactant-cyclodextrin interactions. *Anal Chem*, 70(23):5024–8, 1998.

[126] Marina Tsianou and Ankitkumar I Fajalia. Cyclodextrins and surfactants in aqueous solution above the critical micelle concentration: Where are the cyclodextrins located? *Langmuir*, 30 (46):13754–13764, 2014.

[127] De R Lisi, S Milioto, and N Muratore. Calorimetric study of sodium n alkanoate-modified cyclodextrin water ternary systems. *Langmuir*, 16(10):4441–4446, 2000.

[128] Akihito Hashidzume and Akira Harada. Recognition of polymer side chains by cyclodextrins. *Polymer Chemistry*, 2, 2011.

[129] ACF Ribeiro, MA Esteso, VMM Lobo, AJM Valente, SMN Simões, AJFN Sobral, L Ramos, HD Burrows, AM Amado, and Amorim AM da Costa. Interactions of copper (II) chloride with β-Cyclodextrin in aqueous solutions. *J Carbohyd Chem*, 25(2-3):173–185, 2006.

[130] ACF Ribeiro, VMM Lobo, AJM Valente, N Simões, AJFN Sobral, ML Ramos, and Hugh D Burrows. Association between ammonium monovanadate and β-Cyclodextrin as seen by NMR and transport techniques. *Polyhedron*, 25, 2006.

[131] Thorsteinn Loftsson and Marcus E Brewster. Cyclodextrins as functional excipients: Methods to enhance complexation efficiency. *J Pharm Sci.*, 101(9):3019–3032, 2012.

[132] Chao Yuan, Lei Du, Zhengyu Jin, and Xueming Xu. Storage stability and antioxidant activity of complex of astaxanthin with hydroxypropyl-β-cyclodextrin. *Carbohydr Polym.*, 91(1): 385–389, 2013.

[133] Abhishek Singh, Zelalem Worku, and Guy den Mooter. Oral formulation strategies to improve solubility of poorly water-soluble drugs. *Expert Opin Drug Deliv.*, 8(10):1361–1378, 2011.

[134] Ji-Yeon Chun, Sung-Kyu You, Mi-Yeon Lee, Mi-Jung Choi, and Sang-Gi Min. Characterization of β-cyclodextrin self-aggregates for eugenol encapsulation. *International Journal of Food Enginnering*, 8, 2012.

[135] Nikolay E Polyakov, Vladimir K Khan, Marc B Taraban, Tatyana V Leshina, Nariman F Salakhutdinov, and Genrikh A Tolstikov. Complexation of lappaconitine with glycyrrhizic acid: stability and reactivity studies. *PLoS Computational Biology*, 109(51):24526–24530, 2005.

[136] Cristiano Andrade Dias, Sergio Lima, Jose JC Teixeira Dias, and Jose Teixeira. Why do methylated and unsubstituted cyclodextrins interact so differently with sodium decanoate micelles in water? *J Phys Chem B*, 112(48):15327–15332, 2008.

[137] Thorsteinn Loftsson, Auethur Magnúsdóttir, Már Másson, and Jóhanna F F Sigurjónsdóttir. Self-association and cyclodextrin solubilization of drugs. *J Pharm Sci*, 91(11):2307–16, 2002.

[138] Massimo Bonini, Simona Rossi, Göran Karlsson, Mats Almgren, Pierandrea Nostro, and Piero Baglioni. Self-assembly of β-cyclodextrin in water part 1: Cryo tem and dynamic and static light scattering. *Langmuir*, 22(4):1478–1484, 2006.

[139] Valérie Gabelica, Nives Galic, and Edwin Pauw. On the specificity of cyclodextrin complexes detected by electrospray mass spectrometry. *J Am Soc Mass Spectr*, 13(8):946–953, 2002.

[140] Nicolas Taulier and Tigran V Chalikian. Hydrophobic hydration in cyclodextrin complexation. *J Phys Chem B*, 110(25):12222–12224, 2006.

[141] M.E. Bellringer, T.G. Smith, R Read, C Gopinath, and Ph. Olivier. β-Cyclodextrin: 52-Week toxicity studies in the rat and dog. *Food Chem Toxicol.*, 33(5):367–376, 1995.

[142] Yoshikazu Oka, Shinnosuke Nakamura, Tatsuya Morozumi, and Hiroshi Nakamura. TritonX-100 selective chemosensor based on β-cyclodextrin modified by anthracene derivative. *Talanta*, 82(4):1622–1626, 2010.

[143] Jiang Bing-ying, Zang Rong-rong, Xie jia-qing, Du Juan, Meng Xiang-guang, and Zeng Xian-cheng. Catalytic hydrolyses of carboxylic acid esters in the presence of gemini surfactant. *J Disper Sci Technol*, 26(1):105–110, 2005.

[144] Jie Hu, Rong Huang, Shunsheng Cao, and Yinqun Hua. Unique structure and property of cyclodextrin and its utility in polymer synthesis. *e-Polymers*, 8, 2008.

[145] G Astray, Gonzalez-Barreiro, C, JC Mejuto, Rial-Otero, R, and Simal-Gándara, J. A review on the use of cyclodextrins in foods. *Food Hydrocolloids*, 23, 2009.

[146] Maelle Monteil, Marc Lecouvey, David Landy, Steven Ruellan, and Isabelle Mallard. Cyclodextrins: A promising drug delivery vehicle for bisphosphonate. *Carbohyd Polym*, 156: 285–293, 2017.

[147] Mark E Davis and Marcus E Brewster. Cyclodextrin-based pharmaceutics: past, present and future. *Nat Rev Drug Discov.*, 3(12):1023–35, 2004.

[148] H Dodziuk. *Cyclodextrins and their complexes: chemistry, analytical methods, applications*. Wiley-VCH Verlag GmbH Co., 2006.

[149] József Szejtli and József Szejtli. *Cyclodextrins*, volume 1. Pergamon, 1988.

[150] Jacob Israelachvili and Håkan Wennerström. Role of hydration and water structure in biological and colloidal interactions. *Nature*, 379(6562):219–225, 1996.

[151] J Szejtli. Introduction and general overview of cyclodextrin chemistry. *Chemical Reviews*, 98:1743–1758, 1998.

[152] Myron L Bender, Makoto Komiyama, Myron L Bender, and Makoto Komiyama. *Introduction*, volume 6. 1978.

[153] J Szejtli. Highly soluble β Cyclodextrin derivatives. *Starch - Stärke*, 36(12):429–432, 1984.

[154] J L Atwood and J M Lehn. *Comprehensive Supramolecular chemistry*, volume 3. Pergamon, 1996.

[155] O Söderman, WS Price, and M Schönhoff. NMR diffusometry applied to liquids. *Langmuir*, 156:38–44, 2010.

[156] Martin Messner, Sergey V Kurkov, Marcus E Brewster, Phatsawee Jansook, and Thorsteinn Loftsson. Self-assembly of cyclodextrin complexes: Aggregation of hydrocortisone/cyclodextrin complexes. *Int J Pharm.*, 407(1-2):174–183, 2011.

[157] Wolfgang Linert, Peter Margl, and Franz Renz. Solute-solvent interactions between cyclodextrin and water: a molecular mechanical study. *Chemical Physics*, 161(3):327–338, 1992.

[158] Phillip W Snyder, Jasmin Mecinović, Demetri T Moustakas, Samuel W Thomas, Michael Harder, Eric T Mack, Matthew R Lockett, Annie Héroux, Woody Sherman, and George M Whitesides. Mechanism of the hydrophobic effect in the biomolecular recognition of arylsulfonamides by carbonic anhydrase. *Proc National Acad Sci*, 108(44):17889–17894, 2011.

[159] Mikhail V Rekharsky and Yoshihisa Inoue. Complexation thermodynamics of cyclodextrins. *Chemical Reviews*, 98(5):1875–1918, 1998.

[160] Yifeng He, Pei Fu, Xinghai Shen, and Hongcheng Gao. Cyclodextrin-based aggregates and characterization by microscopy. *Micron*, 39(5):495–516, 2007.

[161] Nimmagadda Jyothirmayi, Candadai S Ramadoss, and Soundar Divakar. Nuclear magnetic resonance studies of cyclodextrin complexes of linoleic acid and arachidonic acid. *Journal of Agricultural and Food Chemistry*, 39(12):2123–2127, 1991.

[162] Wolfram Saenger and Müller-Fahrnow, Anke. Cyclodextrins increase surface tension and critical micelle concentrations of detergent solutions. *Angewandte Chemie*, 27(3):393–394, 1988.

[163] Volker Zabel, Wolfram Saenger, and Sax A Mason. Topography of cyclodextrin inclusion complexes. part 23. neutron diffraction study of the hydrogen bonding in .beta.-cyclodextrin undecahydrate at 120 k: from dynamic flip-flops to static homodromic chains. *JACS*, 108 (13):3664–3673, 1986.

[164] Anthony W. Coleman, Ioannis Nicolis, Nelly Keller, and Jean Pierre Dalbiez. Aggregation of cyclodextrins: An explanation of the abnormal solubility ofβ-cyclodextrin. *Journal of inclusion phenomena and molecular recognition in chemistry*, 13(2):139–143, 1992.

[165] Rodríguez P. Isasi J. R. Fuentes M. Tardajos G. Sánchez M. González-Gaitano, G. The aggregation of cyclodextrins as studied by photon correlation spectroscopy. *Journal of inclusion phenomena and macrocyclic chemistry*, 44(1):101–105, 2002.

[166] Artur J M Valente, Rui A. Carvalho, and Olle Söderman. Do Cyclodextrins Aggregate in Water? Insights from NMR Experiments. *Langmuir*, 31(23):6314–6320, 2015.

[167] W Blokzijl and JBFN Engberts. Hydrophobic effects. opinions and facts. *Angewandte Chemie*, 32:1545–1579, 1993.

[168] Hernandez-Pascacio, Jorge, Angel Pineiro, Juan M Ruso, Natalia Hassan, Richard A Campbell, Campos-Teran, Jose, and Miguel Costas. Complex behavior of aqueous α-Cyclodextrin solutions. interfacial morphologies resulting from bulk aggregation. *Langmuir*, 32(26): 6682–90, 2016.

[169] Helena Dodziuk, Wiktor Koźmiński, and Andrzej Ejchart. NMR studies of chiral recognition by cyclodextrins. *Chirality*, 16(2):90–105, 2004.

[170] Helena Dodziuk, Jerzy Sitkowski, Lech Stefaniak, Janusz Jurczak, and Danuta Sybilska. 13 c NMR differentiation of diastereoisomeric complexes of cis -decalin with β-cyclodextrin. *J Chem Soc Chem Commun*, 0(3):207–208, 1992.

[171] Ana M Amado and Ribeiro-Claro, Paulo JA. H/D and D/H exchange rates in α-cyclodextrin and α-cyclodextrin inclusion compounds raman spectroscopic study. *J Chem Soc Faraday Transactions*, 93(14):2387–2390, 1997.

[172] Y Ohtani, T Irie, K Uekama, K Fukunaga, and J Pitha. Differential effects of alpha-, beta- and gamma-cyclodextrins on human erythrocytes. *European Journal of Biochemistry*, 186 (1-2):17–22, 1989.

[173] Patricia G. Yancey, Wendi V. Rodrigueza, Elisabeth P.C. Kilsdonk, Genevieve W. Stoudt, William J. Johnson, Michael C. Phillips, and George H. Rothblat. Cellular cholesterol efflux mediated by cyclodextrins: Demonstration of kinetic pools and mechanism of efflux. *Journal of Biological Chemistry*, 271(27):16026–16034, 1996.

[174] J. Mascetti, S. Castano, D. Cavagnat, and B. Desbat. Organization of β-cyclodextrin under pure cholesterol, DMPC, or DMPG and mixed cholesterol/phospholipid monolayers. *Langmuir*, 24(17):9616–9622, 2008.

[175] Cesar A. Lopez, Alex H. de Vries, and Siewert J. Marrink. Molecular mechanism of cyclodextrin mediated cholesterol extraction. *PLoS Computational Biology*, 7(3), 2011.

[176] Marie-Cécile Giocondi, Pierre Emmanuel Milhiet, Patrice Dosset, and Christian Le Grimellec. Use of Cyclodextrin for AFM Monitoring of Model Raft Formation. *Biophysical Journal*, 86(2):861–869, 2004.

[177] Rania Leventis and John R. Silvius. Use of cyclodextrins to monitor transbilayer movement and differential lipid affinities of cholesterol. *Biophysical Journal*, 81(4):2257 – 2267, 2001.

[178] Thomas G. Anderson, Anmin Tan, Peter Ganz, and Joachim Seelig. Calorimetric Measurement of Phospholipid Interaction with Methyl-β-Cyclodextrin. *Biochemistry*, 43(8):2251–2261, 2004.

[179] Wasinee Khuntawee, Peter Wolschann, Thanyada Rungrotmongkol, Jirasak Wong-Ekkabut, and Supot Hannongbua. Molecular Dynamics Simulations of the Interaction of Beta Cyclodextrin with a Lipid Bilayer. *Journal of Chemical Information and Modeling*, 55(9): 1894–1902, 2015.

[180] Sunil S Jambhekar and Philip Breen. Cyclodextrins in pharmaceutical formulations i: structure and physicochemical properties, formation of complexes, and types of complex. *Drug Discov Today*, 21(2):356–362, 2016.

[181] Thorsteinn Loftsson and Dominique Duchêne. Cyclodextrins and their pharmaceutical applications. *Int J Pharm.*, 329(1-2):1–11, 2007.

[182] Jonathan P Litz, Niket Thakkar, Thomas Portet, and Sarah L Keller. Depletion with cyclodextrin reveals two populations of cholesterol in model lipid membranes. *Biophysical Journal*, 110(3):635–645, 2016.

[183] C. A. Keller, K. Glasmästar, V. P. Zhdanov, and B. Kasemo. Formation of supported membranes from vesicles. *Phys. Rev. Lett.*, 84:5443–5446, 2000.

[184] Joshua A Jackman, Min Kim, Vladimir P Zhdanov, and Nam-Joon Cho. Relationship between vesicle size and steric hindrance influences vesicle rupture on solid supports. *Physical Chemistry Chemical Physics*, 18(4):3065–3072, 2015.

[185] ImageJ. Particle Analysis imagej, 2017. URL `https://imagej.net/Particle_Analysis`.

[186] Bastien Seantier and Bengt Kasemo. Influence of mono- and divalent ions on the formation of supported phospholipid bilayers via vesicle adsorption. *Langmuir*, 25(10):5767–5772, 9 2009.

[187] Ralf P Richter, Rémi Bérat, and Alain R Brisson. Formation of Solid-Supported lipid bilayers: An integrated view. *Langumir*, 22(8):3497–3505, 2006.

[188] Kathleen F Wang, Ramanathan Nagarajan, Charlene M Mello, and Terri A Camesano. Characterization of supported lipid bilayer disruption by chrysophsin-3 using QCM-D. *J Phys Chem B*, 115(51):15228–35, 2011.

[189] Joshua A Jackman, Min Kim, Vladimir P Zhdanov, and Nam-Joon Cho. Relationship between vesicle size and steric hindrance influences vesicle rupture on solid supports. *Phys Chem Chem Phys.*, 18(4):3065–3072, 2015.

[190] József Szejtli. Introduction and general overview of cyclodextrin chemistry. *Chemical Reviews*, 98(5):1743–1754, 7 1998.

[191] Cesar A Lopez, Alex H de Vries, and Siewert J Marrink. Molecular mechanism of cyclodextrin mediated cholesterol extraction. *PLoS Computational Biology*, 7(3):e1002020, 11 2011.

[192] Cesar A Lopez, Alex H de Vries, and Siewert J Marrink. Computational microscopy of cyclodextrin mediated cholesterol extraction from lipid model membranes. *Scientific Reports*, 3, 2013.

[193] Edgar Mixcoha, José Campos-Terán, and Ángel Piñeiro. Surface adsorption and bulk aggregation of cyclodextrins by computational molecular dynamics simulations as a function of temperature: α-cd vs β-cd. *The Journal of Physical Chemistry B*, 118(25):6999–7011, 2014.

[194] John F. Nagle and Stephanie Tristram-Nagle. Structure of lipid bilayers. *Biochimica et Biophysica Acta (BBA) - Reviews on Biomembranes*, 1469(3):159–195, 2000.

[195] Andreas Weinberger, Feng-Ching Tsai, Gijsje H Koenderink, Thais F Schmidt, Rosângela Itri, Wolfgang Meier, Tatiana Schmatko, André Schroder, and Carlos Marques. Gel-assisted formation of giant unilamellar vesicles. *Biophysical Journal*, 105(1):154–164, 2013.

[196] Kathleen F. Wang, Ramanathan Nagarajan, Charlene M. Mello, and Terri A. Camesano. Characterization of supported lipid bilayer disruption by chrysophsin-3 using qcm-d. *The Journal of Physical Chemistry B*, 115(51):15228–35, 12 2011.

[197] Tereza Pereira de Souza, Guilherme Volpe Bossa, Pasquale Stano, Frank Steiniger, Sylvio May, Pier Luigi Luisi, and Alfred Fahr. Vesicle aggregates as a model for primitive cellular assemblies. *Phys. Chem. Chem. Phys.*, 19:20082–20092, 2017.

[198] Reinhard Lipowsky. Coupling of bending and stretching deformations in vesicle membranes. *Advances in Colloid and Interface Science*, 208:14 – 24, 2014.

[199] O. Kahraman, N. Stoop, and M. M. Müller. Morphogenesis of membrane invaginations in spherical confinement. *EPL (Europhysics Letters)*, 97(6):68008, 2012.

[200] Baghali G Mathapa and Vesselin N Paunov. Cyclodextrin stabilised emulsions and cyclodextrinosomes. *Physical chemistry chemical physics : PCCP*, 15(41):17903–14, 2013.

[201] Xue Li, Haiyan Li, Qun Xiao, Liuyi Wang, Manli Wang, Xiaolong Lu, Peter York, Senlin Shi, and Jiwen Zhang. Two-way effects of surfactants on pickering emulsions stabilized by the self-assembled microcrystals of [small alpha]-cyclodextrin and oil. *Phys. Chem. Chem. Phys.*, 16:14059–14069, 2014.

[202] Erika Specogna, King Wo Li, Madeleine Djabourov, Florent Carn, and Kawthar Bouchemal. Dehydration, dissolution, and melting of cyclodextrin crystals. *The Journal of Physical Chemistry B*, 119(4):1433–1442, 2015.

[203] Xue Li, Haiyan Li, Qun Xiao, Liuyi Wang, Manli Wang, Xiaolong Lu, Peter York, Senlin Shi, and Jiwen Zhang. Two-way effects of surfactants on pickering emulsions stabilized by the self-assembled microcrystals of α-cyclodextrin and oil. *Physical Chemistry Chemical Physics*, 16(27):14059–14069, 2014.

[204] Zhang Qian Zhang Chong Zhao Qiang Ai Hongqi Sun Dezhi Xing, Shengkai. Isothermal titration calorimetry and theoretical studies on host-guest interaction of ibuprofen with α-, β- and γ-cyclodextrin. *Journal of Solution Chemistry*, 38(5):531–543, May 2009.

[205] Małgorzata Wszelaka-Rylik and Paweł Gierycz. Isothermal titration calorimetry (itc) study of natural cyclodextrins inclusion complexes with tropane alkaloids. *Journal of Thermal Analysis and Calorimetry*, 121(3):1359–1364, 2015.

[206] Edith González-Mondragón, Armando Torralba-González, Ponciano García-Gutiérrez, Vania S. Robles-González, Alma Y. Salazar-Govea, and Rafael A. Zubillaga. Thermodynamic analysis of ferulate complexation with α-, β- And γ-cyclodextrins. *Thermochimica Acta*, 634:1–5, 2016.

[207] Artur J M Valente and Olle Söderman. The formation of host-guest complexes between surfactants and cyclodextrins. *Advances in Colloid and Interface Science*, 205:156–176, 2014.

[208] Torsten Wieprecht, Ognjan Apostolov, Michael Beyermann, and Joachim Seelig. Membrane binding and pore formation of the antibacterial peptide pgla: thermodynamic and mechanistic aspects. *Biochemistry*, 39(2):442–452, 2000.

[209] Gabriela Klocek, Therese Schulthess, Yechiel Shai, and Joachim Seelig. Thermodynamics of melittin binding to lipid bilayers. aggregation and pore formation. *Biochemistry*, 48(12): 2586–2596, 2009.

[210] J. R. Henriksen and T. L. Andresen. Thermodynamic profiling of peptide membrane interactions by isothermal titration calorimetry: A search for pores and micelles. *Biophysical Journal*, 101(1):100–109, 2011.

[211] Bert Ph.M. Menco Keizo Takeshita Nanda K. Subbarao Lan-rong Hu Robert C. MacDonald, Ruby I. MacDonald. Small-volume extrusion apparatus for preparation of large, unilamellar vesicles. *Biochimica et Biophysica Acta (BBA) - Biomembranes*, 1061(2):297 – 303, 1991.

[212] Wye-Khay Fong, Tracey Hanley, and Ben J Boyd. Stimuli responsive liquid crystals provide ‘on-demand’ drug delivery in vitro and in vivo. *J Control Release.*, 135(3):218–226, 2009.

[213] Anan Yaghmur and Otto Glatter. Characterization and potential applications of nanostructured aqueous dispersions. *Adv Colloid Interface Sci.*, 147:333–342, 2009.

[214] Georg Pabst, Norbert Kucerka, Mu-Ping Nieh, and John Katsaras. *Liposomes, Lipid Bilayers and Model Membranes: From Basic Research to Application*. CRC Press, USA, 1 edition, 20016.

[215] Jacob N. and Israelachvili. *Intermolecular and surface forces - 3rd Edition*. 2011.

[216] Krister Holmberg, Bo Jonsson, Bengt Kronberg, and Bjorn Lindman. *Surfactants and Polymers in Aqueous Solution, Second Edition*. 2017.

[217] Jacob N Israelachvili, John D Mitchell, and Barry W Ninham. Theory of self-assembly of hydrocarbon amphiphiles into micelles and bilayers. *J Chem Soc Faraday Transactions 2 Mol Chem Phys*, 72(0):1525–1568, 1976.

[218] J Engblom, Y Miezis, T Nylander, V Razumas, and K Larsson. On the swelling of monoolein liquid-crystalline aqueous phases in the presence of distearoylphosphatidylglycerol. *Surface and Colloids Science*, pages 9–15, 2001.

[219] Vadim Cherezov, Jeffrey Clogston, Yohann Misquitta, Abdel-Gawad, Wissam, and Martin Caffrey. Membrane protein crystallization in meso: Lipid Type-Tailoring of the cubic phase. *Biophys J.*, 83(6):3393–3407, 2002.

[220] Changchang Liu, Xiaoming Wang, Sungchul Lee, Lisa D Pfefferle, and Gary L Haller. Surfactant chain length effect on the hexagonal-to-cubic phase transition in mesoporous silica synthesis. *Microporous and Mesoporous Materials*, 147(1):242–251, 2012.

[221] Arwen II Tyler, Hanna MG Barriga, Edward S Parsons, McCarthy, Nicola LC, Oscar Ces, Robert V Law, John M Seddon, and Nicholas J Brooks. Electrostatic swelling of bicontinuous cubic lipid phases. *Soft Matter*, 11(16):3279–3286, 2015.

[222] Anan Yaghmur, Liliana de Campo, Laurent Sagalowicz, Martin E Leser, and Otto Glatter. Emulsified microemulsions and Oil-Containing liquid crystalline phases. *Langmuir*, 21(2): 569–577, 2005.

[223] Amar-Yuli, Idit and Nissim Garti. Transitions induced by solubilized fat into reverse hexagonal mesophases. *Colloids and Surfaces B: Biointerfaces*, 43(2):72–82, 2005.

[224] Yao-Da Dong, Ian Larson, Tracey Hanley, and Ben J Boyd. Bulk and dispersed aqueous phase behavior of phytantriol: effect of vitamin e acetate and f127 polymer on liquid crystal nanostructure. *Langumir*, 22(23):9512–9518, 2006.

[225] Tarek S Awad, Yoshihide Okamoto, Shah Masum, and Masahito Yamazaki. Formation of cubic phases from large unilamellar vesicles of Dioleoylphosphatidylglycerol/Monoolein membranes induced by low concentrations of ca2+. *Langmuir*, 21(25):11556–11561, 2005.

[226] Anan Yaghmur, Peter Laggner, Barbara Sartori, and Michael Rappolt. Calcium triggered Lα-H2 phase transition monitored by combined rapid mixing and Time-Resolved synchrotron SAXS. *Plos One*, 3(4):e2072, 2008.

[227] Anan Yaghmur, Barbara Sartori, and Michael Rappolt. The role of calcium in membrane condensation and spontaneous curvature variations in model lipidic systems. *Phys Chem Chem Phys*, 13(8):3115–3125, 2010.

[228] Gregory L Kirk, Sol M Gruner, and DL Stein. A thermodynamic model of the lamellar to inverse hexagonal phase transition of lipid membrane-water systems. *Biochemistry*, 23(6): 1093–1102, 1984.

[229] PM Duesing, RH Templer, and JM Seddon. Quantifying packing frustration energy in inverse lyotropic mesophases. *Langumir*, 13(2):351–359, 1997.

[230] M Hamm and M.M. Kozlov. Tilt model of inverted amphiphilic mesophases. *Eur. Phys. J. B*, 6(4):519–528, 1998.

[231] John M Seddon. Structure of the inverted hexagonal (HII) phase, and non-lamellar phase transitions of lipids. *Biochim Biophys Acta.*, 1031(1):1–69, 1990.

[232] RH Templer, JM Seddon, PM Duesing, R Winter, and J Erbes. Modeling the phase behavior of the inverse hexagonal and inverse bicontinuous cubic phases in 2:1 fatty Acid/Phosphatidylcholine mixtures. *J Phys Chem B*, 102(37):7262–7271, 1998.

[233] RP Rand, NL Fuller, Gruner, and VA Parsegian. Membrane curvature, lipid segregation, and structural transitions for phospholipids under dual-solvent stress. *Biochemistry*, 29(1): 76–87, 1990.

[234] BJ Khoo. *An experimental examination of ideas in the curvature elasticity of lyotropic liquid crystals*. Imperial College London, 1996.

[235] H Vacklin, BJ Khoo, KH Madan, JM Seddon, and RH Templer. The bending elasticity of 1-Monoolein upon relief of packing stress. *Langumir*, 16(10):4741–4748, 2000.

[236] W Helfrich. Elastic properties of lipid bilayers: theory and possible experiments. *Zeitschrift Für Naturforschung Teil C Biochem Biophysik Biologie Virologie*, 28(11):693–703, 1973.

[237] E. Sackmann. Membrane bending energy concept of vesicle- and cell-shapes and shape-transitions. *FEBS Letters*, 346(1):3 – 16, 1994.

[238] GC Shearman, O Ces, RH Templer, and JM Seddon. Inverse lyotropic phases of lipids and membrane curvature. *Journal of Physics: Condensed Matter*, 18(28):S1105, 2006.

[239] Manfredo P do Carmo. *Hypersurfaces of constant mean curvature*, volume 1410. Springer, 1989.

[240] D.P. Siegel and M.M. Kozlov. The gaussian curvature elastic modulus of N-Monomethylated dioleoylphosphatidylethanolamine: Relevance to membrane fusion and lipid phase behavior. *Biophys J.*, 87(1):366–374, 2004.

[241] V Luzzati and F Husson. The structure of the liquid-crystalline phases of lipid-water systems. *J Cell Biol*, 12(2):207–219, 1962.

[242] Scriven, L.E. Equilibrium bicontinuous structure. *Nature*, 263(5573):123–125, 1976.

[243] Alto D Benedicto and O'Brien, David F. Bicontinuous cubic morphologies in block copolymers and amphiphile/water systems: mathematical description through the minimal surfaces. 30(11):3395–3402, 1997.

[244] Alan H Schoen. Infinite periodic minimal surfaces without self-intersections. *NASA technical reports*, page 92, 1970.

[245] ST Hyde and S Andersson. A cubic structure consisting of a lipid bilayer forming an infinite periodic minimum surface of the gyroid type in the glycerolmonooleat-water system. *Crystalline Materials*, 1984.

[246] ES Lutton. Phase behavior of aqueous systems of monoglycerides. *J Am Oil Chem Soc*, 42 (12):1068–1070, 1965.

[247] Hong Qiu and Martin Caffrey. The phase diagram of the monoolein/water system: metastability and equilibrium aspects. *Biomaterials*, 21(3):223–234, 2000.

[248] Jian-Chun Li, Na Zhu, Jin-Xiu Zhu, Wen-Jing Zhang, Hong-Min Zhang, Qing-Qing Wang, Xiao-Xiang Wu, Xiu Wang, Jin Zhang, and Ji-Fu Hao. Self-Assembled cubic liquid crystalline nanoparticles for transdermal delivery of paeonol. *Med Sci Monit.*, 21:3298–3310, 2015.

[249] Tomas Landh. Phase behavior in the system pine needle oil Monoglycerides-Poloxamer 407-Water at 20.degree. *Journal of Physical Chemistry*, 98(34):8453–8467, 1994.

[250] Josephine YT Chong, Xavier Mulet, Lynne J Waddington, Ben J Boyd, and Calum J Drummond. Steric stabilisation of self-assembled cubic lyotropic liquid crystalline nanoparticles : high throughput evaluation of triblock polyethylene oxide-polypropylene oxide-polyethylene oxide copolymers. *Soft Matter*, 7(10):4768–4777, 2011.

[251] Paschalis Alexandridis. Amphiphilic copolymers and their applications. *Curr Opin Colloid Interface Sci*, 1(4):490–501, 1996.

[252] M Nakano, A Sugita, H Matsuoka, and T Handa. Small-angle x-ray scattering and 13C NMR investigation on the internal structure of “cubosomes”. *Langumir*, 17:3917–3922, 2001.

[253] Pelle Stroem and David M Anderson. The cubic phase region in the system didodecyldimethylammonium bromide-water-styrene. *Langumir*, 8(2):691–709, 1992.

[254] Borislav Angelov, Angelina Angelova, Markus Drechsler, Vasil M Garamus, Rada Mutafchieva, and Sylviane Lesieur. Identification of large channels in cationic PEGylated cubosome nanoparticles by synchrotron radiation SAXS and Cryo-TEM imaging. *Sof Matter*, 11(18):3686–3692, 2015.

[255] HMG Barriga, AII Tyler, McCarthy, NLC, ES Parsons, O Ces, RV Law, JM Seddon, and NJ Brooks. Temperature and pressure tuneable swollen bicontinuous cubic phases approaching nature’s length scales. 11(3):600–7, 2014.

[256] Letícia Rodrigues, Konstantinos Kyriakos, Fabian Schneider, Hendrik Dietz, Gerhard Winter, Christine M Papadakis, and Madlen Hubert. Characterization of lipid-based hexosomes as versatile vaccine carriers. *Mol. Pharmaceutics*, 13(11):3945–3954, 2016.

[257] Davide Demurtas, Paul Guichard, Isabelle Martiel, Raffaele Mezzenga, Cécile Hébert, and Laurent Sagalowicz. Direct visualization of dispersed lipid bicontinuous cubic phases by cryo-electron tomography. *Nature Communications*, 6:8915, 2015.

[258] G Pabst, N Kučerka, MP Nieh, and MC Rheinstädter. Applications of neutron and x-ray scattering to the study of biologically relevant model membranes. *Chemistry and Physics of Lipids*, 163:460–479, 2010.

[259] Matthew L Lynch, Ofori-Boateng, Akua, Amanda Hippe, Kelly Kochvar, and Patrick T Spicer. Enhanced loading of water-soluble actives into bicontinuous cubic phase liquid crystals using cationic surfactants. *Journal of Colloid and Interface Science*, 260(2):404–413, 2003.

[260] J Clogston, G Craciun, D.J. Hart, and M Caffrey. Controlling release from the lipidic cubic phase by selective alkylation. *Journal of Control Release*, 102(2):441–461, 2005.

[261] Renata Negrini, Wye-Khay Fong, Ben J Boyd, and Raffaele Mezzenga. pH-responsive lyotropic liquid crystals and their potential therapeutic role in cancer treatment. *Chem. Commun.*, 51(30):6671–4, 2015.

[262] Ewa Nazaruk, Monika Szlęzak, Ewa Górecka, Renata Bilewicz, Yazmin M Osornio, Peter Uebelhart, and Ehud M Landau. Design and assembly of pH-Sensitive lipidic cubic phase matrices for drug release. *Langmuir*, 30(5):1383–90, 2014.

[263] Borislav Angelov, Angelina Angelova, Vasil M Garamus, Geneviève Lebas, Sylviane Lesieur, Michel Ollivon, Sérgio S Funari, Regine Willumeit, and Patrick Couvreur. Small-Angle neutron and x-ray scattering from amphiphilic Stimuli-Responsive Diamond-Type bicontinuous cubic phase. *J. Am. Chem. Soc.*, 129(44):13474–13479, 2007.

[264] Renata Negrini and Raffaele Mezzenga. Diffusion, molecular separation, and drug delivery from lipid mesophases with tunable water channels. *Langmuir*, 28(47):16455–16462, 2012.

[265] Renata Negrini, Sanchez-Ferrer, Antoni, and Raffaele Mezzenga. Influence of electrostatic interactions on the release of charged molecules from lipid cubic phases. *Langmuir*, 30(15): 4280–4288, 2014.

[266] Renata Negrini and Raffaele Mezzenga. pH-Responsive lyotropic liquid crystals for controlled drug delivery. *Langumir*, 27(9):5296–5303, 2011.

[267] Vincent Ho, Nigel Slater, and Rongjun Chen. pH-responsive endosomolytic pseudo-peptides for drug delivery to multicellular spheroids tumour models. *Biomaterials*, 32(11):2953–2958, 2011.

[268] Rongjun Chen, Sariah Khormaee, Mark E Eccleston, and Nigel Slater. The role of hydrophobic amino acid grafts in the enhancement of membrane-disruptive activity of pH-responsive pseudo-peptides. *Biomaterials*, 30(10):1954–1961, 2009.

[269] Shengwen Zhang, Andrew Nelson, Zachary Coldrick, and Rongjun Chen. The effects of substituent grafting on the interaction of pH-Responsive polymers with phospholipid monolayers. *Langmuir*, 27(13):8530–9, 2011.

[270] Angela Falchi, Antonella Rosa, Angela Atzeri, Alessandra Incani, Sandrina Lampis, Valeria Meli, Claudia Caltagirone, and Sergio Murgia. Effects of monoolein-based cubosome formulations on lipid droplets and mitochondria of HeLa cells. *Toxicology Research*, 4(4): 1025–1036, 2015.

[271] Georgeta Popescu, Justas Barauskas, Tommy Nylander, and Fredrik Tiberg. Liquid crystalline phases and their dispersions in aqueous mixtures of glycerol monooleate and glyceryl monooleyl ether. *Langmuir*, 23(2):496–503, 2007.

[272] J Gustafsson, Ljusberg-Wahren, H, and M Almgren. Cubic lipid water phase dispersed into submicron particles. *Langmuir*, 12(20):4611–4613, 1996.

[273] Piotr Garstecki and Robert Hołyst. Scattering patterns of Self-Assembled cubic phases. 1. the model. *Langmuir*, 18(7):2519–2528, 2002.

[274] David C Turner, Zhen-Gang Wang, Sol M Gruner, David A Mannock, and McElhaney, Ronald N. Structural study of the inverted cubic phases of di-dodecyl alkyl-B-D-glucopyranosyl-rac-glycerol. *J. Phys. II France*, 2(11):2039–2063, 1992.

[275] Jason Briggs, Hesson Chung, and Martin Caffrey. The Temperature-Composition phase diagram and mesophase structure characterization of the Monoolein/Water system. *J. Phys. II France*, 6(5):723–751, 1996.

[276] Thomas Bickel and Carlos M. Marques. Entropic interactions in soft nanomaterials. *Journal of Nanoscience and Nanotechnology*, 6(8):2386–2395(10), 2006.

[277] Borislav Angelov, Angelina Angelova, Michel Ollivon, Claudie Bourgaux, and Andrew Campitelli. Diamond-type lipid cubic phase with large water channels. *J Am Chem Soc.*, 125(24):7188–9, 2003.

[278] Rongjun Chen, Mark E Eccleston, Zhilian Yue, and Nigel KH Slater. Synthesis and pH-responsive properties of pseudo- peptides containing hydrophobic amino acid grafts. *J. Mater. Chem.*, 19(24):4217–4224, 2009.

[279] John M Seddon, Adam M Squires, Charlotte E Conn, Oscar Ces, Andrew J Heron, Xavier Mulet, Gemma C Shearman, and Richard H Templer. Pressure-jump x-ray studies of liquid crystal transitions in lipids. *Philosophical Transactions of the Royal Society of London A: Mathematical, Physical and Engineering Sciences*, 364(1847):2635–2655, 2006.

[280] Joseph A Mindell. Lysosomal acidification mechanisms. *Physiology*, 74(1):69–86, 2012.

[281] Sean D Conner and Sandra L Schmid. Regulated portals of entry into the cell. *Nature*, 422 (6927):37–44, 2003.

[282] Junping Wang, Dimitry Mongayt, and Vladimir P. Torchilin. Polymeric micelles for delivery of poorly soluble drugs: Preparation and anticancer activity in vitro of paclitaxel incorporated into mixed micelles based on poly(ethylene glycol)-lipid conjugate and positively charged lipids. *Journal of Drug Targeting*, 13(1):73–80, 2005.

[283] AAl-Muallem H., Wazeer M IM, and Sk.Asrof Ali. Synthesis and solution properties of a new ionic polymer and its behavior in aqueous two-phase polymer systems. *Polymer*, 43(4): 1041 – 1050, 2002.

[284] Eccleston ME., M Kuiper M., Gilchrist FM., and Slater NK. ph-responsive pseudo-peptides for cell membrane disruption. *Journal of Controlled Release*, 69(2):297 – 307, 2000.

[285] William B. Liechty, David R. Kryscio, Brandon V. Slaughter, and Nicholas A. Peppas. Polymers for drug delivery systems. *Annual Review of Chemical and Biomolecular Engineering*, 1:149–173, 2010.

[286] Younjin Min, Mustafa Akbulut, Kai Kristiansen, Yuval Golan, and Jacob Israelachvili. The role of interparticle and external forces in nanoparticle assembly. *Nature Materials*, 7(7): 527–538, 2008.

[287] Rongjun Chen, Sariah Khormaee, Mark E. Eccleston, and Nigel K.H. Slater. The role of hydrophobic amino acid grafts in the enhancement of membrane-disruptive activity of ph-responsive pseudo-peptides. *Biomaterials*, 30(10):1954 – 1961, 2009.

[288] Mahmoud Soliman, Rujikan Nasanit, Samer R. Abulateefeh, Stephanie Allen, Martyn C. Davies, Simon S. Briggs, Leonard W. Seymour, Jon A. Preece, Anna M. Grabowska, Susan A. Watson, and Cameron Alexander. Multicomponent synthetic polymers with viral-mimetic chemistry for nucleic acid delivery. *Molecular Pharmaceutics*, 9(1):1–13, 2012.

[289] Duncan MC Sharp, Andrew Picken, Timothy J Morris, Christopher J Hewitt, Karen Coopman, and Nigel KH Slater. Amphipathic polymer-mediated uptake of trehalose for dimethyl sulfoxide-free human cell cryopreservation. *Cryobiology*, 67(3):305–11, 2013.

[290] Andrew L. Lynch, Rongjun Chen, and Nigel K.H. Slater. ph-responsive polymers for trehalose loading and desiccation protection of human red blood cells. *Biomaterials*, 32(19): 4443 – 4449, 2011.

[291] Sariah Khormaee, Yong Choi, Michael J Shen, Biying Xu, Haitao Wu, Gary L Griffiths, Rongjun Chen, Nigel K Slater, and John K Park. Endosomolytic anionic polymer for the cytoplasmic delivery of sirnas in localized in vivo applications. *Advanced functional materials*, 23(5), 2013.

[292] Vincent H Ho, Nigel K Slater, and Rongjun Chen. ph-responsive endosomolytic pseudo-peptides for drug delivery to multicellular spheroids tumour models. *Biomaterials*, 32(11): 2953–8, 2011.

[293] Derek Marsh. *Handbook of Lipid Bilayers, Second Edition*. 2013.

[294] Jelena Drazenovic, Hairong Wang, Kristina Roth, Jiangyue Zhang, Selver Ahmed, Yanjing Chen, Geoffrey Bothun, and Stephanie L. Wunder. Effect of lamellarity and size on calorimetric phase transitions in single component phosphatidylcholine vesicles. *Biochimica et Biophysica Acta (BBA) - Biomembranes*, 1848(2):532 – 543, 2015.

[295] Bryan R. Cater, Dennis Chapman, Susan M. Hawes, and John Saville. Lipid phase transitions and drug interactions. *Biochimica et Biophysica Acta (BBA) - Biomembranes*, 363(1):54 – 69, 1974.

[296] Geoffrey D Bothun. Hydrophobic silver nanoparticles trapped in lipid bilayers: Size distribution, bilayer phase behavior, and optical properties. *Journal of Nanobiotechnology*, 6(1): 1–10, 2008.

[297] E Drolle, N Kučerka, M.I. Hoopes, Y Choi, J Katsaras, M Karttunen, and Z Leonenko. Effect of melatonin and cholesterol on the structure of dopc and dppc membranes. *Biochimica et Biophysica Acta (BBA) - Biomembranes*, 1828(9):2247–2254, 2013.

[298] J Gallová, D Uhríková, A Islamov, A Kuklin, and P Balgavý. Effect of cholesterol on the bilayer thickness in unilamellar extruded dlpc and dopc liposomes: Sans contrast variation study. *General physiology and biophysics*, 23(1):113–28, 4 2004.

[299] Andrew G Richter, Sergey A Dergunov, Bill Ganus, Zachary Thomas, Sai Pingali, Volker Urban, Yun Liu, Lionel Porcar, and Eugene Pinkhassik. Scattering studies of hydrophobic monomers in liposomal bilayers: An expanding shell model of monomer distribution. *Langmuir*, 27(7):3792–3797, 11 2011.

[300] Pavol Balgavy, Martina Dubnickova, Norbert Kucerka, Mikael A Kiselev, Sergey P Yaradaikin, and Daniela Uhrıikova. Bilayer thickness and lipid interface area in unilamellar extruded 1,2-diacylphosphatidylcholine liposomes: a small-angle neutron scattering study. *Biochimica et Biophysica Acta (BBA) - Biomembranes*, 1512(1):40–52, 2001.

[301] W Knoll, J Haas, HB Stuhrmann, and HH Fuldner. Small-angle neutron scattering of aqueous dispersions of lipids and lipid mixtures. a contrast variation study. *Journal of Applied Crystallographyl*, 14:191–202, 1981.

[302] V. I. Gordeliy, L. V. Golubchikova, A. Kuklin, A. G. Syrykh, and A. Watts. The study of single biological and model membranes via small-angle neutron scattering. *Trends in Colloid and Interface Science VII*, 93, 1993.

[303] Pavol Balgavy, Martina Dubnickova, Norbert Kucerka, Mikhail Kiselev, Sergey P Yaradaikin, and D Uhríkova. Bilayer thickness and lipid interface area in unilamellar extruded 1,2-diacylphosphatidylcholine liposomes: A small-angle neutron scattering study. *Biochimica et biophysica acta*, 1512:40–52, 2001.

[304] V. I. Gordeliy, L. V. Golubchikova, A. Kuklin, A. G. Syrykh, and A. Watts. *The study of single biological and model membranes via small-angle neutron scattering*, pages 252–256. Steinkopff, 1993.

[305] T. Nawroth, K. Dose, and H. Conrad. Neutron small angle scattering of detergent solubilized and membrane bound atp-synthase. *Physica B: Condensed Matter*, 156:489 – 492, 1989.

[306] V.I. Gordeliy, V.G. Cherezov, and J. Teixeira. Evidence of entropic contribution to "hydration" forces between membranes part ii. temperature dependence of the "hydration" force: a small angle neutron scattering study. *Journal of Molecular Structure*, 383(1):117 – 124, 1996.

[307] Michal Belička, Norbert Kučerka, Daniela Uhríková, Akhmed Kh. Islamov, Alexander I. Kuklin, Ferdinand Devínsky, and Pavol Balgavý. Effects of n,n-dimethyl-n-alkylamine-n-oxides on dopc bilayers in unilamellar vesicles: small-angle neutron scattering study. *European Biophysics Journal*, 43(4):179–189, 2014.

Papers and manuscripts

Soft Matter

PAPER

Cite this: *Soft Matter*, 2017, **13**, 7571

Influence of a pH-sensitive polymer on the structure of monoolein cubosomes

Monika Kluzek, *[a] Arwen I. I. Tyler, [bc] Shiqi Wang, [d] Rongjun Chen, [d] Carlos M. Marques, [a] Fabrice Thalmann, *[a] John M. Seddon [b] and Marc Schmutz [a]

Received 11th August 2017,
Accepted 30th September 2017

DOI: 10.1039/c7sm01620d

rsc.li/soft-matter-journal

Cubosomes consist in submicron size particles of lipid bicontinuous cubic phases stabilized by surfactant polymers. They provide an appealing road towards the practical use of lipid cubic phases for pharmaceutical and cosmetic applications, and efforts are currently being made to control the encapsulation and release properties of these colloidal objects. We overcome in this work the lack of sensitivity of monoolein cubosomes to pH conditions by using a pH sensitive polymer designed to strongly interact with the lipid structure at low pH. Our cryo-transmission electron microscope (cryo-TEM) and small-angle X-ray scattering (SAXS) results show that in the presence of the polymer the cubic phase structure is preserved at neutral pH, albeit with a larger cell size. At pH 5.5, in the presence of the polymer, the nanostructure of the cubosome particles is significantly altered, providing a pathway to design pH-responsive cubosomes for applications in drug delivery.

1 Introduction

Since the pioneering work of Luzzati[1,2] and Larsson[3,4] where the monoolein (MO)/water phase behaviour was studied for the first time,[5] several studies have explored the possible use of MO-based cubic phases as potential hosting matrices in pharmaceutical[6–10] and food applications.[11,12] The lipid cubic crystals have distinctive structural and chemical advantages, including highly ordered periodic structures, a large surface area of the lipid/water interface (400 m^2 g^{-1}),[13] tunable structural parameters, and provide a biocompatible platform for entrapment of proteins, peptides, and other biomolecules. A significant emphasis has been placed on cubic phases due to their polar/apolar continuous domains, which allow for the encapsulation of a broad range of hydrophilic/hydrophobic molecules[14] and for controlled release of a cargo, thus maintaining the therapeutic concentration range over a longer period of time.[7]

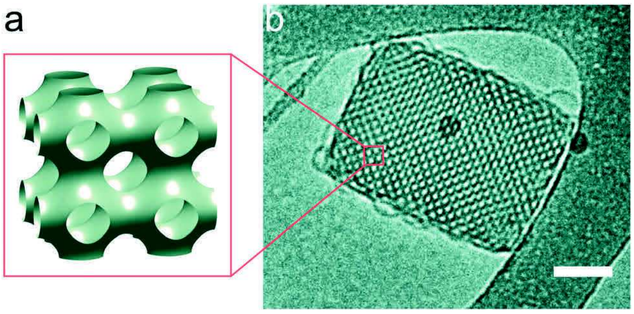

Fig. 1 (a) Graphical picture of an inverse cubic phase with primitive type structure *Im3m*, (b) cryo-TEM image of a monoolein cubosome stabilized with 5 wt% pluronic F127. Scale bar, 100 nm.

Cubosomes are stable nanoparticle dispersions formulated from bulk cubic phases (Fig. 1). They have been gathering increasing attention due to their potential applications in nanomedicine. However, pure MO systems alone do not respond to biological or external stimuli such as temperature, light, pH or ionic strength. Hence, significant efforts are being made towards more accurately controlled release of target biomolecules[15,16] and on modulating the release properties of the host–guest lipid cubic phases in response to specific external conditions.[17–21] This approach recently led to the development of stimuli responsive cubosome-based drug-delivery systems with the capacity of releasing their content in response to external triggers. Several authors have reported the effect of pH changes on mixtures of monoolein-charged lipid bicontinuous cubic phases.[22–25] These systems were shown to reversibly change from a cubic phase to an inverted hexagonal H_{II} or lamellar L_α phase in response to acidic (pH 2) conditions. This strategy was further

---

[a] *Université de Strasbourg, CNRS, Institut Charles Sadron, UPR022, 23 rue du Loess, 67034 Strasbourg Cedex, France. E-mail: monika.kluzek@ics-cnrs.unistra.fr, fabrice.thalmann@ics-cnrs.unistra.fr*
[b] *Department of Chemistry, Imperial College London, South Kensington Campus, London SW7 2AZ, UK*
[c] *Food Colloids and Processing Group, School of Food Science and Nutrition, University of Leeds, Leeds LS2 9JT, UK*
[d] *Department of Chemical Engineering, Imperial College London, South Kensington Campus, London SW7 2AZ, UK*

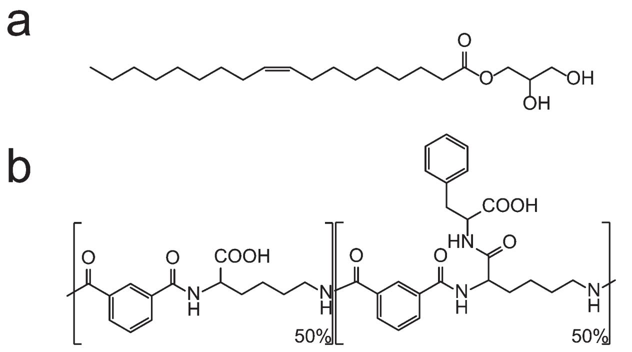

Fig. 2 The chemical structures of (a) monoolein (MO) and (b) poly(L-lysine-iso-phthalamide) chain grafted with phenylalanine (PP50).

exploited by Negrini *et al.*[21] who presented a pH-responsive cubic phase, where controlled release of cargo is achieved by adapted host–guest electrostatic interactions.

In this work, we describe a new MO-based pH-sensitive cubosome system that we have developed, loaded with a pH-sensitive polymer (see Fig. 2a). This polymer, a poly(L-lysine-iso-phthalamide) grafted with L-phenylalanine at the degree of grafting of 50% hereafter referred as PP50, is a promising pseudo-peptidic polymer whose hydrophilic/hydrophobic balance depends on external pH.[26–30] It is by design capable of mimicking the activity of membrane-penetrating peptides. The presence of carboxylic acid side groups causes reversible conformational changes in an aqueous environment from extended charged polyelectrolyte chains at neutral pH, to a globular state at acidic pH, resulting in a higher binding affinity for the lipid membrane, causing its subsequent disruption. Thus, PP50 is an appealing example of a stimulus-responsive material, potentially able to minimise drug losses at neutral pH while conversely triggering rapid intracellular drug release from the cubic phase in an acidic environment.

In this work, we describe how the pseudopeptide PP50 can be associated with standard MO cubosomes prepared by sonication and stabilization with the nonionic Pluronic F127 surfactant.[31] We have studied the structure of MO cubosomes incorporating a small amount (10 wt%) of PP50 at two distinct pH values: pH 7.5 and pH 5.5. The crystallographic structure and the cubic cell size were determined by SAXS, whilst the morphology and topology of the MO-cubosomes were characterised by cryo-TEM.

It was found that under neutral pH conditions, the presence of polymer preserves the original *Im*3*m* cubosome structure, while a significant amount of structural disruption, with a partial disappearance of the cubic phase, is observed under acidic conditions. This suggests that our novel system has a strong potential for developing pH-responsive encapsulation vectors based on cubosomes.

2 Experimental

Materials

Monoolein powder (1-oleoyl-*rac*-glycerol, C18:1c9, M_w = 356.54 Da), Pluronic F127 (PEO_{99}–PPO_{67}–PEO_{99}, M_w = 12 600 Da) and buffer components (HEPES, Citrate buffer) were supplied by Sigma-Aldrich, Co. (Saint-Quentin, France). All chemicals had purities of >98% and were used without further purification.

Polymer synthesis and characterisation

The polymer PP50 was synthesised as described previously.[32] Briefly, the parent polymer PLP (poly(L-lysine-iso-phthalamide)) was synthesized by polycondensation of L-lysine methyl ester dihydrochloride and iso-phthaloyl chloride followed by ester hydrolysis. After purification, PLP was conjugated with L-phenylalanine methyl ester hydrochloride by a DCC-coupling reaction followed by ester hydrolysis. The final PP50 was obtained after dialysis using a Visking membrane tubing (molecular weight cut-off, 12 000–14 000 Da). PP50 is a linear copolymer, composed of a sequence of 50% unsubstituted and 50% phenylalanine substituted L-lysine iso-phthalamide monomers (see Fig. 2b). The polymers used in the present study had a number averaged molecular weight M_n = 23.0 kDa, and a mass averaged molecular weight M_w = 45.8 kDa, as determined using an aqueous gel permeation chromatography (GPC) system (Viscotek, UK). The polymer is a weak acid polyelectrolyte, with an estimated ionization constant $pK_a \sim 6.5$.

Sample preparation

Colloidal dispersions of cubosomes were prepared as described by Landh.[33] Briefly, for each sample, 50 mg of pure lipid was dispersed in chloroform, and the organic solvent removed under a nitrogen stream followed by overnight vacuum pumping.

a. SAXS samples

The lipid deposit was hydrated with 94 wt% buffer solution (0.707 mL), and then subjected to 10 freeze–thaw cycles. The resulting lipid dispersion was a cubic phase in excess water (*Pn*3*m*, characterisation not shown). Following the freeze–thaw cycles, a Pluronic F127 aqueous solution was added (2.68 mg surfactant in 0.30 mL buffer) for the polymer free reference samples, while Pluronic F127 (2.68 mg) dispersed with PP50 (4.84 mg) in 0.294 mL of buffer solution, was added for polymer loaded samples, corresponding to a total volume of 1 mL of buffer.

b. Cryo-TEM samples

The preparation followed similar steps to the preparation of the X-ray samples, but using larger volumes of buffer. The lipid deposit was first hydrated with a buffer solution (1.288 mL), followed by 10 freeze–thaw cycles, and 2.68 mg of Pluronic F127 and 4.84 mg of PP50 polymer dispersed in 1.288 mL of buffer (2.576 mL total volume of a buffer) were added.

Samples were probe-sonicated (Bioblock VibraCell 72412) at 30% amplitude for 5 min total time at 1 s on/off cycle period to prevent overheating. The two hydration solutions used in the study were set to pH 7.5 with HEPES buffer (20 mM) and to pH 5.5 with citrate buffer (100 mM) prior to mixing with lipids. Hydration, sonication and stabilisation with the surfactants transformed the bicontinuous cubic phase into cubosome dispersions. Samples were then characterised by SAXS or cryo-TEM. Cryo-TEM imaging was performed with fresh samples (a couple of hours) while SAXS samples were prepared a day before being placed in the Synchrotron beam.

Cryo-TEM

A laboratory-built humidity-controlled vitrification system was used to prepare the samples for cryo-TEM. Humidity was kept close to 80% for all experiments and the temperature was set at 22 °C. 5 μL of the sample were placed onto a grid covered by the lacey carbon film (Ted Pella), which was rendered hydrophilic *via* glow discharge (Elmo, Cordouan Technologies). Excess sample was removed by blotting with filter paper and the sample grid was vitrified by rapid plunging into liquid ethane (−180 °C). The grids were kept in liquid nitrogen before being transferred into a Gatan 626 cryo-holder. Cryo-TEM imaging was performed on a FEI Tecnai G2 TEM (200 kV) under low dose conditions with an Eagle slow scan CCD camera.

Cryo-TEM image analysis

Fast Fourier transform and sizing of the nanoparticles were performed using ImageJ software (NIH, USA). The error in the determination of the lattice parameter from cryo-TEM images analysis was estimated at ± 5%.

SAXS

The cubosome structures were determined by small-angle X-ray scattering using beamline I22 at Diamond Light Source (DLS) with X-ray wavelengths of 0.73 Å. The 2-D powder diffraction pattern was recorded on an image-intensified Pilatus 2M detector. Silver behenate (a = 58.38 Å) was used to calibrate the small angle X-ray diffraction data for all measurements. SAXS data were analysed using the IDL-based AXcess software package, developed at Imperial College London. Details of the use of AXcess for data analysis can be found in ref. 34.

Dynamic light scattering (DLS)

The size and ζ-potential of the lipid nanoparticles were measured with a ZetaSizer Nano ZS (Malvern Instruments, UK) at 25 °C. Triplicate measurements with a minimum of 10 runs were performed for each sample.

3 Results and discussion

Effect of the addition of polymer on the nanoparticle size

Prior to structural analysis, cubosomes with and without polymer and the polymer solution (3 mg mL^{-1}) were characterised in terms of particle size and ζ-potential (Table 1). As previously reported, the polymer-free cubosome particles formed stable, milky dispersions with particle sizes ranging from 170 to 220 nm under both pH conditions studied. Incorporation of 10 wt% PP50 into the cubic phase at physiological pH moderately increased the size of the nanoparticles, whilst at pH 5.5 the change was more significant (283 nm). The polydispersity index (PDI) was estimated to be in the approximate range of 0.2–0.3, for all systems studied, indicating moderately heterogeneous systems. Moreover, particle dispersions stored at room temperature over a week showed no significant changes in the size and PDI, indicating physically stable systems.

The ζ-potentials of unloaded cubosomes were −1.2 and 1.1 mV for pH 7.5 and 5.5 respectively, and only a slight decrease of these values was observed upon polymer incorporation. This points to a marginal surface coverage of the particles by the negatively charged polymers.

SAXS measurements

The liquid-crystalline structure of MO cubosomes incorporated with the polymer was investigated using SAXS. Reference samples without polymer, at pH 7.5 and 5.5 (Fig. 3a and b), showed a sequence of three well-defined diffraction peaks with relative positions at ratios of $\sqrt{2}$, $\sqrt{4}$ and $\sqrt{6}$ respectively, which corresponds to a primitive *Im*3*m* cubic structure. For the sample without polymer at pH 7.5, the next peaks of this space group symmetry ($\sqrt{10}$ and $\sqrt{12}$) were also visible. The corresponding lattice parameters, a = 143.0 ± 0.1 Å and a = 137.3 ± 0.4 Å for cubosomes at pH 7.5 and pH 5.5 respectively, were in agreement with previously published data.[35] The SAXS profile of the cubosomes prepared with 10 wt% of polymer at pH 7.5 (Fig. 3c) displayed the same sequence of peaks, showing that the *Im*3*m* structure was preserved. The positions of the peaks indicated a lattice parameter of a = 163.2 ± 0.1 Å larger than the reference case, while the peak intensities relative to the diffuse background appeared slightly reduced (Fig. 3 and Table 2).

At lower pH (Fig. 3d), the SAXS data of the cubosome solution incubated with PP50 polymers looked significantly more diffuse. A sequence of well visible but smaller peaks with relative positions at $\sqrt{2}$, $\sqrt{4}$ and $\sqrt{6}$ respectively was observed, still consistent with a P-type *Im*3*m* structure with a = 167.2 ± 0.1 Å. In addition, a new peak at 50 Å (indicated by *) appeared, which was not related to the previous family of diffraction peaks.

Table 1 Hydrodynamic diameter and ζ-potential of cubosomes w/wo polymer and the pure PP50 solution under different pH conditions. Values are shown as averages over 3 samples with 10 runs each, and the standard deviation is used as an error estimate. As anticipated, the polymer was well dispersed at pH 7.5 and aggregated at pH 5.5 (DLS sizing data column)

	Size (nm)		ζ-Potential (mV)	
Sample	pH 7.5	pH 5.5	pH 7.5	pH 5.5
Cubosomes	178.1 ± 5.2	220.9 ± 4.2	−1.2 ± 0.8	1.1 ± 0.4
Cubosomes with PP50	212.7 ± 4.7	283.3 ± 3.6	−2.1 ± 1.0	0.11 ± 0.7
PP50	N/A[a]	50.7 ± 4.2	−13.1 ± 2.1	−28.4 ± 1.0

[a] Not enough scattering from the linear dispersed polymer chains.

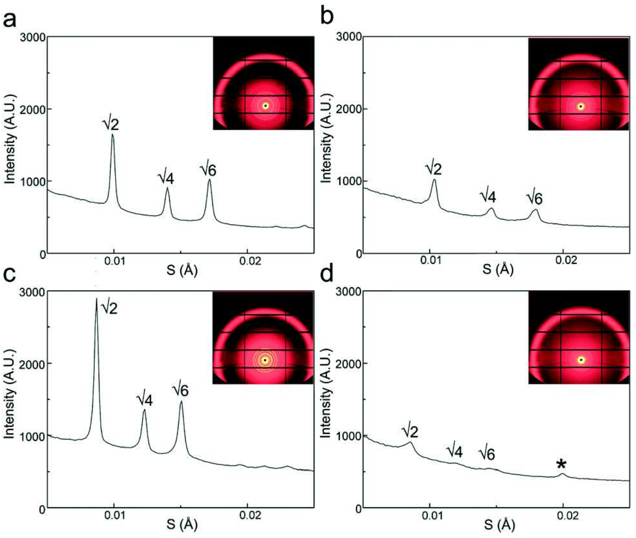

Fig. 3 1-D diffraction plots of intensity *vs.* scattering parameter $S = q/2\pi$ for MO-cubosomes doped with 10 wt% PP50 polymer. (a) Cubosomes at pH 7.5 (lattice parameter a = 143.0 ± 0.1 Å, peak positions: 100.8 Å, 71.4 Å, 58.2 Å); (b) cubosomes at pH 5.5 (lattice parameter a = 137.3 ± 0.4 Å, peak positions: 96.6 Å, 68.5 Å, 55.8 Å); (c) cubosomes with polymer at pH 7.5 (lattice parameter a = 163.2 ± 0.1 Å, peak positions: 114.9 Å, 81.6 Å, 66.8 Å); (d) cubosomes with polymer at pH 5.5 (lattice parameter a = 167.2 ± 0.1 Å, peak positions: 116.7 Å, 84.2 Å, 68.5 Å, 50 Å). The peak indicated by * corresponds to a spacing of 50 Å.

Cryo-TEM observations

We used cryo-TEM to visualize the nanostructure of the cubosome particles in both physiological pH 7.5 and acid pH 5.5 environments. Cryo-TEM images (Fig. 4a and b), combined with fast Fourier transform (FFT) analysis, revealed that at both pHs, the reference samples formed stable bicontinuous cubic phases with an *Im*3*m* symmetry and a measured lattice parameter of the order of 140 Å as commonly observed in previous preparations.[36,37] This indicates that pH alone does not influence the stability of MO cubosome particles. Moreover, the bilayer thickness, as determined by image analysis, was about 36 Å (Table 2) which was in excellent agreement with values reported elsewhere.[36]

The structural symmetry of the primitive *Im*3*m* cubic phase was clearly preserved upon incorporation of the polymer at physiological pH (Fig. 4c and d). More important, a corresponding analysis of the structural parameters showed that the presence of the polymer expanded the unit cell size a. This increase in lattice parameter was similar to what was observed in SAXS (Fig. 3c and Table 2). From the FFT analysis of a number of selected particles, a mean lattice parameter of 160 Å was obtained.

Remarkably, in the low pH regime (5.5), where PP50 is expected to interact strongly with the lipids, some clear disruption of the underlying cubic phase structure was observed (Fig. 4e and 5). A number of changes varied from particle to particle, and within a given particle. There was in some regions a significant collapse of the structure, with disappearance of the lattice structure. FFT analysis confirmed the absence of periodicity. In other regions, the cubic regions were preserved as in the reference sample.

Finally, one could find regions in particles displaying some apparent lamellar ordering, with an anisotropic orientation confirmed by FFT analysis. Whether the cubic structure disappeared totally or only partially, our cryo-TEM images demonstrated the pH dependent disruptive action of the polymer on the MO-bilayer within the cubic phase.

Measurements of cubic lipid phases, pure or with additives, are commonly carried out in buffer solutions of various chemical compositions, ionic strengths, *etc.* It has been reported that such parameters, like the presence of salts of different chemical natures, the exact pH, temperature and pressure values, might all influence the phase behaviour of these lyotropic liquid crystals. In the present study, the addition of 10 wt% polymer (with respect to the lipid mass) was accompanied by a 12% increase in the value of the unit cell size (from 143 to 163 Å) in HEPES buffer (pH 7.5).

Although the polymer cannot be unambiguously located within the sample, the cryo-TEM images and the sharp appearance of the SAXS peaks indicate that the particles were spatially homogeneous and that, if present inside, the polymer was evenly distributed. From the geometry of the primitive cubic structure, one could estimate the amount of water present in the particles compared to the bulk aqueous solution. Ignoring the Pluronic F127 and PP50, it is possible to relate the volume fraction of lipid Φ_l to the cell size a, and lipid length l in the parallel surface approximation:

$$\Phi_l = 2A_0\left(\frac{l}{a}\right) + \frac{4\pi\chi}{3}\left(\frac{l}{a}\right)^3 \qquad (1)$$

where A_0 and χ are respectively the ratio of the area of the minimal surface in the unit cell to the quantity (unit cell volume)$^{2/3}$, and the Euler–Poincare characteristic, which depends on the symmetry of the cubic phase.[38,39] In the case of the *Im*3*m* structure, the values are $A_0 = 2.3451$, and $\chi = -4$. Using the standard monoolein value l = 18 Å in the absence of PP50 at pH 7.5 (consistent with the bilayer thickness of 36 Å seen in cryo-TEM), one gets $\Phi_l = 0.555$. According to this value, 50 mg of monoolein were hydrated by about 40 mg of water. The free water (1 g or more) was present in much larger amount, showing that the cubosome structures

Table 2 Lattice parameters (a), calculated water volume fraction (ϕ_w) and water channel radius (r_w) of MO cubosomes w/wo polymer as a function of pH

	a^a (Å)		a^b (Å)		ϕ_w (%)		r_w (Å)	
Sample	pH 7.5	pH 5.5	pH 7.5	pH 5.5	pH 7.5	pH 5.5	pH 7.5	pH 5.5
Cubosomes	143.0 ± 0.1	137.3 ± 0.4	140.2 ± 0.2	139.0 ± 0.4	44.5 ± 0.1	42.5 ± 0.1	25.8 ± 0.1	24.0 ± 0.1
Cubosomes with PP50	163.2 ± 0.1	167.2 ± 0.1	163.0 ± 0.5	156.0 ± 0.9	50.4 ± 0.1	50.4 ± 0.1	31.8 ± 0.1	33.0 ± 0.1

[a] Measured by SAXS. [b] Obtained from Cryo-TEM images analysis of 7 cubosome nanoparticles.

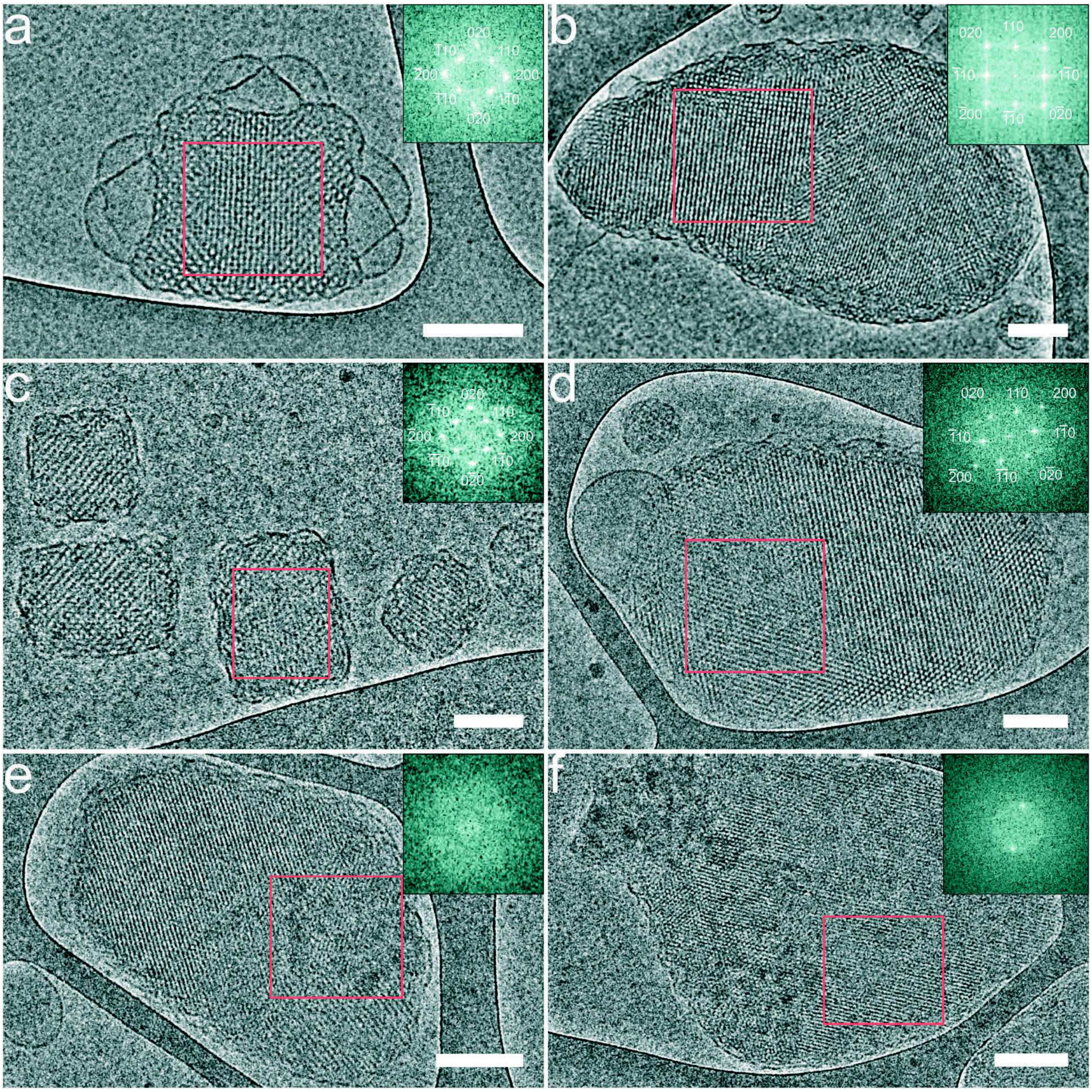

Fig. 4 Representative Cryo-TEM images of cubosome dispersions used in this study, with the corresponding fast Fourier transform (FFT) of red box areas (insets). Unloaded cubosome: (a) pH 7.5; (b) pH 5.5; (c and d) cubosome/PP50 at pH 7.5. (e and f) Cubosomes/PP50 at pH 5.5. FFT was used for determination of the structure of the liquid crystalline particles, independently from SAXS. Scale bar, 100 nm.

were in equilibrium with excess water. If PP50 did not penetrate the nanoparticles and was thus present only in the excess free aqueous solution, it could still act on the cubic phase indirectly, in a solvent-mediated way. An obvious mechanism would be depletion, with PP50 lowering the water chemical potential in the excess solvent region. One would expect to see in this situation a dehydration of the lipid phase, and some decrease in the lattice size, which was contrary to our present observations. With the PP50 being deprotonated at pH 7.5, its adsorption onto the cubosome particles' outer surface should confer them with a negative surface charge, with a correspondingly negative zeta potential. Table 1 indeed reveals that the zeta potential of cubosomes decreased by 0.9 mV in the presence of PP50. The change has the expected sign but was small in magnitude. We, therefore, doubt that PP50 covered the particle surface extensively. The most likely scenario was that PP50 penetrated into the cubic phase water channels. The PP50 sample used in the present study has a number average mass of $M_n = 23.0$ kDa, while the segment represented in Fig. 2b has a molar mass of 700 Da, with an estimated length of 30 Å for a diameter of 14 Å (using a molecular model). Taking $b = 30$ Å as the Kuhn segment length of the repeat units, the polymer consisting of 33 segments has a gyration radius $R_g = \sqrt{33}/\sqrt{6}b = 70$ Å. On the other hand, the water channel radius, r_w, can be estimated using the relation between r_w and the lattice parameter a:[40]

$$r_w = 0.305a - l \tag{2}$$

with a = 163 Å and l = 18 Å one finds r_w = 32 Å. Mobility and penetration of PP50 chains in the cubic nanostructure therefore seems a reasonable assumption.[41] The magnitude of the cell size variation, the uniformity of the structures, the lack of sensitivity to particle dilution and the relative size of the polymer and the cubic cell make of the penetration of PP50 into the cubosome particles the most likely possibility.

We discuss now the possible mechanisms for the cell size increase in the presence of the polymer. We observed first that pH reduction only marginally decreased the measured unit cell size of the reference samples by 6 Å. By comparison, the addition of PP50 at pH 7.5 increased this value by 20 Å. The change of electric charge on the polymer backbone when decreasing pH from 7.5 to 5.5 did not seem to be a prominent factor. The measured lattice parameter at pH 5.5 in the absence and presence of PP50 were 137 and 167 Å respectively. This suggests that electrostatic repulsion is not a likely candidate for explaining the observed swelling. Moreover, all experiments were done under buffered conditions, in which electrostatic interactions were strongly screened. At pH 7.5 it is unlikely that the polymer inserts deeply into the bilayer. Modifications are therefore probably induced by the interaction between the water-soluble polymer and the monoolein interface. For instance, changes in the structure and a decrease in the parameter size of cubic phases exposed to polysaccharides were reported by Mezzenga *et al.*[42] Whether the polymer is depleted or adsorbed by the membrane, its presence between the bicontinuous channels changes the free-energy at two levels. First, it induces direct interactions between different parts of the bilayer over the range of the polymer size. Secondly, the polymer–membrane interaction changes the curvature elastic constants of the bilayer, the bending rigidity κ and the Gaussian rigidity $\bar{\kappa}$. For depletion and equilibrium adsorption this is expected to decrease κ and increase $\bar{\kappa}$, while for inserted polymers, an increase in κ and a decrease in $\bar{\kappa}$ are expected.[43]

The observed swelling of the cubosomes at pH 7.5 suggests that the presence of PP50 promoted a reduction in the magnitude of the spontaneous monolayer curvature. Hence, the spontaneous curvature of the lipid bilayer towards the water region decreased, resulting in a higher water uptake capacity.

Table 2 lists the variation of the lattice parameter a, measured by SAXS, the size of water pores r_w and the water volume fractions Φ_w. As can be observed, the water channel size increased while some polymer was incorporated into the cubic phase. At physiological pH, this suggests that the polymer behaved like a hydration-modulating agent *i.e.* favoured the hydration of the *Im*3*m* phase without changing the structure (Fig. 3c and d). Similar swelling behaviour of cubic phases upon addition of additives was reported previously by Angelov[44] and Negrini *et al.*[20]

Polymer-induced structural changes under acidic pH conditions

The well-resolved diffraction peaks obtained in SAXS (Fig. 3a–c) at pH 7.5 or pH 5.5 without PP50 indicate well-ordered cubic phases. The cryo-TEM images of a selection of particles show cubic ordering established across the whole particles. FFT image analysis displays characteristic fourfold symmetric patterns depending on the orientation of the particles with respect to the electron beam (Fig. 4a–d). We conclude that the reference sample and the polymer loaded sample at pH 7.5 are composed of crystalline pieces of the *Im*3*m* bicontinuous cubic phase.

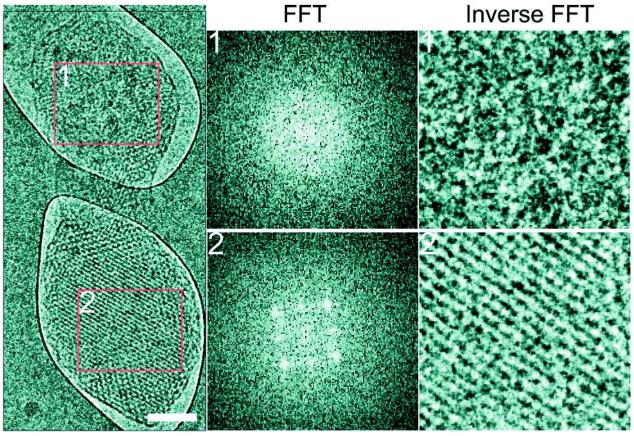

Fig. 5 Cryo-TEM images of a single cubosome at pH 5.5 with incorporated polymer. The red boxes represent the areas used for FFT calculations. Scale bar, 100 nm. (a = 156.0 Å). (1) Upper part of particle; (2) lower part of particle.

Fig. 4e, f and 5 show a selection of nanoparticles with PP50 at pH 5.5. We could see large disordered regions, with no visible periodic ordering, confirmed by the absence of peaks in the FFT image analysis. Disordered and cubic ordered regions coexisted, sometimes within the same particle. Fig. 5 shows a single particle in the same field of view: the upper part of the particle was mostly disordered, while the bottom of the particle still presented a cubic ordering. The particle in Fig. 4f displayed some apparent lamellar order, associated with two spots in its FFT pattern. Therefore, cubosomes with polymer in acidic conditions can be seen as a collection of totally or partially disordered particles coexisting with cubic and lamellar ordered particles. The image analysis performed on the lamellar regions leads to a repeat distance comprised between 65 and 75 Å. The TEM observations account well for the observed SAXS patterns. Indeed, with only a small fraction of the particles retaining their cubic order, the *Im*3*m* diffraction peaks are faint in Fig. 4d. The observed peak at q^* is consistent with a lamellar phase with a repeat distance d = 50 Å rather different from the lamellar periodicity estimated by Cryo-TEM. This discrepancy might be due to a slow time evolution of the cubosome structure interacting with the hydrophobic polymer. The SAXS and the Cryo-TEM measured values could correspond to different ageing stages of the samples. We discussed here the effect of 10 wt% PP50, a compromise between the efficiency of the action and the required amount of polymer, preliminary results from smaller or larger concentrations show as expected corresponding trends.

4 Conclusions

We prepared pH-sensitive cubosomes from monoolein. Besides the monoglyceride, cubosomes contained Pluronic F127, a standard non-ionic surfactant and PP50, a pH-sensitive pseudo-peptide. As expected, F127 swelled the liquid crystal, introducing a primitive cubic phase while stabilizing the monoolein cubic phase particles. Cubosomes without PP50 were not prone to disruption under acidic conditions at pH 5.5. Lipid particles with added PP50 were successfully disrupted when exposed to acidic conditions, paving the way for applications in drug delivery.

Conflicts of interest

There are no conflicts to declare.

Acknowledgements

M. Kluzek, F. Thalmann, C. M. Marques, S. Wang, R. Chen, J. M. Seddon and M. Schmutz all acknowledge funding from the European FP7-MSCA International Training Network (ITN) SNAL 608184 (Smart Nano-objects for Alteration of Lipid-bilayers) to support the work. We thank Diamond Light Source (UK) for provision of X-ray beamtime (SM14217), Dr Andy Smith for his support and assistance and Dr Olga Shebanova for her assistance in using beamline I22. Cryo-TEM images were obtained using the ISO9001 Electron Microscopy platform at ICS Strasbourg.

References

1 P. Mariani, V. Luzzati and H. Delacroix, *J. Mol. Biol.*, 1988, **204**(1), 165–189.
2 V. Luzzati, A. Tardieu, T. Gulik-Krzywicki, E. Rivas and F. Reiss-Husson, *Nature*, 1968, **220**(5166), 485–488.
3 K. Larsson, *Nature*, 1983, **304**(5927), 664.
4 K. Larsson, *Curr. Opin. Colloid Interface Sci.*, 2000, **5**(1–2), 64–69.
5 H. T. McMahon and J. L. Gallop, *Nature*, 2005, **438**(7068), 590–596.
6 X. Mulet, B. J. Boyd and C. J. Drummond, *J. Colloid Interface Sci.*, 2013, **393**, 1–20.
7 B. J. Boyd, D. V. Whittaker, S.-M. Khoo and G. Davey, *Int. J. Pharm.*, 2006, **309**(1–2), 218–226.
8 S. Engstrom, *Lipid Technol.*, 1990, **2**, 42–45.
9 M. Nasr, M. K. Ghorab and A. Abdelazem, *Acta Pharm. Sin. B*, 2015, **5**(1), 79–88.
10 J. C. Shah, Y. Sadhale and D. Chilukuri, *Adv. Drug Delivery Rev.*, 2001, **47**(2–3), 229–250.
11 K. Larsson, *Curr. Opin. Colloid Interface Sci.*, 2009, **14**(1), 16–20.
12 A.-Y. Idit, D. Libster, A. Aserin and N. Garti, *Curr. Opin. Colloid Interface Sci.*, 2009, **14**(1), 21–32.
13 C. J. Drummond and C. Fong, *Curr. Opin. Colloid Interface Sci.*, 1999, **4**(6), 449–456.
14 W.-K. Fong, N. Malic, R. A. Evans, A. Hawley, B. J. Boyd and T. L. Hanley, *Biointerphases*, 2012, **7**(1–4), 1–5.
15 M. L. Lynch, A. Ofori-Boateng, A. Hippe, K. Kochvar and P. T. Spicer, *J. Colloid Interface Sci.*, 2003, **260**(2), 404–413.
16 J. Clogston, G. Craciun, D. J. Hart and M. Caffrey, *J. Controlled Release*, 2005, **102**(2), 441–461.
17 R. Negrini, W.-K. Fong, B. J. Boyd and R. Mezzenga, *Chem. Commun.*, 2015, **51**(30), 6671–6674.
18 E. Nazaruk, M. Szlezak, E. Górecka, R. Bilewicz, Y. M. Osornio, P. Uebelhart and E. M. Landau, *Langmuir*, 2014, **30**(5), 1383–1390.
19 B. Angelov, A. Angelova, V. M. Garamus, G. Lebas, S. Lesieur, M. Ollivon, S. S. Funari, R. Willumeit and P. Couvreur, *J. Am. Chem. Soc.*, 2007, **129**(44), 13474–13479.
20 R. Negrini and R. Mezzenga, *Langmuir*, 2012, **28**(47), 16455–16462.
21 R. Negrini, A. Sanchez-Ferrer and R. Mezzenga, *Langmuir*, 2014, **30**(15), 4280–4288.
22 Y. Aota-Nakano, S. J. Li and M. Yamazaki, *Biochim. Biophys. Acta, Biomembr.*, 1999, **1461**(1), 96–102.
23 Y. Okamoto, S. M. Masum, H. Miyazawa and M. Yamazaki, *Langmuir*, 2008, **24**(7), 3400–3406.
24 R. Negrini and R. Mezzenga, *Langmuir*, 2011, **27**(9), 5296–5303.
25 T. Oka, T. Saiki, J. M. Alam and M. Yamazaki, *Langmuir*, 2016, **32**(5), 1327–1337.
26 V. Ho, N. Slater and R. Chen, *Biomaterials*, 2011, **32**(11), 2953–2958.
27 R. Chen, S. Khormaee, M. E. Eccleston and N. Slater, *Biomaterials*, 2009, **30**(10), 1954–1961.
28 S. Zhang, A. Nelson, Z. Coldrick and R. Chen, *Langmuir*, 2011, **27**(13), 8530–8539.
29 A. L. Lynch, R. Chen, P. J. Dominowski, E. Y. Shalaev, R. J. Yancey Jr. and N. K. H. Slater, *Biomaterials*, 2010, **31**, 6096–6103.
30 A. L. Lynch, R. Chen and N. K. H. Slater, *Biomaterials*, 2011, **32**, 4443–4449.
31 J. Y. T. Chong, X. Mulet, L. J. Waddington, B. J. Boyd and C. J. Drummond, *Soft Matter*, 2011, **7**(10), 4768–4777.
32 R. Chen, M. E. Eccleston, Z. Yue and N. K. H. Slater, *J. Mater. Chem.*, 2009, **19**(24), 4217–4224.
33 T. Landh, *J. Phys. Chem.*, 1994, **98**(34), 8453–8467.
34 J. M. Seddon, A. M. Squires, C. E. Conn, O. Ces, A. J. Heron, X. Mulet, G. C. Shearman and R. H. Templer, *Philos. Trans. R. Soc., A*, 2006, **364**(1847), 2635–2655.
35 A. Falchi, A. Rosa, A. Atzeri, A. Incani, S. Lampis, V. Meli, C. Caltagirone and S. Murgia, *Toxicol. Res.*, 2015, **4**(4), 1025–1036.
36 G. Popescu, J. Barauskas, T. Nylander and F. Tiberg, *Langmuir*, 2007, **23**(2), 496–503.
37 J. Gustafsson, H. Ljusberg-Wahren and M. Almgren, *Langmuir*, 1996, **12**(20), 4611–4613.
38 P. Garstecki and R. Hołyst, *Langmuir*, 2002, **18**(7), 2519–2528.
39 D. C. Turner, Z.-G. Wang, S. M. Gruner, D. A. Mannock and R. N. McElhaney, *J. Phys. II*, 1992, **2**(11), 2039–2063.
40 J. Briggs, H. Chung and M. Caffrey, *J. Phys. II*, 1996, **6**(5), 723–751.
41 R. Ghambari, S. Assenza, A. Saha and R. Mezzenga, *Langmuir*, 2017, **33**(14), 3491–3498.
42 R. Mezzenga, M. Grigorov, Z. Zhang, C. Servais, L. Sagalowicz, A. I. Romoscanu, V. Khanna and C. Meyer, *Langmuir*, 2005, **21**(14), 6165–6169.
43 T. Bickel and C. M. Marques, *J. Nanosci. Nanotechnol.*, 2006, **6**(8), 2386–2395.
44 B. Angelov, A. Angelova, M. Ollivon, C. Bourgaux and A. Campitelli, *J. Am. Chem. Soc.*, 2003, **125**(24), 7188–7189.

Monika KLUZEK

Lipid membrane alteration under exposure to α-Cyclodextrins and pH-responsive pseudopeptide polymers

Résumé

Le développement de nanotransporteurs basés sur des lipides, des polymères et des nanoparticules avec des propriétés «sur mesure» pour augmenter l'efficacité de médicaments, fait l'objet de recherches intensives. Toutefois, la physico-chimie subtile des intéractions polymères-lipides and nanoparticules-lipides présente encore de larges domaines mal compris et de nombreuses questions sans réponse. Ce projet de recherche doctoral utilise des techniques de visualisation (Cryo-MET, LSCM), et de caractérisation (ITC, DSC, SAXS, SANS, QCM-D) avancées pour obtenir des informations nouvelles sur les mécanismes d'interaction entre des Cyclodextrines-α d'autre part, des polymères sensibles au pH d'autre part, et des bicouches modèle de DOPC. La forte influence de ces deux composés sur ces systèmes modèle élucide certains aspects relatifs à la toxicité vis-à-vis des membranes biologiques et suggère de nouvelles approches pour des applications pharmaceutiques.

Résumé en anglais

The primary goal of nanomedicine is to improve clinical outcomes. To this end, the development of nanocarriers based on lipids, polymers and nanoparticles with tailor-made properties that enhance the *in vivo* potency of drugs is a subject of intense research. However, the subtle physical-chemistry of the polymer-lipid and nanoparticle-lipid interactions still present many poorly understood fields of investigation as well as unanswered questions. This doctoral research project utilizes state-of-the-art visualization (Cryo-TEM, SLCM) and characterization (ITC, DSC, SAXS, SANS, QCM-D) techniques to gain novel insights into the interaction between α-Cyclodextrins in the first hand, a pH-responsive polymer in the other hand, and model DOPC bilayers. The strong influence of both compounds on these model systems elucidate some aspects regarding biological membrane toxicity and suggests novel strategies for pharmaceutical applications.